JACOBS UNIVERSITY

Supramolecular Sensing Based on Liposomes and Gold Nanoparticles

by

Mohamed Nilam

A Thesis submitted in partial fulfillment

of the requirements for the degree of

Doctor of Philosophy

in Chemistry

Approved Dissertation Committee

Prof. Dr. Werner M. Nau

Jacobs University Bremen

Dr. Andreas Hennig

Jacobs University Bremen

Prof. Dr. Mathias Winterhalter

Jacobs University Bremen

Dr. Frank Biedermann

Karlsruhe Institute of Technology

Date of Defense: 16. 01. 2020

Department of Life Sciences and Chemistry

Statutory Declaration

Family Name, Given/First Name	Mohamed Nilam
Matriculation number	20331368
What kind of thesis are you submitting: Bachelor-, Master- or PhD-Thesis	PhD-Thesis

English: Declaration of Authorship

I hereby declare that the thesis submitted was created and written solely by myself without any external support. Any sources, direct or indirect, are marked as such. I am aware of the fact that the contents of the thesis in digital form may be revised with regard to usage of unauthorized aid as well as whether the whole or parts of it may be identified as plagiarism. I do agree my work to be entered into a database for it to be compared with existing sources, where it will remain in order to enable further comparisons with future theses. This does not grant any rights of reproduction and usage, however.

The Thesis has been written independently and has not been submitted at any other university for the conferral of a PhD degree; neither has the thesis been previously published in full.

German: Erklärung der Autorenschaft (Urheberschaft)

Ich erkläre hiermit, dass die vorliegende Arbeit ohne fremde Hilfe ausschließlich von mir erstellt und geschrieben worden ist. Jedwede verwendeten Quellen, direkter oder indirekter Art, sind als solche kenntlich gemacht worden. Mir ist die Tatsache bewusst, dass der Inhalt der Thesis in digitaler Form geprüft werden kann im Hinblick darauf, ob es sich ganz oder in Teilen um ein Plagiat handelt. Ich bin damit einverstanden, dass meine Arbeit in einer Datenbank eingegeben werden kann, um mit bereits bestehenden Quellen verglichen zu werden und dort auch verbleibt, um mit zukünftigen Arbeiten verglichen werden zu können. Dies berechtigt jedoch nicht zur Verwendung oder Vervielfältigung.

Diese Arbeit wurde in der vorliegenden Form weder einer anderen Prüfungsbehörde vorgelegt noch wurde das Gesamtdokument bisher veröffentlicht.

26. 11. 2019, Mohamed Nilam
Date, Signature

To my beloved wife

“Life is and will remain an equation incapable of solution, but it contains certain known factors.”

Nikola Tesla

Abstract

The goal of my Ph.D. thesis is the development of supramolecular sensing ensembles based on host-guest complexes for the detection of biological molecules and for monitoring membrane translocation as well as enzymatic transformation. Moreover, these host-guest complexes can be utilized to characterize mixed ligand gold nanoparticles and the deaggregation of perylene-based dyes.

The first part of the thesis focuses on the development of novel, robust, simple, and economic fluorescence-based enzyme assay. An analytical technique has been developed for the continuous monitoring of ornithine decarboxylase (ODC) activity by fluorescence spectroscopy. The assay is composed of a reporter pair, which includes the macrocycle cucurbit[6]uril (CB6) and the fluorescent dye *trans*-4-[4-(dimethylamino)styryl]-1-methylpyridinium iodide (DSMI). Macrocycle (CB6) has a significantly higher binding constant to certain biogenic amines, in particular to the ODC product putrescine, such that the assay with CB6 is much more sensitive. The performance of the assay for the screening was also evaluated in a microplate reader format, which provided an excellent *Z*'-factor, indicating its potential for high-throughput screening (HTS).

The second part of the thesis introduces a fluorescence-based biomembrane assay for molecular recognition by the macrocyclic host inside the liposome. In general, supramolecular receptor molecules suffer from low affinity to analytes; therefore, we have introduced a liposome-based sensing approach based on the supramolecular tandem membrane assay principle. The liposome-encapsulated receptor molecules provide higher sensitivity than a homogeneous solution. Most of the analytes could be detected at nanomolar concentrations through this liposome enhanced sensing approach.

The third part of the thesis focuses on the determination of membrane permeability and activation energy. Time-resolved monitoring of membrane translocation of analytes is of utmost importance in membrane research. Existing methods are limited to single point determinations or flat synthetic membranes, limiting biologically relevant kinetic parameters (permeation rate constant, permeation coefficients). We have introduced a fluorescent artificial receptor membrane assay (FARMA), which is used to monitor in real-time the permeation of indole derivatives through liposomal membrane. FARMA method is a label-free method that enabled the determination of permeation rate and permeability coefficients. FARMA is also applicable to determine the fast permeating analyte tryptophan methyl ester passing through the liposomal membrane using stopped-flow fluorescent measurements. Furthermore, to study the effect of phase transitions on membrane permeability, we have performed experiments with 1,2-dipalmitoyl-*sn*-glycero-3-phosphocholine (DPPC)/,2-dioleoyl-*sn*-glycero-3-phospho-L-serine (DOPS) vesicles, which were in perfect agreement with the biphasic nature of the lipids. During the transport of indole derivatives through DPPC/DOPS liposomes, the expected non-linearity was observed in the Arrhenius plot.

The fourth part of the thesis focuses on the characterization of mixed ligand gold nanoparticles and the sensing of the lysine decarboxylase product. The quantification of the ligand density of modified gold nanoparticles is technically challenging, but is of utmost importance for quality control in many applications. Herein, we describe the characterization of mixed ligand shells on gold nanoparticles by a simple, fast, straightforward, and sensitive colorimetric method and a CB7 supramolecular assay to assess the total ligand density and accessible ligand density. The decarboxylase enzyme activity could be monitored by a

colorimetric method based on gold nanoparticles aggregation. Substrate decarboxylation, resulting in the product (diamine), triggered gold nanoparticles aggregation, thus changing the color of the gold nanoparticles solution. In the last part, we report that host-guest complexation affects aggregation of perylene diimide (PDI) dyes, wherein complexation of PDIs by CB7 and CB8 enhances the fluorescence and reduces the self-aggregation of the PDI in aqueous solution.

Acknowledgements

I would like to show my greatest appreciation to Prof. Dr. Werner M. Nau for providing me the opportunity to pursue the Doctor of Philosophy. I am so profoundly grateful for his help, professionalism, valuable guidance, and financial support throughout my Ph.D., and I do not have enough words to express my deep and sincere appreciation.

I would also like to thank Dr. Andreas Hennig, and I cannot say thank you enough for his tremendous support and help. I feel motivated and encouraged every time I attend his meeting, without his encouragement and guidance, this thesis would not have materialized.

Special thanks go to Dr. Khaleel Assaf to collaborate on different projects with me and sharing his knowledge in various aspects and always being helpful and humble with assisting me. I am also thankful to Prof. Aurica Farcas for collaborating with me and sharing knowledge in rotaxane synthesis. I would like to gratefully acknowledge Prof. Dr. Mathias Winterhalter and Dr. Frank Biedermann for accepting to be members of my thesis committee.

I am also thankful to all former and present members of the Nau group for collaborative work and fruitful discussion. In particular, I thank Dr. Alexandra Lazar, Dr. Andrea Barba-Bon, Dr. Suhang He, Dr. Chusen Huang, Dr. Shuai Zhang, Dr. Maik Jacob, Thomas Schwarzlose, Mohammad Al-Najjar, Yan Liu-Cen, Yao Chen and Shreya Karmacharya. Also, I thank my best friend Mahmoud Aljoumhawy for sharing with me a pleasant and challenging time in Bremen.

I also thank Deutsche Forschungsgemeinschaft (DFG), Deutsche Akademischer Austauschdienst (DAAD) and European Screeningport GmbH, Hamburg for financial support.

Last but certainly not least, I must express my profound gratitude to my parents and my wife, providing me with unfailing support and continuous encouragement throughout my years of studies. This accomplishment would not have been possible without them. Thank you!

List of Publications

1. **Nilam, M**.; Gribbon, P.; Reinshagen, J.; Cordts, K.; Schwedhelm, E.; Nau, W. M.; Hennig, A., A Label-Free Continuous Fluorescence-Based Assay for Monitoring Ornithine Decarboxylase Activity with a Synthetic Putrescine Receptor. *SLAS Discov.* (formerly *J. Biomol. Screen.*) **2017**, *22*, 906-914.
2. **Nilam, M**.; Hennig, A.; Nau, W. M.; Assaf, K. I., Gold Nanoparticle Aggregation Enables Colorimetric Sensing Assays for Enzymatic Decarboxylation. *Anal. Methods* **2017**, *9*, 2784-2787.
3. Zhang, S.; Domínguez, Z.; Assaf, K. I.; **Nilam, M**.; Thiele, T.; Pischel, U.; Schedler, U.; Nau, W. M.; Hennig, A., Precise Supramolecular Control of Surface Coverage Densities on Polymer Micro-and Nanoparticles. *Chem. Sci.* **2018**, *9*, 8575-8581.
4. Alnajjar, M. A.; Bartelmeß, J.; Hein, R.; Ashokkumar, P.; **Nilam, M**.; Nau, W. M.; Rurack, K.; Hennig, A., Rational Design of Boron-dipyrromethene (BODIPY) Reporter Dyes for Cucurbit[7]uril. *Beilstein J. Org. Chem.* **2018**, *14*, 1961-1971.
5. **Nilam, M**.; Ahmed, M.; Alnajjar, M. A.; Hennig, A., Characterization of Mixed-Ligand Shells on Gold Nanoparticles by Transition Metal and Supramolecular Surface Probes. *Analyst* **2019**, *144*, 579-586.
6. Farcas, A.; Liu, Y.-C.; **Nilam, M**.; Balan-Porcarasu, M.; Ursu, E.-L.; Nau, W. M.; Hennig, A., Synthesis and Photophysical Properties of Inclusion Complexes Between Conjugated Polyazomethines with γ-Cyclodextrin and its Tris-O-methylated Derivative. *Eur. Polym. J.* **2019**, *113*, 236-243.
7. Assaf, K. I.; Begaj, B.; Frank, A.; **Nilam, M**.; Mougharbel, A. S.; Kortz, U.; Nekvinda, J.; Grüner, B.; Gabel, D.; Nau, W. M., High-Affinity Binding of Metallacarborane Cobalt Bis(dicarbollide) Anions to Cyclodextrins and Application to Membrane Translocation. *J. Org. Chem.* **2019**, *84*, 11790-11798.
8. Barba-Bon, A.; **Nilam, M.;** Hennig, A., Supramolecular Chemistry in the Biomembrane. *ChemBioChem*, DOI:10.1002/cbic.201900646.

Manuscripts in Preparation

1. **Nilam, M.**; Collin, S.; Karmacharya, S.; Nau, W. M.; Hennig, A., Determination of Membrane Permeability and Activation Energy by Fluorescent Artificial Receptor Membrane Assays (FARMA) *Manuscript in Preparation.*
2. **Nilam, M.**; Karmacharya, S.; Nau, W. M.; Hennig, A., Liposome Enhanced Sensing, *Manuscript in Preparation.*
3. **Nilam, M.**; Huang, C.; Karmacharya, S.; Aryal, G. H.; Huang, L.; Nau, W. M.; Assaf, K. I., Host-Guest Complexation Affects Perylene-Based Dye Aggregation, *Manuscript in Preparation.*

List of Attended Conferences

I have attended the following conferences during my Ph.D. studies.

1. Life Sciences Meeting, Bremen, 01.06.2015. Poster: “Towards Fluorescent Supramolecular Tandem Assays for L-Arginine:Glycine Amidinotransferases (AGAT)”.
2. Suprachem, 24-26.02.2019, Würzburg. Poster: “Determination of Membrane Permeability and Activation Energy by Fluorescent Artificial Receptor Membrane Assays (FARMA)”.
3. Indo-German Workshop, Multivalent and Adaptive Bioinspired Materials, 25-27.09.2019, Essen. Poster: “Determination of Activation Energies for Membrane Permeation by Using Supramolecular Host-Guest Reporter Pairs”.

Table of Contents

Chapter 1

Introduction

Chapter 1

1. Introduction

1.1 Supramolecular Host-Guest Complexes

The study of supramolecular chemistry focused on non-covalent interaction within and between molecules. Supramolecular chemistry is specified as the chemistry that goes beyond the covalent bond and the individual molecules.[1] In biological systems, natural molecules such as proteins, nucleic acids, lipids, and their multimolecular complexes, have been the important source for the supramolecular research field. In 1890, the German scientist Emil Fischer explained non-covalent interaction *via* "lock and key" principle, where substrate bind to the enzyme active site.[2] To understand the non-covalent interaction, Cram,[3] Lehn,[4] and Pedersen[5] synthesized different host molecules such as crown ethers, cryptands, cavitands, and carcerands. These host molecules are able to encapsulate a variety of guest molecules and change the chemical reactivity. For instance, highly reactive, unstable, antiaromatic cyclobutadiene became stable at ambient temperature, when encapsulated inside a carcerand cavity.[6] Further, the supramolecular host-guest complex provides a robust platform to analyte recognition,[7] delivery of drug molecule to a target site,[8] catalysis of chemical reaction,[9] and synthesis of macrocycle and polymer using template effect.[10] Recently, the supramolecular chemist has begun to handle larger complex host structure, e.g., cyclodextrins,[11] cucurbiturils,[12] calixarenes[13] and resorcinarenes.[14] In this chapter, I will focus on the use of the macrocyclic hosts, cucurbiturils in combination with fluorescent dyes.

1.2 Cucurbiturils

Cucurbit[*n*]urils (CB*n*) are a class of cyclic oligomers of *n* glycoluril units self-assembled from the acid-catalyzed condensation reaction of glycoluril and formaldehyde.[15] The parent member, CB6, was synthesized by Behrend and coworkers in 1905 and known as Behrend's polymer.[16] The exact molecular structure remained unclear until 1981 when Mock and coworkers established the macrocyclic structure, which is composed of six glycoluril units and connected by twelve methylene groups in a pumpkin shape.[17] This initial discovery is reinforced to synthesis new CB*n* homologues such as CB5, CB7, CB8, CB10, and CB14 by the research groups of Kim, Day, and Tao.[18] Currently, research based on cucurbiturils has overcome most of the early problems, for instance, poor solubility, unavailability of homologues of the different sized hosts, methods for preparing functionalized cucurbiturils and provides an excellent platform for fundamental molecular recognition and self-assembly studies.

1.3 Molecular Recognition of Cucurbit[*n*]urils

Macrocycle CB5 is the smallest unit in the cucurbiturils family, and synthesis of CB5 was first reported by Kim and coworkers.[18a] The limited cavity volume of CB5 restricts the encapsulation of guest molecules compared to the larger homologues of the CB*n* family. The binding affinities of CB5 with respect to metal ions and organic cations ($K_a \sim 10^3\ M^{-1}$), which is bound to the portal of CB5.[7a] Furthermore, recently, Nau and coworkers demonstrated that the encapsulation of noble gases inside the cavity of CB5 in an aqueous environment.[19] The limited size of decamethyl-CB5 is highly suitable to bind gases such as N_2, O_2, CO_2, and CO.[20] The most common and abundant homolog is CB6, which is well-known to bind

aliphatic diamines. The binding affinity is in the range of 10^2 - 10^8 M^{-1} depending on the alkyl chain length.[7a] Further, CB6 has a moderate binding affinity in water with neutral and cationic organic species.[21]

Chart 1.1. Chemical structures of cucurbiturils in different sizes.

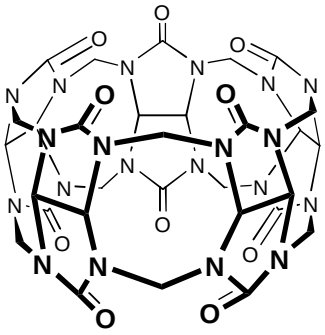

cucurbit[5]uril

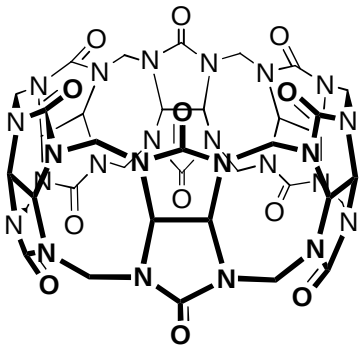

cucurbit[6]uril

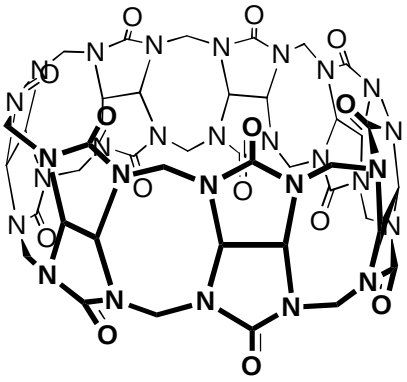

cucurbit[7]uril

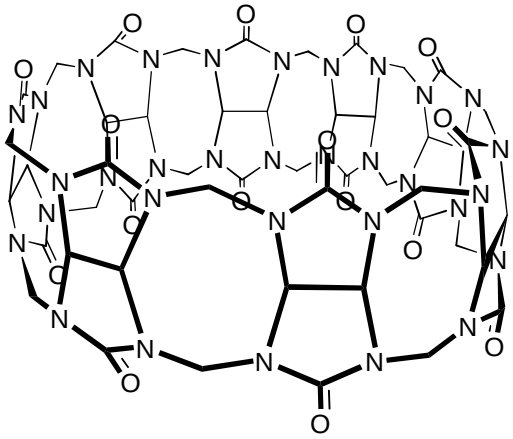

cucurbit[8]uril

The homologue CB7 has larger cavity size and higher aqueous solubility relative to the CB6, such that CB7 can encapsulate a wide range of analytes, particularly adamantylamine and ferrocene derivatives associated with higher binding affinity $K_a > 10^{12}$ M^{-1}. This bulky molecule (adamantylamine and ferrocene) perfectly matched the cavity size of CB7 and therefore release the high energy water molecules from the macrocycle cavity.[22] CB8 has larger cavity volume than CB7

and the larger cavity of CB8 allows for the encapsulation of one aromatic guest molecules or two molecules.[23] For instance, electron-deficient methyl viologen (MV) forms a 1:1 complex with CB8 in water with an association constant of 1.1×10^5 M^{-1}, and further, the addition of electron-rich 2,6-dihydroxynapthalene to the MV•CB8 complex resulted in ternary complex with electron donor-acceptor pair.[24]

1.4 Cucurbit[*n*]uril and Fluorescent Dye-Based Sensor Systems

The inclusion of a fluorescent dye into cucurbit[*n*]urils can alter the photophysical properties of the fluorescent dye. Several studies have investigated the change of photophysical properties upon complexation.[12] Conventional, supramolecular sensor systems were designed based on the "receptor-spacer-reporter" system, where the macrocycle acts as a receptor for molecular recognition and dye molecules acts as a reporter. However, this system is required extensive synthesis.[25] Additionally, Anslyn and coworkers developed indicator displacement assay (IDA). With these systems, addition of analytes displaces the indicator from the receptor molecule, resulting in optical signal modulation.[26] Displacement of the dye from the receptor molecule recovers the original fluorescence of the dye. This changes the photophysical properties upon complexation with macrocycle and decomplexation due to an analyte. This reporting element is called "reporter pair" or "chemosensing ensemble."

Encapsulation of the dye molecule inside the macrocycle, alters the fluorescence of the dye molecule due to following reason: *i*) Protection by macrocycle from quencher and solvent[27], *ii*) dye molecule is located inside hydrophobic environment,[28] *iii*) rotational and vibrational freedom of the dye molecules is restricted inside the macrocycle.[29] In the case of cucurbiturils, ion-dipole

interactions between carbonyl groups and cationic dyes play a vital role in altering the photophysical properties of the dye. For instance,host-assisted dye protonation increased the fluorescence of the dye upon complexation with CB7.[30]

1.5 Supramolecular Tandem Enzyme Assay

Tandem assays rely on reporter pairs composed of a macrocyclic receptor and a fluorescent dye, as a host-guest complex, leading to a change in the fluorescence spectroscopic properties of the dye.[31] In the tandem assays, the receptor additionally interacts either with the substrate or the product of the enzymatic reaction leading to a displacement of the fluorescent dye.[32] Upon enzymatic conversion of the substrate into the product, the overall propensity of the reaction mixture to displace the fluorescent dye from the macrocyclic host changes, i.e., the enzymatic reaction, either converts a weakly binding substrate into a strongly binding product or *vice versa*, which generates a detectable fluorescence change. This affords an alternative, simple, inexpensive, and label-free method to monitor enzymatic reactions continuously.[33]

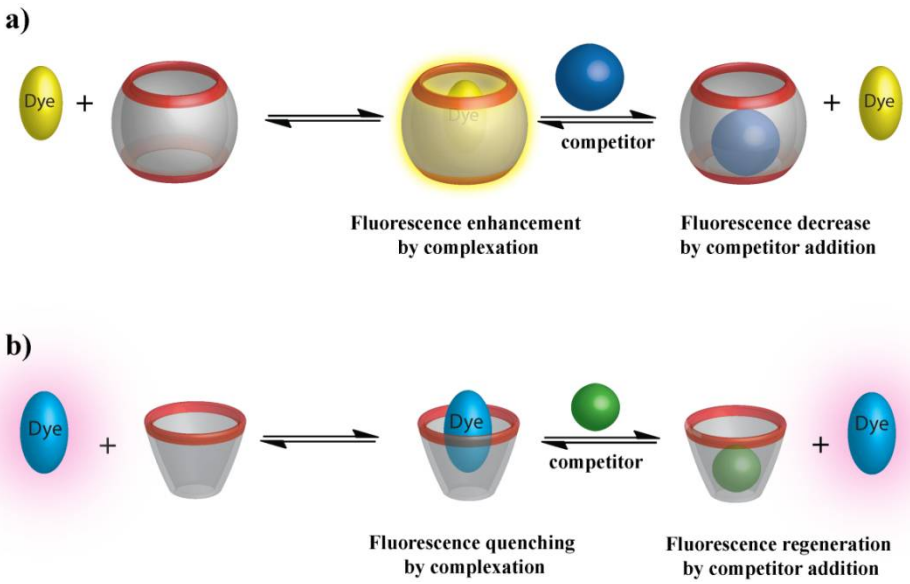

Figure 1.1. The operational principle of fluorescent tandem assays. Upon formation of the macrocycle-dye complexes either a) fluorescence enhancement or b) fluorescence quenching is observed. Further addition of competitor molecule displaces the fluorescent dye and restores the optical properties of the free dye.

1.6 Supramolecular Tandem Membrane Assay

The permeation of drugs through lipid membranes is a crucial factor in pharmacokinetics and early drug design.[34] To investigate the permeation of drugs, robust and sensitive methods are desirable. Thus, suitable membrane assays for rapid screening of analytes are in demand.[34] The standard biophysical method to investigate the translocation/permeation of analytes is electrophysiology, which is unable to distinguish between translocation and binding of analytes.[35] Different methods are available to determine the translocation of the analytes, such as radioactivity-based methods,[36] isothermal titration calorimetry,[37] or NMR spectroscopy.[38] However, these methods are not preferable for HTS of drugs. Fluorescence-based membrane assays are suitable for HTS in pharmaceutical industries.

The *in vitro* fluorescence-based supramolecular tandem membrane assay affords label-free method, real-time kinetics, and is suitable to analyze a variety of structurally related biomolecules (**Figure 1.2**).[39] Reporter pair encapsulated liposomes are prepared and purified, such that a subsequently added analyte permeate through membrane and displaces the dye molecule from the macrocycle. Further, selection of reporter pair is crucial, and it should fulfill the following conditions: *i*) receptor molecule (macrocycle) should exhibit high affinity to the target analyte *ii*) dye molecules need to show enough fluorescence change after the addition of the analytes *iii*) reporter pair (host/dye) should not permeate through lipid membrane, and *iv*) reporter pair encapsulated liposome should be stable.[39]

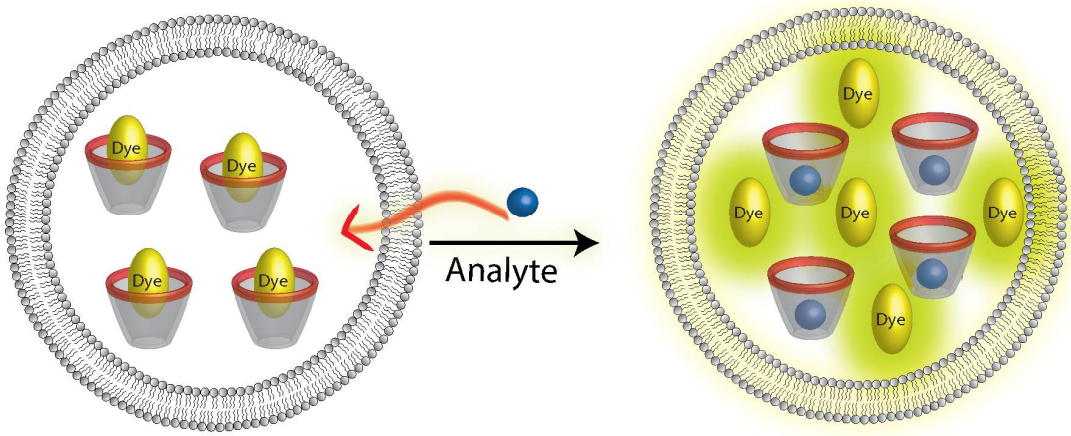

Figure 1.2. The operational principle of supramolecular fluorescent tandem membrane assays. The reporter pair is encapsulated inside the liposome. Upon the addition of an analyte to the lipid membrane, analyte permeates through the membrane and binds to the macrocycle, and thus, displaces the fluorescent dye.

1.7 Scope of the Thesis

The scope of the thesis is the development of novel fluorescence-based assays using supramolecular host-guest complexes. I have developed several assays, including supramolecular tandem enzyme assay for ODC, supramolecular tandem membrane assays for determining lipid membrane permeability and activation

energies of permeation, as well as enhanced liposome-based supramolecular sensors. In addition, mixed ligand shells gold nanoparticles were characterized by a supramolecular surface probe and transition metal ions. Further, gold nanoparticles were utilized for the sensing of decarboxylase products.

Polyamines are associated with several types of cancer, including breast, skin, colorectal, bladder, and cervical cancer.[40] The rate-limiting enzyme, in the biosynthesis of polyamines is ODC, which catalyzes the decarboxylation of L-ornithine into putrescine and carbon dioxide.[41] ODC is considered as a vital target in the treatment of certain types of cancer and parasitic diseases.[41a] Further, ODC inhibitors are hard to identify due to the lack of suitable ODC enzyme assays. In particular, HTS-compatible enzyme assays for ODC are currently not available, such that systematic identification and exploration of large libraries of potential inhibitors is currently not possible. In Chapter 2, we describe a label-free, simple, convenient fluorescent assay for continuously monitoring ODC activity and screening potential ODC inhibitors based on the previously reported supramolecular tandem enzyme assay principle.[31-33]

A liposome is a potential tool for an analytical application as a sensor for detecting relevant chemical and biological analytes.[42] Further, numerous liposome-based assays as signal amplifiers have been reported, including flow-injection liposome immunoanalysis,[43] liposome immunosorbent assay,[44] and liposome immunolysis assay.[45] Sensitivity is a pivotal factor in the development of biosensors. To increase sensitivity, signal amplification is an essential approach during sensor development. In this sense, liposome acts as a powerful signal amplifier when molecules interact with the particular receptor or signal marker compound.[46]

Liposomes as a sensor platform have several advantages such as the possibility for amplification of the sensor signal, biocompatibility, and simple preparation without chemical synthesis. Several sensors based on liposomes have been developed.[42] These sensors are typically composed of fluorescent dyes, electrochemical marker, and specific receptor molecules located in the interior volume of the liposome or within the lipid bilayer.[39, 47] When the target analytes enter the liposomal system, receptors molecules interact with analytes, which cause a signal change in the liposomal sensor system. However, host-guest binding interaction in the interior of the liposomes is currently inexplicable, it inspired us to a more advanced method to increase the sensitivity of liposome-encapsulated supramolecular sensor systems (Chapter 3). The supramolecular sensors are often suffered from a limited sensitivity owing to low affinities (typically in high μM to mM range). Further several supramolecular receptor molecules have been developed for the sensing application of several analytes.[1, 7a, 12, 14a, 48] However, these receptor molecules suffer from poor sensitivity of analytes.

The permeability of molecules across lipid membranes is a fundamental process. Passive diffusion through the lipid membrane is a preferred route entry of most drugs.[49] Several membrane permeability assays have been developed, two of which have become popular in the pharmaceuticals industry: the parallel artificial membrane assay (PAMPA)[50] and the Caco-2 cell permeability assay.[50] The PAMPA assay quantifies the molecules after passive diffusion in flat synthetic membranes. The Caco-2 cell assay is desired to identify molecules that can pass through a monolayer of epithelial cells. However, several problems persist in routine permeability assays. Particularly, PAMPA and Caco-2 cell assay is usually restricted to single-point measurements and it is challenging to obtain fundamental

kinetic parameters.[51] Caco-2 cell assay measures the sum of the active and passive permeability [50]. The aim of Chapter 4 is addressing some of the existing problems. In particular, the development of membrane assay based on the fluorescent artificial receptor (FAR). This provides an alternative simple, sensitive, and label-free method to continuously monitor the analytes permeation across the membrane.

Monolayer and mixed-monolayer protected gold nanoparticles have been extensively studied for their use in a variety of applications, including biological sensing,[52] imaging,[52] biocompatibility cell targeting applications,[53] nanowires,[54] and nanotubes.[55] The addition of functional groups like amine or carboxylate moieties to the surface of gold nanoparticles allows forming chemical bonds with target ligands.[56] For example, the carboxylate group is able to form amide bonds directly with an amino group of a molecule.[57] Ligand footprint, coupling efficiency, and accessibility of functional groups on the particle surface are the parameters that are of utmost importance for quality control in many applications.[58] To assess these parameters, a fast, simple, and reliable screening method is required. In Chapter 5, we have demonstrated the characterization of the mixed-ligand shells on gold nanoparticles (AuNPs) by transition metal ion and supramolecular surface probes.

Monitoring enzymatic activity is essential to understand the kinetic parameter of the enzyme. In Chapter 5, we describe that AuNPs can be used to readily monitor amino acid decarboxylase activity by a colorimetric assay.

Perylene diimide (PDIs) dyes are potential building blocks for the development of functional materials.[59] Further, these dyes have excellent absorption, fluorescent properties, and outstanding thermal, and photochemical stability.[60] PDI-based dyes

are familiar for the formation of H or J type aggregation[60] Thus, water-soluble PDIs, including monomeric form, have been studied in a variety of research fields such as biomedical application,[61] supramolecular architectures,[62] as well as optoelectronic applications.[63] However, the formation of π-π stacks between the perylene backbone in water reduces the fluorescence quantum yield of the dye.[64] The formation of π-π stacks generates a significant challenge for the application in several research fields. For instance, PDI dyes limit the usage of confocal microscopy or single-molecule spectroscopy techniques. In Chapter 6, we have demonstrated that supramolecular host-guest complexes can be used to inhibit aggregation of PDIs in water by using large macrocycles such as CB8, CB7 and, cyclodextrin (CD).

Chapter 2

Supramolecular Tandem Enzyme Assay

Chapter 2

2. Supramolecular Tandem Enzyme Assay

Corresponds to: **Appendix 10.3.1**

Nilam, M.; Gribbon, P.; Reinshagen, J.; Cordts, K.; Schwedhelm, E.; Nau, W. M.; Hennig, A., A Label-Free Continuous Fluorescence-Based Assay for Monitoring Ornithine Decarboxylase Activity with a Synthetic Putrescine Receptor. *SLAS Discov.* (formerly *J. Biomol. Screen*) **2017**, *22*, 906-914.
 DOI: 10.1177/2472555216689288.

2.1 Ornithine Decarboxylase

Measuring enzymatic activity is essential for drug targets.[65] Many drugs function through inhibition of target enzymes. The development of a robust enzymatic assay for HTS applications is critical.[66] Thus, understanding the enzyme biochemistry and the kinetics of enzyme action is essential. Mammalian ODC, (EC 4.1.1.17) is the crucial enzyme in the polyamine biosynthetic pathway,[41] and catalyzes the decarboxylation of L-ornithine into putrescine and carbon dioxide utilizing pyridoxal 5'-phosphate (PLP) as a cofactor.[41] The polyamines are involved in cell growth, and the ODC enzyme is a potential targets in the treatment of certain types of cancer and parasitic diseases.[41] Polyamines are associated with numerous processes in carcinogenesis.[67] Elevated polyamines levels are linked with increased cell proliferation, decreased apoptosis and increased expression of genes, which are affecting tumor invasion and metastasis.[68] Also, polyamines are involved in certain types of cancer, such as breast, skin, colorectal, bladder, and cervical cancers.[67]

2.2 ODC Activity and Polyamine Measurements Overview

Different methods for monitoring ODC activity have been reported,[69] which are radioactive assay, radioimmunoassay, chemiluminescence-based method, colorimetric measurements, amperometric measurements, and LC/MS-based measurements. All these methods have intrinsic advantages and disadvantages. Radioactive ornithine acts as a substrate, and the radioactive assay is built on the use of [1-^{14}C] trapping the resulting $^{14}CO_2$ and determining its radioactivity.[70] An alternative method is based on tritium labeled putrescine from uniformly labeled ornithine. Putrescine is captured by negatively charged phosphocellulose paper, and radioactivity is determined after washing with ammonium hydroxide.[69b] Chemiluminescence based method is a sensitive method, which permits the detection of putrescine in the picomolar range.[69g] In the chemiluminescence based method, cellular extracts are incubated with ornithine and spotted onto p81 phosphocellulose paper strips. After drying, paper is washed with ammonium hydroxide to remove the impurities. Then, diamine oxidase (DAO) is used to oxidize the putrescine, which resulted in hydrogen peroxide (**Scheme 2.1**).

Scheme 2.1. Ornithine is converted into putrescine by ODC and putrescine is oxidized by diamine oxidase and formed hydrogen peroxide, which is assayed by the chemiluminescence-based method using luminol and peroxidase**.**

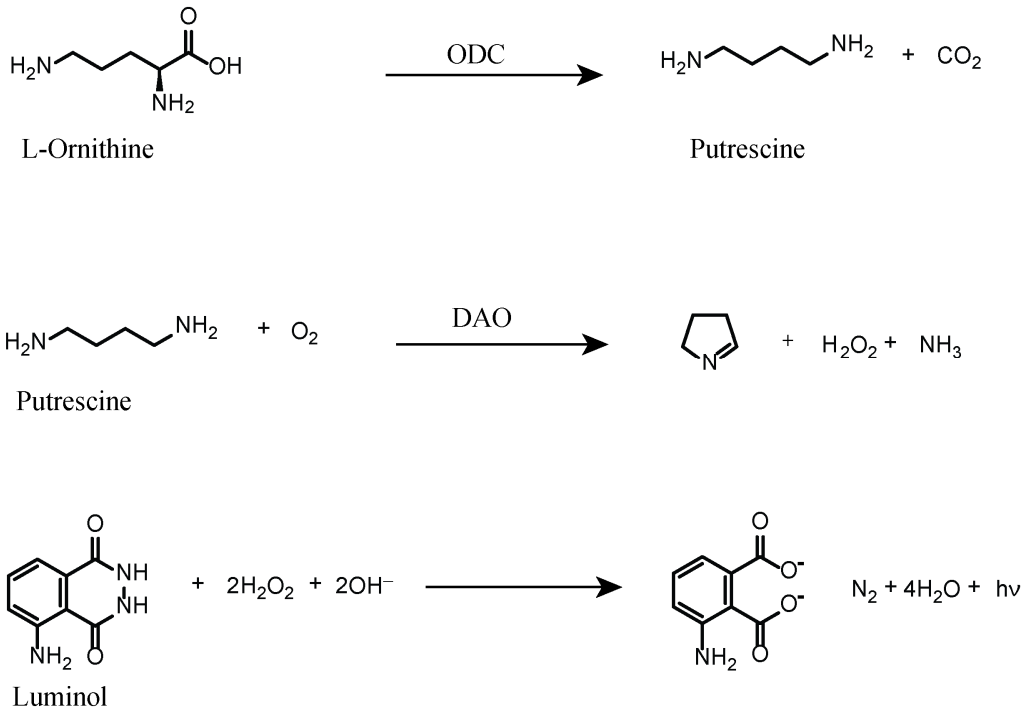

The colorimetric method is a sensitive method for the determination of the polyamine, which permits the detection of putrescine in the picomole range.[69e, 71] Two different colorimetric methods have been reported, where putrescine is measured by colorimetric quantification of the H_2O_2, which is released after its oxidation by soybean amine oxidase (SAO). The oxidations of putrescine by SAO produces H_2O_2, which reacts with 4-aminoantipyrin and phenol to yield colored complexes that absorb at 492 nm (**Scheme 2.2**).[71]

Scheme 2.2. Colorimetric enzymatic assay for ODC activity.

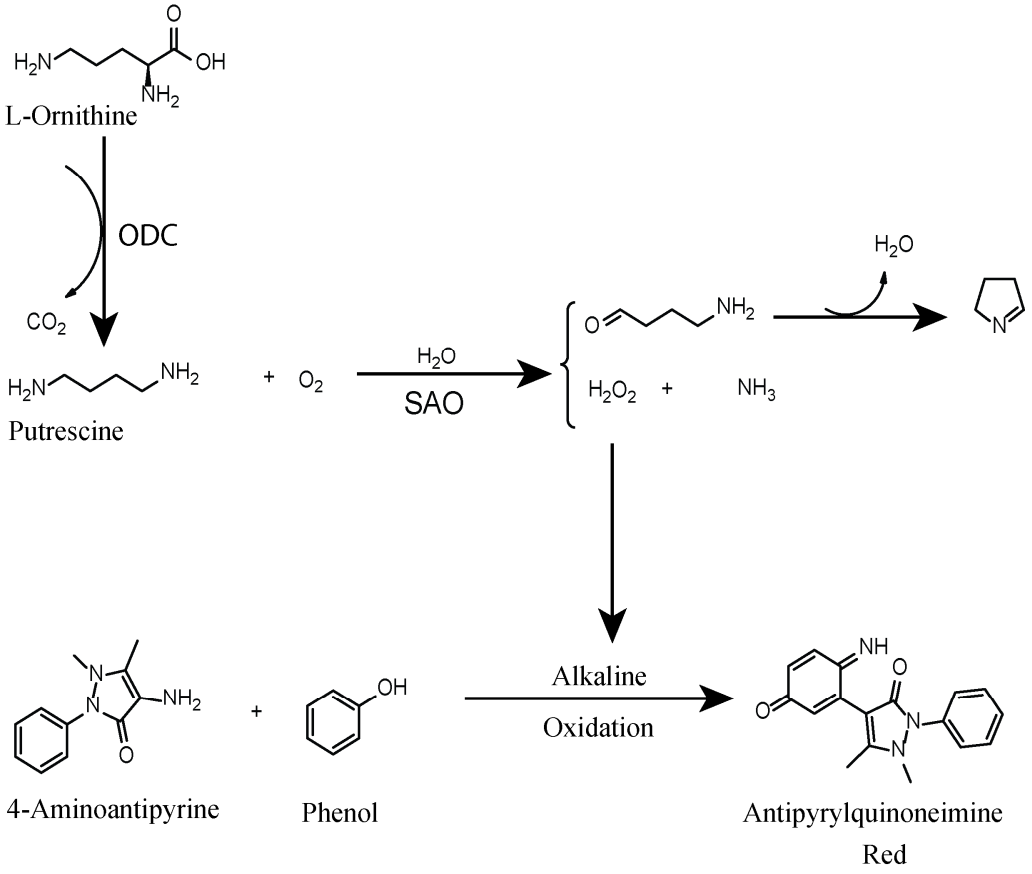

2.3 Fluorescence-Based ODC Assay

We have introduced supramolecular tandem enzyme assays, in which reporter pairs composed of a macrocyclic receptor and a fluorescent dye interact either with the substrate or the product of the enzymatic reaction leading to a displacement of the fluorescent dye.[31-33, 72] Upon conversion of the substrate into the product by the enzyme, the overall propensity of the reaction mixture to displace the fluorescent dye from the macrocyclic host changes, i.e., the enzymatic reaction either converts a weakly binding substrate into a strongly binding product or *vice versa* generating a detectable fluorescence change. This affords an alternative simple, inexpensive, and label-free method to continuously monitor enzymatic reactions.

A robust and convenient approach for monitoring ODC activity is based on the supramolecular tandem enzyme assay principle is introduced.[31-33, 72] We apply *trans*-4-[4-(dimethylamino)styryl]-1-methylpyridinium (DSMI) iodide as a fluorescent dye and CB6 as a macrocyclic receptor, which was recently reported to form a highly fluorescent inclusion complex.[73] The substrate of ODC binds very weakly to CB6, whereas the product putrescine is a strong competitor. As a consequence, ODC activity continuously generates a strongly binding product, which more strongly displaces the fluorescent dye leading to a concomitant decrease in fluorescent intensity.[31, 72] With the resulting product-selective tandem assay, we determine enzyme kinetic parameters of ODC, and we demonstrate the potential for inhibitor screening with two known inhibitors [67, 74] namely, DL-α-difluoromethylornithine (DFMO) and epigallocatechin gallate (EGCG).

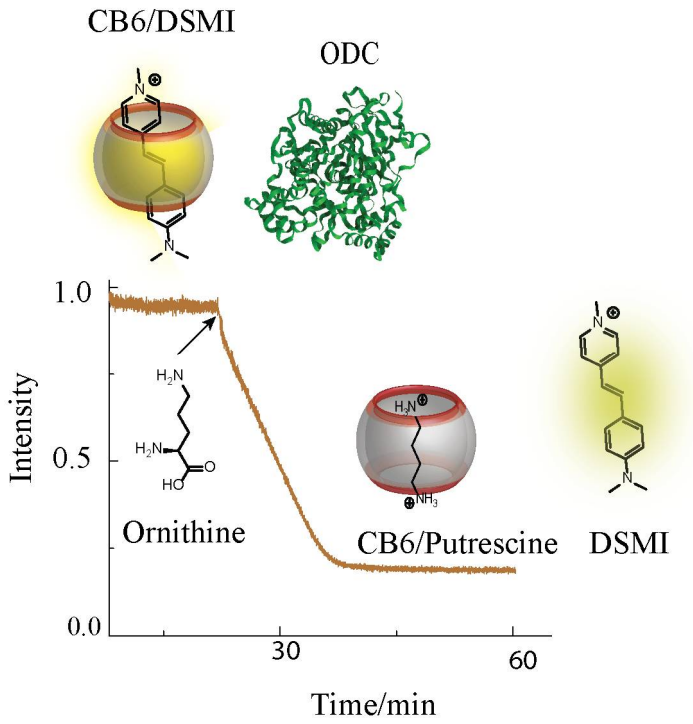

Figure 2.1. The operational principle of the fluorescence-based supramolecular tandem enzyme assay for ODC.

Chapter 3

Liposome-Based Sensing

Chapter 3

3. Liposome-Based Sensing

This chapter is derived from the content of the following manuscript and publication:

1. **Nilam, M.**; Karmacharya, S.; Nau, W. M.; Hennig, A., Liposome Enhanced Sensing, *Manuscript in Preparation.*

1. Assaf, K. I.; Begaj, B.; Frank, A.; **Nilam, M**.; Mougharbel, A. S.; Kortz, U.; Nekvinda, J.; Grüner, B.; Gabel, D.; Nau, W. M., High-Affinity Binding of Metallacarborane Cobalt Bis(dicarbollide) Anions to Cyclodextrins and Application to Membrane Translocation. *J. Org. Chem.* **2019**, *84*, 11790-11798.

3.1 Supramolecular Sensing

Chemical sensors are capable of transform the chemical information into useful signals. The word chemosensor has been established as a molecule of abiotic origin.[75] The pivotal importance in the development of chemosensor is that analytes must communicate reversibly with the receptor molecule.[25] The interest guest analytes bind with chemosensors by non-covalent interaction; this can be coined supramolecular chemosensors. Optical chemosensors are composed of a binding site and chromophore. When analyte binds to chemosensor, it alters the chemosensor optical properties.[25]

Naturally obtained biological receptors in biosensors might have higher affinity and selectivity for biological analytes.[76] However, artificial receptors have much superiority than biotic receptors. Biological relevant molecules are sensitive to an oxidizing agent, pH, and temperature. Further, optimum conditions are required to function as biosensors.[77] Artificial receptors are tailored from a variety of robust

components, and their chemical and physical properties can be altered to meet the specific requirement. The development of optical chemosensor design should meet the following key factors, which include the selection of chromophore, analyte affinity and selectivity, response mechanism, and immobilization technique.

The affinity of the analyte is of pivotal importance in the development of chemosensors. The common challenge is to enhance the sensitivity of the analyte by increasing binding affinity. Artificial receptors often have low binding affinity than biotic receptors. In this context, the high concentration of the analyte is able to saturate the chemosensor. Thus, the guest concentration may not produce enough optical signals. In the chemosensor design, the rule of thumb is dissociation constant (K_d) must match approximately of the guest concentration or host concentration.

Another essential aspect of the development of chemosensor is the selection of chromophore, which is used to report analyte detection. The absorption wavelength should be suitable with light-absorbing substance. For instance, protein absorbs light in the ultraviolet region, and therefore, for the detection of biological analytes, an optical chemosensor should have λ_{max} value higher than 400 nm.[78] Artificial receptors binding the analytes are driven by electrostatic, hydrogen bonding, and van der Waals interactions. These intermolecular interactions effectively controlled molecular recognition by host-guest mechanism and host pre-organization, which leads to a stronger and more selective binding.[3] Further, several supramolecular receptor molecules have been developed for the sensing application of several analytes. However, supramolecular sensors often suffer from a limited sensitivity owing to low affinities (typically in high μM to mM range).

3.1.1 Indicator Displacement Assay

Indicator displacement assays (IDAs) have become very familiar for optical sensing applications, and this provides sensing analytes at low concentrations using spectroscopic methods.[79] IDAs are based on an indicator, which binds to a receptor *via* non-covalent interactions, and this leads to alter the optical properties of the indictor (**Figure 3.1**). Further, an analyte enables the displacement of the indicator and binds to the receptor. Thus, the indicator restores its original optical properties.[31] IDAs utilizing artificial host molecules have become a potential tool in the research field of supramolecular chemistry, because IDAs have many advantages compared to other sensing methods. First, covalent attachment of the receptor and the indicator is not required, second, one receptor has an affinity to a variety of different analyte, it provides to displace the indicator, and third, the IDA is suitable in organic solvents and aqueous media.

3.1.2 Associative Binding Assay

Instead of displacing the indicator dye from a macrocycle, sufficiently large macrocycles, such as CB8, can form ternary complexes composed of the fluorescent dye dimethyldiazapyrenium dication (MDAP) and an analyte.[80] The binding of the analyte to the CB8/MDAP complex resulted in fluorescence quenching of MDAP. This was successfully established in homogeneous solution the recognition of a large variety of electron-rich aromatic guests, e.g., alkoxynaphthalenes, indole derivatives including the neurotransmitter tryptamine, and *N*-terminal phenylalanine residues in peptides. Furthermore, complex formation was sufficiently fast to provide real-time monitoring of enzymatic reactions.[81]

Scheme 3.1. Schematic illustration of associative binding of the analyte with a host•dye complex.

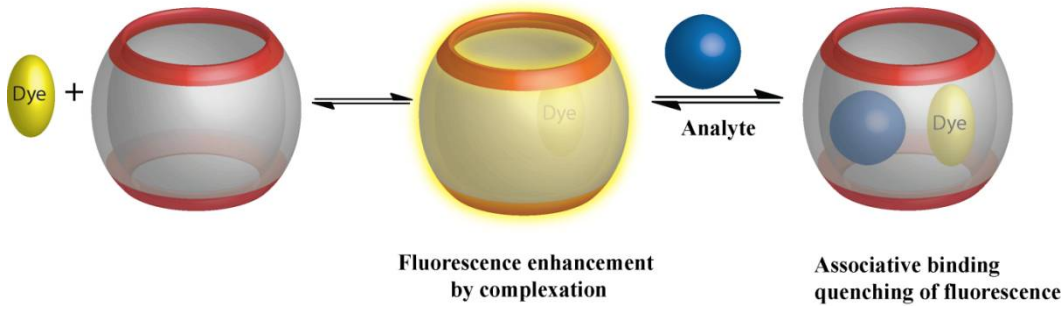

3.2 Sensing-Based on Liposome

A liposome is a powerful tool for an analytical application as a sensor for detecting relevant chemical and biological analytes.[42] Liposomes as a sensor platform have several advantages such as amplification of the sensor signal, biocompatibility, and simple preparation without chemical synthesis. Several sensors based on liposomes have been developed.[42] These sensors are typically composed of fluorescent dyes, electrochemical marker, and specific receptor molecules located in the interior volume of the liposome or within the lipid bilayer.[39, 47] When the target analytes enter the liposomal system, receptor molecules interact with analytes, which cause the signal change in the liposomal system.

3.2.1 Membrane Surface Bound Receptor

Few membrane surface-bound receptor molecules have higher binding interaction for the analytes than in bulk solution. Also, the membrane interface has significantly different polarities than the homogeneous solution, and this microenvironment is expected to have a dramatic effect on binding interactions.[82] Hydrogen bonding interaction is noticeably enhanced at the lipid-water (or lipid-air)

interface. The latter is developed by self-assembly of amphiphiles on pure water.[83] For example, guanidinium-functionalized lipid monolayer effectively senses the ATP or AMP with a binding constant about 10^6 times larger than the value of 1.3 M^{-1} in homogeneous solution.[84] Further, another binding enhancement has been found based on the chelate effect on the lipid membrane surface. The binding affinity between Cu^{2+} and membrane-bound receptor molecules significantly enhanced binding constant relative to the homogeneous solution. This significant binding constant enhancement can be demonstrated by the polarity difference in the membrane-water interface and concentrating effect by the membrane.[82a] Thus, lipid-water (or air) interface behaves like a signal amplifier in intermolecular binding.[84c]

3.2.2 Analyte Enrichment inside Liposome Based on pH Gradient

Encapsulation of a chemical compound inside the phospholipids vesicles or liposomes is an active research field.[85] This encapsulation technique is utilized by several industries such as pharmaceuticals,[86] food,[87] and textiles.[88] Effective encapsulation of ionizable chemical compounds inside the vesicle interior involves the establishment of a pH gradient between the vesicles interior and surrounding solution.[89] In liposomal systems, transmembrane pH gradients can facilitate the encapsulation of commonly employed drugs.[90] The pH outside the liposome provides that some of the analytes exist in neutral form, which is highly membrane permeable. Inside the liposome, the analyte becomes ionized due to the pH variation and trapped inside the liposome. The pH gradient between the membranes is the driving force to trap the ionizable analytes into small volumes for detection and quantification.[91] Furthermore, neutral basic compounds (amine) diffuse across the phospholipids membrane, inside the vesicle amine will be protonated, and

accumulated inside the vesicles.[91-92] This diffusion process continues until the concentration of the neutral amine is balanced between the membranes.[91] The enrichment inside the vesicle increases with increasing pH of the external solution up to the limit, when pH outside > pK_a, where all of the basic analyte will be in the neutral form (**Figure 3.1**).[89a, 91, 93]

Utilizing the pH gradient in liposome or phospholipid vesicles would be useful for concentrating ionizable molecules into a small volume of vesicles, which could be used for detection and quantifications.[90] The typical vesicles interior volume is on the order of femto to attolitres when a low concentration of the analyte is transported into a small volume of vesicles; change in internal concentration of the analytes is observed inside the vesicles.[91] It was shown that drugs could be loaded into liposomes by pH gradient method, which gave >1000 times increased local concentrations.[94] More recently, theoretical modeling of such pH gradients indicated a 520,000 fold increased local concentration in the liposome, which was also experimentally verified by confocal Raman microscopy.[91] Furthermore, the transport rate of the analyte to the liposome is given by the following equation 1, and 2 and the difference between the transport rates of analyte from outside to inside and *vice versa* will be the overall transport rate.

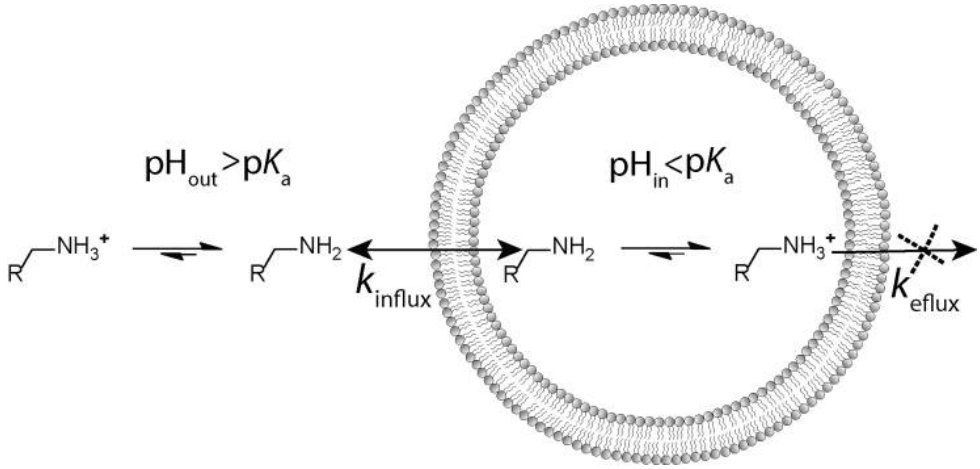

Figure 3.1. Liposome-enhanced sensing with a pH gradient. The concentration of an analyte inside a liposome can reach much higher values than in the surrounding medium when a mechanism prevents the analyte efflux. This can be achieved, for example, by a lower pH inside the liposome. This protonated the analyte and entrapped it inside the liposome. The much-increased local concentration yields an overall enhanced sensitivity**.**

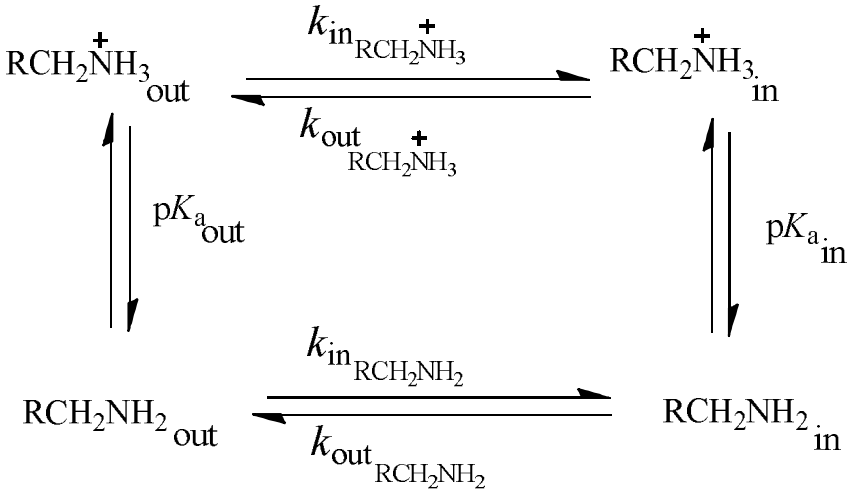

$$k_{in}{}_{RCH_2NH_2} = k_{out}{}_{RCH_2NH_2}$$

$$k_{in}{}_{RCH_2\overset{+}{N}H_3} = k_{out}{}_{RCH_2\overset{+}{N}H_3}$$

$$v_{in} = k_{in}{}_{RCH_2NH_2}{}^{[RCH_2NH_2]_{out}} + k_{in}{}_{RCH_2\overset{+}{N}H_3}{}^{[RCH_2\overset{+}{N}H_3]_{out}} \quad (1)$$

$$v_{out} = k_{out}{}_{RCH_2NH_2}{}^{[RCH_2NH_2]_{in}} \quad k_{out}{}_{RCH_2\overset{+}{N}H_3}{}^{[RCH_2\overset{+}{N}H_3]_{in}} \quad (2)$$

Now $pH_{inside} << pH_{outside}$

if $k_{in}{}_{RCH_2NH_2} = k_{out}{}_{RCH_2NH_2} >> k_{in}{}_{RCH_2\overset{+}{N}H_3} = k_{out}{}_{RCH_2\overset{+}{N}H_3}$

$$v_{in} >> v_{out}$$

Scheme 3.2. Supramolecular tandem membrane assays to monitor the diffusion of analytes through a lipid membrane exploiting associative binding and competitive binding of analytes with different host•dye complexes.

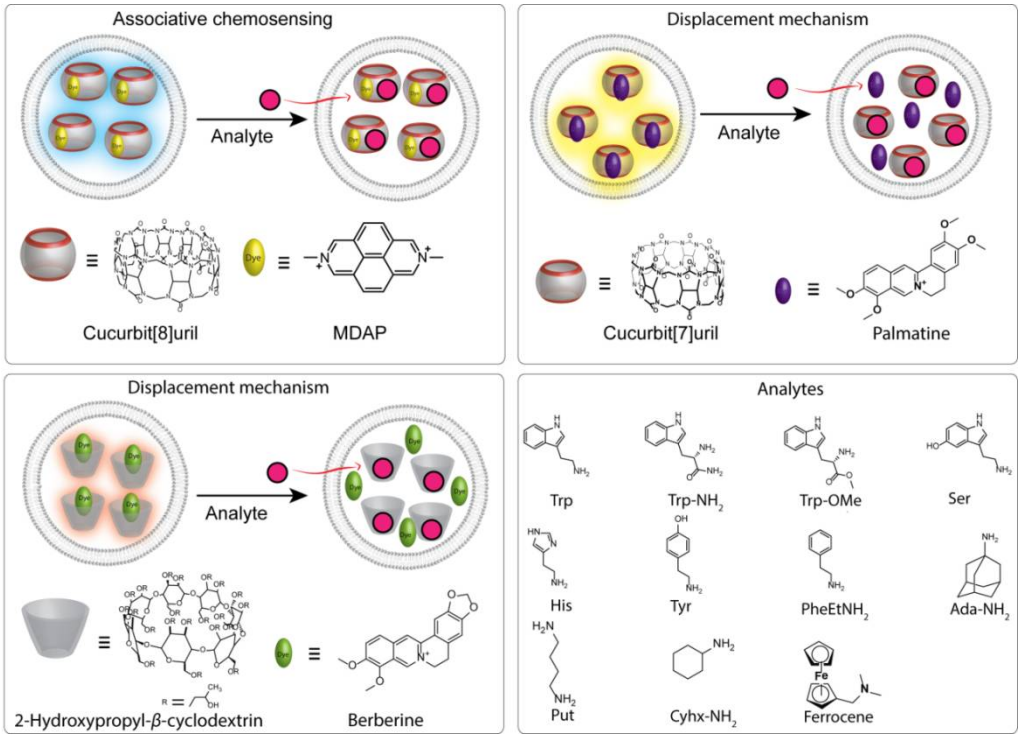

3.3 Liposome Enhanced Sensing

3.3.1 Selection of Reporter Pair

We report our systematic approach to develop a novel liposome-based supramolecular sensing platform to enhance the sensitivity of supramolecular sensing systems. Further, we have used the supramolecular host-guest method to determine the apparent binding affinity of the analytes. To assess the binding affinity of the analytes, we have used previously reported supramolecular host-guest based tandem assay principle.[31-33, 95]

To adapt the tandem assay principle and enhance the sensitivity of the analytes, we encapsulated three reporter pairs separately inside the liposome (**Scheme 3.2**). Two of the encapsulated reporter pairs (CB7/palmatine (PLM) and hydroxypropyl-*β*-cyclodextrin (HP-*β*-CD)/berberine (BE)) interact with transported analytes, which

cause a displacement of the fluorescent dye, further, the larger cavity of CB8 can also form ternary complexes.[23] The residual cavity space of reporter pair CB8/MDAP complex provides enough space for subsequent binding of aromatic analytes into the residual cavity space, leading to net fluorescence quenching.[81]

Most interestingly, liposome encapsulated reporter pair provide strong fluorescence response at lower analyte concentrations, than in homogeneous solution, which is lead to the sensitivity enhancements for analytes. To assess this phenomenon, we used three different liposomes with encapsulated reporter pair (CB8/MDAP, CB7/PLM, and HP-*β*-CD/BE) for the sensing of amines using the pH gradient between inside and outside of the vesicles. This method is based on the competitive fluorescence titration (CB7/PLM, HP-*β*-CD/BE) and associative binding (CB8/MDAP) against the amine concentration. By monitoring the fluorescence changes against the concentration of the amine, we could accurately compare the apparent binding affinity of analytes with liposome-encapsulated reporter pair and homogeneous solution (without liposome) of the reporter pair.

3.3.2 Chemosensing-Based on Associative Binding

We have prepared the liposomes with a 9:1 molar ratio of 1-palmitoyl-2-oleoyl-*sn*-glycero-3-phosphocholine (POPC)/1-palmitoyl-2-oleoyl-*sn*-glycero-3-phospho-L-serine (POPS). Further, we prepared liposomes with an acidic interior and a basic exterior (**Figure 3.1**). The resulting pH gradient allows a deprotonated (and thus uncharged) amine to diffuse into the liposome with minimal effort. As soon as the amine has reached the acidic interior, it will become protonated, and the resulting ammonium ion will have a much-reduced efflux rate. The resulting difference in influx and efflux rate leads to an enrichment of the molecule in the liposome

interior; in this context, the analyte becomes encapsulated inside the liposome. Further, we have recently demonstrated that reporter pair calixarene (CX4)/lucigenin (LCG) and CB7/BE can be encapsulated into the aqueous interior of the liposome.[39] Addition of the outer membrane protein (OmpF) to CX4/LCG-entrapped liposomes indicated no efflux of the dye or CX4. Subsequent addition of the antimicrobial peptide protamine, the cell-penetrating peptide heptaarginine, or the neurotransmitter acetylcholine to the solution led to a strong increase in fluorescence intensity with time. This clearly indicated that the molecules were transported through OmpF and reached the liposome interior, where they displaced the fluorescent dye from the macrocycle.

The binding of the analyte to the preformed CB8/MDAP complex results in fluorescence quenching of MDAP.[81] This was successfully applied in the aqueous interior of the liposome and in homogeneous solution to detect a large variety of electron-rich aromatic guests, e.g., indole derivatives including neurotransmitters tryptamine and serotonin. Furthermore, complex formation was sufficiently fast to allow real-time monitoring of the transport of the analytes *via* membrane tandem assay.

In a typical tandem membrane assay, increasing concentration of guests was successively added into a liposome suspension, and the fluorescence was monitored as a function of time until further addition of guests resulted in negligible changes (**Figure 3.2a**). Furthermore, to compare apparent binding affinity, we have performed typical fluorescent titration in homogeneous solution (**Figure 3.2a**), with similar instrumental conditions. The constant fluorescence intensity after guest addition was then plotted against the guest (serotonin) concentration and analyzed by a 1:1 host-guest titration curve, which provides an apparent binding constant of

K_a = 2.3 × 10^6 M^{-1}. Further, conventional fluorescence titration in homogeneous solution (without liposome) was carried out. A plot of the fluorescence intensity at maximum emission wavelength (423 nm) and analysis by a 1:1 host-guest titration curve provides a binding constant of K_a = 3.9 ×10^3 M^{-1}, which is good accordance with the literature value.[81] The combined results revealed (**Figure 3.2b**), liposome-encapsulated reporter pair CB8/MDAP provides higher sensitivity to the guest molecules than the homogeneous solution. Similar experiments were performed with other analytes (**Figure A.1 - Figure A.3** see in appendix**)**, all analytes exhibited higher sensitivity for liposome-encapsulated CB8/MDAP reporter pair compared to the homogeneous solution (**Table 3.1**).

3.3.3 Chemosensing-Based on Displacement Mechanism (CB7/PLM)

Apart from the CB8-based associative binding, we have performed experiments based on the dye displacement mechanism. Therefore, liposome-encapsulated reporter pairs are prepared, in which, added analyte was transported inside the vesicles and affects the fluorescence by displacing the dye molecule from the macrocycle (**Scheme 3.2**). However, the selection of reporter pairs is crucial, because the concentration of the reporter pair inside the liposome is higher than the rehydration buffer, which is used to prepare the liposome.[43] Therefore, low binding affinity (<10^4 M^{-1}) between the host-dye reporter pair is highly desirable. Higher binding affinity reporter pairs display low affinity to the target analytes, which is competing for the receptor molecules with high affinity dye molecule. Considering the above observation, we have selected the CB7/PLM reporter pair, which has a moderate binding affinity (K_a = 4.3 × 10^4 M^{-1}) with receptor molecule of CB7.[96]

Table 3.1. Apparent binding constant values for the complex formation between different host molecules with amines.

Reporter pair	Analyte	Apparent binding constant (M^{-1})		E_f[a]	Apparent binding constant (M^{-1})		E_f[a]
		Inside liposome	Homogeneous solution		Inside liposome	Homogeneous solution	
		pH gradient 3.5 - 10.8	pH 3.5		pH gradient 7.5 -10.8	pH 7.5	
CB8/MDAP	Trp-NH_2	$(2.1 \pm 0.9)10^7$	$(2.3 \pm 0.2)10^5$	91	$(8.1 \pm 0.6)10^5$	$(1.1 \pm 0.1)10^5$	7.3
	Trp	$(1.6 \pm 0.6)10^7$	$(9.9 \pm 0.8)10^4$	161	$(1.6 \pm 0.2)10^7$	$(8.0 \pm 0.6)10^4$	200
	Trp-OMe	$(3.6 \pm 0.9)10^6$	$(1.3 \pm 0.2)10^5$	28	$(6.3 \pm 0.5)10^4$	$(3.8 \pm 0.2)10^4$	1.6
	Ser	$(2.7 \pm 0.5)10^6$	$(5.5 \pm 0.4)10^3$	491	$(2.3 \pm 0.9)10^6$	$(3.9 \pm 0.1)10^3$	589
	Tyr	$(3.6 \pm 0.8)10^5$	$(6.0 \pm 0.9)10^3$	60	$(1.1 \pm 0.1)10^5$	$(2.7 \pm 0.2)10^3$	41
CB7/PLM	$PheEtNH_2$	$(1.4 \pm 0.9)10^8$	$(2.4 \pm 0.1)10^7$	5.8	$(1.0 \pm 0.9)10^8$	$(3.1 \pm 0.9)10^7$	3.2
	Tyr	$(5.5 \pm 0.8)10^6$	$(1.2 \pm 0.6)10^6$	4.6	$(4.6 \pm 0.8)10^5$	$(4.5 \pm 0.2)10^5$	1.0
	Put	$(3.8 \pm 0.1)10^6$	$(1.0 \pm 0.2)10^5$	38	$(1.1 \pm 0.9)10^6$	$(4.6\pm 0.5)10^5$	2.4
	Trp	$(1.1 \pm 0.2)10^6$	$(4.5 \pm 0.3)10^4$	24	$(3.2 \pm 0.9)10^5$	$(2.2 \pm 0.2)10^4$	14.5
	Trp-NH_2	$(7.8 \pm 0.3)10^5$	$(3.0 \pm 0.3)10^5$	2.6	n.d.[b]	n.d.[b]	n.d.[b]
	His	$(3.8 \pm 0.7)10^5$	$(1.4 \pm 0.1)10^4$	27	$(2.4 \pm 0.6)10^4$	$(1.1 \pm 0.1)10^4$	2.2
HP-*β*-CD/BE	Ada-NH_2	$(4.3 \pm 0.7)10^5$	$(7.1 \pm 0.1)10^3$	61	$(5.3 \pm 0.2)10^5$	$(5.4 \pm 0.2)10^3$	98
	$CyhxNH_2$	$(7.0 \pm 0.3)10^4$	$(9.0 \pm 0.9)10^1$	778	$(1.7 \pm 0.4)10^4$	$(1.7 \pm 0.2)10^1$	1000
	$PheEtNH_2$	$(6.0 \pm 0.7)10^4$	$(1.5 \pm 0.1)10^1$	4000	$(2.0 \pm 0.2)10^4$	$(3.0 \pm 0.2)10^1$	666
	Ferrocene	$(1.0 \pm 0.3)10^6$	$(1.6 \pm 0.7)10^3$	625	$(5.1 \pm 0.9)10^4$	$(1.3 \pm 0.7)10^3$	39
	His	$(8.5 \pm 0.9)10^4$	n.a.[c]	n.a.[c]	$(6.4 \pm 0.1)10^3$	n.a.[c]	n.a.[c]
	Trp	$(5.1 \pm 0.2)10^4$	$(1.2 \pm 0.2)10^2$	425	$(1.1 \pm 0.2)10^3$	$(5.5 \pm 0.6)10^1$	20

[a] E_f = Enhancement factor, which is ratio between apparent binding constant inside liposome and homogeneous solution. [b] Not determined. [c] Could not be determined binding constant due to low affinity to receptor molecule.

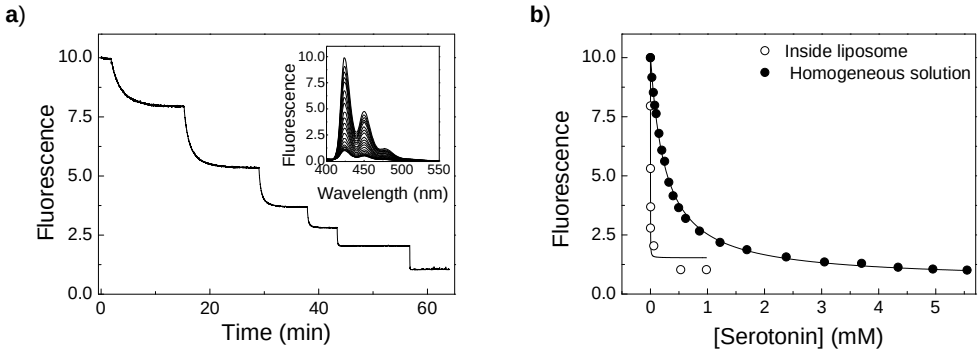

Figure 3.2. a) Time-dependent fluorescence changes of POPC/POPS⊃CB8/MDAP liposomes (28.4 μM final phospholipid concentration) during the successive addition of serotonin *via* the pH gradient (aqueous interior of the liposome 100 mM Hepes, pH 7.5 and exterior of the liposome 100 mM Na_2HPO_4, pH 10.8). The inset shows fluorescence spectral changes upon the addition of serotonin to CB8/MDAP complexes in 100 mM Hepes, pH 7.5 b) Comparison of liposomes encapsulated (CB8/MDAP) reporter pair fluorescence changes with a homogeneous solution against serotonin concentration. Apparent binding constant was determined by 1:1 host-guest binding equation (CB8, 0.35 μM), (λ_{ex} = 338 nm and λ_{em} = 423 nm).

The response of the liposome-encapsulated CB7/PLM reporter pair toward the transported analytes into the vesicles was explored by competitive kinetics method, in which analytes successively added in small portions to a solution containing the liposome-encapsulated reporter pair CB7/PLM (**Figure 3.3**). This revealed that a low concentration of tryptamine was required to efficiently displace dye PLM, and fitting of the resulting titration curve by nonlinear regression gave a binding constant of $K_a = 1.1 \times 10^6$ M^{-1} for tryptamine (**Figure 3.3**). In contrast, titration in a homogeneous solution gave a low binding constant of $K_a = 4.5 \times 10^4$ M^{-1} (**Figure 3.3**), which is almost similar to the previously reported value.[97] Similarly, we have analyzed some of the analytes, which indicates that liposome-encapsulated reporter pair has higher apparent binding affinity than the homogeneous solution (**Table 3.1, Figure A.4 - Figure A.7** see in appendix).

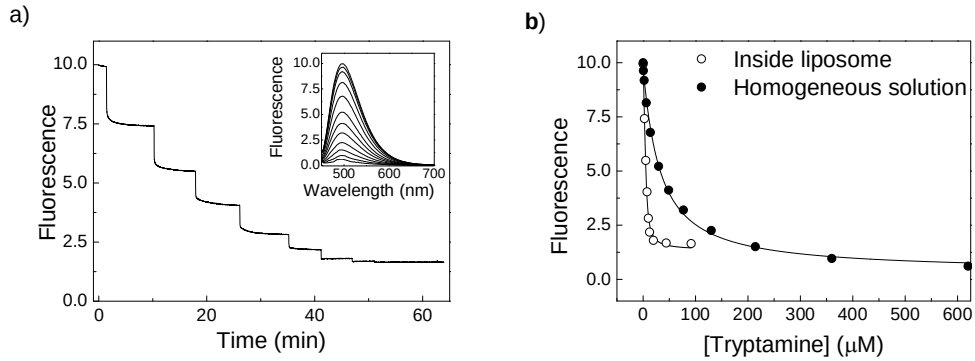

Figure 3.3. a) Time-dependent fluorescence changes of POPC/POPS ⊃CB7/PLM liposomes (25.7 μM final phospholipid concentration) during the successive addition of tryptamine *via* the pH gradient (aqueous interior of the liposome 100 mM sodium citrate, pH 3.5 and exterior of the liposome 100 mM Na_2HPO_4, pH 10.8). The inset shows fluorescence spectral changes upon the addition of tryptamine to CB7/PLM complexes in 100 mM sodium citrate, pH 3.5 b) Comparison of liposomes encapsulated (CB7/PLM) reporter pair fluorescence changes with a homogeneous solution against tryptamine concentration. Apparent binding constant was determined by 1:1 host-guest binding equation (CB7 = 6 μM, PLM = 1 μM), (λ_{ex} = 425 nm and λ_{em} = 495 nm).

3.3.4 Chemosensing-Based on Displacement Mechanism (HP-*β*-CD/BE)

To further apply our method, we have selected low-affinity receptor molecule HP-*β*-CD, which has a binding affinity in the range of $(10 - 10^4)\ M^{-1}$ to the analytes.[12] This indicates that millimolar macrocycle concentration is required to achieve significant complexation with the analytes. The binding constant between HP-*β*-CD and BE was found to be (K_a = (137 ± 4) M^{-1}. Furthermore, liposome-encapsulated reporter pair HP-*β*-CD/BE provide micromolar affinity to the analytes (**Table 3.1**). The response of the HP-*β*-CD/BE reporter pair toward the analytes was explored by competitive titrations. In a typical experiment, increasing concentration of guest phenethylamine ($PheEtNH_2$) was successively added to a liposome suspension, and the fluorescence was monitored as a function of time until further addition of guest resulted in a negligible change (**Figure 3.4a**). The constant fluorescent intensity after guest addition was then plottedagainst the guest concentration (**Figure 3.4b**). An expected, the resulting plots showed a high affinity to the $PheEtNH_2$ (**Table3.1**).

In contrast, titration inhomogeneous solution provides millimolar affinity to the $PheEtNH_2$ (**Figure 3.4b**). Similarly, other analytes also exhibited high binding affinity to the liposome-encapsulated reporter pair (**Table 3.1, Figure A.8 - Figure A.9,** see in appendix). For all analytes, the binding constant is higher in the pH gradient of 3.5 - 10.8 compared to the pH gradient of 7.5 - 10.8 (**Table 3.1**). This is in accordance with analyte enrichment inside vesicles; the higher the pH gradient, the higher the enrichment of the analytes are previously established.[89b, 91] Further, enhancement factor (E_f) was slightly different with different pH gradient, and this presumably originates from that acidic pH slightly increase the binding affinity in homogeneous solution.

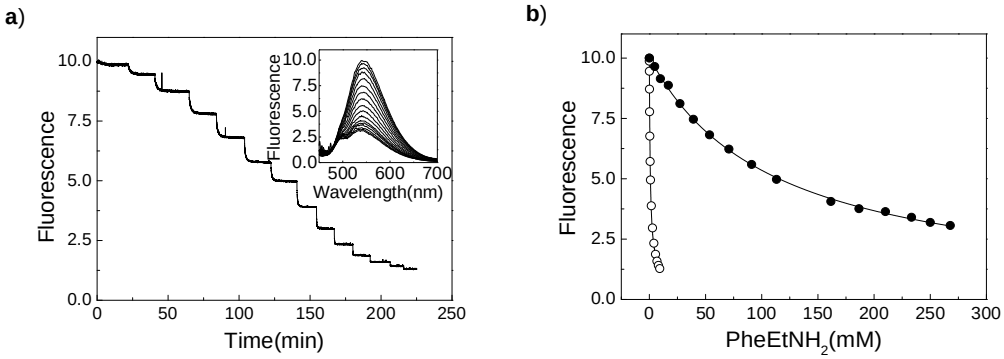

Figure 3.4. a) Time-dependent fluorescence changes of POPC/POPS⊃HP-*β*-CD/BE liposomes (53.5 µM final phospholipid concentration) during the successive addition of $PheEtNH_2$ *via* the pH gradient (aqueous interior of the liposome 100 mM sodium phosphate, pH 7.5 and exterior of the liposome 100 mM Na_2HPO_4, pH 10.8). Fluorescence spectral changes upon the addition of $PheEtNH_2$ to HP-*β*-CD/BE complexes in 100 mM sodium phosphate pH 7.5 (inset). b) Comparison of liposomes encapsulated (HP-*β*-CD/BE) reporter pair fluorescence changes with a homogeneous solution against $PheEtNH_2$ concentration. Apparent binding constant was determined by 1:1 host-guest binding equation (HP-*β*-CD = 20 µM, BE= 1 µM), (λ_{ex} = 420 nm and λ_{em} = 540 nm).

In summary, we have evaluated the liposome-based sensing system to sense the analytes. The liposome-encapsulated receptor molecules provided higher sensitivity than in homogeneous solution. Receptor molecules that are encapsulated in the interior of the liposomes have a higher apparent binding affinity for the analytes due to higher concentration of host-guest molecules in the interior of the liposome leading to enhance the formation of host-guest complexes, thus increasing the sensitivity of the reporter pair. Most of the analytes exhibited detection of nanomolar concentration through liposome-enhanced sensing approach. In general, supramolecular receptor molecules suffer from a low affinity to analytes. The alternative method is to syntheses receptor molecules for different analytes. However, our liposome-based methods provide higher sensitivity without chemical synthesis; therefore, we believe the liposome-based sensing method will become useful in the supramolecular sensing research field.

3.4 Membrane Translocation of Metallacarborane Cobalt bis(dicarbollide) Anions

3.4.1 Boron Clusters

Boron has been used in several applications in chemistry, electronics, material research, and the life sciences. The chemistry of boron has many attractive features: location in the elements of the periodic table and electronic structure. Boron exists beside the carbon atom in the periodic table and exhibits some closeness and also shows some differences.[98] Boron related compounds are not frequently observed in nature. However, they can be synthesized and create a three-dimensional structure. The large boron hydrides can create a polyhedral boron cluster; in this context, metallabisdicarbollide was discovered by Hawthorne.[99] Polyhedral boranes create cage compounds with general molecular formula $B_nH_n^{2-}$. The stability of these compounds under standard conditions is restricted to boron hydride anions

where n = 6 - 12.[100] Carboranes are formed by replacement of one or more BH units by CH units. Further, carboranes can accommodate metals and provide a new branch of coordination compounds known as metallacarboranes.

3.4.2 Hydrophobicity of Boron Clusters

The existence of hydride beside boron atoms makes specific properties in the boron cluster. Partially negatively charged hydrogen atoms inhibit the formation of a hydrogen bond with water that makes hydrophobic characteristics. Further, the electronegativity difference of hydrogen and boron atom allows forming dihydrogen bond, which is formed between the positively charged hydrogen atom of proton donor and hydric proton acceptor.[101] Dihydrogen bonds are weaker than classic hydrogen bonds; thus, the repulsive force toward the surrounding water molecules is overcome; this renders to the boron cluster hydrophobic.[101]

3.4.3 Metallacarboranes

In metallacarboranes transition metals (Fe, Ni, Co) are sandwiched between two anionic carboranyl ligands to create species with a negative charge. Further, weakly polarized B–H bond and C–H bond generate non-electrostatic intermolecular interactions, thus create hydrophobic and hydrophilic simultaneously. In the past few decades cobalt bis(dicarbollide) $[(C_2B_9H_{11})_2Co]^-$ also known as COSAN has been extensively studied in many research field including boron neutron capture therapy,[102] extraction of Cs^+ from nuclear fuel,[103] and as inhibitor of HIV protease.[104]

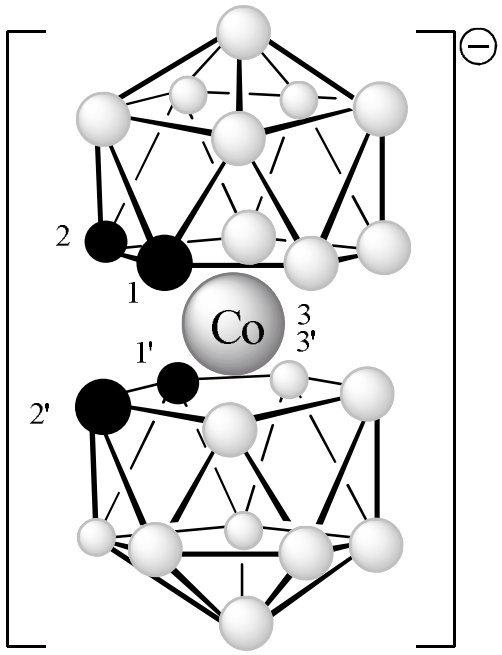

Figure 3.5. Molecular structure of COSAN $[(1,2\text{-}C_2B_9H_{11})_2\text{-}3,3'\text{-}Co)]^-$.

3.4.4 Binding Affinity of Boron Cluster with Cyclodextrin

Encapsulation of the guest molecules inside the macrocyclic host is an interesting phenomenon in aqueous solution. The main driving force for the encapsulation of the analytes is the hydrophobic effect. However, the chaotropic effect also plays a vital role in the formation of inclusion complexes of highly water-soluble dianionic dodecaborates $B_{12}X_{12}^{2-}$ and $B_{12}X_{11}Y^{2-}$where X = H, Cl, Br, I and Y = OH, SH, NH_3^+, NR_3^+, which form inclusion complexes with γ-cyclodextrin. The binding affinity was assessed by NMR and ITC. That shows dianionic dodecaborates have a micromolar affinity to γ-cyclodextrin.[105] Recently, we have demonstrated that COSANs have a micromolar affinity to γ-cyclodextrin. The binding of the COSANs inside the cavity of the γ-cyclodextrin was investigated by NMR, ITC, UV-visible spectroscopy, mass spectrometry, and cyclic voltammetry.[106] The entrapment of COSANs inside the cavity of γ-cyclodextrin alters the photophysical properties and electrochemical properties.

3.4.5 Membrane Translocation of COSAN

The transport of COSANs was initially investigated using synthetic DOPC membrane. Also, COSAN is not required driving force to cross the membrane.[107] Further, in electrophysiology measurements electrical capacitance of the membrane is constant throughout COSAN transport, which indicates that COSANs transfer through the membrane without creating pore or membrane disruption. This electrophysiological measurement agreed with COSAN translocation monitored by ICP-MS.[107] In contrast, COSAN was not expected to overcome the energy barrier of the lipid membrane.[107] Further, unusual amphiphilic nature of the COSAN overcomes the energy barrier of the lipid membrane.

3.4.6 Stability of Reporter Pair (γ-CD/dapoxyl) Encapsulated Liposomes

Liposomes have been investigated for drug delivery, drug targeting, and controlled release; however, the major drawback of the drug delivery system is instability. The use of liposomes as a drug delivery vehicle has several advantages over unencapsulated compounds. Liposomes act as storage of the interesting compounds, and enhance sufficient time of administered drugs to reach the target site,[108] encapsulation of the interesting drugs in liposomes provide protection against clearance from blood or degradation before reaching the target site.[109] However, leakage of the liposome content encountered several problems. Fluorescence probe carboxyfluorescein was used (CF) to investigate the liposomes leakage.[110]

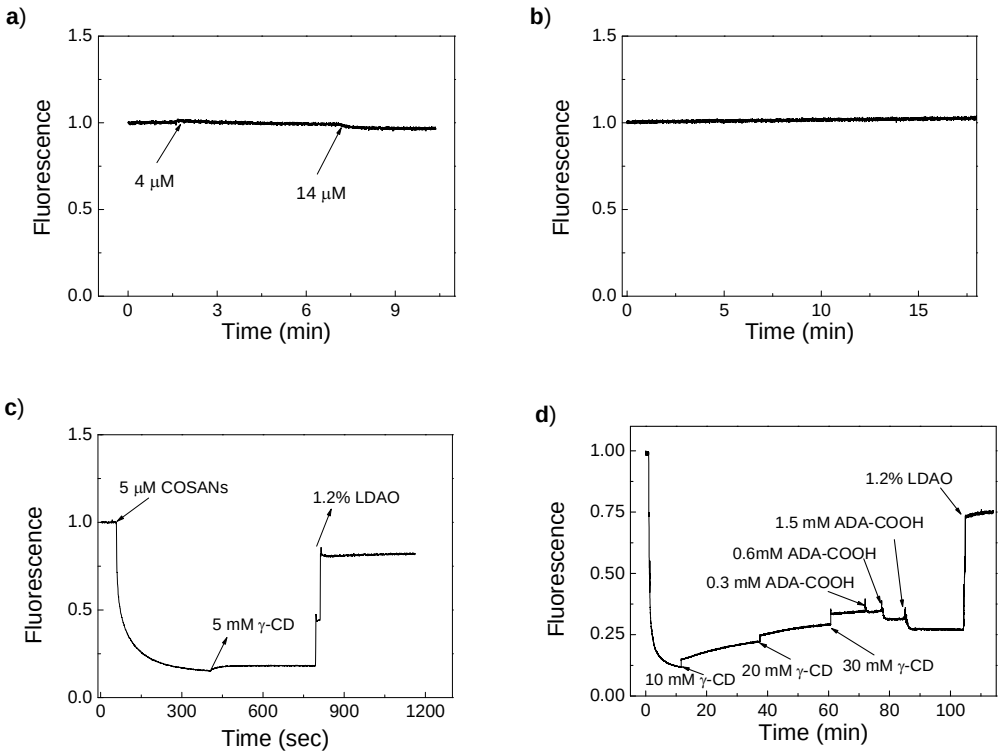

Figure 3.6. Time-dependent fluorescence changes a) upon addition of COSAN b) without COSAN of EYPC⊃CF liposomes c) translocation of COSAN was observed with addition of 5 μM COSAN to reporter pair (20 mM*γ*-CD/ 0.8 mM dapoxyl) loaded POPC/POPS liposomes, to further confirm leakage of the dapoxyl, when reached to the plateau 5 mM *γ*-CD was added. To lyse the vesicles 1.2% LDAO was added, this almost restores initial fluorescence intensity d) translocation of the COSAN further verified by the addition subsequent addition of *γ*-CD and adamantanecarboxylic acid.

Chapter 4

Fluorescent Artificial Receptor Membrane Assay (FARMA)

Chapter 4

4. Fluorescent Artificial Receptor Membrane Assay

This chapter is derived from the content of the following manuscript:

Nilam, M.; Collin, S.; Karmacharya, S.; Nau, W. M.; Hennig, A., Determination of Membrane Permeability and Activation Energy by Fluorescent Artificial Receptor Membrane Assays (FARMA) *Manuscript in Preparation*.

4.1 Membrane Permeability

Most drugs need to cross the cellular membrane to reach the predetermined target. Strong binding of a drug molecule to its expected target is significant for potency, and reduced cellular membrane permeability leads into low or non-existent *in vivo* efficacy.[34] Detailed understanding of the membrane permeability of the given molecule is essential in the viewpoint of pharmacokinetics and drug design.[34] Two different transport mechanisms are available in eukaryotic systems: active and passive. Active transport of molecules is associated with transport proteins, which utilize ATP to cross the membrane. However, passive transport allows diffusion of the molecules through the membrane without energy input, and is the most dominant route of the molecules to cross the membrane.[34]

Membrane permeability is a critical factor in the drug design channel. Several well-characterized *in vitro* and *in silico* permeability determination methods have been developed.[49, 111] These methods are highly useful in the early stages of the drug discovery process. The most common relatively simple methods are the parallel artificial membrane permeability assay (PAMPA)[112] and Caco-2 cell assay.[113]

4.1.1 Planar Lipid Membrane Permeability

The planar lipid membrane is one of the first model membrane, which is used to measure the permeability of analytes.[114] Planar lipid membranes are prepared by mixing lipids in an organic solvent using an aperture for isolating two aqueous compartments.[115] The perimeter of the aperture collects the solvent and generates the lipid bilayer across it. The benefits of the planar membranes are easy that it is to introduce the electrode and that the solution can be altered rapidly. Also, highly sensitive ion gradients can be obtained.[116] The major drawback of this method include a little amount of lipid present and the residual organic solvent can influence permeability changes at the lipid-aperture interface.[117]

The rate of the permeation of the analytes through the lipid bilayer membrane is defined by its flux (*J*), which is providing the number of molecules cross-unit area of the membrane per unit time (mol s^{-1} cm^{-2}). The flux can be explained as product of the permeability coefficient (P_m) and the concentration gradient of the analytes between the membranes (ΔC).[118]

$$J = P_m . \Delta C \qquad (3)$$

Permeability coefficient depends on several factors, such as analytes, the composition of the membrane, and experimental conditions (temperature). Further, the permeability coefficient reflects the intrinsic membrane permeability of the analyte at a set of constant experimental conditions.

4.1.2 Liposomes

Liposome were first prepared by mixing water and bilayer forming lipids.[119] Liposomes as a model system for study of the permeability of the analyte have several advantages. This includes, large membrane surface area, which allows investigating infrequent membrane permeation of analytes in addition, liposome solution can be investigated with a variety of instruments such as NMR, fluorometer, and UV-vis spectrometer.[120] Different sizes of the liposomes can be prepared, depending on the techniques used. For instance, dispersing the lipids in buffer generated multilamellar vesicles (MLVs). However, MLVs are not suitable to study the membrane permeability due to multilamellar nature and heterogeneous size distributions. Large unilamellar vesicles (LUVs) are suitable for the permeation measurements. These LUVs have a single bilayer and encapsulate an aqueous volume in the interior of the LUVs.

4.1.3 Determination of Rate Constants and Permeability Coefficients Using Liposomes

The efflux of the encapsulated analytes can be measured *via* marker molecules (probes). For example, fluorescamine was used to identify the amino acid permeability. Fluorescamine has high sensitivity (nmole) to the amino acid. Kinetic analysis of the entrapped molecules (efflux process) used initial rate analysis, which assumes that the concentration of the analyte in the interior is higher than the exterior of the liposome; thus, the efflux process obeyed the following relation.[121]

$$At_{(ex)} = A(eq)_{ex}(1 - e^{-kt}) \qquad (4)$$

Where, $At_{(ex)}$ is the exterior concentration of analyte at a time *t*, $A(eq)_{ex}$ is the exterior concentration of the analyte at equilibrium at $t = \infty$ and *k* is the rate constant

of the efflux process. Permeability coefficients (P_m) were calculated using following equations.[121]

$$P_m = (V_0 / A_m)\, k \quad (5)$$

Where, P_m is expressed in cm s^{-1}, V_0 is volume of the lipid vesicle, A_m is the area of the lipid vesicles and k is the rate constant, This expression further can be simplified to

$$P_m = (r/3)\, k \quad (6)$$

where r is the radius of the vesicle.

4.2 Determination of Membrane Permeability by Different Experimental Techniques

A variety of experimental techniques have been used to measure the membrane permeability coefficient. Most of the common techniques used in a planar bilayer membrane. The concentration gradient is generated between the membrane and change in the concentration is measured at particular time intervals. Concentration changes can be measured using radiolabeling,[36] UV-vis spectroscopy,[122] fluorescence spectroscopy,[118] and LC-MS.[123] Further, concentrations of electrochemically active molecules are obtainable using microelectrodes near the surface of the lipid membrane; for instance, permeation of K^+ was measured directly with the electrode.[124] The neutral form of weak acids and bases permeate through the membrane, and permeation of weak acid, and base can be measured using microelectrode. Further, ionic forms of the analytes are created in the surface of the membrane, for examples ammonia permeability is measured by the ammonium-selective electrode.[125] Several weak acid permeabilities have been measured using a pH-sensitive electrode, which is sensitive to small changes of the pH at the

surface of the membrane.[126] Permeability of H_2O_2 can be measured using a O_2-selective electrode, where O_2 can be generated by the reduction of the H_2O_2 inside the cell.[127] Magnetic resonance techniques are also applicable to study the permeability of analytes. Permeability of analytes has been measured using electron paramagnetic resonance (EPR); but, these techniques are limited to analytes with unpaired electrons.[128] EPR is a potential tool to study membrane permeability, and this technique provides the rate of diffusion at different depths of the membrane.[129] Nuclear magnetic resonance (NMR) is also suitable to measure the membrane permeability of analytes.[38]

Fluorescence spectroscopy has been used to measure the membrane permeability of analytes. A fluorescent dye molecule is encapsulated inside the liposome and permeation of the dye molecules is monitored by fluorescence spectroscopy. For instance, pH-sensitive fluorescent dye HPTS was encapsulated inside the liposome, and permeation of the proton was measured by the change in fluorescence.[130] Permeation of the analytes can be monitored by change in fluorescence, for example, liposome loaded with Tet receptor (TetR), which forms the complex with tetracycline and enhances the fluorescence.[131] Further salicylic acid permeation has been measured by the Tb^{3+} and carboxylate complex. Permeation of salicylic acid into Tb^{3+}-encapsulated liposome, and chelate enhances the fluorescence of Tb^{3+} by energy transfer from the aromatic system to the Tb^{3+} ion.[132]

4.3 Fluorescent Artificial Receptor Membrane Assay

Monitoring the permeability of aromatic molecules is of potential importance because, most of peptides, hormones, neurotransmitters, toxins, and drugs contain aromatic moiety in its structures.[133] Further, aromatic compounds are

chromophoric and detectable by spectrophotometry; however, some of the aromatic molecules are spectroscopically silent due to low solubility.[134] Thus, the development of sensitive fluorescence-based permeability assay is required for the understanding of permeability of these molecules. The fluorescent labeled assay has been developed to measure the membrane permeability but, label-free assays are highly preferable, because the addition of fluorescent tags to analytes can influence the permeability parameter of the analytes.[135]

To adapt the tandem assay principle to liposome-encapsulated reporter pair, we have selected (MDAP) as a fluorescent dye and CB8 as a macrocyclic receptor, which formed a highly fluorescent inclusion complex.[23, 80-81] The residual cavity space of CB8/MDAP complex provides subsequent binding of aromatic analytes into the residual cavity space, leading to net fluorescence quenching. Reporter pair CB8/MDAP based associative binding of analytes is much more sensitive than the displacement of the dye, which required suitable analytes with appropriate binding affinity to displace the fluorescent dye from the macrocycle molecule.[81] The transport of the analytes to reporter pair CB8/MDAP encapsulated liposomes, resulted in fluorescence quenching of MDAP. Furthermore, herein we describe fluorescent artificial receptor (FAR), which is a combination of macrocycle CB8 and fluorescent dye MDAP (**Scheme 4.1**). FAR encapsulated the liposome and a fluorescent artificial receptor membrane assay (FARMA) (**Scheme 4.1**) method was established, FARMA method can be used for monitoring the permeation of aromatic analytes across the membrane.

4.3.1 Binding Affinity and Translocations of the Analytes

The receptor molecules CB8 bind strongly (K_a = (10^4 - 10^6) × M^{-1}) to indole derivatives (**Table 4.1**), which have aromatic ring as a recognition motif. Binding constants (K_a) inside liposome for whole analytes decreases when increasing the temperature (**Table 4.1**). Further, increasing temperature weakens the noncovalent interactions between CB8 and analytes.[136] The translocation of the analytes becomes detectable in real-time with ease.[39] Transport of analytes into CB8/MDAP encapsulated liposomes affects dye fluorescence, only analyte able to move into the liposome where it forms a ternary complex with macrocycle. Macrocycle CB8 has residual cavity volume, which allows the subsequent binding of the aryl functionalized analytes into the cavity volume.

Scheme 4.1. The operational principle of fluorescent artificial receptor membrane assay (FARMA). Fluorescent artificial receptor CB8/MDAP was encapsulated inside the liposome, where the permeation of analytes with aromatic moiety binds to the FAR, which provides quenching of the emission of the FAR.

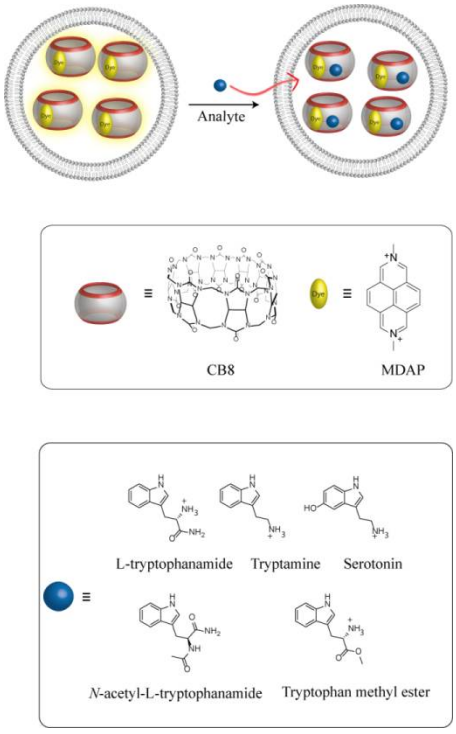

For the tandem membrane assay, 500 µM CB8 and 550 µM MDAP were encapsulated inside the liposome. Furthermore, tryptamine, tryptophan methyl ester (Trp-OMe), tryptophanamide (Trp-NH_2), *N*-acetyl tryptophanamide (Ac-Trp-NH_2), and serotonin translocations were tested. Increasing the analyte concentration resulted in faster kinetics and lowered the final fluorescence intensity, which led to a plateau at micromolar concentrations (**Figure 4.2 a, b**). Similar kinetics behavior is observed for all the analytes (**Figure A.10 - Figure A.19** see in appendix). This indicates that the translocation rate of the analytes exhibits a limiting value, in addition to that associative binding of the analyte with macrocycle CB8 became quantitative at high analyte concentration (**Figure 4.2b**).

4.3.2 Initial Rate Method by FARMA

In the FARMA method (**Figure 4.1**), an analyte permeates across the phospholipids membrane of the liposomes and binds to the internally entrapped FAR, which leads to an immediate modulation of the spectroscopic signal of the FAR. The rate constants for ingression, k_{in}, and egression, k_{out}, are same, and reflect the permeation rate constant $k_{\mathrm{P}} = k_{\mathrm{in}} = k_{\mathrm{out}}$. The net transport rate v depends thus on the concentrations of the transported analyte outside, $[A]_{\mathrm{out}}$, and the internal concentration of free (unbound) analyte, $[A]_{\mathrm{in,free}}$, which gives the rate law:

$$v = \frac{d[A]_{\mathrm{in,tot}}}{dt} = k_{\mathrm{P}}\left([A]_{\mathrm{out}} - [A]_{\mathrm{in,free}}\right) \quad (7)$$

In the initial rate method, $[A]_{\mathrm{in,tot}} = 0$ and thus $[A]_{\mathrm{in,free}} = 0$ at $t = 0$ and $[A]_{\mathrm{out}} = [A]_{\mathrm{tot}}$. The initial rate v_{in} is thus:

$$v_{\mathrm{in}} = \frac{[A]_{\mathrm{in,tot,t}}}{t} = k_{\mathrm{P}}[A]_{\mathrm{tot}} \quad (8)$$

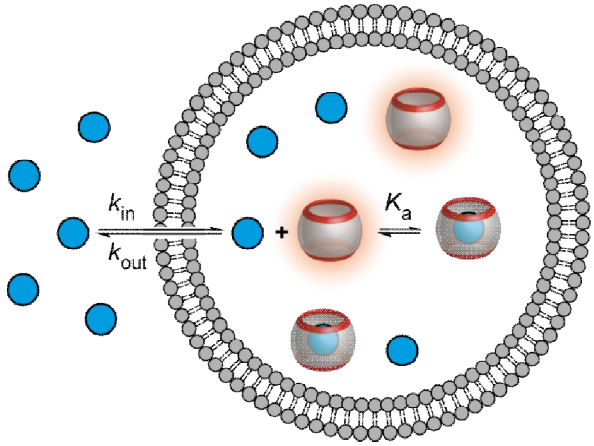

$$[A]_{out} \underset{k_{out}}{\overset{k_{in}}{\rightleftharpoons}} [A]_{in,free} + [CB8{\bullet}MDAP]_{in,free} \overset{K_a}{\rightleftharpoons} [CB8{\bullet}MDAP{\bullet}A]$$

Figure 4.1. General model for analyzing membrane transport kinetics obtained with the FARMA method.

The challenge in the FARMA method is to determine the internal total concentration at time *t*, $[A]_{in,tot,t}$, from the spectroscopic output signal. We therefore consider the dependence of the final fluorescence intensity in the plateau region of the time-resolved traces (**Figure 4.2, a**), I_∞, on $[A]_{tot}$ (**Figure 4.2, b**). This dependence reflects the binding equilibrium in the vesicle lumen, and the data can be analyzed with a 1:1 host-guest binding isotherm using the FAR concentration with respect to the total volume to give the binding constant, K_a, and the fluorescence intensity of the bound receptor, I_b, relative to the free receptor ($I_f = 1$) Reaching the plateau region indicates that no net transport occurs any longer (as long as the receptor is not saturated) such that $[A]_{out} = [A]_{in,free} \approx [A]_{tot}$. The total internal analyte concentration, $[A]_{in,tot}$, i.e. the amount of analyte that has crossed the membrane to reach the fluorescence plateau region and thus the transport equilibrium, is accordingly the sum of the free analyte inside the liposome and the analyte bound to the host:

$$[A]_{\mathrm{in,tot}} = [A]_{\mathrm{in,free}} + [HA] \approx [A]_{\mathrm{tot}} + [HA] \quad (9)$$

The internal concentration of the receptor–analyte complex $[HA]$ can be determined from the transport equilibrium fluorescence intensity, I_∞, which is given by the molar fractions of bound and free receptor, x_b and x_f, and their respective fluorescence intensities, I_b and I_f:

$$I_\infty = x_\mathrm{b} I_\mathrm{b} + x_\mathrm{f} I_\mathrm{f} = \frac{[HA]}{[H]_{\mathrm{tot}}} I_\mathrm{b} + \frac{[H]_{\mathrm{tot}} - [HA]}{[H]_{\mathrm{tot}}} I_\mathrm{f} \quad (10)$$

The total internal concentration is thus:

$$[A]_{\mathrm{in,tot}} \approx [A]_{\mathrm{tot}} + \frac{I_\infty - I_\mathrm{f}}{I_\mathrm{b} - I_\mathrm{f}} [H]_{\mathrm{tot}} \quad (11)$$

This allows converting the x-axis in **Figure 4.2, b** into total internal analyte concentrations to afford **Figure 4.2, c** which thus relates the fluorescence intensity of the plateau region I_∞ to the total internal analyte concentration $[A]_{\mathrm{in,tot}}$ by the fitted line with the slope β. Because the response of FAR (establishing the binding equilibrium) is immediate on the time scale of membrane transport, this equation holds true at any time during the transport process and not only, when equilibrium has been reached ($I_\infty = I$):

$$I = 1 + \beta\, [A]_{\mathrm{in,tot}} \quad (12)$$

The dependence of the initial rate in fluorescence change v_0' (in units of $[v_0'] = \mathrm{a.u.\,min^{-1}}$) can thus be converted into initial rates v_in (in units of $[v_\mathrm{in}] = \mu\mathrm{M\,min^{-1}}$):

$$v_0' = \frac{\Delta I}{\Delta t} = \frac{I-1}{t} = \frac{\beta\, [A]_{\mathrm{in,tot}}}{t} = \beta v_\mathrm{in} \Leftrightarrow v_\mathrm{in} = \frac{v_0'}{\beta} \quad (13)$$

This yields **Figure 4.2, d**, which can be analyzed by linear fitting to afford $k_\mathrm{P} = 3.04\ \mathrm{s^{-1}}$ for tryptophanamide at 25 °C. Furthermore, permeation rate constant k_P

can be converted into permeability coefficients P_m. The relationship between permeability coefficients P_m and permeation rate k_P has been established. [94]

$$P_m = k_P(\frac{r}{3})$$

Where, r is the radius of the vesicle (67 nm) and permeability $Pm = 6.8 \times 10^{-6}\ cm\ s^{-1}$ at 25 ˚C which is in agreement with the literature.[137] Moreover, smaller vesicles exhibit apparently faster permeation rates.[94] This procedure also has been applied to other analytes with different temperature (**Table 4.1**).

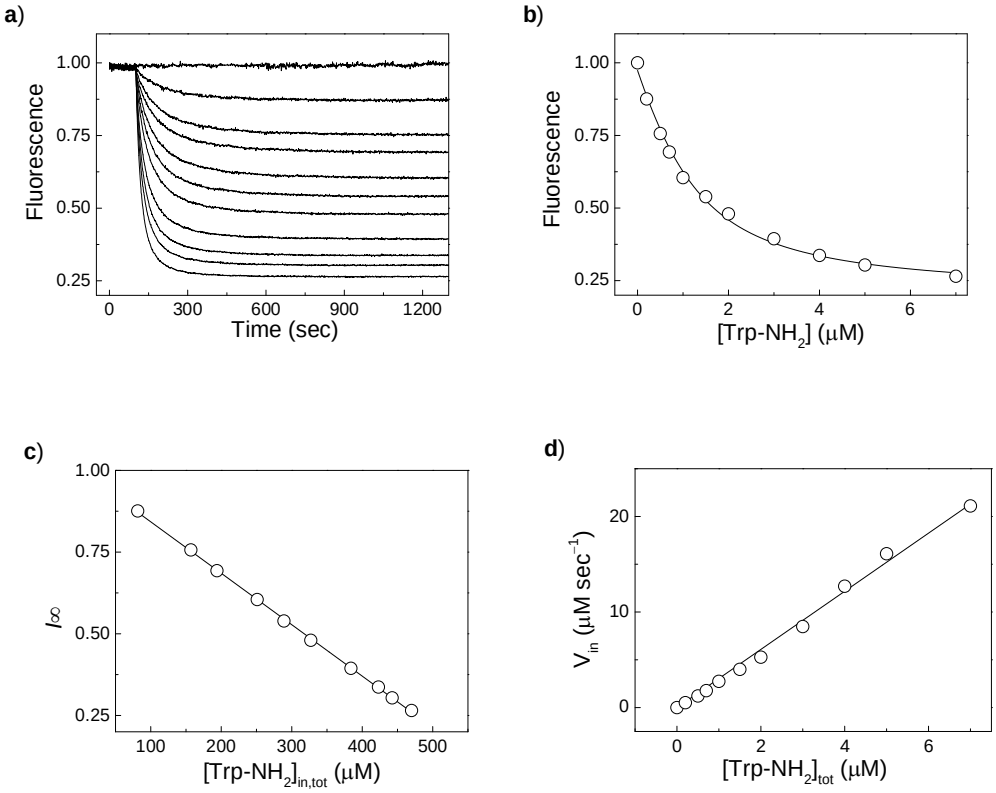

Figure 4.2. Data analysis by the initial rate method for Trp-NH_2 at 25 ˚C a) Normalized ($I_{norm} = I_t/I_{t=0}$) fluorescence kinetic traces. b) Dependence of the final fluorescence intensity I_∞ on total analyte concentration added. c) Dependence of the final fluorescence intensity on total internal analyte concentration including linear fit according to equation 12, $I_\infty = 1 + \beta\,[A]_{in,tot}$. d) Dependence of initial transport rates on added external analyte according to according to equation 8, $v_{in} = k_P[A]_{tot}$.

Table 4.1. Permeation rate constant (k_P) and permeability coefficients (P_m) for the permeation of analytes through liposomal POPC/POPS bilayer membranes (r = 67 nm).

Analyte	T (°C)	k_p (s^{-1})	P_m (10^{-6} cm s^{-1})	$K_a \times 10^5$ (M^{-1})
Tryptamine	10	3.1 ± 0.06	6.9 ± 0.1	(25 ± 5)
	15	5.9 ± 0.1	13 ± 0.2	(16 ± 2)
	20	12 ± 0.06	27 ± 0.1	(12 ± 1)
	25	15 ± 0.3	33 ± 0.7	(6.2 ± 0.8)
	30	23 ± 1.0	51 ± 2	(4.0 ± 0.5)
Trp-NH_2	10	0.36 ± 0.006	0.80 ± 0.01	(34 ± 7)
	15	0.64 ± 0.01	1.4 ± 0.02	(30 ± 4)
	20	1.3 ± 0.01	2.8 ± 0.02	(15 ± 3)
	25	3.0 ± 0.05	6.8 ± 0.1	(14 ± 2)
	30	4.7 ± 0.08	10 ± 0.2	(5.0 ± 0.5)
Ac-Trp-NH_2	10	0.035 ± 0.0003	0.078 ± 0.0007	(3.0 ± 0.3)
	15	0.062 ± 0.0004	0.14 ± 0.0009	(1.6 ± 0.08)
	20	0.12 ± 0.0006	0.27 ± 0.001	(1.0 ± 0.07)
	25	0.21 ± 0.002	0.47 ± 0.005	(0.65 ± 0.04)
	30	0.31 ± 0.002	0.69 ± 0.005	(0.45 ± 0.03)
Serotonin	15	0.0078 ± 0.0002	0.017 ± 0.0005	(0.45 ± 0.02)
	20	0.014 ± 0.0003	0.031 ± 0.0007	(0.37 ± 0.04)
	25	0.028 ± 0.0007	0.063 ± 0.002	(0.30 ± 0.02)
	30	0.044 ± 0.0009	0.098 ± 0.002	(0.22 ± 0.01)
	35	0.080 ± 0.001	0.18 ± 0.002	(0.17 ± 0.008)
Trp-OMe[a]	10	75 ± 2	168 ± 5	(1.12 ± 0.3)
	15	88 ± 2	196 ± 5	(0.91 ± 0.04)
	20	95 ± 3	212 ± 7	(0.53 ± 0.01)
	25	144 ± 5	321 ± 11	(0.18 ± 0.06)

[a] Measured by stopped-flow fluorescence measurement.

4.3.3 Effect of Temperature on the Membrane Permeability

Membrane permeation is highly temperature-dependent.[138] The effects of temperature on the permeability of the indole derivative through liposome were investigated using kinetic fluorescence analyses. These indole derivatives are well-known membrane-permeable analytes,[118, 137, 139] which have an appreciable binding affinity to the receptor molecules CB8.[23, 81] The permeability was measured at a given temperature. Kinetics measurements were performed at five different temperatures between 10 to 35 ˚C for POPC/POPS vesicles. Permeation of the analytes is increased with temperature. The activation energies for permeation were determined according to the Arrhenius equation by plotting the logarithms of permeation rate constant against the inverse of the absolute temperature (**Figure 4.3**, **Table 4.3**).

4.3.4 Comparison of Membrane Permeability Values by Other Assay Types and Membrane Composition

Permeability of the analytes across the membrane depends on several factors such as membrane thickness, membrane surface area, temperature, pH of the medium, and type of phospholipids.[94, 118, 140] According to the literature, several assay types are performed to estimate the permeability coefficient, for example, Caco-2, PAMPA, aliquot analysis/flat lipid bilayer. However, direct comparison of reported permeability coefficient is difficult, due to different type of assay and different lipid compositions as well as different membranes. For example, flat bilayer against liposomes that strongly affects the permeability coefficient. We have obtained permeability rates and permeability coefficients with a different temperature for

indole derivatives at low concentrations (**Table 4.1**). That fulfilled the anticipated linear dependence for analytes.

Table 4.2. The permeability coefficient of analytes through liposomal POPC/POPS bilayer membranes and comparison of other assay types.

Analyte	P_m (10^{-6} cm s^{-1})		Reference	Assay/Lipid type
	This work	Reference value		
Serotonin	0.098[b]	1.1	[118]	Flat lipid bilayer
Ac-Trp-NH_2	0.47[a]	0.3	[141]	PAMPA
Trp-NH_2	6.8[a]	2.7, 4.3	[137, 142]	PAMPA, Caco-2 cell
Tryptamine	33[a]	1.8[d], 5.4, 6.7[e], 74[f]	[118, 142]	Flat lipid bilayer/aliquot analysis, Caco-2 cell
Trp-OMe	321[c]	n.p.[g]	[143]	aliquot analysis

[a] Determined by FARMA in liposomal POPC/POPS bilayer membrane at 25˚C.[b] Determined by FARMA in liposomal POPC/POPS bilayer membrane at 30˚C.[c] Determined by FARMA using stopped-flow fluorescent measurement in liposomal POPC/POPS bilayer membrane at 25˚C. [d] Lipid composition: sphingomyelin-cholesterol,[e] lipid composition: brain phospholipids, [f] lipid composition: sphingomyelin. [g] n.p. = no permeability data has been reported.

Furthermore, permeability coefficient values determined by the FARMA method are slightly higher than other assay types. This is because POPC/POPS lipid membranes have higher permeability than the other lipid membranes (DPPC, DOPS and cholesterol) to amine molecules.[91] We have compared previously reported permeability values (**Table 4.2**) and the FARMA method. It exhibits that the FARMA methods provide permeability coefficients, which are on the same order of magnitude as those determined by other methods (**Table 4.2**). The permeability coefficient of tryptamine is different according to lipid composition, particularly tryptamine shows higher permeability coefficient through sphingomyelin,[118] which increases membrane permeability for the analytes.[144] Moreover, rapid permeation is observed for the analyte Trp-OMe,[143, 145] which required stopped-flow

fluorescent measurements to analyze the permeation rate constant and permeation coefficient. Further, the addition of aromatic methyl ester into POPC bilayer induces packing and conformation change in the POPC bilayer.[146]

4.3.5 Activation Energy for Permeations

Water-soluble molecules have a low rate of permeation comparatively lipophilic molecules where all these molecules have enough energy to permeate water-lipid interphase, therefore relatively low activation energy required for lipophilic compounds.[94] Further, the rate constants of each permeation step are important to investigate the main barrier of permeation of analytes. Transfer of molecules from the aqueous phase to the membrane phase correlates with activation energy, which associated with diffusion across the membrane that has been explored based on the hydrogen bond.[147] Transfer of molecules into the lipid membrane phase has been demonstrated with the number of the hydrogen bond,[147] which need to break to enter the membrane phase.[147]

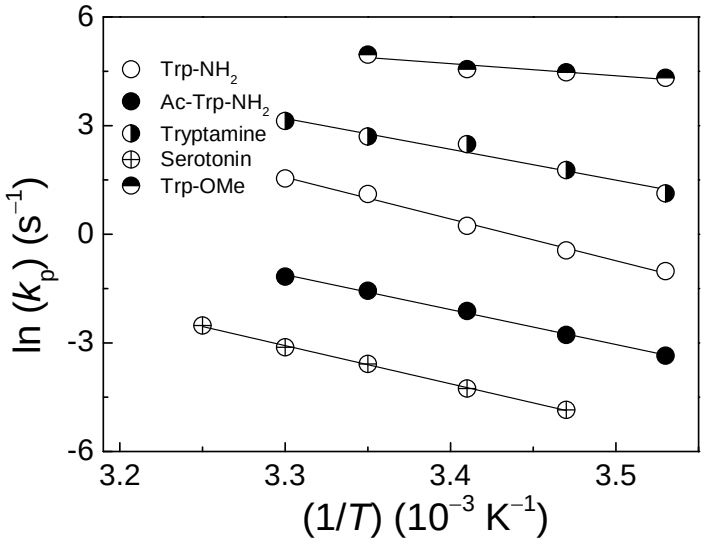

Figure 4.3. Arrhenius plot for the permeability of analytes across POPC/POPS liposomes.

Table 4.3. Activation energies (E_a) of indole derivatives through liposomal POPC/POPS bilayer membrane and estimated activation energies through the lipid membrane.

Analyte	Experimental E_a (kJ/mol)	Assigned number of H-bond[a]	Estimated E_a (kJ/mol)[b]	Reference value (kJ/mol)	Reference
Trp-NH_2	96 ± 4.0	6.0	100	n.r.[f]	
Ac-Trp-NH_2	80 ± 2.4	6.0	100	75[c]	[141]
Serotonin	88 ± 2.0	5.0	84.0	62,[d] 50 - 122[e]	[148]
Tryptamine	71 ± 2.0	3.0	50.0	n.r.[f]	
Trp-OMe	28 ± 7.0	3.5	58.5	n.r.[f]	

[a] assigned number of hydrogen bond, which is calculated based on the functional group of molecules. [b] Assigned based on hydrogen bonding energy (16.7 kJ/mol) (see details in main text). [c] Based on potential of mean force (PMF) simulation through DOPC bilayer. [d] Based on carrier-mediated transport through porcine platelets. [e] Based on chromaffin-granule membrane using ATPase-driven pump. [f] n.r. = no E_a has been reported.

For Trp-NH_2 the number of hydrogen bonds to be broken would be four for the primary amine and primary amide, and the secondary amine contribute one and the carbonyl group another one (total number of hydrogen bond is 6 for tryptophanamide, see **Table 4.3**). To break each hydrogen bond, 16.7 kJ/mol was assumed.[147b] Thus, Trp-NH_2 affords an activation energy of 100.2 kJ/mol, which is most similar to the experimental value. Similarly, the calculation method was applied to other analytes (**Table 4.3**). However, tryptamine activation energy is higher than the calculated value (**Table 4.3**) which might be POPC/POPS bilayer membrane increased the ability to form an intramolecular hydrogen bond.[149]

A similar observation has been reported for lysine methyl ester, which has higher experimental E_a through egg phosphatidylcholine membrane than estimated E_a.[149] The transport of Trp‑OMe through POPC/POPS lipid membrane was found to be surprisingly fast. Addition of aromatic amino acid methyl ester to the POPC bilayer

can influence physicochemical properties of POPC bilayer, for instance, molecular packing order, fluidity, and conformation of POPC acyl chains.[146] This study suggests a reason for the fast permeation of Trp-OMe through the POPC/POPS lipid membrane. Thus, to analyze Trp-OMe through POPC/POPS lipid membrane, stopped-flow measurements were performed. Further, increasing the Trp-OMe concentration resulted in faster kinetics and a lower fluorescence intensity was observed that reached a plateau at high Trp-OMe concentration (**Figure A.18** and **A.19** see in appendix).

4.4 Phase transition of the Membrane and Permeability

4.4.1 Phase Transition

To study phase transition and membrane transport, we have chosen a mixture of DPPC and DOPS lipids. Phase transitions of lipids have been established that the temperature for the gel to liquid-crystalline transition (T_c) depends on the chain-length, unsaturation of the acyl chains, and head group of the lipids.[150] The well-known phospholipid in this regard is DPPC, which has phase transition at approximately 41˚C.[151] Phase transition of lipid membranes leads to change of membrane rigidity. Thus, it is reasonable to predict that the gel to liquid-crystalline phase transitions would have a considerable effect on the permeability of the lipid membrane and temperature-dependent changes of permeability would be of physiological interest.[150] To investigate phase transition of the DPPC/DOPS (9:1) liposomes, we have performed differential scanning calorimetry (DSC), which shows phase transition temperature of particular lipid mixture is (37 ± 0.1) ˚C (**Figure A.20**). Further to study the permeability properties of the analytes through liposomes, we have measured fluorescence intensity changes of reporter pair

(CB8/MDAP) encapsulated liposomes. The effect of temperature on permeability rate constant and permeability coefficient of the analytes is shown in **Table 4.4**, **Figure A.21 - Figure A.23 (**see in appendix). A slow rate of permeation is observed below the transition temperature.

Table 4.4. Permeation rate constant (k_p) and permeability coefficients (P_m) for the permeation of analytes through liposomal DPPC/DOPS bilayer membranes (r = 65.5 nm).

Analyte	T (°C)	k_p (s^{-1})	P_m (10^{-6} cm s^{-1})	$K_a \times 10^5$ (M^{-1})
Tryptamine	20	2.0 ± 0.02	4.3 ± 0.04	(98 ± 8)
	25	7.4 ± 0.09	16 ± 0.2	(83 ± 8)
	30	29 ± 0.1	63 ± 0.2	(47 ± 3)
	35	50 ± 2	109 ± 4	(20 ± 2)
	40	104 ± 6	227 ± 13	(11 ± 3)
	45	128 ± 4	279 ± 8	(8.9 ± 0.3)
	50	144 ± 9	314 ± 20	(5.8 ± 0.2)
	55	155 ± 7	338 ± 15	(4.3 ± 0.7)
	60	165 ± 11	360 ± 24	(3.5 ± 0.7)
Trp-NH_2	20	0.066 ± 0.002	0.14 ± 0.004	(67 ± 2)
	25	0.26 ± 0.001	0.57 ± 0.002	(52 ± 4)
	30	1.4 ± 0.01	3.1 ± 0.02	(45 ± 6)
	35	7.9 ± 0.1	17 ± 0.2	(25 ± 2)
	40	26 ± 0.09	57 ± 0.2	(11 ± 3)
	45	43 ± 0.4	94 ± 0.9	(3.3 ± 0.3)
	50	59 ± 6	130 ± 13	(5.5 ± 0.2)
	55	64 ± 7	141 ± 15	(4.0 ± 0.5)
	60	85 ± 3	186 ± 7	(3.4 ± 0.4)
Ac-Trp-NH_2	20	0.013 ± 0.00005	0.028 ± 0.0001	(1.6 ± 0.3)
	25	0.045 ± 0.00006	0.098 ± 0.0001	(0.80 ± 0.05)
	30	0.14 ± 0.001	0.31 ± 0.002	(0.50 ± 0.02)
	35	0.45 ± 0.007	0.98 ± 0.02	(0.35 ± 0.02)
	40	1.2 ± 0.06	2.5 ± 0.1	(0.20 ± 0.01)
	45	2.0 ± 0.07	4.4 ± 0.1	(0.10 ± 0.01)
	50	2.2 ± 0.05	4.8 ± 0.1	(0.080 ± 0.006)
	55	2.9 ± 0.2	6.4 ± 0.1	(0.070 ± 0.008)

4.4.2 Lipid Phase Transition and Activation Energy for Permeations

The permeation rate of the analytes through DPPC/DOPS liposomal membrane exhibited discontinuities in the Arrhenius plot (**Figure 4.4**), which are unique for each type of analytes and membrane.[152] Discontinuities in the Arrhenius plots of several membranes and analytes have been reported in terms of phase transition of lipids.[153] Arrhenius plots of Trp-NH_2, Ac-Trp-NH_2, and tryptamine transport were biphasic. The breaks in the Arrhenius plots at 39˚C follow the gel to liquid-crystalline phase in the membrane. Similar biphasic behavior is observed for the transport of tyrosine and phenylalanine through *Brevibacterium linens* cells.[153e]

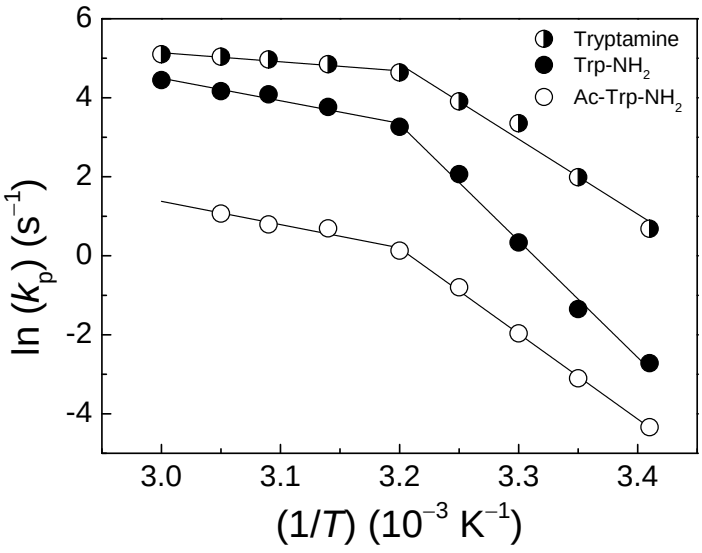

Figure 4.4. Arrhenius plot for the permeability of analytes across DPPC/DOPS liposomes.

The increases of the activation energy (**Table 4.5**) below discontinuity is exhibited closer packing of the hydrocarbon chain in the liposomal membrane.[153d] Further, low activation energy is obtained above the phase transition temperature. Below, the transition temperature of lipids is formed rigid semicrystalline structure[152a] and thus decrease the permeability of the analytes. When increasing the temperature,

semicrystalline structure melts and increases the fluidity, which increases the membrane permeability.

Table 4.5. Activation energies of indole derivatives through liposomal DPPC/DOPS bilayer membrane.

Analyte	E_a (kJ/mol) gel phase	E_a (kJ/mol) crystalline-liquid phase
Trp-NH_2	245 ± 11	47 ± 5.0
Ac-Trp-NH_2	180 ± 3.5	49 ± 8.0
Tryptamine	158 ± 14	19 ± 2.0

In summary, the FARMA method allows with real-time optical monitoring of the permeation of analytes through the liposomal membrane and avoids the use of labeled analytes. Moreover, FARMA assay can be used as alternative to the assays for well-known membrane assays PAMPA and Caco-2 assay. FAR-based membrane assay allows the real-time monitoring of rapid permeation of analytes based on stopped-flow fluorescent measurements. As a consequence, we believe that FARMA will become a significant tool in the membrane research field.

Chapter 5

Gold Nanoparticles-Based Sensing

Chapter 5

5. Characterization of Mixed-Ligand Shells on Gold Nanoparticles

Corresponds to: **Appendix 10.3.2**

1. **Nilam, M.;** Ahmed, M.; Alnajjar, M. A.; Hennig, A., Characterization of Mixed-Ligand Shells on Gold Nanoparticles by Transition Metal and Supramolecular Surface Probes. *Analyst* **2019**, *144*, 579-586. Reproduced with permission from the Royal Society of Chemistry.

Corresponds to: **Appendix 10.3.3**

1. **Nilam, M.;** Hennig, A.; Nau, W. M.; Assaf, K. I., Gold Nanoparticles Aggregation Enables Colorimetric Sensing Assays for Enzymatic Decarboxylation. *Anal. Methods* **2017**, *9*, 2784-2787. Reproduced with permission from the Royal Society of Chemistry.

Monolayer and mixed‐monolayer protected AuNPs have been extensively studied for their use in a variety of applications, including biological sensing,[52] imaging,[52] biocompatibility cell targeting applications,[53] nanowires,[54] and nanotubes.[55] The addition of functional groups like amine or carboxylate moieties to the surface of AuNPs allows forming chemical bonds with target ligands.[56] For example, the carboxylate group is able to form amide bonds directly with an amino group of a molecule.[57] Ligand footprint, coupling efficiency, and accessibility of functional groups on the particle surface are the parameters which are of utmost importance for quality control in many applications.[58] To assess these parameters, fast, simple, and reliable screening methods are required. Quantification of the ratio of ligands on multifunctional nanoparticles has proven a challenge, whereas many techniques are available for determining the presence of functional groups on nanoparticles (**Scheme 5.1**).[154]

Scheme 5.1. Experimental techniques used to characterize the AuNPs surface and analyzing techniques (left) and AuNPs decomposition or ligand exchange analyzing techniques (right).

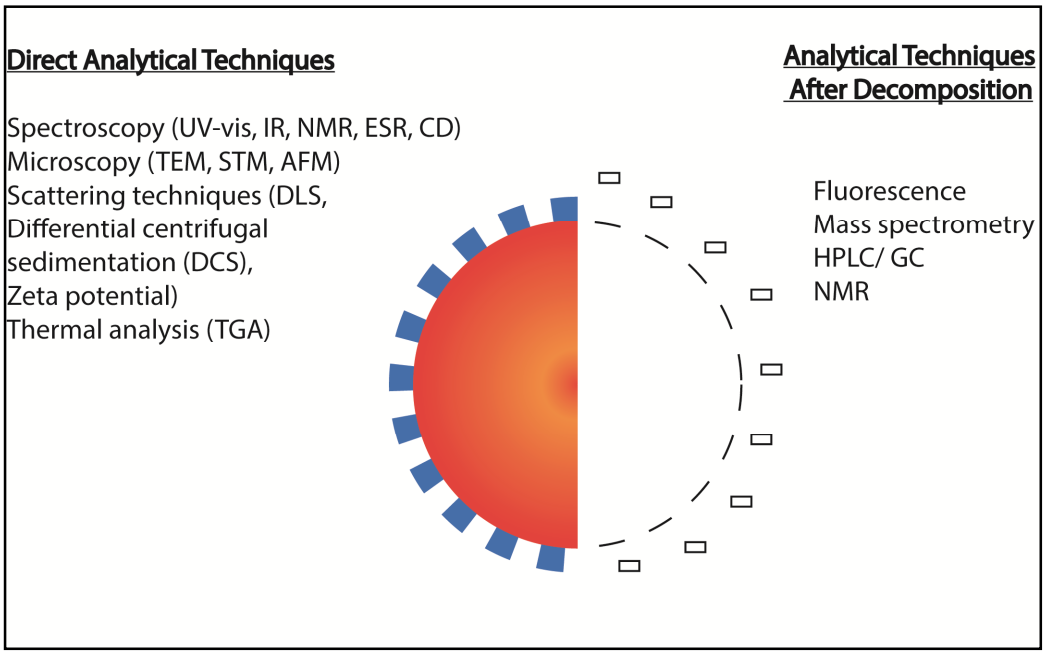

5.1 General Ligand Quantification Techniques

Thermogravimetric analysis (TGA) has been used to assess nanoparticles ligand density.[155] In a typical experiment, nanoparticles were dried prior to the TGA, and then TGA was performed under N_2 atmosphere and the sample was heated from 30 ˚C to 700 ˚C (ramp rate 5‑20 ˚C min^{-1}). The weight is decreased due to the heating process, which is due to decomposition of the organic ligands in the nanoparticles.[154b] Weight loss as a function of temperature can be correlated to the ligand density of the nanoparticles. However, TGA is limited to a single ligand attached to the nanoparticles and cannot differentiate mixed ligand shells with temperatures. for example, similar mass ligands are attached to nanoparticles.[154b]

NMR spectroscopy is the most valuable tool for the determination of the ligand density on nanoparticles, where an internal standard was used with nanoparticles.[156] The ligand of interest peak area was compared to an internal standard peak area. The following methods can determine the interesting ligand concentration. Calibration curve was constructed using an internal standard, unknown ligand concentration can be determined.[156] The alternative method is associated with the number of ^{1}H nuclei and involves the internal standard peak area and the ligand of the peak area of interest.[58] Here, a known concentration of an internal standard is added to the unknown sample. The ligand concentration of interest can be determined by comparing the integrated peak area of the internal standard to the integrated peak area of the ligand of interest.[58] However, line broadening was observed in ^{1}H NMR of nanoparticles ligands shells and limited direct NMR to small nanoparticles < 3 nm.[157] Also, potential interference from the solvent and other functional groups limits the accuracy in the quantification of ligands.[158]

To bypass the adverse effects linked with line broadening and chemical shift changes, the ligand can be removed from the core of the nanoparticles ("off particle"). Several methods are used to remove the ligands from the core of the nanoparticles, for example, oxidative cleavage of thiol ligands from gold nanoparticles using I_2, where organic ligands are released to the solution as a disulfide.[159] Furthermore, cyanide anions are induced decomposition ("etching") of the gold core and produced a colorless solution of $Au(CN)_2^-$. Etchings of the gold core depend on the monolayer of the particles.[157b, 160] Moreover, aqua regia can be used to remove the ligands from the gold surface. The resulting reaction mixture was then analyzed by NMR and ICP‑MS (**Scheme 5.2**).[156] However, off particle

analysis has some adverse effects associated with long experiment time due to the low sensitivity of NMR and potential challenges in spectral peak assignment.[154b]

Absorption spectroscopy can be used to quantify the ligand density of nanoparticles, typically requires optically active indicators. Several conjugation techniques have been developed to couple optically active molecules to various inorganic nanoparticles, including EDC condensation reaction,[161] thiol-ene reaction,[162] and avidin-biotin binding reaction.[163]

Scheme 5.2. Typical aqua regia digestion of gold nanoparticles, here nanoparticles capped gold nanoparticles are digested, and released ligands are quantified by ^{1}H NMR, and metal ion can be quantified by ICP-MS.

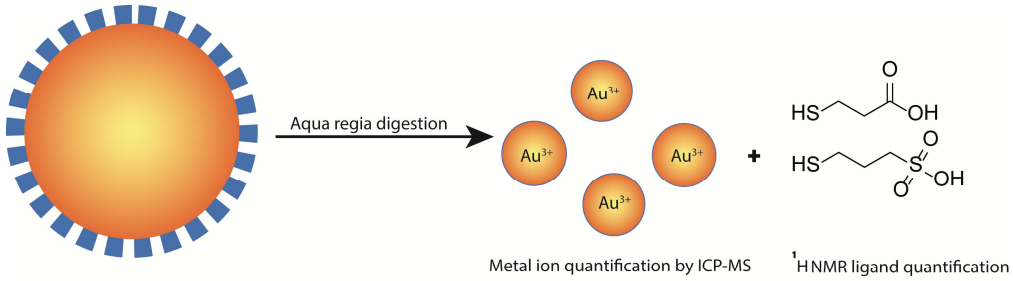

Furthermore, the external indicator was used to study the ligand density of the nanoparticles. In this approach, free ligand concentration was monitored by UV-vis absorption spectroscopy before and after incubation with the ligand. To determine the ligand density of α-amino-ω-mercapto-poly(ethylene glycol) (NH_2PEGSH) capped AuNPs, ninhydrin was used as an external indicator, which reacts with primary amines to produce a dark purple color.[164] Here the known concentration of AuNPs was incubated with the known concentration of (NH_2PEGSH). Aliquots (supernatant) of the free NH_2PEGSH were removed before and after this incubation step and were mixed with ninhydrin. The difference in absorbance before and after

incubation was measured at 565 nm and compared to the standard curve, which allowed the difference in NH_2PEGSH concentration. In addition to that, Ellman's reagent was used as an external indicator to quantify the ligand density of polyethylene capped gold nanoparticles. Ellman's reagent reacts with free sulfhydryl group and produces an absorption band at 412 nm.[165] Here, to investigate the effect of PEGSH grafting on both, serum protein absorption and subsequent macrophage intake of AuNPs, were analyzed. Furthermore, AuNPs were incubated with various concentrations of PEGSH and it was assumed that all particle-bound thiol groups were unavailable for further reaction. After incubation, the remaining thiol content was quantified by thiol depletion assay. Recently, a simple colorimetric method established quantification of surface carboxylate group on acrylate polymer micro and nanoparticles by utilizing the binding of the surface functional groups to divalent transition metal ions (Ni^{2+}, Co^{2+}, Cd^{2+}) and subsequent colorimetric determination of excess metal ions with pyrocatechol violet (PV) after a single centrifugation step.[166]

Fluorescence-based methods for determining surface coverage of AuNPs have been reported,[167] where gold nanoparticles were modified with fluorescently labeled ligand and purified to remove the excess ligand. During the ligand exchange, the release of the ligand fluorescence was monitored, and ligand density was quantified.[167a] Furthermore, to determine the number of accessible (functionalizable) group, fluorescein has been used as a labeling compound. Therefore, mixed monolayer (carboxy and amino-terminated PEG-thiols) protected AuNPs were prepared. The *N*-hydroxysuccinimidyl (NHS)-ester of fluorescein was used as a labeling compound. This assay gives an approximate, number of molecules that can be accessible to the gold nanoparticles using NHS-ester

chemistry. Noteworthy, this assay does not give the total average number of amino groups per particle. These assays reflect only accessible, functional groups under a defined set of conditions.[167b] Furthermore, recently, we have investigated chemically available (accessible) functional groups on acrylate polymer micro and nanoparticle surfaces, using supramolecular host-guest interaction between CB7 and adamantylmethylamine derivative.[168]

ATR-FTIR is also used to quantify the ligand density of the nanoparticles. However, FTIR related method required calibration curves by plotting the intensity of IR absorbance against the concentration of the free ligand to quantify the ligand density of the particles.[169] Furthermore, FTIR spectroscopy allows to simultaneously quantify the mixed ligands. X-ray photoelectron spectroscopy (XPS) has also been used to quantify nanoparticle ligand density.[170] However, XPS is a surface-sensitive technique; therefore, several factors have to be considered to determine the ligand density of the particles such as radius of curvature, substrate thickness, and signal to noise ratio between core and surface elements.[170]

5.2 Mixed Ligand and Quantification Technique

Herein, we present a new class of mixed monolayer protected MPA/MPS-AuNPs and MUA/TEG-AuNPs. Moreover, NMR methods, colorimetric assay, and supramolecular CB7 assay were used to quantify the extent of ligand exchange between different types of thiolated molecules on the surface of AuNPs. Our objective was to assess the quantification of the surface carboxy group and the suitability of a more straightforward approach by employing colorimetric and fluorescent measurements. We thus used gold nanoparticles with mixed ligands and

with the different molar ratios of the ligands on the gold nanoparticles surface. Moreover, we studied surface functionalities on AuNPs by ^{1}H NMR as well as with NiPV assay. Also, to investigate accessible functional group on nanoparticles surface, the supramolecular host guest interaction between CB7 and adamantylmethylbutane-1,4-diamine (AMADA‑Put) was used.

Also, we determine the footprint value of the AuNPs and then use these data to describe ligand exchange behavior with a second thiolated molecule. Using these techniques, we identified trends in AuNP functionalization efficiency with respect to ligand type, concentration as well as identified functionalization pathways, where the new ligand may either alter the existing ligand shell (exchange) or add to it. These studies have significant implications for how AuNPs surface chemistry can be modified and used in a wide variety of applications.

Scheme 5.3. Representation of the three key methods for the analysis of mixed ligand capped gold nanoparticles.

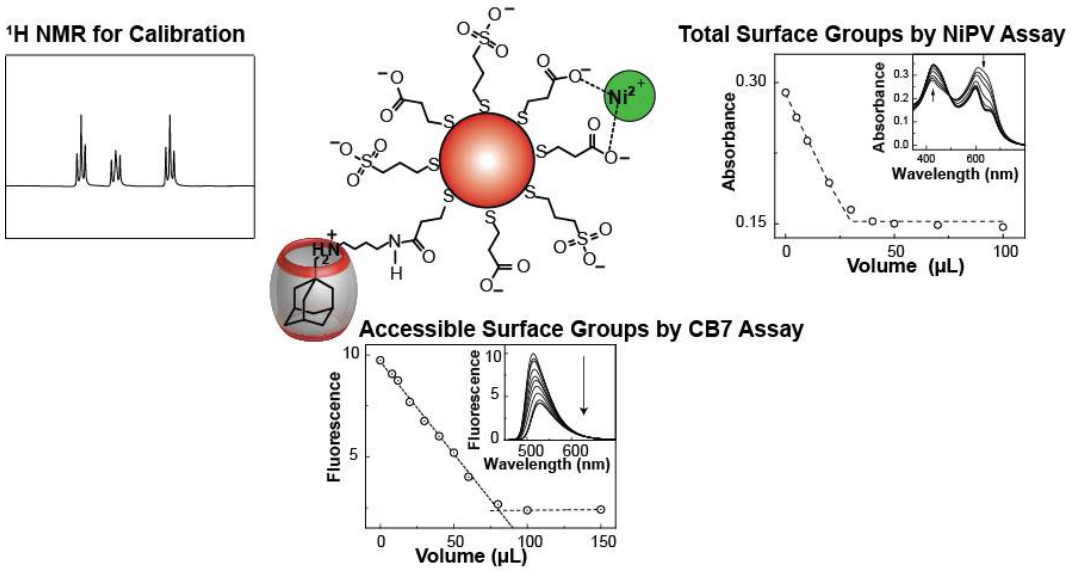

5.3 Gold Nanoparticles-Based Colorimetric Sensing

Gold nanoparticles have been used in a variety of biomedical applications and the attractive size‑dependent chemical, electronic, and optical properties, high surface to volume ratio, and biocompatibility of the AuNPs are useful in the development of several assays. Further, the size of the AuNPs is compatible with biomolecules (DNA, enzyme, and antibody), which have sizes in the range of 2 - 20 nm and thus admit the structural compatibility of these materials.[171] AuNPs can be easily functionalized with different probes and other compounds of interest.[172]

Colorimetric sensing based on AuNPs depends on the surface plasmon resonance property.[173] Biomolecular interaction can be monitored to control the dispersion and aggregation of the nanoparticles.[174] Aggregation of the particles will lead to color changes, from pink to violet to pale blue.[173] This phenomenon has been used for the colorimetric detection of several analytes. Particularly, nanoparticles biosensors are composed of immobilized ligand or biological substrate, which is undergoes conversion in the presence of an analyte. The change in substrate composition or conformation induces aggregation of the nanoparticles and leads to the color changes.[175]

Conventional detection of analytes and quantification methods are based on recording the absorbance and fluorescence from the particular chromophoric molecule. Further, these techniques are adequate for many applications; however, improving the sensitivity is required in a variety of other applications.[176] Nanoparticles-based assays have been developed to measure minute changes in enzyme activity with high accuracy. Nanoparticles-based colorimetric sensing is a valuable tool in HTS and drug discovery process.

5.3.1 Surface Resonance Band and Aggregation

The unique surface plasmon resonance band is associated with aggregation and dispersion of particles and makes AuNPs a colorimetric reporter. Changes in the external environment of the AuNPs will lead to aggregation or dispersion of the particles. That can be detected by the shift in the absorption spectrum. The shift in absorption spectra is proportional to the extent of aggregation or re-dispersion.[177] In size range of 13 - 300 nm, AuNPs are prone to aggregation. This can be characterized by plasmon resonance band at 520 nm, which gradually decreases and a new band appears between 600 - 700 nm resulting in a color change from red to purple or dark blue depending on the degree of aggregation.[178] The molar extinction coefficient of AuNPs plays a vital role in the sensitivity of the colorimetric assay. The absorption ratio (A_{600}/A_{520}) of aggregated particles and non-aggregated particles of AuNPs is often used to measure the extent of aggregation and also well-known as the aggregation parameter for AuNPs.[179]

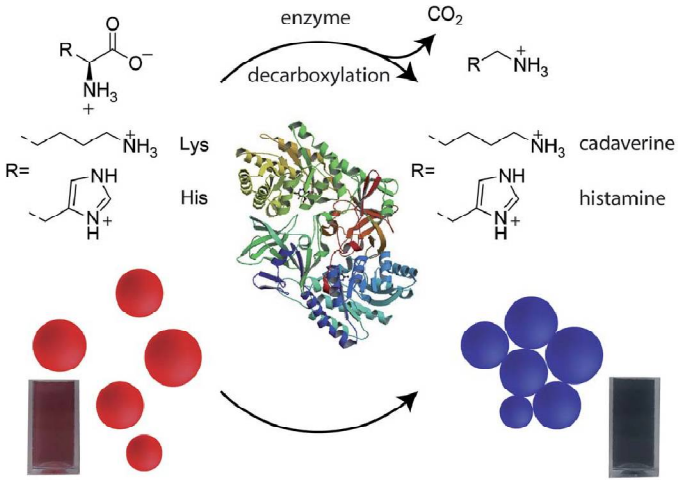

Figure 5.1. Assay principle illustrating the colorimetric response of AuNPs in the course of enzymatic decarboxylase reaction.

Chapter 6

Host-Guest Complexation Affects Perylene-Based Dye Aggregation

Chapter 6

6. Host-Guest Complexation Affects Perylene-Based Dye Aggregation

Corresponds to: **Appendix 10.3.4**

Nilam, M.; Chusen, H.; Shreya, K.; Aryal, G. H.; Huang, L.; Nau, W. M.; Assaf, K. I., Host-Guest Complexation Affects Perylene-Based Dye Aggregation (*manuscript in preparation*).

6.1 Perylene Dye

A rigid, polycyclic, aromatic perylene core is attached with two dicarboxylic acid imide groups at the 3,4-and 9,10-positions. Electron-rich perylene core and electron-withdrawing imide groups have strong conjugation in the perylene molecules, thereby, it has a strong UV-vis absorption and shifts absorption band of perylene from 440 nm to 525 nm.[60] Further, perylene diimide (PDI) has a quantum yield of ~ 0.90 in all common solvents, these dyes have excellent thermal and photochemical stability. PDI dyes have been investigated for optoelectronic applications, in dye lasers, and as probes for biomacromolecules recognition (DNA, RNA, and proteins).[60]

However, PDIs show poor water solubility and weak fluorescence in aqueous solution and form aggregates due to π-π stacking interaction between perylene cores.[180] This generates a significant problem in the application in biological and medicinal fields. For instance, PDI dyes are of limited usefulness in confocal microscopy or single molecule spectroscopy techniques.

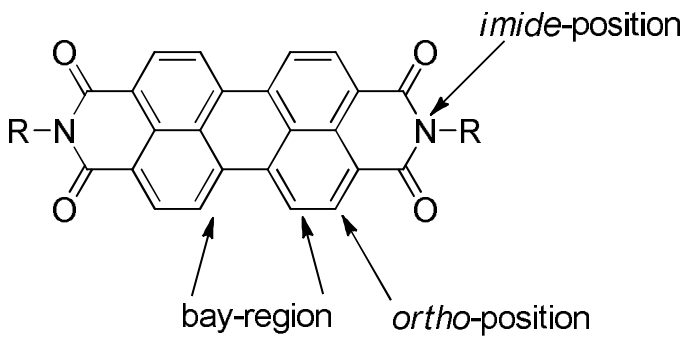

Figure 6.1. General structure of PDIs.

6.2 Water Soluble PDI Chromophore

Several attempts have been made to achieve a higher water solubility of PDIs by adding hydrophilic groups in the bay-region or imide and *ortho*-positions.[181] To increase the water solubility of PDIs ionic groups such as cationic ammonium salts, anionic carboxylic acids, sulfonic acids, and phopsphonic acid have been included in PDI chromophores.[182] An alternative strategy is to increase the water solubility of PDI dyes by introducing non-ionic molecules such as polyglycerol,[183] polyethylene glycol[184] and dendrons[185] in the bay-region or imide positions of the PDI chromophore (**Figure 6.1**). Additions of water-soluble functional groups reduces the aggregation of the perylene cores and affords excellent photophysical properties, it also suppresses the π-π stacking interaction between perylene cores.

The substituent at the imide-positions is used to change solubility of the PDIs in a variety of solvents and minimally affects the optical and electronic properties. These derivatives possess green-yellow emission of PDI with higher fluorescence

quantum yield. The substituent at the bay-region is primarily used to tune the photophysical properties resulting in derivatives with red shifted absorption maximum and increased the Stokes shift. Modifications in the *ortho*-position affect the optical and electronic properties without changing the planarity of the perylene core.[182] However, these synthetic approaches inhibit aggregation of the PDI chromophore, and functionalized PDI dyes show excellent photophysical properties. However, the addition of particular components in the bay–region or imide positions is more critical from the synthetic point of view.

6.3 Supramolecular Approach to Prevent PDI Aggregation

Host-guest complexation efficiently inhibits aggregation of the PDI dyes in water using host molecules such as CB8,[186] CD,[187] and Exbox[188] *via* non-covalent interactions. Particularly entrapment of PDI core inside the large macrocycle CB8 gives fluorescence enhancement, and binding affinity was determined to be in the range of 10^4 - 10^5 M^{-1}, because loose fitting of perylene core inside CB8 cavity.[189] To increase the binding affinity with macrocycle CB8, PDI dyes have been modified with phenyl groups introduced, resulting in ternary complexes with higher binding affinity.[190]

Scheme 6.1. Chemical and cartoon representations of the PDI dye, the investigated macrocyclic hosts, and potential binding modes with different hosts.

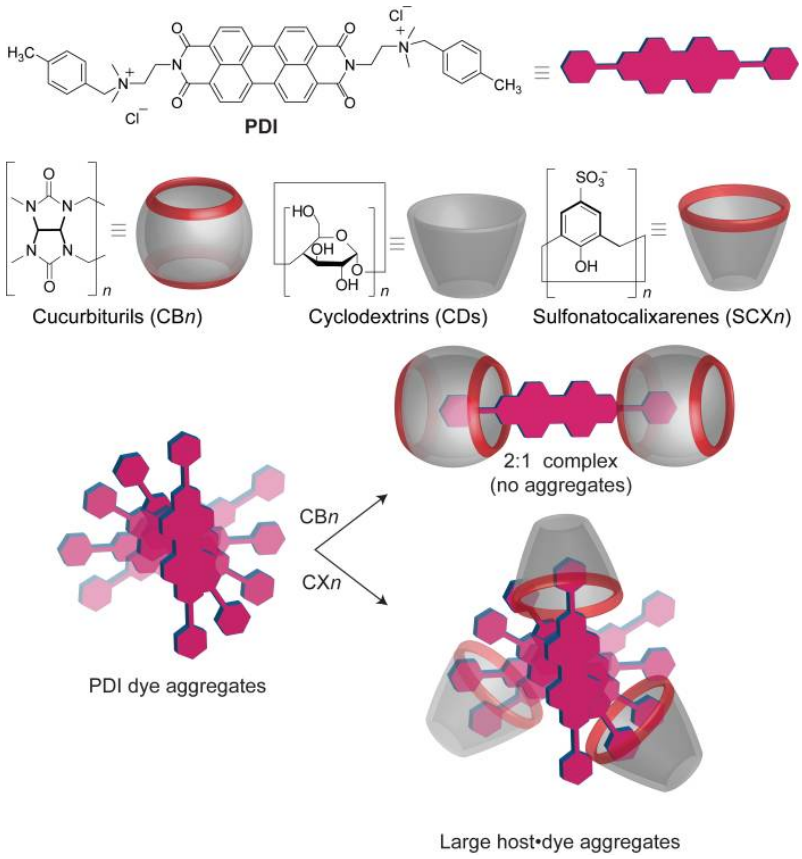

Chapter 7

Materials and Methods

Chapter 7

7. Materials and Methods

7.1 Supramolecular Tandem Membrane Assay

7.1.1 Materials

Lipids: 1-palmitoyl-2-oleoyl-*sn*-glycero-3-phosphocholine (POPC),1-palmitoyl-2-oleoyl-*sn*-glycero-3-phospho-L-serine (POPS), 1,2-dipalmitoyl-*sn*-glycero-3-phosphocholine (DPPC) and 1,2-dioleoyl-*sn*-glycero-3-phospho-L-serine (DOPS) were purchased from Avanti Polar Lipids (Alabaster, AL, USA).

Macrocyclic hosts: CB8 and CB7 were purchased from Strem Chemicals (Kehl, Germany) but have been also synthesized according to previous literature.[18a, 191] (2-hydroxypropyl)-*β*-cyclodextrin was obtained from Cyclolab (Budapest, Hungary).

Fluorescent dyes: Berberine chloride and palmatine chloride were obtained from Sigma-Aldrich (Steinheim-Germany). Dye MDAP was synthesized according to previous literature[192] but with some modification of the procedure (see next page).

Analytes: Tryptamine hydrochloride (Trp), L-tryptophan methyl ester hydrochloride (Trp-OMe), L-tryptophanamide hydrochloride (Trp-NH_2), serotonin hydrochloride and *N*-acetyl-L-tryptophanamide (Ac-Trp-NH_2), tyramine hydrochloride, 2-phenylethylamine hydrochloride, 1-adamantylamine, and cyclohexylamine were obtained from Sigma-Aldrich (Steinheim-Germany). *N*,*N*-dimethylaminomethylferrocene was purchased from Alfa Aesar (Karlsruhe, Germany).

NAP-25 sephadex columns G-25 DNA grade were from GE Healthcare (Buckinghamshire, United Kingdom).

7.1.2 Synthesis of 2,7-Dimethyldiazapyrenium (MDAP)

Scheme 7. 1. Synthesis of MDAP

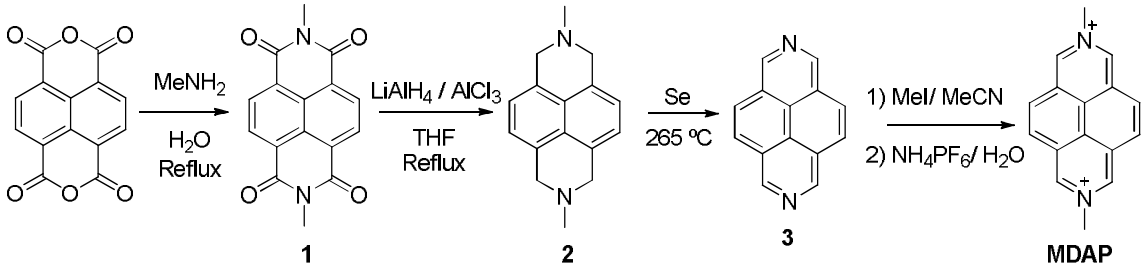

*2,7-Dimethyl-1,4,5,8-naphthalenetetracarboxylic Diimide **(1)**:* 1,4,5,8-naphthalenetetracarboxylic dianhydride (5,0 g; 20 mmol) was added slowly to an aqueous solution of $MeNH_2$ (40% wt. 160 mL). The mixture was heated under reflux for 4 h. After cooling down to RT, the suspension was filtered and the precipitate was washed with MeOH (3 x 50 mL) to give **1** (5.79 g, 98%) as a brownish/pink powder. ^1H NMR (CD_3Cl): δ 8.78 (4H, s); 3.61 (6H, s).

*2,7-Dimethyl-1,4,5,8- tetrahydrodiazapyrene **(2)**:* A suspension of $AlCl_3$ (1.20 g, 9 mmol) in THF (100 mL) was cooled in ice bath and maintained under N_2. $LiAlH_4$ (1.07g, 28.17 mmol) and then **1** (1.14g, 3.9 mmol) were added slowly in portions. The reaction mixture was stirred under reflux for 3h, and allows cooling down to ambient temperature; then was pouring on ice/THF (250 g/100 mL) and filtering. The solid residue was washed with THF and suspended in DCM (100 mL). After refluxing 30 min and cool down to ambient temperature, the suspension was filtered. This treatment was repeated twice more. The combined organic solutions were concentrated under reduced pressure. The residue was re-disolved in DCM

and washed with H_2O (3 x 50 mL). The organic phase was dried over $MgSO_4$ and concentrated under reduced pressure to give **2** (476 mg, 51%) as a light yellow solid. ^{1}H NMR (CD_3Cl): δ 7.17 (4H, s); 3.98 (8H, s); 2.61 (6H, s).

*2,7-Diazapyrene **(3):*** Compound **2** (476 mg, 2 mmol) and Se (880 mg, 11.2 mmol) were ground together and heated at 265 °C for 4 h and then at 300 °C for 1h. After cooling down to ambient temperature, aqueous HCl (1M, 10 mL) was added. The resulting suspension was stirred under reflux for 20 min and filtered. This procedure was repeated three more times. The pH of the combined aqueous solutions was adjusted to 10 with NaOH (1M) yielding a cloudy dark orange solution that was extracted three times with DCM. The combined organic portions were dried with anhydrous $MgSO_4$ and concentrated under reduced pressure. The residue was recrystallized with toluene to give **3** as yellow solid. (70 mg, 17%). ^{1}H NMR (CD_3Cl): δ 9.54 (4H, s); 8.24 (6H, s).

*2,7-dimethyldiazapyrenium (**MDAP**):* Compound **3** (50 mg, 0.25 mmol) was dissolved in CH_3CN (8 mL) and was heated under reflux, then CH_3I (50 µL, 0.55 mmol) was added. The mixture was stirred under reflux for 3 h. After cooling down to ambient temperature, the suspension was filtered and washed with ethyl acetate. The resulting solid was re-dissolved in H_2O (5 mL) and NH_4PF_6 (0.41 g, 2.5 mmol) was added. The reaction was stirred at ambient temperature for 30 min. The resulting precipitate was filtered and washed with H_2O (10 mL) to give **MDAP** (97 mg, 74%). ^{1}H NMR (CD_3CN): δ 9.81 (4H, s); 8.82 (4H, s); 4.85 (6H, s).

Counterion exchange: MDAP.2Cl was prepared by counterion exchange from MDAP.2PF_6 by the addition of tetrabutylammonium chloride to acetonitrile solution of MDAP.2PF_6 in order to precipitate MDAP.2Cl.

7.1.3 Fluorescence Kinetic Measurements

Fluorescence was measured with a Varian Cary Eclipse spectrophotometer equipped with a temperature controller. In all experiments, liposome solutions of 20 µL CB8/MDAP, CB7/PLM, and HP-β-CD/BE encapsulated POPC/POPS liposome were diluted with 100 mM Na_2HPO_4, pH 10.8 to a total volume in the cuvette of 2000 µL and gently stirred. Fluorescence was monitored according to reporter pair emission wavelength (CB8/MDAP λ_{em} = 423 nm, λ_{exc} = 338 nm, CB7/PLM λ_{em} = 495 nm, λ_{exc} = 425 nm, HP-β-CD/BE λ_{em} = 540 nm, λ_{exc} = 420 nm) as a function of time after addition of analytes. Further, fluorescence titrations were carried out with similar instrument conditions (slit width, PMT voltage) as in kinetic measurements.

Permeability measurements: In all experiments, liposome solutions of 20 µL (CB8/MDAP encapsulated POPC/POPS liposome or DPPC/DOPS liposome) were diluted with 10 mM Hepes, pH 7.0 to a total volume in the cuvette of 2000 µL and gently stirred. The sample was allowed to equilibrate for at least 12 min with different temperature (10 - 60 ˚C). Fluorescence was monitored at λ_{em} = 450 nm (λ_{exc} = 338 nm) as a function of time after the addition of analytes.

7.1.4 Stopped-flow Fluorescence Measurements.

Stopped-flow measurements were carried out with a BioLogic stopped-flow SFM-20 module coupled with a JASCO FP-8500 spectrophotometer and temperature controller Julabo F25. In the experimental setup, 200 µL of POPC/POPS liposome encapsulated CB8/MDAP solution was diluted with 9800 µL of 10 mM Hepes, pH 7.0 buffer. This solution was placed in syringe 1, and syringe 2 was filled with different concentrations of tryptophan methyl ester (0 -240 µM). Fluorescent measurements were initiated by mixing the contents of two syringes in equal

volume (total volume 200 µL and flow speed 4.5 mL/s) in a stopped-flow chamber. All experiments were performed with 10 mM Hepes, pH 7.0 and the temperature was changed between 10 - 25 ˚C and samples were allowed to equilibrate at least 10 - 12 minutes. Fluorescence was monitored at λ_{em} = 450 nm (λ_{exc} = 338 nm) as a function of time after the addition of analytes and liposomes. For each experiment, measurements from 8 to 14 injections were accumulated and the average of these traces was used for the analysis.

7.1.5 Preparation of POPC/POPS Vesicles with Reporter Pair

A solution of 100 µL, 25 mg/ml of POPC, and 33 µL, 10 mg/ml of POPS in chloroform was purged with nitrogen and dried overnight under high vacuum. Then, the lipid film was hydrated with 1 mL of particular buffer. For instance, CB8/MDAP encapsulated liposome was prepared with 100 mM Hepes, pH 7.5, containing 0.5 mM CB8 and 0.55 mM MDAP; reporter pair CB7/PLM encapsulated liposome was prepared with 100 mM NaH_2PO_4/Na_2HPO_4, pH 7.5 containing 1 mM CB7 and 1 mM PLM; and for reporter pair HP-β-CD/BE encapsulated liposome, lipid concentration was changed (25 mg/ml of POPC, 200 µL and, 10 mg/ml of POPS 66 µL). Then, the lipid film was hydrated with 100 mM sodium citrate, pH 3.5 containing 20 mM HP-β-CD, and 1mM BE. Then, resulting suspension was gently stirred at room temperature for 30 minutes. After that, the liposome suspension was subjected to 20 freeze-thaw cycles. The resulting reporter pair-loaded liposomes were separated from unencapsulated macrocycle and dye by size exclusion chromatography (NAP-25) with a particular buffer. The size of the liposomes (*see Appendix)* was obtained by using a Zetasizer Nano from Malvern Instruments. Final lipid concentration was determined through ^{1}H NMR according to our recently published article.[193]

7.1.6 Preparation of DPPC/DOPS Vesicles with CB8/MDAP

A solution of 100 µL, 25 mg/ml of DPPC, and 33 µL, 10 mg/ml of DOPS, in chloroform was purged with nitrogen and dried overnight under high vacuum. Then, the lipid film was hydrated with 1 mL of 10 mM Hepes, pH 7.0, containing 0.5 mM CB8 and 0.55 mM MDAP and then gently stirred at 65 ˚C temperatures for 30 minutes. After that, the liposome suspension was subjected to 15 freeze-thaw cycles (4 minutes freezing in liquid N_2 and thawing in the water bath at 65˚C) and 15 times extruded with 100 nm pore size poly carbonate membrane (extrusion setup kept at 65˚C). Extravesicular components were removed by size exclusion chromatography (NAP-25) with 10 mM Hepes. The size of the liposomes (131 nm) (**Figure A.24**) was obtained by using a Zetasizer Nano from Malvern Instruments.

Chapter 8

Summary and Outlook

Chapter 8

8. Summary and Outlook

This doctoral thesis mainly describes liposome-based enhanced sensing and determination of membrane permeability and activation energy by fluorescent artificial receptor membrane assay (FARMA). I have noted that all analytes exhibited an apparently stronger binding to the liposome-encapsulated CB8/MDAP, CB7/PLM, HP-β-CD/BE reporter pairs compared to homogeneous solution. In other words, the liposome-encapsulated reporter pair gave a stronger fluorescence response at lower analyte concentrations, which consistently resulted in a sensitivity enhancement for a small set of randomly selected analytes. This entirely unexpected result is of immediate relevance for sensing applications and we coined the name "liposome-enhanced sensing" for this phenomenon. Within this thesis, I have explored whether this is a general effect and measured a similar series of analytes with a different reporter pair (using pH gradient)

Time-resolved monitoring of membrane translocation of analytes is of utmost importance in the membrane research field. Existing methods are limited to single point determinations or flat synthetic membranes, limiting biologically relevant kinetic parameters (permeation rate constant, permeation coefficients). With the established supramolecular approach to membrane transport assays, a facile and straightforward method is now available to assess the ability of a molecule to permeate through the phospholipid membrane. This has been applied to translocation through membrane pores, and I have now explored for monitoring passive diffusion. I have used the self-assembled CB8/MDAP receptor, which binds aromatic molecules with an unprecedented combination of high affinity and

comparably low selectivity by ternary complex formation. Noteworthy, a low selectivity is considered here as an advantage because the same receptor responds to a large class of related molecules, which is ideal for screening applications. The addition of these compounds to CB8/MDAP-encapsulated liposomes allowed us to judge their ability to permeate through the phospholipid membrane qualitatively. With this FARMA method, we can determine the dependence of membrane transport rates and activation energies (by temperature-dependent measurements) of small molecules.

Chapter 9

References

Chapter 9

9. References

[1] J.-M. Lehn, *Science* **1985**, *227*, 849-856.
[2] H. Kunz, *Angew. Chem. Int. Ed.* **2002**, *41*, 4439-4451.
[3] D. J. Cram, *Angew. Chem. Int. Ed.* **1988**, *27*, 1009-1020.
[4] J.-M. Lehn, *Angew. Chem. Int. Ed.* **1988**, *27*, 89-112.
[5] C. J. Pedersen, *Angew. Chem. Int. Ed.* **1988**, *27*, 1021-1027.
[6] D. J. Cram, M. E. Tanner, R. Thomas, *Angew. Chem. Int. Ed.* **1991**, *30*, 1024-1027.
[7] a) S. J. Barrow, S. Kasera, M. J. Rowland, J. del Barrio, O. A. Scherman, *Chem. Rev.* **2015**, *115*, 12320-12406; b) S. B. Nimse, T. Kim, *Chem. Soc. Rev.* **2013**, *42*, 366-386.
[8] M. J. Webber, R. Langer, *Chem. Soc. Rev.* **2017**, *46*, 6600-6620.
[9] a) V. I. Parvulescu, H. García, *Catal. Sci. Technol.* **2018**, *8*, 4834-4857; b) C. Yang, Y. Inoue, *Chem. Soc. Rev.* **2014**, *43*, 4123-4143.
[10] a) V. Martí-Centelles, M. D. Pandey, M. I. Burguete, S. V. Luis, *Chem. Rev.* **2015**, *115*, 8736-8834; b) R. Saito, H. Kobayashi, *Macromolecules* **2002**, *35*, 7207-7213.
[11] G. Crini, *Chem. Rev.* **2014**, *114*, 10940-10975.
[12] R. N. Dsouza, U. Pischel, W. M. Nau, *Chem. Rev.* **2011**, *111*, 7941-7980.
[13] J. S. Kim, D. T. Quang, *Chem. Rev.* **2007**, *107*, 3780-3799.
[14] a) A. Jasat, J. C. Sherman, *Chem. Rev.* **1999**, *99*, 931-968; bA. Shivanyuk, J. Rebek, *J. Am. Chem. Soc.* **2003**, *125*, 3432-3433.
[15] K. I. Assaf, W. M. Nau, *Chem. Soc. Rev.* **2015**, *44*, 394-418.
[16] R. Behrend, E. Meyer, F. Rusche, *Liebigs Ann.* **1905**, *339*, 1-37.
[17] W. A. Freeman, W. L. Mock, N. Y. Shih, *J. Am. Chem. Soc.* **1981**, *103*, 7367-7368.
[18] a) J. Kim, I.-S. Jung, S.-Y. Kim, E. Lee, J.-K. Kang, S. Sakamoto, K. Yamaguchi, K. Kim, *J. Am. Chem. Soc.* **2000**, *122*, 540-541; b) A. I. Day, R. J. Blanch, A. P. Arnold, S. Lorenzo, G. R. Lewis, I. Dance, *Angew. Chem. Int. Ed.* **2002**, *41*, 275-277; c) A. Day, A. P. Arnold, R. J. Blanch, B. Snushall, *J. Org. Chem.* **2001**, *66*, 8094-8100; d) X.-J. Cheng, L.-L. Liang, K. Chen, N.-N. Ji, X. Xiao, J.-X. Zhang, Y.-Q. Zhang, S.-F. Xue, Q.-J. Zhu, X.-L. Ni, Z. Tao, *Angew. Chem. Int. Ed.* **2013**, *52*, 7252-7255.
[19] S. He, F. Biedermann, N. Vankova, L. Zhechkov, T. Heine, R. E. Hoffman, A. De Simone, T. T. Duignan, W. M. Nau, *Nat. Chem.* **2018**, *10*, 1252-1257.
[20] K. A. Kellersberger, J. D. Anderson, S. M. Ward, K. E. Krakowiak, D. V. Dearden, *J. Am. Chem. Soc.* **2001**, *123*, 11316-11317.
[21] J. Lagona, P. Mukhopadhyay, S. Chakrabarti, L. Isaacs, *Angew. Chem. Int. Ed.* **2005**, *44*, 4844-4870.
[22] F. Biedermann, V. D. Uzunova, O. A. Scherman, W. M. Nau, A. De Simone, *J. Am. Chem. Soc.* **2012**, *134*, 15318-15323.
[23] F. Biedermann, W. M. Nau, *Angew. Chem. Int. Ed.* **2014**, *53*, 5694-5699.
[24] Y. H. Ko, E. Kim, I. Hwang, K. Kim, *Chem. Commun.* **2007**, *13*, 1305-1315.

[25] A. P. de Silva, H. Q. N. Gunaratne, T. Gunnlaugsson, A. J. M. Huxley, C. P. McCoy, J. T. Rademacher, T. E. Rice, *Chem. Rev.* **1997**, *97*, 1515-1566.
[26] S. L. Wiskur, H. Ait-Haddou, J. J. Lavigne, E. V. Anslyn, *Acc. Chem. Res.* **2001**, *34*, 963-972.
[27] J. Mohanty, W. M. Nau, *Angew. Chem. Int. Ed.* **2005**, *44*, 3750-3754.
[28] B. D. Wagner, S. J. Fitzpatrick, *J. Inclusion Phenom. Macrocyclic Chem.* **2000**, *38*, 467-478.
[29] W. M. Nau, J. Mohanty, *Int. J. Photoenergy* **2005**, *7*.
[30] a) M. A. Alnajjar, J. Bartelmeß, R. Hein, P. Ashokkumar, M. Nilam, W. M. Nau, K. Rurack, A. Hennig, *Beilstein J. Org. Chem.* **2018**, *14*, 1961-1971; b) A. Praetorius, D. M. Bailey, T. Schwarzlose, W. M. Nau, *Org. Lett.* **2008**, *10*, 4089-4092.
[31] G. Ghale, W. M. Nau, *Acc. Chem. Res.* **2014**, *47*, 2150-2159.
[32] A. Hennig, H. Bakirci, W. M. Nau, *Nat. Methods* **2007**, *4*, 629-632.
[33] R. N. Dsouza, A. Hennig, W. M. Nau, *Chem.: Eur. J.* **2012**, *18*, 3444-3459.
[34] K. Sugano, M. Kansy, P. Artursson, A. Avdeef, S. Bendels, L. Di, G. F. Ecker, B. Faller, H. Fischer, G. Gerebtzoff, H. Lennernaes, F. Senner, *Nat. Rev. Drug Discov.* **2010**, *9*, 597.
[35] K. R. Mahendran, E. Hajjar, T. Mach, M. Lovelle, A. Kumar, I. Sousa, E. Spiga, H. Weingart, P. Gameiro, M. Winterhalter, M. Ceccarelli, *J. Phys. Chem. B* **2010**, *114*, 5170-5179.
[36] A. Walter, J. Gutknecht, *J. Membr. Biol.* **1986**, *90*, 207-217.
[37] G. Wu, K. Y. C. Lee, *J. Phys. Chem. B* **2009**, *113*, 15522-15531.
[38] J. Andrasko, *J. Magn. Reson.* **1976**, *21*, 479-484.
[39] G. Ghale, A. G. Lanctôt, H. T. Kreissl, M. H. Jacob, H. Weingart, M. Winterhalter, W. M. Nau, *Angew. Chem. Int. Ed.* **2014**, *53*, 2762-2765.
[40] E. W. Gerner, F. L. Meyskens, *Nat. Rev. Cancer* **2004**, *4*, 781-792.
[41] a) C. S. Coleman, G. Hu, A. E. Pegg, *Biochem. J.* **2004**, *379*, 849-855; b) V. T. Dufe, D. Ingner, O. Heby, A. R. Khomutov, L. Persson, S. Al-Karadaghi, *Biochem. J.* **2007**, *405*, 261-268.
[42] Q. Liu, B. J. Boyd, *Analyst* **2013**, *138*, 391-409.
[43] L. Locascio-Brown, A. L. Plant, R. Chesler, M. Kroll, M. Ruddel, R. A. Durst, *Clin. Chem.* **1993**, *39*, 386-391.
[44] H. A. H. Rongen, H. M. van der Horst, G. W. K. Hugenholtz, A. Bult, W. P. van Bennekom, P. H. van der Meide, *Anal. Chim. Acta* **1994**, *287*, 191-199.
[45] E. L. Chang, B. A. Waite, *J. Immunol. Methods* **1987**, *102*, 33-43.
[46] H. Chen, J. Huang, A. Palaniappan, Y. Wang, B. Liedberg, M. Platt, A. I. Y. Tok, *Analyst* **2016**, *141*, 2335-2346.
[47] a) S. Viswanathan, L.-c. Wu, M.-R. Huang, J.-a. A. Ho, *Anal. Chem.* **2006**, *78*, 1115-1121; b) K. A. Edwards, A. J. Baeumner, *Talanta* **2006**, *68*, 1421-1431; c) U. Kauscher, M. C. A. Stuart, P. Drücker, H.-J. Galla, B. J. Ravoo, *Langmuir* **2013**, *29*, 7377-7383.
[48] a) T. Ogoshi, T.-a. Yamagishi, Y. Nakamoto, *Chem. Rev.* **2016**, *116*, 7937-8002; b) R. Pinalli, E. Dalcanale, *Acc. Chem. Res.* **2013**, *46*, 399-411; c) M. V. Rekharsky, Y. Inoue, *Chem. Rev.* **1998**, *98*, 1875-1918.
[49] B. J. Bennion, N. A. Be, M. W. McNerney, V. Lao, E. M. Carlson, C. A. Valdez, M. A. Malfatti, H. A. Enright, T. H. Nguyen, F. C. Lightstone, T. S. Carpenter, *J. Phys. Chem. B* **2017**, *121*, 5228-5237.

[50] J. M. Reis, B. Sinko, C. H. Serra, *Mini-Rev. Med. Chem.* **2010**, *10*, 1071-1076.
[51] A. Avdeef, in *Absorption and Drug Development*, John Wiley & Sons, Inc., **2012**, pp. 319-498.
[52] V. Biju, *Chem. Soc. Rev.* **2014**, *43*, 744-764.
[53] I. Fratoddi, I. Venditti, C. Cametti, M. V. Russo, *J. Mater. Chem. B* **2014**, *2*, 4204-4220.
[54] a) Y. Xia, P. Yang, Y. Sun, Y. Wu, B. Mayers, B. Gates, Y. Yin, F. Kim, H. Yan, *Adv. Mater.* **2003**, *15*, 353-389; b) J. Hu, T. W. Odom, C. M. Lieber, *Acc. Chem. Res.* **1999**, *32*, 435-445.
[55] H. Dai, *Acc. Chem. Res.* **2002**, *35*, 1035-1044.
[56] a) L. Foti, A. Sionek, E. M. Stori, P. P. Soares, M. M. Pereira, M. A. Krieger, C. L. Petzhold, W. H. Schreiner, M. J. Soares, S. Goldenberg, C. K. Saul, *J. Mater. Chem. B* **2015**, *3*, 2725-2731; b) H. Hakkinen, *Nat. Chem.* **2012**, *4*, 443-455.
[57] M. Zheng, X. Huang, *J. Am. Chem. Soc.* **2004**, *126*, 12047-12054.
[58] L. Tong, E. Lu, J. Pichaandi, P. Cao, M. Nitz, M. A. Winnik, *Chem. Mater.* **2015**, *27*, 4899-4910.
[59] S. S. Babu, V. K. Praveen, A. Ajayaghosh, *Chem. Rev.* **2014**, *114*, 1973-2129.
[60] F. Würthner, C. R. Saha-Möller, B. Fimmel, S. Ogi, P. Leowanawat, D. Schmidt, *Chem. Rev.* **2016**, *116*, 962-1052.
[61] a) F. Yukruk, A. L. Dogan, H. Canpinar, D. Guc, E. U. Akkaya, *Org. Lett.* **2005**, *7*, 2885-2887; b) M. Sun, K. Müllen, M. Yin, *Chem. Soc. Rev.* **2016**, *45*, 1513-1528.
[62] F. Würthner, *Chem. Commun.* **2004**, *14*, 1564-1579.
[63] a) S. Chen, P. Slattum, C. Wang, L. Zang, *Chem. Rev.* **2015**, *115*, 11967-11998; b) T. Weil, T. Vosch, J. Hofkens, K. Peneva, K. Müllen, *Angew. Chem. Int. Ed.* **2010**, *49*, 9068-9093.
[64] B. Zhang, H. Soleimaninejad, D. J. Jones, J. M. White, K. P. Ghiggino, T. A. Smith, W. W. H. Wong, *Chem. Mater.* **2017**, *29*, 8395-8403.
[65] a) P. Imming, C. Sinning, A. Meyer, *Nat. Rev. Drug Discov.* **2006**, *5*, 821-834; b) L. C. Wienkers, T. G. Heath, *Nat. Rev. Drug Discov.* **2005**, *4*, 825-833.
[66] a) M. G. Acker, D. S. Auld, *Perspect. Sci.* **2014**, *1*, 56-73; b) J.-P. Goddard, J.-L. Reymond, *Curr. Opin. Biotechnol.* **2004**, *15*, 314-322; c) S. L. Sjostrom, Y. Bai, M. Huang, Z. Liu, J. Nielsen, H. N. Joensson, H. Andersson Svahn, *Lab Chip* **2014**, *14*, 806-813.
[67] E. W. Gerner, F. L. Meyskens, *Nat. Rev. Cancer.* **2004**, *4*, 781-792.
[68] a) N. Babbar, N. A. Ignatenko, R. A. Casero, Jr., E. W. Gerner, *J. Biol. Chem.* **2003**, *278*, 47762-47775; b) N. A. Ignatenko, H. Zhang, G. S. Watts, B. A. Skovan, D. E. Stringer, E. W. Gerner, *Mol. Carcinog.* **2004**, *39*, 221-233.

[69] a) F. Botrè, F. Mazzei, *Bioelectrochem. Bioenerg.* **1999**, *48*, 463-467; b) R. Djurhuus, *Anal. Biochem.* **1981**, *113*, 352-355; c) F. Gaboriau, R. Havouis, J.-P. Moulinoux, J.-G. Delcros, *Anal. Biochem.* **2003**, *318*, 212-220; d) T. Hyvonen, T. A. Keinanen, A. R. Khomutov, R. M. Khomutov, T. O. Eloranta, *J Chromatogr* **1992**, *574*, 17-21; e) T. T. Ngo, K. L. Brillhart, R. H. Davis, R. C. Wong, J. H. Bovaird, J. J. Digangi, J. L. Ristow, J. L. Marsh, A. P. H. Phan, H. M. Lenhoff, *Anal. Biochem.* **1987**, *160*, 290-293; f) N. Qu, N. A. Ignatenko, P. Yamauchi, D. E. Stringer, C. Levenson, P. Shannon, S. Perrin, E. W. Gerner, *Biochem. J.* **2003**, *375*, 465-470; g) Y. Wang, U. Bachrach, *Anal. Biochem.* **2000**, *287*, 299-302.

[70] D. Russell, S. H. Snyder, *Proc. Natl. Acad. Sci. U.S.A.* **1968**, *60*, 1420-1427.

[71] L. Badolo, V. Berlaimont, M. Helson-Cambier, M. Hanocq, J. Dubois, *Talanta* **1999**, *48*, 127-134.

[72] W. M. Nau, G. Ghale, A. Hennig, H. Bakirci, D. M. Bailey, *J. Am. Chem. Soc.* **2009**, *131*, 11558-11570.

[73] Z. Li, S. Sun, F. Liu, Y. Pang, J. Fan, F. Song, X. Peng, *Dyes. Pigm.* **2012**, *93*, 1401-1407.

[74] a) U. Bachrach, Y. C. Wang, *Amino Acids* **2002**, *22*, 1-13; b) A. E. Pegg, L. M. Shantz, C. S. Coleman, *J. Cell. Biochem.* **1995**, *59*, 132-138.

[75] D. Wu, A. C. Sedgwick, T. Gunnlaugsson, E. U. Akkaya, J. Yoon, T. D. James, *Chem. Soc. Rev.* **2017**, *46*, 7105-7123.

[76] H. Stieve, *Sens. Actuators, B* **1983**, *4*, 689-704.

[77] O. Livnah, E. A. Bayer, M. Wilchek, J. L. Sussman, *Proc. Natl. Acad. Sci. U. S. A.* **1993**, *90*, 5076-5080.

[78] H. He, M. A. Mortellaro, M. J. P. Leiner, R. J. Fraatz, J. K. Tusa, *J. Am. Chem. Soc.* **2003**, *125*, 1468-1469.

[79] E. V. Anslyn, *J. Org. Chem.* **2007**, *72*, 687-699.

[80] V. Sindelar, M. A. Cejas, F. M. Raymo, W. Chen, S. E. Parker, A. E. Kaifer, *Chem.: Eur. J.* **2005**, *11*, 7054-7059.

[81] F. Biedermann, D. Hathazi, W. M. Nau, *Chem. Commun.* **2015**, *51*, 4977-4980.

[82] a) E. L. Doyle, C. A. Hunter, H. C. Phillips, S. J. Webb, N. H. Williams, *J. Am. Chem. Soc.* **2003**, *125*, 4593-4599; b) R. M. Epand, R. Kraayenhof, *Chem. Phys. Lipids* **1999**, *101*, 57-64.

[83] a) K. Kurihara, K. Ohto, Y. Honda, T. Kunitake, *J. Am. Chem. Soc.* **1991**, *113*, 5077-5079; b) D. Y. Sasaki, K. Kurihara, T. Kunitake, *J. Am. Chem. Soc.* **1992**, *114*, 10994-10995.

[84] a) B. Springs, P. Haake, *Bioorg. Chem.* **1977**, *6*, 181-190; b) H. Tamagawa, M. Sakurai, Y. Inoue, K. Ariga, T. Kunitake, *J. Phys. Chem. B* **1997**, *101*, 4817-4825; c) M. Onda, K. Yoshihara, H. Koyano, K. Ariga, T. Kunitake, *J. Am. Chem. Soc.* **1996**, *118*, 8524-8530.

[85] B. S. Pattni, V. V. Chupin, V. P. Torchilin, *Chem. Rev.* **2015**, *115*, 10938-10966.

[86] a) V. P. Torchilin, *Nat. Rev. Drug Discov.* **2005**, *4*, 145; b) C. Zylberberg, S. Matosevic, *Drug Delivery* **2016**, *23*, 3319-3329.

[87] C. Johnson, S. Hatziantoniou, C. Demetzos, *J. Liposome Res.* **2008**, *18*, 309-327.

[88] G. Nelson, *Int. J. Pharm.* **2002**, *242*, 55-62.

[89] a) P. R. Cullis, M. B. Bally, T. D. Madden, L. D. Mayer, M. J. Hope, *Trends Biotechnol.* **1991**, *9*, 268-272; b) P. R. Cullis, M. J. Hope, M. B. Bally, T. D. Madden, L. D. Mayer, D. B. Fenske, *Biochim. Biophys. Acta, Rev. Biomembr.* **1997**, *1331*, 187-211.
[90] J. Gubernator, *Expert Opin. Drug Deliv.* **2011**, *8*, 565-580.
[91] C. D. Hardcastle, J. M. Harris, *Anal. Chem.* **2015**, *87*, 7979-7986.
[92] P. R. Harrigan, M. J. Hope, T. E. Redelmeier, P. R. Cullis, *Biophys. J.* **1992**, *63*, 1336-1345.
[93] N. Bertrand, C. Bouvet, P. Moreau, J.-C. Leroux, *ACS Nano* **2010**, *4*, 7552-7558.
[94] A. C. Chakrabarti, *Amino Acids* **1994**, *6*, 213-229.
[95] M. Nilam, P. Gribbon, J. Reinshagen, K. Cordts, E. Schwedhelm, W. M. Nau, A. Hennig, *SLAS Discov.* **2017**, *22*, 906-914.
[96] C. Li, J. Li, X. Jia, *Org. Biomol. Chem.* **2009**, *7*, 2699-2703.
[97] D. M. Bailey, A. Hennig, V. D. Uzunova, W. M. Nau, *Chem.: Eur. J.* **2008**, *14*, 6069-6077.
[98] R. N. Grimes, *J. Chem. Educ.* **2004**, *81*, 657-672.
[99] M. F. Hawthorne, D. C. Young, P. A. Wegner, *J. Am. Chem. Soc.* **1965**, *87*, 1818-1819.
[100] R. W. Rudolph, *Acc. Chem. Res.* **1976**, *9*, 446-452.
[101] R. Custelcean, J. E. Jackson, *Chem. Rev.* **2001**, *101*, 1963-1980.
[102] I. Fuentes, T. García-Mendiola, S. Sato, M. Pita, H. Nakamura, E. Lorenzo, F. Teixidor, F. Marques, C. Viñas, *Chem. Eur. J.* **2018**, *24*, 17239-17254.
[103] B. P. Dash, R. Satapathy, B. R. Swain, C. S. Mahanta, B. B. Jena, N. S. Hosmane, *J. Organomet. Chem.* **2017**, *849-850*, 170-194.
[104] P. Cígler, M. Kožíšek, P. Řezáčová, J. Brynda, Z. Otwinowski, J. Pokorná, J. Plešek, B. Grüner, L. Dolečková-Marešová, M. Máša, J. Sedláček, J. Bodem, H.-G. Kräusslich, V. Král, J. Konvalinka, *Proc. Natl. Acad. Sci. U.S.A.* **2005**, *102*, 15394-15399.
[105] K. I. Assaf, M. S. Ural, F. Pan, T. Georgiev, S. Simova, K. Rissanen, D. Gabel, W. M. Nau, *Angew. Chem. Int. Ed.* **2015**, *54*, 6852-6856.
[106] K. I. Assaf, B. Begaj, A. Frank, M. Nilam, A. S. Mougharbel, U. Kortz, J. Nekvinda, B. Grüner, D. Gabel, W. M. Nau, *J. Org. Chem.* **2019**, *84*, 11790-11798.
[107] C. Verdiá-Báguena, A. Alcaraz, V. M. Aguilella, A. M. Cioran, S. Tachikawa, H. Nakamura, F. Teixidor, C. Viñas, *Chem. Commun.* **2014**, *50*, 6700-6703.
[108] E. Mayhew, D. Papahadjopoulos, Y. M. Rustum, C. Dave, *Cancer Res.* **1976**, *36*, 4406-4411.
[109] T. Heath, R. Fraley, D. Papahdjopoulos, *Science* **1980**, *210*, 539-541.
[110] R. M. Straubinger, K. Hong, D. S. Friend, D. Papahadjopoulos, *Cell* **1983**, *32*, 1069-1079.
[111] C. Chen, Y.-L. S. Tse, G. E. Lindberg, C. Knight, G. A. Voth, *J. Am. Chem. Soc.* **2016**, *138*, 991-1000.
[112] L. Di, E. H. Kerns, K. Fan, O. J. McConnell, G. T. Carter, *Eur. J. Med. Chem.* **2003**, *38*, 223-232.
[113] L. Peng, Z. He, W. Chen, I. R. Holzman, J. Lin, *Pediatr Res.* **2007**, *61*, 37-41.
[114] M. Montal, P. Mueller, *Proc. Natl. Acad. Sci. U. S. A.* **1972**, *69*, 3561-3566.

[115] A. Barnett, J. C. Weaver, *J. electroanal. chem. interfacial electrochem.* **1991**, *320*, 163-182.
[116] E. Zakharian, *Methods Mol. Biol.* **2013**, *998*, 109-118.
[117] M. J. Hope, M. B. Bally, G. Webb, P. R. Cullis, *Biochim. Biophys. Acta.* **1985**, *812*, 55-65.
[118] R. C. Bean, W. C. Shepherd, H. Chan, *J. Gen. Physiol.* **1968**, *52*, 495-508.
[119] A. D. Bangham, M. M. Standish, J. C. Watkins, *J. Mol. Biol.* **1965**, *13*, 238-IN227.
[120] K. A. Edwards, A. J. Baeumner, *Talanta* **2006**, *68*, 1432-1441.
[121] A. C. Chakrabarti, D. W. Deamer, *Biochim. Biophys. Acta, Biomembr.* **1992**, *1111*, 171-177.
[122] L. Kellard, M. Engelstein, *J. Lab. Autom.* **2007**, *12*, 104-109.
[123] H. Liu, C. Sabus, G. T. Carter, C. Du, A. Avdeef, M. Tischler, *Pharm. Res.* **2003**, *20*, 1820-1826.
[124] S. Paula, A. G. Volkov, A. N. Van Hoek, T. H. Haines, D. W. Deamer, *Biophys. J.* **1996**, *70*, 339-348.
[125] Y. N. Antonenko, P. Pohl, G. A. Denisov, *Biophys. J.* **1997**, *72*, 2187-2195.
[126] A. Walter, D. Hastings, J. Gutknecht, *J. Gen. Physiol.* **1982**, *79*, 917-933.
[127] M. R. Branco, H. S. Marinho, L. Cyrne, F. Antunes, *J. Biol. Chem.* **2004**, *279*, 6501-6506.
[128] a) A. Ligeza, A. N. Tikhonov, J. S. Hyde, W. K. Subczynski, *Biochim. Biophys. Acta, Bioenerg.* **1998**, *1365*, 453-463; b) W. K. Subczynski, J. S. Hyde, A. Kusumi, *Proc. Natl. Acad. Sci. U.S.A.* **1989**, *86*, 4474-4478.
[129] W. K. Subczynski, E. Markowska, J. Sielewiesiuk, *Biochim. Biophys. Acta, Biomembr.* **1991**, *1068*, 68-72.
[130] L. G. Hermida, M. Sabés-Xamaní, R. Barnadas-Rodríguez, *J. Liposome Res.* **2009**, *19*, 207-219.
[131] A. Sigler, P. Schubert, W. Hillen, M. Niederweis, *Eur. J. Biochem.* **2000**, *267*, 527-534.
[132] A. V. Thomae, H. Wunderli-Allenspach, S. D. Krämer, *Biophys. J.* **2005**, *89*, 1802-1811.
[133] G. R. Bickerton, G. V. Paolini, J. Besnard, S. Muresan, A. L. Hopkins, *Nat. Chem.* **2012**, *4*, 90-98.
[134] H. Liu, C. Sabus, G. T. Carter, C. Du, A. Avdeef, M. Tischler, *Pharm. Res.* **2003**, *20*, 1820-1826.
[135] H. H. Szeto, P. W. Schiller, K. Zhao, G. Luo, *FASEB J.* **2005**, *19*, 118-120.
[136] a) R. Khurana, N. Barooah, A. C. Bhasikuttan, J. Mohanty, *Org. Biomol. Chem.* **2017**, *15*, 8448-8457; b) F. Biedermann, M. Vendruscolo, O. A. Scherman, A. De Simone, W. M. Nau, *J. Am. Chem. Soc.* **2013**, *135*, 14879-14888.
[137] M. Urakami, R. Ano, Y. Kimura, M. Shima, R. Matsuno, T. Ueno, M. Akamatsu, *Z. Naturforsch.* **2003**, *58*, 135-142.
[138] Y. D. Lei, F. Wania, W. Y. Shiu, D. G. B. Boocock, *J. Chem. Eng. Data* **2000**, *45*, 738-742.
[139] R. Ano, Y. Kimura, M. Urakami, M. Shima, R. Matsuno, T. Ueno, M. Akamatsu, *Bioorg. Med. Chem.* **2004**, *12*, 249-255.
[140] W. Shinoda, *Biochim. Biophys. Acta, Biomembr.* **2016**, *1858*, 2254-2265.
[141] B. L. Lee, K. Kuczera, C. R. Middaugh, G. S. Jas, *J. Chem. Phys.* **2016**, *144*, 245103-2451014.

[142] M. Fujikawa, R. Ano, K. Nakao, R. Shimizu, M. Akamatsu, *Bioorg. Med. Chem.* **2005**, *13*, 4721-4732.
[143] J. Rebek, B. Askew, D. Nemeth, K. Parris, *J. Am. Chem. Soc.* **1987**, *109*, 2432-2434.
[144] a) F. X. Contreras, J. Sot, A. Alonso, F. M. Goñi, *Biophys. J.* **2006**, *90*, 4085-4092; b) F. M. Goñi, A. Alonso, *Biochim. Biophys. Acta, Biomembr.* **2006**, *1758*, 1902-1921.
[145] R. Goldman, A. Kaplan, *Biochim. Biophys. Acta, Biomembr.* **1973**, *318*, 205-216.
[146] B. Peng, X.-Y. Ding, C. Sun, W. Liu, J. Z. H. Zhang, X. Zhao, *RSC Adv.* **2016**, *6*, 45569-45577.
[147] a) B. E. Cohen, *J. Membr. Biol.* **1975**, *20*, 205-234; bW. D. Stein, in *The Movement of Molecules Across Cell Membranes* (Ed.: W. D. Stein), Academic Press, New York, **1967**, pp. 65-125.
[148] a) J. A. Wilkins, J. W. Greenawalt, L. Huang, *J. Biol. Chem.* **1978**, *253*, 6260-6265; b) J. H. Phillips, *Biochem. J.* **1974**, *144*, 319-325.
[149] A. C. Chakrabarti, I. Clark-Lewis, P. R. Harrigan, P. R. Cullis, *Biophys. J.* **1992**, *61*, 228-234.
[150] G. van Meer, D. R. Voelker, G. W. Feigenson, *Nat. Rev. Mol. Cell Biol.* **2008**, *9*, 112.
[151] P. F. Almeida, F. E. Carter, K. M. Kilgour, M. H. Raymonda, E. Tejada, *Langmuir* **2018**, *34*, 9798-9809.
[152] a) M. E. Dockter, J. A. Magnuson, *Arch. Biochem. Biophys.* **1975**, *168*, 81-88; b) F. Jähnig, J. Bramhall, *Biochim. Biophys. Acta, Biomembr.* **1982**, *690*, 310-313.
[153] a) G. Wilson, C. F. Fox, *J. Mol. Biol.* **1971**, *55*, 49-60; b) J. K. Raison, J. M. Lyons, R. J. Mehlhorn, A. D. Keith, *J. Biol. Chem.* **1971**, *246*, 4036-4040; c) H. K. Kimelberg, D. Papahadjopoulos, *Biochim. Biophys. Acta* **1972**, *282*, 277-292; d) D. Papahadjopoulos, K. Jacobson, S. Nir, I. Isac, *Biochim. Biophys. Acta, Biomembr.* **1973**, *311*, 330-348; e) P. Boyaval, E. Moreira, M. J. Desmazeaud, *J. Bacteriol.* **1983**, *155*, 1123-1129.
[154] a) E. Colangelo, J. Comenge, D. Paramelle, M. Volk, Q. Chen, R. Lévy, *Bioconjug. Chem.* **2017**, *28*, 11-22; b) A. M. Smith, K. A. Johnston, S. E. Crawford, L. E. Marbella, J. E. Millstone, *Analyst* **2017**, *142*, 11-29.
[155] a) D. N. Benoit, H. Zhu, M. H. Lilierose, R. A. Verm, N. Ali, A. N. Morrison, J. D. Fortner, C. Avendano, V. L. Colvin, *Anal. Chem.* **2012**, *84*, 9238-9245; b) K. Rahme, L. Chen, R. G. Hobbs, M. A. Morris, C. O'Driscoll, J. D. Holmes, *RSC Adv.* **2013**, *3*, 6085-6094.
[156] A. M. Smith, L. E. Marbella, K. A. Johnston, M. J. Hartmann, S. E. Crawford, L. M. Kozycz, D. S. Seferos, J. E. Millstone, *Anal. Chem.* **2015**, *87*, 2771-2778.
[157] a) B. Schuetze, C. Mayer, K. Loza, M. Gocyla, M. Heggen, M. Epple, *J. Mater. Chem. B* **2016**, *4*, 2179-2189; b) X. Liu, M. Yu, H. Kim, M. Mameli, F. Stellacci, *Nat. Commun.* **2012**, *3*, 1-9.
[158] B. Zhou, M. Shen, I. Banyai, X. Shi, *Analyst* **2016**, *141*, 5390-5397.
[159] L. Sun, R. M. Crooks, V. Chechik, *Chem. Commun.* **2001**, *4*, 359-360.
[160] F. Schulz, T. Vossmeyer, N. G. Bastús, H. Weller, *Langmuir* **2013**, *29*, 9897-9908.
[161] E. Oh, K. Susumu, J. B. Blanco-Canosa, I. L. Medintz, P. E. Dawson, H. Mattoussi, *Small* **2010**, *6*, 1273-1278.

[162] C.-Y. Zhang, H.-C. Yeh, M. T. Kuroki, T.-H. Wang, *Nat. Mater.* **2005**, *4*, 826-831.
[163] X. Wu, H. Liu, J. Liu, K. N. Haley, J. A. Treadway, J. P. Larson, N. Ge, F. Peale, M. P. Bruchez, *Nat. Biotechnol.* **2003**, *21*, 41-46.
[164] X. Xia, M. Yang, Y. Wang, Y. Zheng, Q. Li, J. Chen, Y. Xia, *ACS Nano* **2012**, *6*, 512-522.
[165] C. D. Walkey, J. B. Olsen, H. Guo, A. Emili, W. C. W. Chan, *J. Am. Chem. Soc.* **2012**, *134*, 2139-2147.
[166] A. Hennig, A. Hoffmann, H. Borcherding, T. Thiele, U. Schedler, U. Resch-Genger, *Anal. Chem.* **2011**, *83*, 4970-4974.
[167] a) L. M. Demers, C. A. Mirkin, R. C. Mucic, R. A. Reynolds, R. L. Letsinger, R. Elghanian, G. Viswanadham, *Anal. Chem.* **2000**, *72*, 5535-5541; b) L. Maus, J. P. Spatz, R. Fiammengo, *Langmuir* **2009**, *25*, 7910-7917.
[168] A. Hennig, A. Hoffmann, H. Borcherding, T. Thiele, U. Schedler, U. Resch-Genger, *Chem. Commun.* **2011**, *47*, 7842-7844.
[169] D.-H. Tsai, M. Davila-Morris, F. W. DelRio, S. Guha, M. R. Zachariah, V. A. Hackley, *Langmuir* **2011**, *27*, 9302-9313.
[170] J. E. B. Katari, V. L. Colvin, A. P. Alivisatos, *J. Phys. Chem. A* **1994**, *98*, 4109-4117.
[171] G. M. Whitesides, *Nat. Biotechnol.* **2003**, *21*, 1161-1165.
[172] M. Nilam, M. Ahmed, M. A. Alnajjar, A. Hennig, *Analyst* **2019**, *144*, 579-586.
[173] X. Liu, Y. Wang, P. Chen, Y. Wang, J. Zhang, D. Aili, B. Liedberg, *Anal. Chem.* **2014**, *86*, 2345-2352.
[174] M. H. Jazayeri, T. Aghaie, A. Avan, A. Vatankhah, M. R. S. Ghaffari, *Sens. Biosensing Res.* **2018**, *20*, 1-8.
[175] Y. Chen, Y. Xianyu, X. Jiang, *Acc. Chem. Res.* **2017**, *50*, 310-319.
[176] S. R. Corrie, J. W. Coffey, J. Islam, K. A. Markey, M. A. F. Kendall, *Analyst* **2015**, *140*, 4350-4364.
[177] G. Song, C. Chen, J. Ren, X. Qu, *ACS Nano* **2009**, *3*, 1183-1189.
[178] J. X. Xu, K. Siriwardana, Y. Zhou, S. Zou, D. Zhang, *Anal. Chem.* **2018**, *90*, 785-793.
[179] A. Laromaine, L. Koh, M. Murugesan, R. V. Ulijn, M. M. Stevens, *J. Am. Chem. Soc.* **2007**, *129*, 4156-4157.
[180] D. Görl, X. Zhang, F. Würthner, *Angew. Chem. Int. Ed.* **2012**, *51*, 6328-6348.
[181] C. Huang, S. Barlow, S. R. Marder, *J. Org. Chem.* **2011**, *76*, 2386-2407.
[182] A. Nowak-Król, F. Würthner, *Org. Chem. Front.* **2019**, *6*, 1272-1318.
[183] A. T. Zill, K. Licha, R. Haag, S. C. Zimmerman, *New J. Chem.* **2012**, *36*, 419-427.
[184] T. Heek, C. Fasting, C. Rest, X. Zhang, F. Würthner, R. Haag, *Chem. Commun.* **2010**, *46*, 1884-1886.
[185] M. Bagui, T. Dutta, H. Zhong, S. Li, S. Chakraborty, A. Keightley, Z. Peng, *Tetrahedron* **2012**, *68*, 2806-2818.
[186] F. Biedermann, E. Elmalem, I. Ghosh, W. M. Nau, O. A. Scherman, *Angew. Chem. Int. Ed.* **2012**, *51*, 7739-7743.
[187] M. Zhu, G. H. Aryal, N. Zhang, H. Zhang, X. Su, R. Schmehl, X. Liu, J. Hu, J. Wei, J. Jayawickramarajah, *Langmuir* **2015**, *31*, 578-586.

[188] S. T. J. Ryan, J. Del Barrio, I. Ghosh, F. Biedermann, A. I. Lazar, Y. Lan, R. J. Coulston, W. M. Nau, O. A. Scherman, *J. Am. Chem. Soc.* **2014**, *136*, 9053-9060.
[189] G. H. Aryal, L. Huang, K. W. Hunter, *RSC Adv.* **2016**, *6*, 82566-82570.
[190] G. H. Aryal, K. I. Assaf, K. W. Hunter, W. M. Nau, L. Huang, *Chem. Commun.* **2017**, *53*, 9242-9245.
[191] C. Marquez, H. Fang, W. M. Nau, *IEEE Trans. Nanobiosci.* **2004**, *3*, 39-45.
[192] a) A. J. Blacker, J. Jazwinski, J.-M. Lehn, *Helv. Chim. Acta* **1987**, *70*, 1-12; b) V. Sindelar, A. Cejas Mabel, M. Raymo Françisco, W. Chen, E. Parker Samantha, E. Kaifer Angel, *Chem. Eur. J.* **2005**, *11*, 7054-7059.
[193] R. Hein, C. B. Uzundal, A. Hennig, *Org. Biomol. Chem.* **2016**, *14*, 2182-2185.

Chapter 10

Appendices

Chapter 10

10. Supporting Information

10.1 Supporting Information for Chapter 3

10.1.1 Liposome Enhanced Sensing-Based on Different Reporter Pair

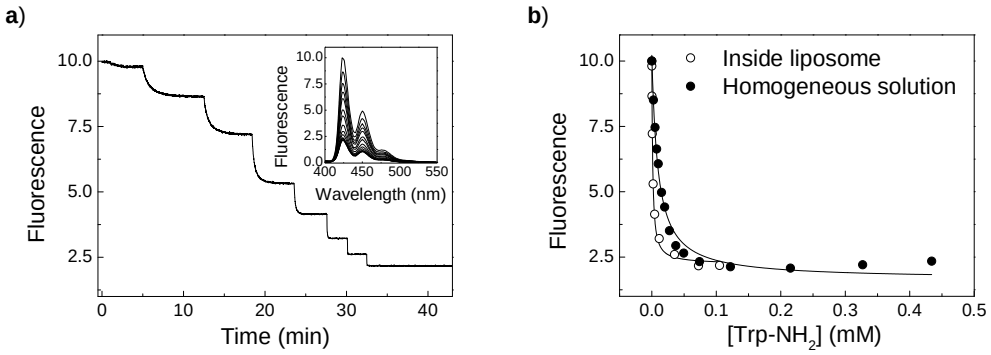

Figure A.1. a) Time-dependent fluorescence changes of POPC/POPS⊃CB8/MDAP liposomes (28.4 µM final phospholipid concentration) during the successive addition of Trp-NH_2 *via* the pH gradient (aqueous interior of the liposome 100 mM Hepes, pH 7.5 and exterior of the liposome 100 mM Na_2HPO_4, pH 10.8). Fluorescence spectral changes upon addition of Trp-NH_2 to CB8/MDAP complexes in 100 mM Hepes, pH 7.5(inset) b) Comparison of liposomes encapsulated (CB8/MDAP) reporter pair fluorescence changes with homogeneous solution against Trp-NH_2 concentration. Apparent binding constant was determined by 1:1 host-guest binding equation (CB8, 0.35 µM) (λ_{ex} = 338 nm and λ_{em} = 423 nm).

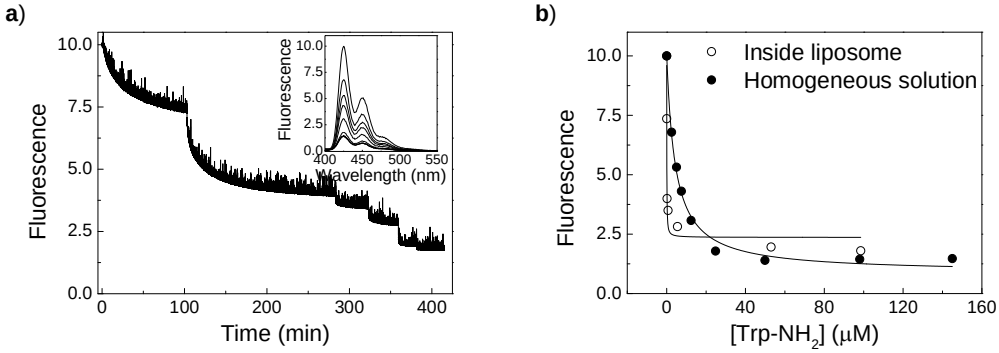

Figure A.2. a) Time-dependent fluorescence changes of POPC/POPS⊃ CB8/MDAP liposomes (27.3 μM final phospholipid concentration) during successive addition of Trp-NH_2 *via* the pH gradient (aqueous interior of the liposome 100 mM sodium citrate, pH 3.5 and exterior of the liposome 100 mM Na_2HPO_4, pH 10.8). Fluorescence spectral changes upon addition of Trp-NH_2 to CB8/MDAP complexes in 100 mM Hepes, pH 7.5 (inset) b) Comparison of liposomes encapsulated (CB8/MDAP) reporter pair fluorescence changes with homogeneous solution against Trp-NH_2 concentration. Apparent binding constant was determined by 1:1 host-guest binding equation (CB8, 50 nM) (λ_{ex} = 338 nm and λ_{em} = 423 nm).

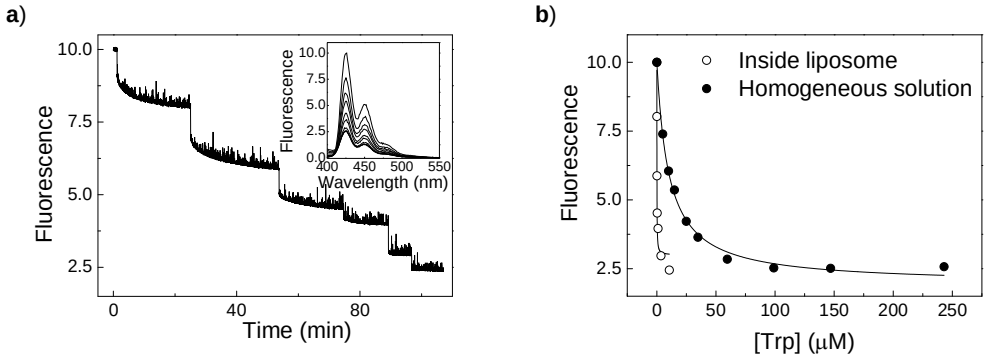

Figure A.3 a) Time-dependent fluorescence changes of POPC/POPS⊃CB8/MDAP liposomes (27.3 μM final phospholipid concentration) during the successive addition of Tryptamine *via* the pH gradient (aqueous interior of the liposome 100 mM sodium citrate, pH 3.5 and exterior of the liposome 100 mM Na_2HPO_4, pH 10.8). Fluorescence spectral changes upon addition of Tryptamine to CB8/MDAP complexes in 100 mM Hepes, pH 7.5 (inset) b) Comparison of liposomes encapsulated (CB8/MDAP) reporter pair fluorescence changes with homogeneous solution against Trp concentration. Apparent binding constant was determined by 1:1 host-guest binding equation (CB8, 50 nM) (λ_{ex} = 338 nm and λ_{em} = 423 nm).

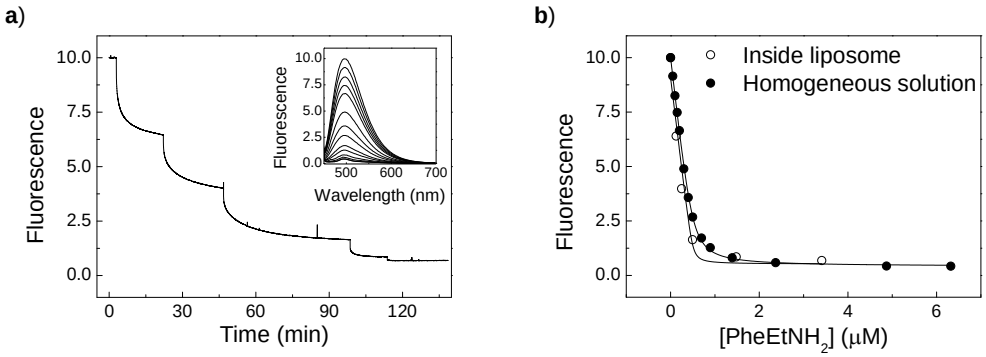

Figure A.4. a) Time-dependent fluorescence changes of POPC/POPS⊃CB7/PLM liposomes (25.7 μM final phospholipid concentration) during the successive addition of $PheEtNH_2$ *via* the pH gradient (aqueous interior of the liposome 100 mM, sodium citrate pH 3.5 and exterior of the liposome 100 mM Na_2HPO_4, pH 10.8). Fluorescence spectral changes upon addition of $PheEtNH_2$ to CB7/PLM complexes in 100 mM sodium citrate pH 3.5 (inset) b) Comparison of liposomes encapsulated (CB7/PLM) reporter pair fluorescence changes with homogeneous solution against $PheEtNH_2$ concentration. Apparent binding constant was determined by 1:1 host-guest binding equation (CB7 = 6 μM, PLM = 1 μM) (λ_{ex} = 425 nm and λ_{em} = 495 nm).

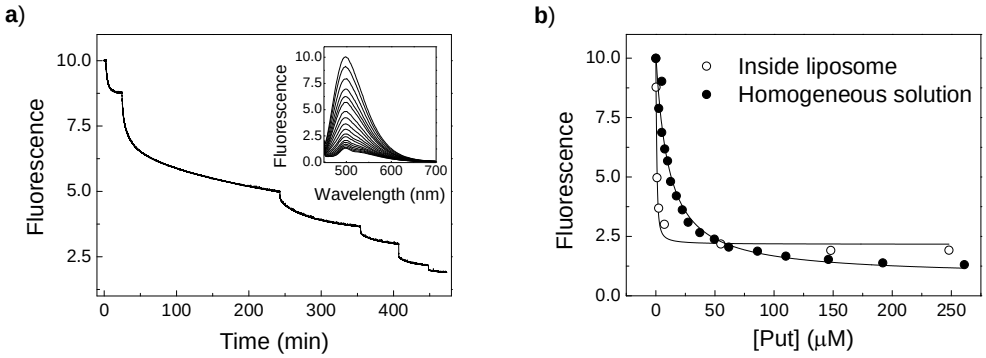

Figure A.5. a) Time-dependent fluorescence changes of POPC/POPS⊃CB7/PLM liposomes (25.7 μM final phospholipid concentration) during the successive addition of Put *via* the pH gradient (aqueous interior of the liposome 100 mM, sodium citrate pH 3.5 and exterior of the liposome 100 mM Na_2HPO_4, pH 10.8). Fluorescence spectral changes upon addition of Put to CB7/PLM complexes in 100 mM sodium citrate pH 3.5 (inset) b) Comparison of liposomes encapsulated (CB7/PLM) reporter pair fluorescence changes with homogeneous solution against Put concentration. Apparent binding constant was determined by 1:1 host-guest binding equation (CB7 = 6 μM, PLM = 1 μM) (λ_{ex} = 425 nm and λ_{em} = 495 nm).

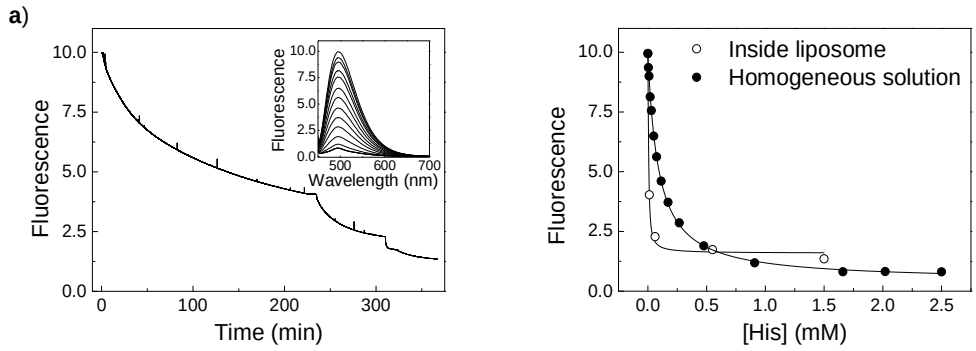

Figure A.6. a) Time-dependent fluorescence changes of POPC/POPS⊃CB7/PLM liposomes (25.7 µM final phospholipid concentration) during the successive addition of His *via* the pH gradient (aqueous interior of the liposome 100 mM, sodium citrate pH 3.5 and exterior of the liposome 100 mM Na_2HPO_4, pH 10.8). Fluorescence spectral changes upon addition of His to CB7/PLM complexes in 100 mM sodium citrate pH 3.5 (inset) b) Comparison of liposomes encapsulated (CB7/PLM) reporter pair fluorescence changes with homogeneous solution against His concentration. Apparent binding constant was determined by 1:1 host-guest binding equation (CB7 = 6 µM, PLM = 1 µM) (λ_{ex} = 425 nm and λ_{em} = 495 nm).

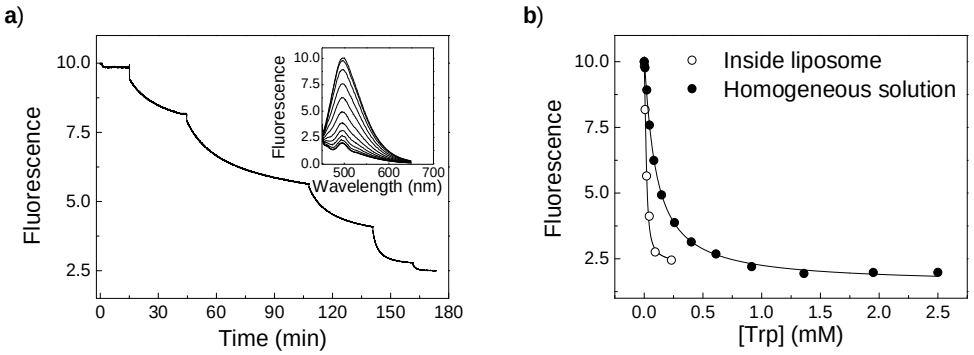

Figure A.7. a) Time-dependent fluorescence changes of POPC/POPS⊃CB7/PLM liposomes (26.5µM final phospholipid concentration) during the successive addition of Trp *via* the pH gradient (aqueous interior of the liposome 100 mM, NaH_2PO_4/Na_2HPO_4 pH 7.5 and exterior of the liposome 100 mM Na_2HPO_4, pH 10.8). Fluorescence spectral changes upon addition of Trp to CB7/PLM complexes in 100 mM NaH_2PO_4/Na_2HPO_4 pH 7.5 (inset) b) Comparison of liposomes encapsulated (CB7/PLM) reporter pair fluorescence changes with homogeneous solution against Trp concentration. Apparent binding constant was determined by 1:1 host-guest binding equation (CB7 = 6 µM, PLM = 1 µM) (λ_{ex} = 425 nm and λ_{em} = 495 nm).

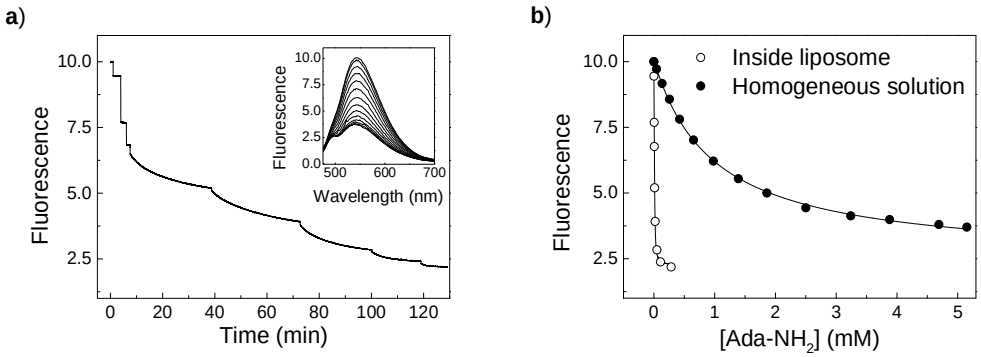

Figure A.8. a)Time-dependent fluorescence changes of POPC/POPS⊃HP-*β*-CD/BE liposomes (53.5 µM final phospholipid concentration) during the successive addition of Ada-NH_2 *via* the pH gradient (aqueous interior of the liposome 100 mM sodium citrate, pH 3.5 and exterior of the liposome 100 mM Na_2HPO_4, pH 10.8). Fluorescence spectral changes upon addition of Ada-NH_2 to HP-*β*-CD/BE complexes in 100 mM sodium citrate, pH 3.5 (inset) b) Comparison of liposomes encapsulated (HP-*β*-CD/BE) reporter pair fluorescence changes with homogeneous solution against Ada-NH_2 concentration. Apparent binding constant was determined by 1:1 host-guest binding equation (HP-*β*-CD = 100 µM, BE = 1 µM) (λ_{ex} = 420 nm and λ_{em} = 540 nm).

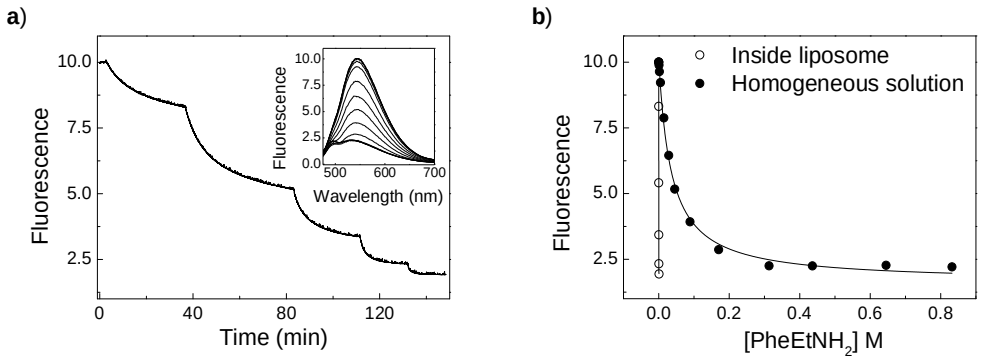

Figure A.9. a)Time-dependent fluorescence changes of POPC/POPS⊃HP-*β*-CD/BE liposomes (62.6 µM final phospholipid concentration) during the successive addition of $PheEtNH_2$ *via* the pH gradient (aqueous interior of the liposome 100 mM NaH_2PO_4/Na_2HPO_4, pH 3.5 and exterior of the liposome 100 mM Na_2HPO_4, pH 10.8). Fluorescence spectral changes upon addition of $PheEtNH_2$ to HP-*β*-CD/BE complexes in 100 mM NaH_2PO_4/Na_2HPO_4, pH 3.5 (inset) b) Comparison of liposomes encapsulated (HP-*β*-CD/BE) reporter pair fluorescence changes with homogeneous solution against $PheEtNH_2$ concentration. Apparent binding constant was determined by 1:1 host-guest binding equation (HP-*β*-CD = 100 µM, BE = 1 µM) (λ_{ex} = 420 nm and λ_{em} = 540 nm).

Table A.1 Hydrodynamic diameter of liposome measured by DLS.

Liposome	Aqueous interior pH	Diameter (nm)
CB8/MDAP	3.5	145 ± 2.0
	7.5	134 ± 1.0
CB7/PLM	3.5	139 ± 1.0
	7.5	143 ± 1.0
HP-β-CD/BE	3.5	163 ± 2.0
	7.5	178 ± 2.0

10.2 Supporting Information for Chapter 4

10.2.1 Permeability Parameter Measurements Using FARMA

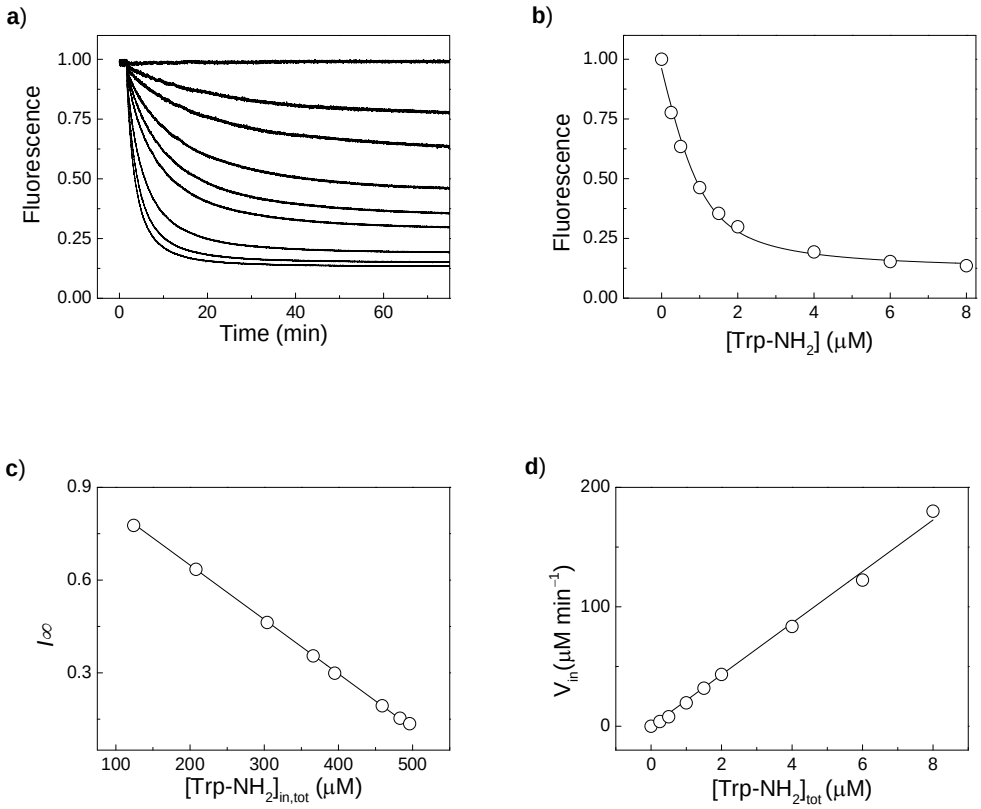

Figure A.10. Data analysis by the initial rate method for Trp-NH_2 at 10 ˚C through POPC/POPS liposomal a) Normalized ($I_{\mathrm{norm}} = I_t / I_{t=0}$) fluorescence kinetic traces. b) Dependence of the final fluorescence intensity I_∞ on total analyte concentration added. c) Dependence of the final fluorescence intensity on total internal analyte concentration including linear fit according to $I_\infty = 1 + \beta\,[A]_{\mathrm{in,tot}}$. d) Dependence of initial transport rates on added external analyte according to $v_{\mathrm{in}} = k_{\mathrm{P}}[A]_{\mathrm{tot}}$.

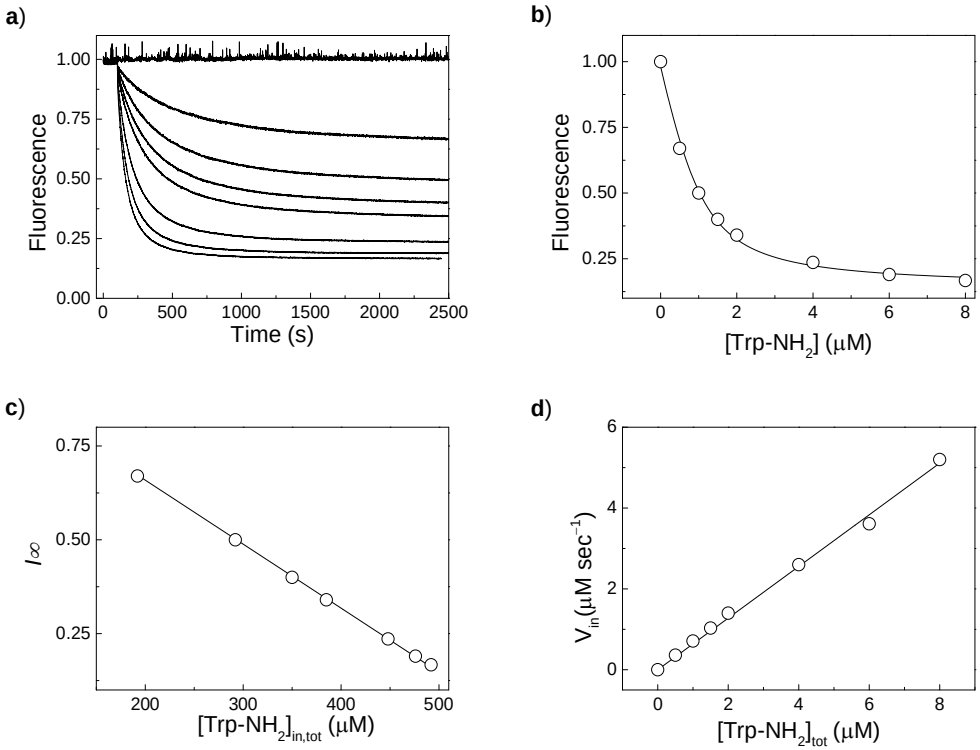

Figure A.11. Data analysis by the initial rate method for Trp-NH_2 at 15 ˚C through POPC/POPS liposomal a) Normalized ($\boldsymbol{I_{norm} = I_t/I_{t=0}}$) fluorescence kinetic traces. b) Dependence of the final fluorescence intensity $\boldsymbol{I_\infty}$ on total analyte concentration added. c) Dependence of the final fluorescence intensity on total internal analyte concentration including linear fit according to $\boldsymbol{I_\infty = 1 + \beta\,[A]_{in,tot}}$. d) Dependence of initial transport rates on added external analyte according to $\boldsymbol{v_{in} = k_P[A]_{tot}}$.

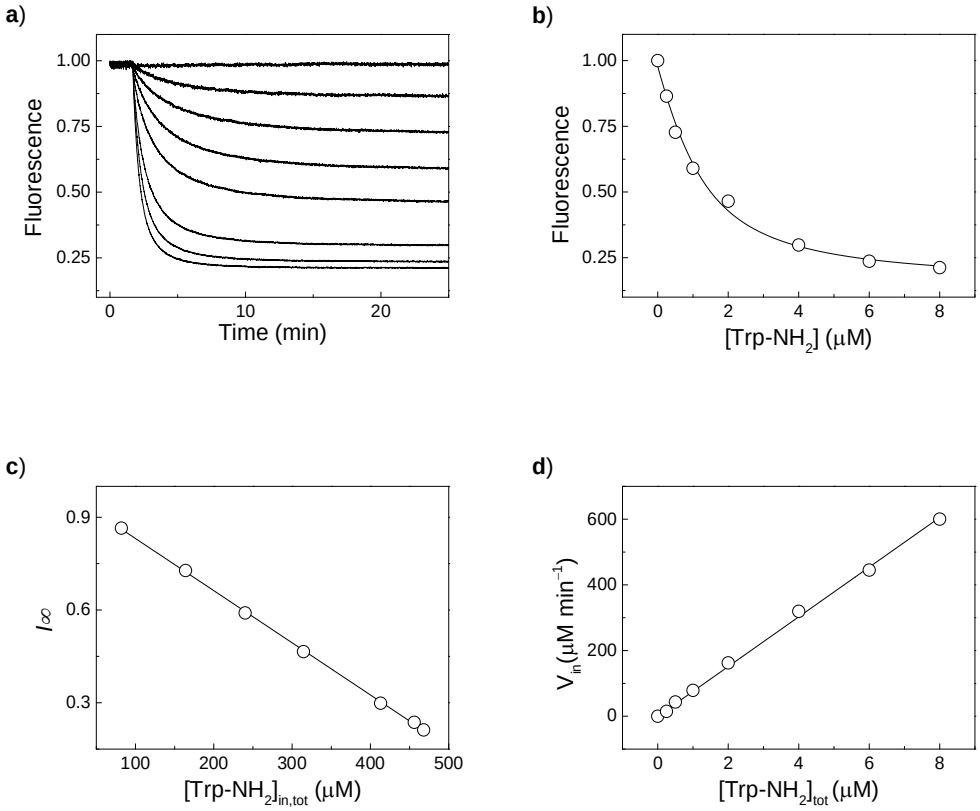

Figure A.12. Data analysis by the initial rate method for Trp-NH_2 at 20 ˚C through POPC/POPS liposomal a) Normalized ($\boldsymbol{I_{norm} = I_t / I_{t=0}}$) fluorescence kinetic traces. b) Dependence of the final fluorescence intensity $\boldsymbol{I_\infty}$ on total analyte concentration added. c) Dependence of the final fluorescence intensity on total internal analyte concentration including linear fit according to $\boldsymbol{I_\infty = 1 + \beta\,[A]_{in,tot}}$. d) Dependence of initial transport rates on added external analyte according to $\boldsymbol{v_{in} = k_P[A]_{tot}}$.

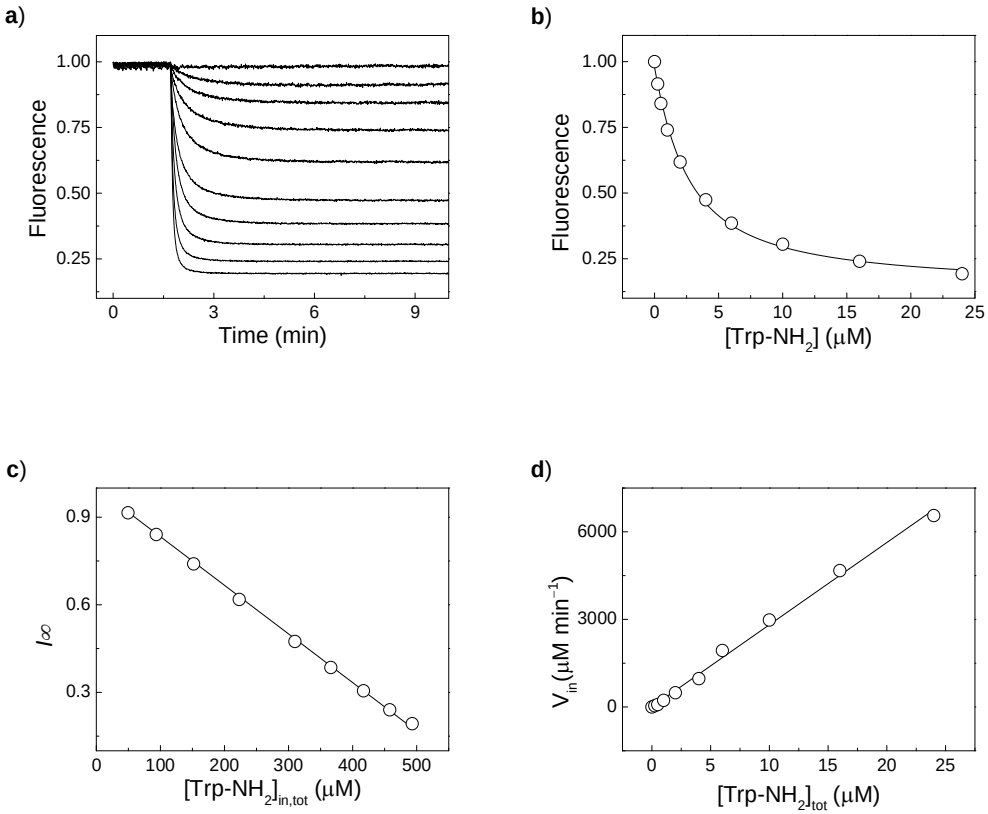

Figure A.13. Data analysis by the initial rate method for Trp-NH_2 at 30 ˚C through POPC/POPS liposomal a) Normalized ($\boldsymbol{I_{norm} = I_t / I_{t=0}}$) fluorescence kinetic traces. b) Dependence of the final fluorescence intensity $\boldsymbol{I_\infty}$ on total analyte concentration added. c) Dependence of the final fluorescence intensity on total internal analyte concentration including linear fit according to $\boldsymbol{I_\infty = 1 + \beta\,[A]_{in,tot}}$. d) Dependence of initial transport rates on added external analyte according to $\boldsymbol{v_{in} = k_P [A]_{tot}}$.

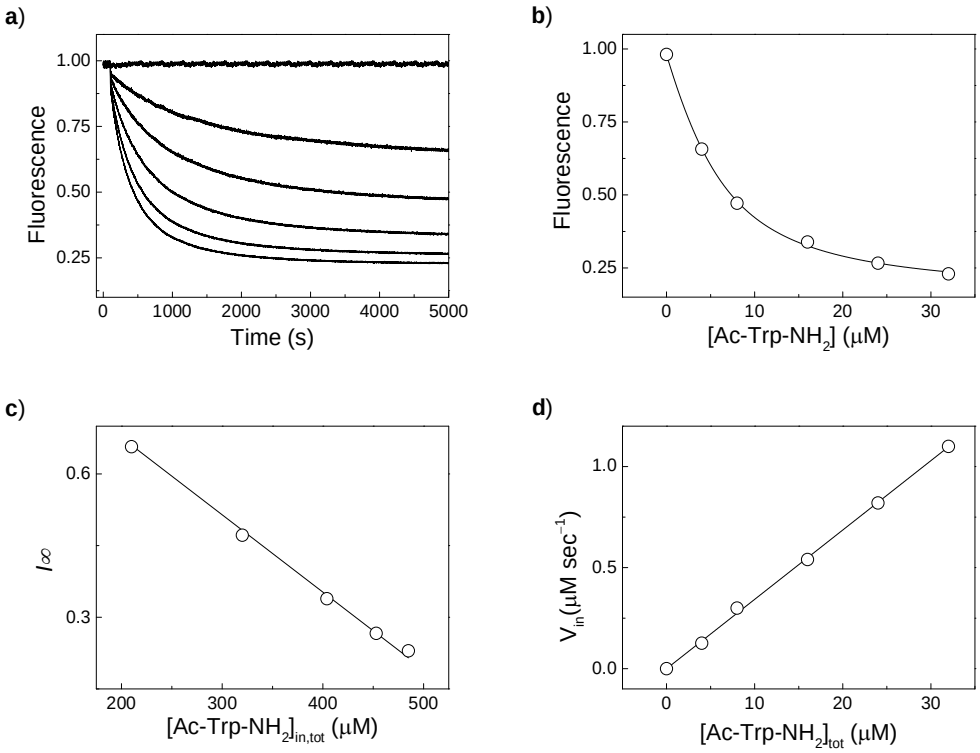

Figure A.14. Data analysis by the initial rate method for Ac-Trp-NH_2 at 10 ˚C through POPC/POPS liposomal a) Normalized ($\boldsymbol{I_{norm} = I_t / I_{t=0}}$) fluorescence kinetic traces. b) Dependence of the final fluorescence intensity $\boldsymbol{I_\infty}$ on total analyte concentration added. c) Dependence of the final fluorescence intensity on total internal analyte concentration including linear fit according to $\boldsymbol{I_\infty = 1 + \beta\,[A]_{in,tot}}$. d) Dependence of initial transport rates on added external analyte according to $\boldsymbol{v_{in} = k_P[A]_{tot}}$.

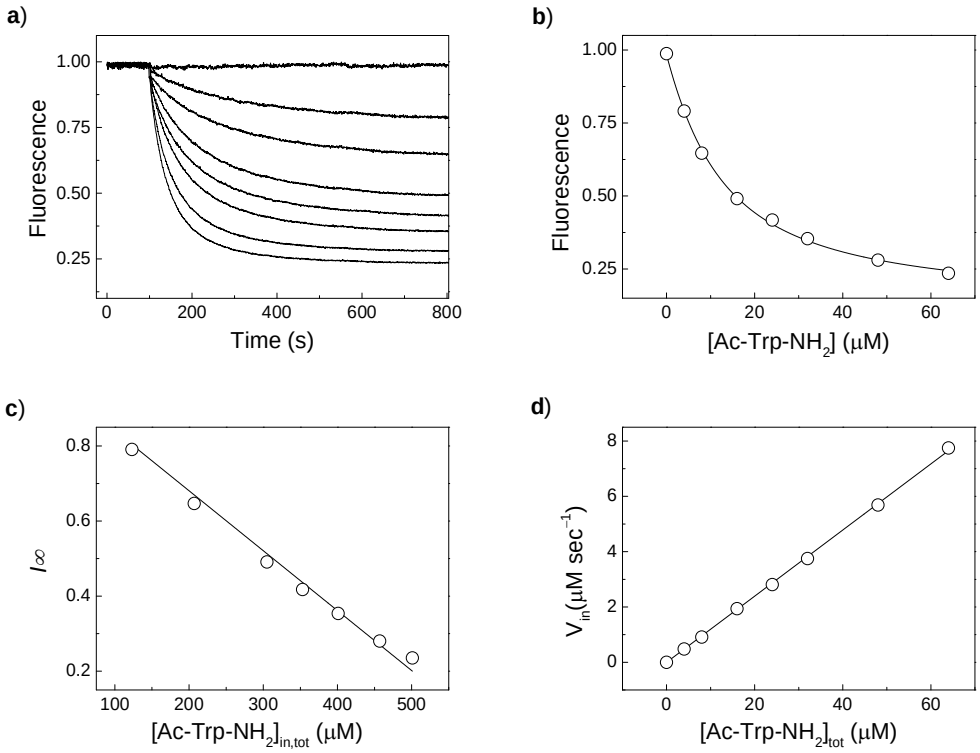

Figure A.15. Data analysis by the initial rate method for Ac-Trp-NH_2 at 20 ˚C through POPC/POPS liposomal a) Normalized ($\boldsymbol{I_{norm} = I_t / I_{t=0}}$) fluorescence kinetic traces. b) Dependence of the final fluorescence intensity $\boldsymbol{I_\infty}$ on total analyte concentration added. c) Dependence of the final fluorescence intensity on total internal analyte concentration including linear fit according to $\boldsymbol{I_\infty = 1 + \beta\,[A]_{in,tot}}$. d) Dependence of initial transport rates on added external analyte according to $\boldsymbol{v_{in} = k_P[A]_{tot}}$.

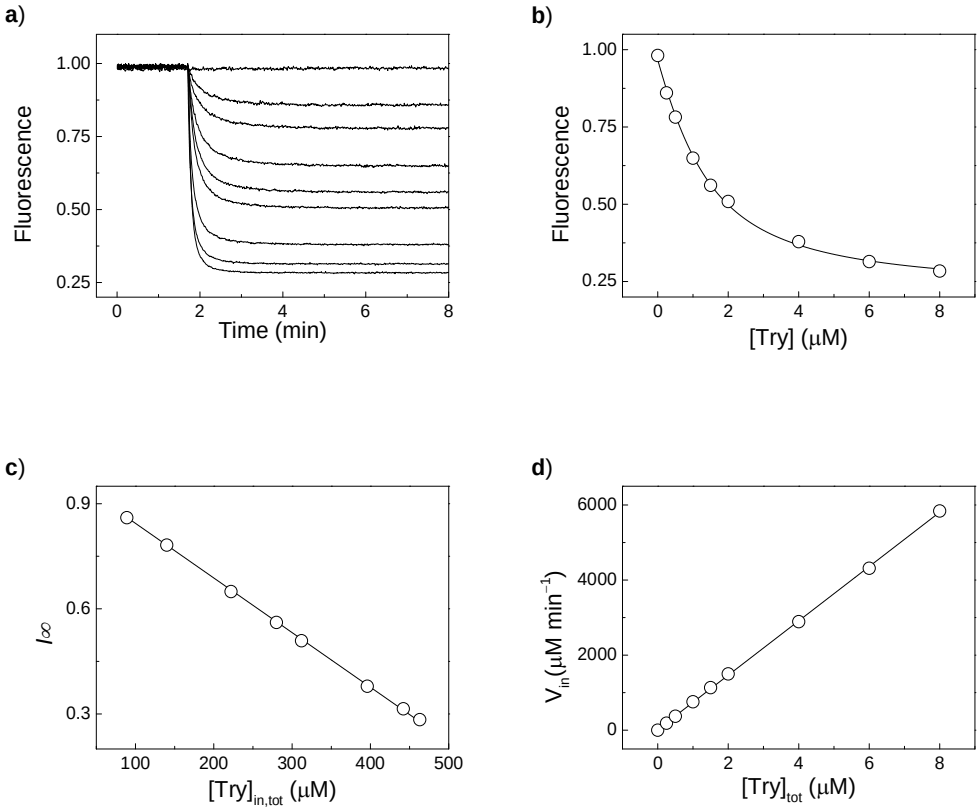

Figure A.16. Data analysis by the initial rate method for Try at 20 ˚C through POPC/POPS liposomal a) Normalized ($\boldsymbol{I_{norm} = I_t / I_{t=0}}$) fluorescence kinetic traces. b) Dependence of the final fluorescence intensity $\boldsymbol{I_\infty}$ on total analyte concentration added. c) Dependence of the final fluorescence intensity on total internal analyte concentration including linear fit according to $\boldsymbol{I_\infty = 1 + \beta\,[A]_{in,tot}}$. d) Dependence of initial transport rates on added external analyte according to $\boldsymbol{v_{in} = k_P[A]_{tot}}$.

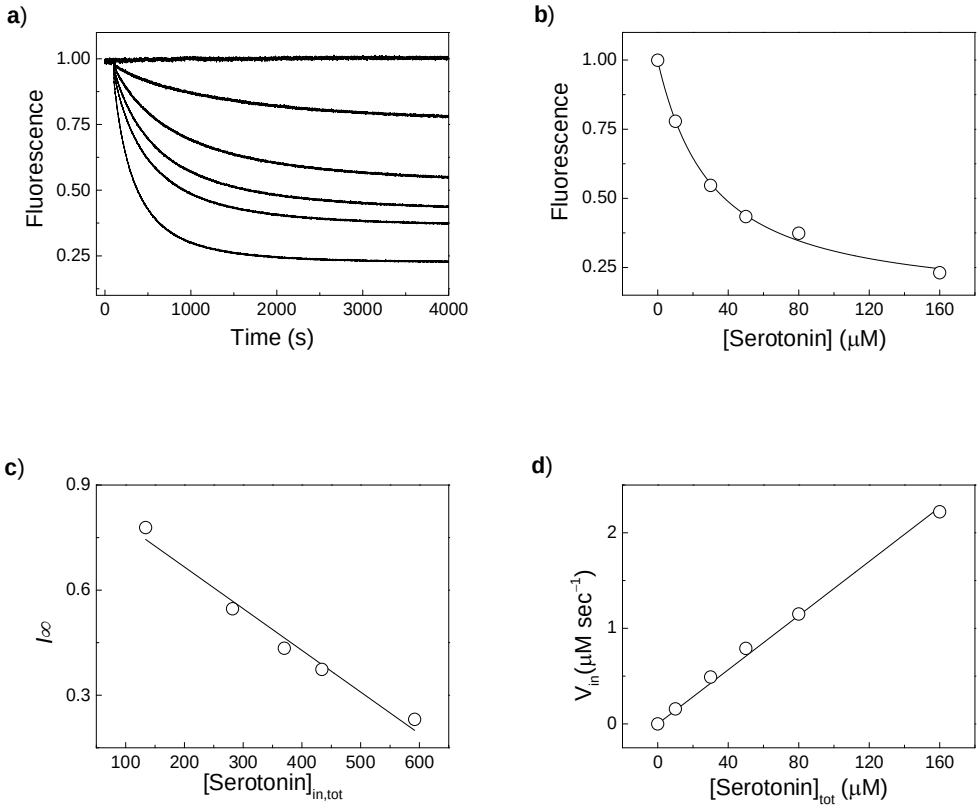

Figure A.17. Data analysis by the initial rate method for serotonin at 20 ˚C through POPC/POPS liposomal a) Normalized ($\boldsymbol{I_{norm} = I_t / I_{t=0}}$) fluorescence kinetic traces. b) Dependence of the final fluorescence intensity $\boldsymbol{I_\infty}$ on total analyte concentration added. c) Dependence of the final fluorescence intensity on total internal analyte concentration including linear fit according to $\boldsymbol{I_\infty = 1 + \beta\,[A]_{in,tot}}$. d) Dependence of initial transport rates on added external analyte according to $\boldsymbol{v_{in} = k_P [A]_{tot}}$.

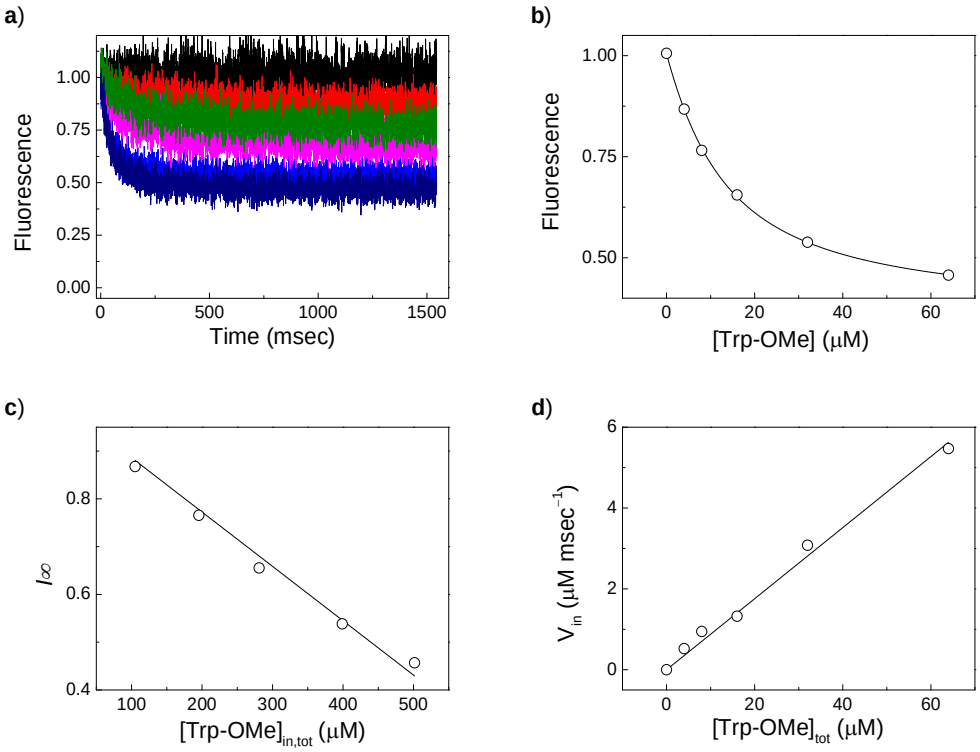

Figure A.18. Stopped-flow measurements data analysis by the initial rate method for Trp-OMe at 15 ˚C through POPC/POPS liposome a) Normalized ($\boldsymbol{I_{norm} = I_t/I_{t=0}}$) fluorescence kinetic traces. b) Dependence of the final fluorescence intensity $\boldsymbol{I_\infty}$ on total analyte concentration added. c) Dependence of the final fluorescence intensity on total internal analyte concentration including linear fit according to $\boldsymbol{I_\infty = 1 + \beta\,[A]_{in,tot}}$. d) Dependence of initial transport rates on added external analyte according to $\boldsymbol{v_{in} = k_P[A]_{tot}}$.

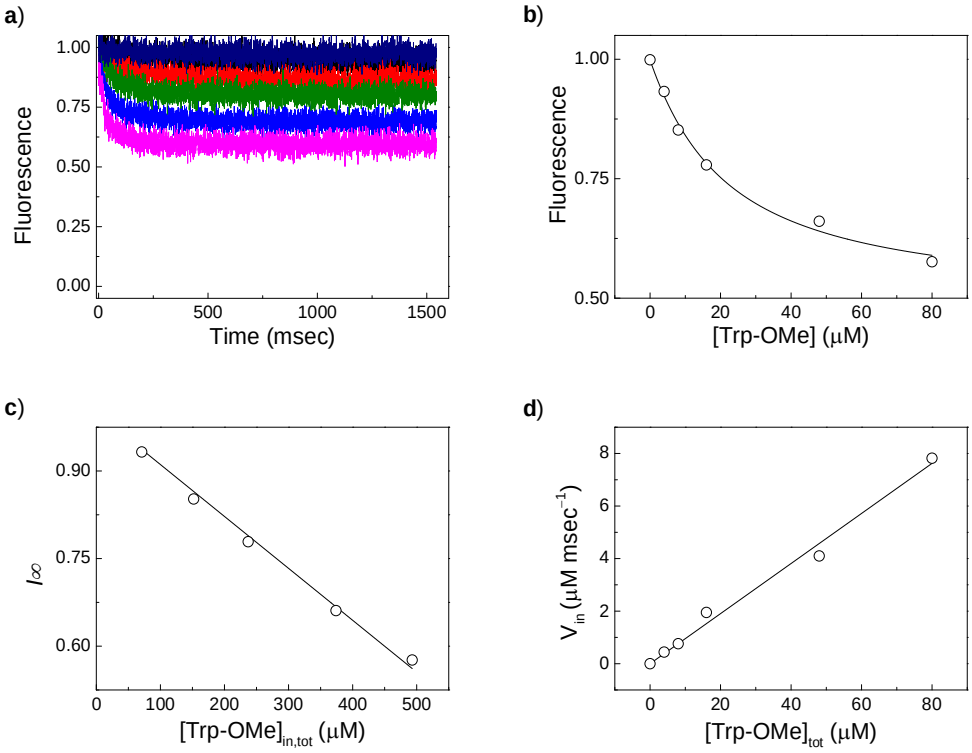

Figure A.19. Stopped-flow measurements data analysis by the initial rate method for Trp-OMe at 20 ˚C through POPC/POPS liposome a) Normalized ($\boldsymbol{I_{norm} = I_t/I_{t=0}}$) fluorescence kinetic traces. b) Dependence of the final fluorescence intensity $\boldsymbol{I_\infty}$ on total analyte concentration added. c) Dependence of the final fluorescence intensity on total internal analyte concentration including linear fit according to $\boldsymbol{I_\infty = 1 + \beta\,[A]_{in,tot}}$. d) Dependence of initial transport rates on added external analyte according to $\boldsymbol{v_{in} = k_P[A]_{tot}}$.

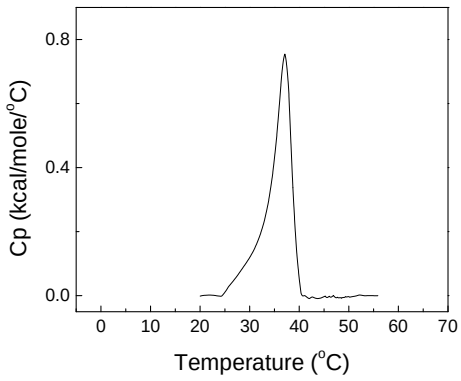

Figure A.20. DSC heating thermograms for DPPC/DOPS vesicles at 10 mM pH 7.0 Hepes buffer solution.

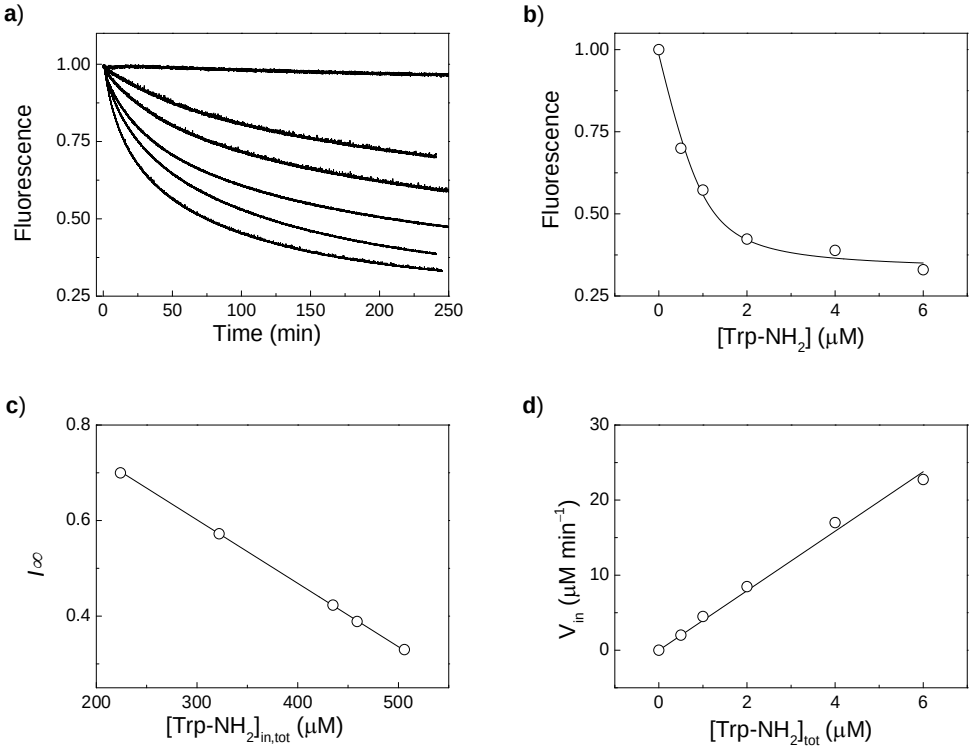

Figure A.21. Data analysis by the initial rate method for tryptophanamide at 20 ˚C through DPPC/DOPS vesicles a) Normalized ($\boldsymbol{I_{norm} = I_t / I_{t=0}}$) fluorescence kinetic traces. b) Dependence of the final fluorescence intensity $\boldsymbol{I_\infty}$ on total analyte concentration added. c) Dependence of the final fluorescence intensity on total internal analyte concentration including linear fit according to $\boldsymbol{I_\infty = 1 + \beta\,[A]_{in,tot}}$. d) Dependence of initial transport rates on added external analyte according to $\boldsymbol{v_{in} = k_P[A]_{tot}}$.

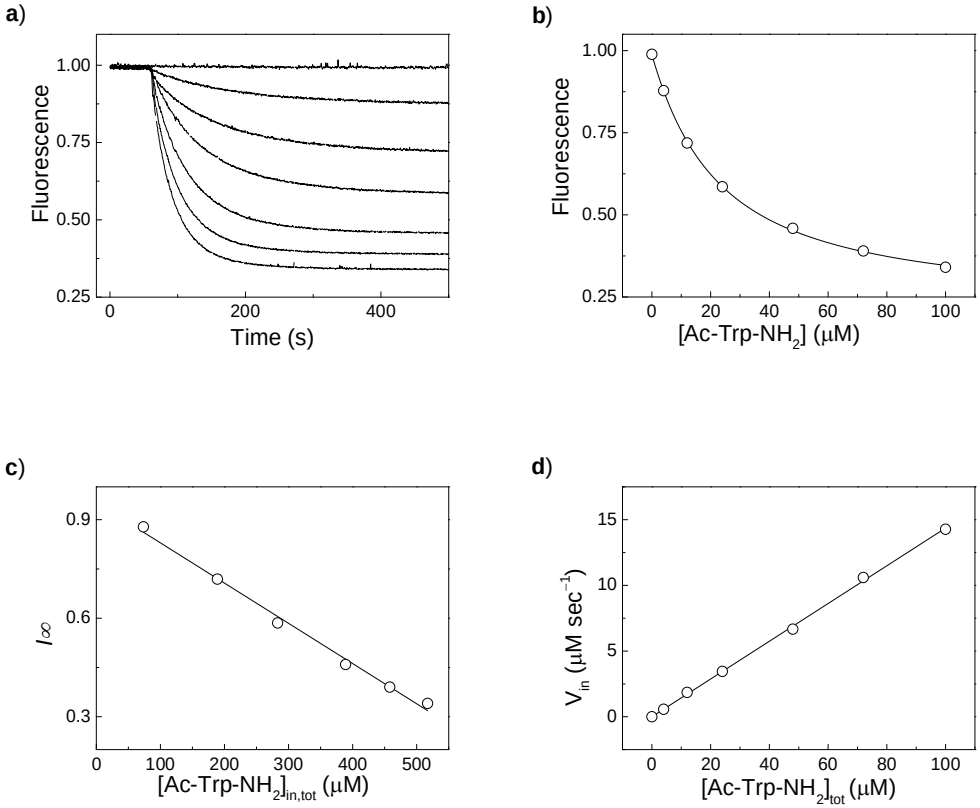

Figure A.22. Data analysis by the initial rate method for Ac-Trp-NH_2 at 30 ˚C, DPPC/DOPS vesicles a) Normalized ($I_{\mathrm{norm}} = I_t/I_{t=0}$) fluorescence kinetic traces. b) Dependence of the final fluorescence intensity I_∞ on total analyte concentration added. c) Dependence of the final fluorescence intensity on total internal analyte concentration including linear fit according to $I_\infty = 1 + \beta\,[A]_{\mathrm{in,tot}}$. d) Dependence of initial transport rates on added external analyte according to $v_{\mathrm{in}} = k_{\mathrm{P}}[A]_{\mathrm{tot}}$.

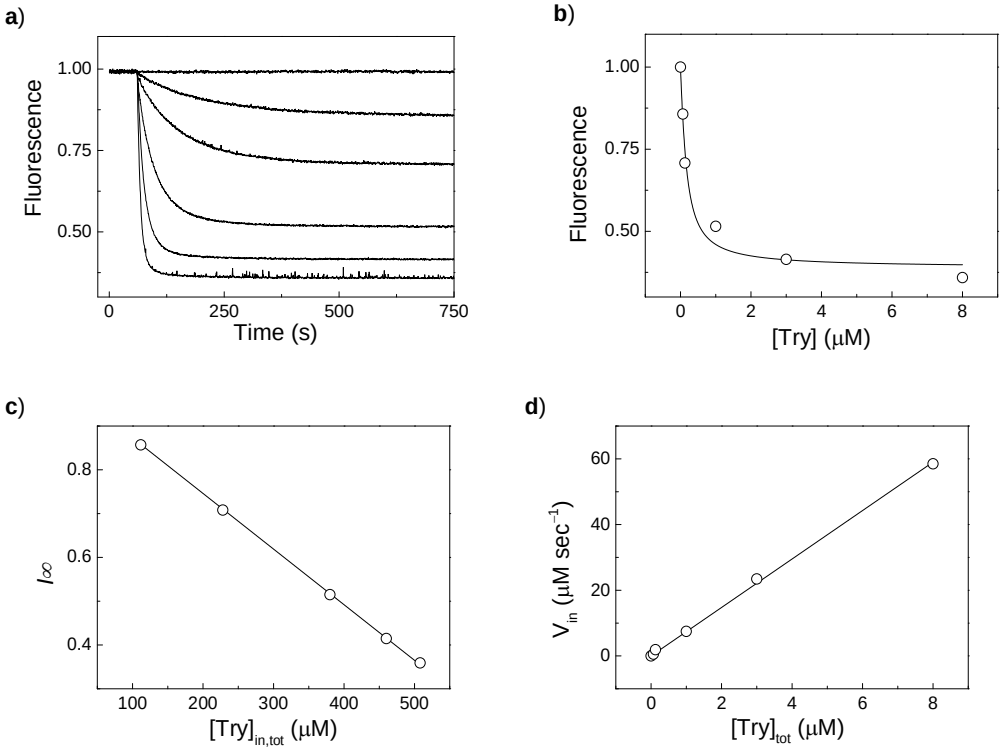

Figure A.23. Data analysis by the initial rate method for Try at 25 ˚C, DPPC/DOPS through vesicles a) Normalized ($\boldsymbol{I_{norm} = I_t / I_{t=0}}$) fluorescence kinetic traces. b) Dependence of the final fluorescence intensity $\boldsymbol{I_\infty}$ on total analyte concentration added. c) Dependence of the final fluorescence intensity on total internal analyte concentration including linear fit according to $\boldsymbol{I_\infty = 1 + \beta\,[A]_{in,tot}}$. d) Dependence of initial transport rates on added external analyte according to $\boldsymbol{v_{in} = k_P[A]_{tot}}$.

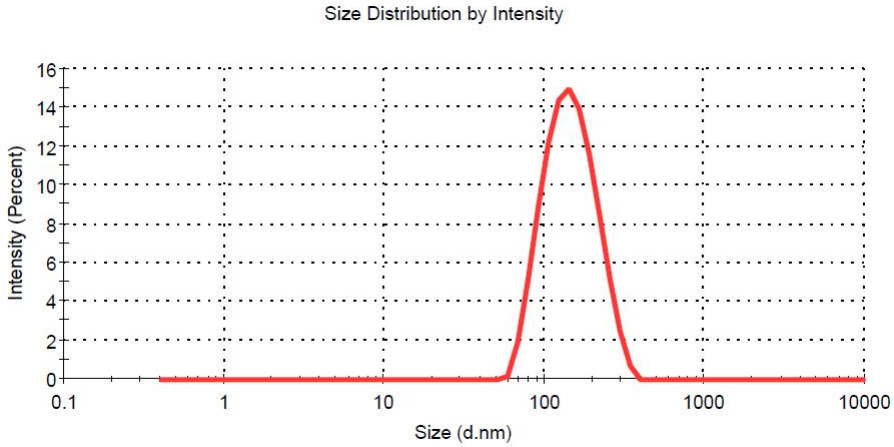

Figure A.24. Size distribution of POPC/POPS vesicles by dynamic light scattering (DLS), d = 134 nm.

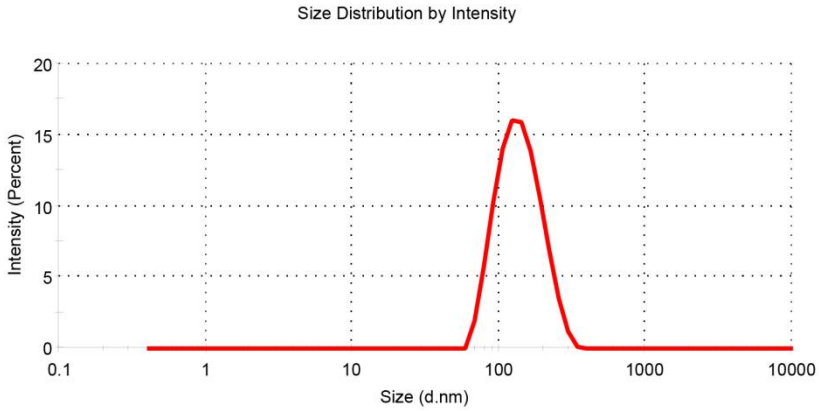

Figure A.25. Size distribution of DPPC/DOPS vesicles by dynamic light scattering (DLS), d = 131 nm.

10.3 Selected Publication and Manuscript

10.3.1 ODC Fluorescent Enzyme Assay

A Label-Free Continuous Fluorescence-based Assay for Monitoring Ornithine Decarboxylase Activity with a Synthetic Putrescine Receptor

Mohamed Nilam[1], Philip Gribbon[2], Jeanette Reinshagen[2], Kathrin Cordts[3,4], Edzard Schwedhelm[3,4], Werner M. Nau[1], and Andreas Hennig[1]

[1] Department of Life Sciences and Chemistry, Jacobs University Bremen, Campus Ring 1, 28759 Bremen (Germany)

[2] Fraunhofer IME ScreeningPort, Schnackenburgallee 114 , 22525 Hamburg (Germany)

[3] Institute of Clinical Pharmacology and Toxicology, University Medical Center Hamburg-Eppendorf, Martinistr. 52, 20246 Hamburg (Germany),

[4] German Center for Cardiovascular Research (DZHK), partner site Hamburg/Kiel/Lübeck, Hamburg, Germany

Corresponding Author: Andreas Hennig, Department of Life Sciences and Chemistry, Jacobs University Bremen, Campus Ring 1, 28759 Bremen (Germany), Email: a.hennig@jacobs-university.de

Abstract

Polyamines play an important role in cell growth, differentiation and cancer development, and the biosynthetic pathway of polyamines is established as a valid drug target for the treatment of parasitic diseases, neoplasia, and cancer chemoprevention. The key enzyme in polyamine biosynthesis is ornithine decarboxylase (ODC). We report herein an analytical method for the continuous fluorescence monitoring of ODC activity based on the supramolecular receptor cucurbit[6]uril (CB6) and the fluorescent dye *trans*-4-[4-(dimethylamino)styryl]-1-methylpyridinium iodide (DSMI). CB6 has a significantly higher binding constant to the ODC product putrescine ($<10^7$ M^{-1}) than to the substrate L-ornithine (340 M^{-1}). This enables a real-time monitoring of the enzymatic reaction through a continuous fluorescence change caused by dye displacement from the macrocycle by the formed product, which allowed a straightforward determination of enzyme kinetic parameters (k_{cat} = 0.12 s^{-1} and K_M = 24 μM) and inhibition constants of the two known ODC inhibitors α-difluoromethylornithine (DFMO) and epigallocatechin gallate (EGCG). The potential for high-throughput screening was demonstrated by excellent Z'-factors (> 0.9) in a microplate reader format, and the sensitivity of the assay is comparable or better than most established complementary methods, which have invariably the disadvantage of not being compatible with direct implementation and up-scaling to high-throughput screening format in the drug discovery process.

Introduction

Enzymes play a crucial role in physiological processes and their upregulated or downregulated activity has been associated with major diseases including numerous types of cancer.[1] Moreover, many pathogens require specific enzymes for cellular entry or infection. Enzymes are thus considered important therapeutic targets for drug discovery by the pharmaceutical industry. Identification of novel, specific, and potent modulators of enzymatic function relies to a high degree on developing scalable in-vitro assay methods and performing high-throughput screening (HTS) of collections of small molecules.[2,3] The HTS paradigm in turn requires the careful design of enzyme assays, which are compatible with existing plate-based screening infrastructure and use of sensitive optically based readouts, such as fluorescence intensity measurements, as a measure of target function.[4]

Polyamines are a class of compounds, which are associated with the genesis and metastasization of various types of cancer including breast, skin, colorectal, bladder, and cervical cancer.[5] For example, increased cell proliferation, decreased apoptosis, and increased expression levels of genes, which influence tumor invasion and metastasis, are accompanied by elevated polyamine levels. The rate-limiting enzyme in the mammalian biosynthesis of polyamines is ornithine decarboxylase (ODC), which catalyzes the decarboxylation of L-ornithine into putrescine and carbon dioxide.[6-8] ODC is consequently considered as a potential target in the treatment of certain types of cancer and parasitic diseases. One important example is α-difluoromethylornithine (DFMO), an irreversibly binding suicide inhibitor for ODC, which is currently marketed under the brand name Eflornithine and belongs to the WHO Model List of Essential Medicines to treat sleeping sickness. Moreover, it is currently in multiple clinical trials

as an adjuvant or chemopreventive agent and it appears to be highly useful in treating neuroblastoma.[5,9,10]

Because of these promising avenues, new ODC inhibitors are currently being sought in academia and industry with the goal to either identify more potent inhibitors of human ODC with improved pharmacokinetic properties or to find ODC inhibitors, which are selective towards pathogen-specific ODC variants.[11,12] However, ODC inhibitors are difficult to identify, because of the lack of suitable ODC enzyme assays. The established methods for monitoring ODC activity include assays based on detection of radio-labeled putrescine,[13] chemiluminescence-based[14] or colorimetric detection of H_2O_2 produced by oxidation of putrescine by amine oxidases,[8,15] electrochemical measurements,[16] and HPLC-based methods.[17-19] All these methods require several incubation or washing steps, for example, spotting of cellular extracts onto phosphocellulose,[14] differential extraction of picrylsulfonic acid adducts from water into 1-pentanol,[8] as well as post-column or pre-column derivatization for HPLC.[18] This renders these methods unfavorable for HTS such that no HTS-compatible enzyme assays for ODC are currently available, which would allow for systematic identification and exploration of large libraries of potential inhibitors.

We now report a robust and convenient fluorescence-based assay for continuously monitoring ODC activity based on our previously reported supramolecular tandem enzyme assay principle (Scheme 1).[20-22] Tandem assays rely on reporter pairs composed of a macrocyclic receptor and a fluorescent dye, which bind to each other affecting a change in the fluorescence-spectroscopic properties of the dye. In the tandem assays, the receptor additionally interacts either with the substrate or the product of the enzymatic reaction leading to a displacement of the fluorescent dye. Upon enzymatic conversion of the substrate into the product, the overall propensity of the

reaction mixture to displace the fluorescent dye from the macrocyclic host changes, i.e., the enzymatic reaction either converts a weakly binding substrate into a strongly binding product or vice versa, which generates a detectable fluorescence change in any case. This affords an alternative, simple, inexpensive, sensitive, and label-free method to continuously monitor enzymatic reactions.[21]

To adapt the tandem assay principle to ODC (Scheme 1), we selected *trans*-4-[4-(dimethylamino)styryl]-1-methylpyridinium (DSMI) iodide as the fluorescent dye and cucurbit[6]uril (CB6) as the macrocyclic receptor, which were recently reported to form a highly fluorescent inclusion complex.[23,24] The substrate of ODC binds only very weakly to CB6, whereas the product putrescine is a strong competitor. As a consequence, ODC activity generates a strongly binding product, which continuously displaces the fluorescent dye with time and results in a concomitant decrease in fluorescent intensity. We demonstrate that the resulting product-selective tandem assay[21] can be used to determine enzyme-kinetic parameters of ODC and for inhibitor screening with DFMO and (−)-epigallocatechin gallate (EGCG) as two exemplary known inhibitors.[5,8,25,26] The performance of the assay was also evaluated in a microplate reader format, which gave excellent *Z'*-factors revealing its potential for HTS.[27]

Materials and Methods

Materials. All chemicals, including the fluorescent dye DSMI, were from Sigma-Aldrich (Steinheim, Germany) and used as received, except for CB6, which was received from Strem Chemicals (Kehl, Germany). Human ornithine decarboxylase (0.702 µg/µl) expressed in HEK cells was received from Origene (Rockville, USA) and stored at −60 °C. The Tris buffer was prepared from Tris base and the pH was adjusted by addition of HCl. Stock solutions of

pyridoxal 5`-phosphate (PLP) and dithiothreitol (DTT) were prepared freshly on a daily basis and stored at 4 °C.

Spectroscopic measurements. Absorbance measurements were performed with a Varian Cary 4000 spectrophotometer. Fluorescence was measured with a Varian Eclipse spectrofluorometer equipped with a temperature controller. All spectroscopic measurements were performed in 0.5 ml or 3.5 ml quartz glass cuvettes (Hellma Analytics, Germany).

Binding titrations. Fluorescence titrations were performed at ambient temperature by successive addition of known concentrations of the titrant. It was ensured that the concentrations of all other components were kept constant. Commonly, the change in fluorescence intensity in the spectral area of largest variation was plotted against the concentration of titrant and analyzed by nonlinear regression by using a 1:1 host-guest binding equation (for CB6 with DSMI) or a competitive binding equation (all other) implemented in OriginPro 8.5 (OriginLab Corporation, Northampton, MA).

Continuous enzyme assays. Continuous fluorescence assays were performed in 0.5 mL quartz glass cuvettes (Hellma Analytics, Germany) with 3 µM DSMI in 10 mM Tris-HCl, pH 7.5 at (37 ± 0.1) °C. The sample was allowed to equilibrate for at least 15 minutes, and the fluorescence intensity was subsequently continuously monitored (λ_{exc} = 450 nm and λ_{em} = 582 nm) as a function of time during the addition of 0.5 µM CB6, varying amounts of ODC (typically 0.6 ng/µl, all added from stock solutions containing EDTA, DTT, PLP, and Tween 80 to afford final concentrations of 0.1 mM EDTA, 2.5 mM DTT, 0.1 mM PLP, 0.1% Tween 80). Reactions were initiated by addition of L-ornithine (typically 3–800 µM). The catalytic turnover number, k_{cat}, and Michaelis-Menten constant, K_M, were determined by nonlinear regression of the saturation curve by using the Michaelis-Menten equation. For inhibition studies, DFMO and EGCG were

pre-incubated for 12 min and the reaction was initiated by addition of 200 µM L-ornithine. Inhibition constants were obtained from Hill plots.

Microplate Measurements. Microplate measurements were performed with a JASCO FP-8500 spectrofluorometer coupled with a JASCO FMP-825 microplate reader accessory in 96-well microplates and with an EnSpire multimode plate reader (PerkinElmer, Waltham, USA) in 384-well microplates. Both microplates were flat-bottom microplates with a non-binding surface from Corning (New York, USA, Product #3820).

For the enzymatic reactions in 96-well microplates, 234 µL of a 3 µM DSMI solution and 0.5 µM of CB6 in 10 mM Tris-HCl, pH 7.5, were added to each well and equilibrated for > 8 min. Then, 24 µL of 0.5 ng/µl ODC (added from a stock solution containing EDTA, DTT, PLP, and Tween 80 to afford final concentrations of 0.1 mM EDTA, 2.5 mM DTT, 0.1 mM PLP, 0.1% Tween 80) were added and the reaction was initiated by addition of 2 µL L-ornithine (typically 3–500 µM in the Tris buffer). The total final volume in each well was 260 µL.

For the enzymatic reactions in 384-well microplates, 6 µL of 3 µM DSMI solution and CB6 (0.5-0.03 µM) in 10 mM Tris-HCl, pH 7.5, were added to each well and equilibrated for > 15 min. Then, 3 µL of 1 ng/µl ODC (added from a stock solution containing EDTA, DTT, PLP, and Tween 80 to afford final concentrations of 0.1 mM EDTA, 2.5 mM DTT, 0.1 mM PLP, 0.1% Tween 80) were added and the reaction was initiated by addition of 1 µL of a 200 µM L-ornithine solution. The total final volume in each well was 10 µL. For the inhibitor studies, DFMO was incubated with ODC for 15 min.

After initiating the reactions, the microplate was immediately placed into the reader and the fluorescence intensity (λ_{exc} = 450 nm and λ_{em} = 582 nm) of each well was recorded at specific time intervals.

Results and Discussion

Characterization of the CB6/DSMI Reporter Pair

To date, various supramolecular tandem assays have been introduced, including supramolecular tandem assays for amino acid decarboxylases.[20] In these cases, two different supramolecular reporter pairs were used, calix[4]arene (CX4) with 2,3-diazabicyclo[2.2.2]oct-2-ene as a fluorescent dye and cucurbit[7]uril (CB7) with dapoxyl. Literature precedence, however, suggested that the smaller homologue CB6 has a significantly higher binding constant to certain biogenic amines, in particular to the ODC product putrescine,[28] such that CB6 was considered superior to CB7 in an ODC assay and expected to afford an increased sensitivity. So far, the utility of CB6 was limited by the lack of suitable fluorescent dyes. While the cavity of CB7 is sufficiently large to accommodate various fluorescent dyes, for example, dapoxyl, acridine orange, and berberine chloride, the choice of dyes binding to CB6 had been limited to UV-absorbing dyes.[29] The recently reported DSMI lifted this limitation and shows an absorbance as well as fluorescence emission at relatively long wavelengths when bound to CB6 (λ_{abs} = 450 nm and λ_{em} = 582 nm), accompanied by a strong increase in fluorescence intensity by a factor of ca. 270.[23]

To ensure that these beneficial properties are retained under the conditions relevant for enzyme assays, titrations of DSMI with CB6 in 10 mM Tris-HCl at pH 7.5 were performed. In accordance with titrations performed in neat water,[23] addition of CB6 to DSMI produced a negligible decrease in absorbance, whereas the fluorescence increased strongly (Figure 1). A plot of the fluorescence intensity at maximum emission wavelength (582 nm) and analysis by a 1:1 host-guest titration curve gave a binding constant of K_a = 7.0 × 10^5 M^{-1}, which is in good

accordance with the literature value.[23] The combined results revealed DSMI as the dye of choice for supramolecular tandem enzyme assays with CB6. The reported standard buffer for ODC additionally contains the reducing agent DTT, EDTA, the cofactor PLP, and Tween 80.[6,7] Therein, the apparent binding constant of DSMI to CB6 was slightly reduced ($K_a = 1.3 \times 10^5$ M^{-1}, see Figure S1 in Supplemental Material), which is most likely due to competitive binding of the buffer components. Also noteworthy, the standard concentration of PLP in ODC buffer led to a relatively strong absorbance at the excitation wavelength of DSMI (ca. 0.4 at 0.1 mM PLP), which may have led to a non-linear fluorescence response due to the inner filter effect, which was not explicitly corrected for.

The response of the CB6/DSMI reporter pair towards the substrate and product of the enzymatic reaction was explored by competitive titrations, in which the substrate or product are successively added in small portions to a solution containing the reporter pair. This revealed that large quantities of ornithine (> 1 mM) were required to efficiently displace DSMI, and fitting of the resulting titration curve by non-linear regression gave a very small binding constant of (340±10) M^{-1} (Figure 1c). In contrast, the enzymatic reaction product putrescine efficiently displaced DSMI at nanomolar concentrations, yielding an almost linear dependence ($R^2 > 0.99$ in the range of 0 to 0.5 µM) of the fluorescence intensity on putrescine concentration (Figure 1d). This indicates that binding of putrescine to CB6 is quantitative under these conditions, pointing to a very high binding constant, $K_a > 10^7$ M^{-1}. Interesting to note, the linear response also demonstrates that the high absorbance of PLP at the DSMI excitation wavelength (see above) is not further detrimental for a quantitative analysis of the fluorescence data. Presumably, the influence of the inner filter effect on the fluorescence intensity remains constant, because the absorbance of the additive, albeit significant, remains constant in the course of the titration.

Generally, supramolecular tandem assays can even be performed with moderate binding constants and comparably low selectivity for either substrate or product, but in these cases a more elaborate data analysis is required, which involves several interrelated binding equilibria to extract reaction rates from the resulting nonlinear fluorescence response.[20,21] The stark difference between the binding constants of the substrate ornithine and the product putrescine (> 4 orders of magnitude), offers a simplified analysis with the added possibility to investigate a large working range of substrate concentrations. In detail, a simple *linear* dependence of the fluorescence intensity on the amount of formed product applies at all concentrations.

ODC Assay and Enzyme Kinetics

The ability to follow the reaction of ODC with the DSMI/CB6 reporter was demonstrated next (Figure 2). Here, the fluorescence intensity of a solution containing DSMI in 10 mM Tris-HCl, pH 7.5, was continuously monitored with time upon addition of CB6, ODC, and ornithine. As expected, addition of CB6 led to a strong increase in fluorescence due to complexation of DSMI by CB6. Subsequent addition of ODC in a buffer containing sufficient amounts of DTT, EDTA, PLP, and Tween 80 to give the desired final concentrations after dilution gave a ca. 2.7fold decrease in fluorescence, due to a slightly reduced binding constant and quenching. Lastly, addition of the substrate ornithine resulted in a continuous, time-dependent decrease in fluorescence, which is indicative of the progress of the enzymatic reaction and which was absent when no ODC was present (Figure 2b).

The time-dependent change in fluorescence progressed until a plateau of constant fluorescence was reached (Figure 2a). Of note is that the fluorescence changed almost linearly, a response which differs from many conventional enzyme assays. Usually, the final plateau region indicates

that all substrate has been converted into its product, and the overall reaction rate decreases as the enzymatic reaction proceeds due to substrate depletion. In the supramolecular tandem assays presented herein, however, the fluorescence becomes constant, because all CB6 is occupied by the product putrescine. In fact, the overall change in fluorescence in Figure 2a refers to only 0.25% substrate conversion (i.e., 200 µM L-ornithine were used as substrate concentration, but only 0.5 µM putrescine is needed to give a full fluorescence response, see Figure 1).

The peculiar response, which is desirable because it signals minute conversions and reflects the critical initial rates, could be further verified by addition of an excess of CB6 after reaching the plateau value, which regenerated the fluorescence and showed again a time-dependent decrease until a plateau region of the same final intensity was reached. This control experiment also demonstrated that the decrease in fluorescence is due to the conversion of ornithine to putrescine and not an artifact, e.g., from thermal or photodecomposition. As additional control experiment, an excess of putrescine was added at the end (after ca. 200 min), which had no influence on the final fluorescence intensity and confirmed that no undesirable interactions occur in this complex mixture.

The large selectivity between substrate and product results in a linear response of the reporter pair on product concentration, whereas the substrate does not interfere in a wide concentration range. This allows an easy conversion of the fluorescence data into concentration changes by considering that at the time point of enzyme addition, no product has yet formed ([product] = 0 µM) while the plateau region indicates that all DSMI has been displaced from the available CB6 ([product] = [CB6]). Normalization of the fluorescence traces with these considerations (see Figure 2c and Figure 2d) and linear fitting of the fluorescence progress curve thus allows a quantitative determination of the initial enzyme reaction rates, v_0.

The dependence of the v_0 values on varying enzyme and substrate concentrations could thus be conveniently investigated, and showed the expected linear dependence of the reaction rate on the ODC concentration (inset of Figure 2c) and the expected Michaelis-Menten behavior, including saturation at high substrate concentration (inset of Figure 2d). Analysis of the Cornish-Bowden diagram with the Michaelis-Menten equation afforded the catalytic turnover number (k_{cat} = (0.12 ± 0.01) s^{-1}) and the Michaelis-Menten constant (K_M = (24 ± 1) µM) for human ODC expressed in HEK cells. Considering differences in reaction conditions, assay types, and enzyme sources, the obtained values are in satisfactory agreement with previously reported literature values (e.g., k_{cat} = 3.3 s^{-1} and K_M = 80 µM for a human ODC expressed with the pUC vector in *E. coli*).[7]

Determination of Inhibition Constants

ODC is a potential target enzyme for treating certain types of cancer as well as parasitic infections,[6-8] and, consequently, a simple fluorescence-based enzyme assay would be desirable to identify additional ODC inhibitors in the future.[11,12] To demonstrate the utility of our supramolecular tandem assay in identifying ODC inhibitors, we selected DFMO and EGCG as two established inhibitors (see Chart 1).[25,26] DFMO is the most widely studied prototypical suicide inhibitor of ODC. It forms after decarboxylation a covalent bond with a cysteine residue in the active site of ODC and, thereby, irreversibly suppresses ODC activity.[19,26] DFMO is currently in clinical trials as a promising chemopreventive agent in the therapy of colorectal cancer, non-melanoma cutaneous cancer, bladder cancer, cervical cancer, and neuroblastoma.[5,9,10] EGCG is the most abundant polyphenol in green tea, and may be associated with the claimed beneficial effects of green tea. It has been shown that EGCG inhibits various

kinds of protein kinases, thus interfering with their signal transduction pathway, and EGCG is a known competitive inhibitor of ODC.[25]

To study the inhibition of ODC by DFMO and EGCG with our supramolecular tandem assay involving the CB6/DSMI reporter pair, the time-dependent fluorescence changes in the presence of varying inhibitor concentrations were recorded and normalized in the same manner as described above for the determination of its enzyme kinetics (Figure 3a and c). Importantly, both inhibitors did not significantly bind to CB6 (K_a < 500 M^{-1}, see Figure S2 in Supplemental Material), which would otherwise need to be accounted for (but which is generally only likely for polycationic molecules or residues with sufficiently low molecular weight to become encapsulated into the cavity of CB6). The initial enzyme reaction rate obtained by linear fitting of the fluorescence progress curve was then plotted against the inhibitor concentration and analyzed with the common Hill equation (Figure 3b and d). This yielded the IC_{50} of both inhibitors, i.e., the inhibitor concentrations needed to reduce the enzyme activity by 50%, which approximates to the inhibition constant K_i, when the actual concentration of the enzyme falls far below the IC_{50} value, which is fulfilled.

The inhibition constants obtained with our supramolecular tandem assay were K_i = (4.4 ± 0.2) µM for DFMO and K_i = (166 ± 8) µM for EGCG. The value for DMFO is in good agreement with a literature value of 2.2 µM for the racemic mixture,[19] and a K_i > 100 µM was previously deduced for EGCG.[30] This demonstrates that our supramolecular tandem assay for ODC can be used to reliably determine inhibition constants, even for weakly inhibiting compounds such as EGCG.

Microplate Measurements

To demonstrate the potential of our ODC assay in HTS applications, we have also miniaturized the detection system and performed measurements in microtiter plates, which would allow screening several inhibitors or activators in parallel. This allowed to judge the statistical variability of the assay by the *Z'*-factor,[27] which considers the average fluorescence signal of a sample, I_S, and of a control, I_C, and their respective standard deviations, σ_S and σ_C (Eq. 1).

$$Z' = 1 - \frac{3\,\sigma_S + 3\,\sigma_C}{|I_S - I_C|} \qquad \text{(Eq. 1)}$$

Here, the fluorescence signal in the absence of enzyme was taken as control and the signal of the plateau region after addition of enzyme was taken as the sample. This gave a *Z'*-factor for this assay of 0.96 in 96-well microplates and of 0.90 in 384-well microplates, which is considered excellent, as a *Z'*-value of 1.0 represents an ideal HTS assay and even a value of 0.5 is normally taken as an acceptable HTS assay. We could also determine the inhibition constant of DFMO in a 384-well microplate format which gave a value of (4.9 ± 0.2) µM, in excellent agreement with our cuvette-based measurements (see above).

Importantly, only 130 pmol putrescine is needed to afford a complete dye displacement and, thus, a maximal fluorescence response in 96-well microplates with our supramolecular ODC tandem assay. This value is significantly lower than the reported limits of detection for colorimetric and electrochemical detection (Table 1). Using 384-well microplates allowed a further miniaturization to a working volume of 10 µL. A maximal fluorescence response under these conditions is achieved with only 5 pmol putrescine (*Z'* = 0.90), a concentration which could be even lowered to 0.5 pmol (*Z'* = 0.56, which is still sufficient for HTS). This places our supramolecular tandem assay among the most sensitive methods reported so far.

In conclusion, we have introduced a label-free method for the real-time, continuous monitoring of ODC activity by fluorescence spectroscopy. The assay requires simply the addition of the commercially available host molecule CB6 and the fluorescent dye DSMI to the reaction mixture. We have shown that the resulting supramolecular tandem assay is suitable for determination of enzyme kinetic parameters and inhibition constants. In addition, we have demonstrated the potential of the assay in HTS applications and its sensitivity by using a 384-well microplate format. The novel supramolecular tandem assay for ODC thus presents a rapid, simple, and affordable method to allow its routine application, for example, for screening of drug candidates in HTS or for medical diagnosis of ODC levels as a disease marker.

Acknowledgements

This work was part supported under the EURhythDia collaborative project funded by the European Commission (FP-7, grant agreement no 278397) and by the DFG.

References

1. Casero, R. A.; Marton, L. J., Targeting Polyamine Metabolism and Function in Cancer and Other Hyperproliferative Diseases. *Nat. Rev. Drug Discov.* **2007,** *6*, 373-390.

2. Imming, P.; Sinning, C.; Meyer, A., Drugs, Their Targets and the Nature and Number of Drug Targets. *Nat. Rev. Drug Discov.* **2006,** *5*, 821-834.

3. Copeland, R. A., *Evaluation of Enzyme Inhibitors in Drug Discovery: A Guide for Medicinal Chemists and Pharmacologists*. John Wiley & Sons, Inc.: Hoboken, New Jersey, 2013.

4. Acker, M. G.; Auld, D. S., Considerations for the Design and Reporting of Enzyme Assays in High-Throughput Screening Applications. *Perspect. Sci.* **2014,** *1*, 56-73.

5. Gerner, E. W.; Meyskens, F. L., Polyamines and Cancer: Old Molecules, New Understanding. *Nat. Rev. Cancer* **2004,** *4*, 781-792.

6. Coleman, C. S.; Hu, G.; Pegg, A. E., Putrescine Biosynthesis in Mammalian Tissues. *Biochem. J.* **2004,** *379*, 849-855.

7. Dufe, V. T.; Ingner, D.; Heby, O., et al. A Structural Insight into the Inhibition of Human and *Leishmania Donovani* Ornithine Decarboxylases by 1-amino-oxy-3-aminopropane. *Biochem. J.* **2007,** *405*, 261-268.

8. Luqman, S.; Masood, N.; Srivastava, S., et al. A Modified Spectrophotometric and Methodical Approach to Find Novel Inhibitors of Ornithine Decarboxylase Enzyme: A Path through the Maze. *Protoc. Exch.* **2013**, doi:10.1038/protex.2013.045.

9. Mohammed, A.; Janakiram, N. B.; Ritchie, R. L., et al. Combinational Targeting of EGFR and ODC Pathways by Gefitinib and DFMO Lead to Complete Blockade of PanIN Progression to Pancreatic Ductal Adenocarcinoma. *Cancer Res.* **2014**, doi:10.1158/1538-7445.AM2014-2969.

10. Saulnier Sholler, G. L.; Gerner, E. W.; Bergendahl, G., et al. A Phase I Trial of DFMO Targeting Polyamine Addiction in Patients with Relapsed/Refractory Neuroblastoma. *PLoS ONE* **2015,** *10*, 1-20.

11. Das, M.; Singh, S.; Dubey, V. K., Novel Inhibitors of Ornithine Decarboxylase of *Leishmania* Parasite (LdODC): The Parasite Resists LdODC Inhibition by Overexpression of Spermidine Synthase. *Chem. Biol. Drug Des* **2016,** *87*, 352-360.

12. Sanchita; Chauhan, R.; Soni, G., et al. Docking and Molecular Dynamics Studies of Peptide Inhibitors of Ornithine Decarboxylase: A Rate-Limiting Enzyme for the Metabolism of *Fusarium Solani*. *J. Biomol. Struct. Dyn.* **2013,** *31*, 874-887.

13. Djurhuus, R., Ornithine Decarboxylase (EC 4.1.1.17) Assay Based Upon the Retention of Putrescine by a Strong Cation-Exchange Paper. *Anal. Biochem.* **1981,** *113*, 352-355.

14. Wang, Y.; Bachrach, U., A Luminescence-Based Test for Determining Ornithine Decarboxylase Activity. *Anal. Biochem.* **2000,** *287*, 299-302.

15. Badolo, L.; Berlaimont, V.; Helson Cambier, M., et al. Simple and Rapid Enzymatic Assay of Ornithine Decarboxylase Activity. *Talanta* **1999,** *48*, 127-134.

16. Botrè, F.; Mazzei, F., Interactions between Carbonic Anhydrase and Some Decarboxylating Enzymes as Studied by a New Bioelectrochemical Approach. *Bioelectrochem. Bioenerg.* **1999,** *48*, 463-467.

17. Gaboriau, F.; Havouis, R.; Groussard, K., et al. Measurement of Ornithine Decarboxylase Activity in Cell Extracts Using Mass Spectrometry Detection of Dansylated Putrescine. *Anal. Biochem.* **2005,** *341*, 385-387.

18. Hyvonen, T.; Keinanen, T. A.; Khomutov, A. R., et al. Monitoring of the Uptake and Metabolism of Aminooxy Analogues of Polyamines in Cultured Cells by High-Performance Liquid Chromatography. *J. Chromatogr.* **1992,** *574*, 17-21.

19. Qu, N.; Ignatenko, N. A.; Yamauchi, P., et al. Inhibition of Human Ornithine Decarboxylase Activity by Enantiomers of Difluoromethylornithine. *Biochem. J.* **2003,** *375*, 465-470.

20. Hennig, A.; Florea, M.; Roth, D., et al. Design of Peptide Substrates for Nanosecond Time-Resolved Fluorescence Assays of Proteases: 2,3-Diazabicyclo[2.2.2]oct-2-ene as a Noninvasive Fluorophore. *Anal. Biochem.* **2007,** *360*, 255-265.

21. Dsouza, R. N.; Hennig, A.; Nau, W. M., Supramolecular Tandem Enzyme Assays. *Chem. Eur. J.* **2012,** *18*, 3444-3459.

22. Hennig, A., Supramolecular Enzyme Assays. In *Supramolecular Systems in Biomedical Fields*, Schneider, H., Ed. RSC Publishing: 2013; pp 355-396.

23. Li, Z.; Sun, S.; Liu, F., et al. Large Fluorescence Enhancement of a Hemicyanine by Supramolecular Interaction with Cucurbit[6]uril and Its Application as Resettable Logic Gates. *Dyes Pigm.* **2012,** *93*, 1401-1407.

24. Ghale, G.; Nau, W. M., Dynamically Analyte-Responsive Macrocyclic Host-Fluorophore Systems. *Acc. Chem. Res.* **2014**, *47*, 2150-2159.

25. Bachrach, U.; Wang, Y. C., Cancer Therapy and Prevention by Green Tea: Role of Ornithine Decarboxylase. *Amino Acids* **2002,** *22*, 1-13.

26. Pegg, A. E.; Shantz, L. M.; Coleman, C. S., Ornithine Decarboxylase as a Target for Chemoprevention. *J. Cell. Biochem.* **1995,** *59*, 132-138.

27. Zhang, J. H.; Chung, T. D. Y.; Oldenburg, K. R., A Simple Statistical Parameter for Use in Evaluation and Validation of High Throughput Screening Assays. *J. Biomol. Screen.* **1999,** *4*, 67-73.

28. Rekharsky, M. V.; Ko, Y. H.; Selvapalam, N., et al. Complexation Thermodynamics of Cucurbit[6]uril with Aliphatic Alcohols, Amines, and Diamines. *Supramol. Chem.* **2007,** *19*, 39-46.

29. Dsouza, R. N.; Pischel, U.; Nau, W. M., Fluorescent Dyes and Their Supramolecular Host/Guest Complexes with Macrocycles in Aqueous Solution. *Chem. Rev.* **2011,** *111*, 7941-7980.

30. Wolter, F.; Turchanowa, L.; Stein, J., Resveratrol-Induced Modification of Polyamine Metabolism is Accompanied by Induction of c-Fos. *Carcinogenesis* **2003**, *24*, 469-474.

Tables and Table Legends

Table 1. Limits of detection (L.O.D.) of various ODC assays and comparison of desirable performance features of functional and HTS up-scalable assays.[a]

method	L.O.D. (pmol)	single incubation, single aliquots	direct real-time monitoring	reference
radiolabeling	n.d.[b]	no	no	13
chemiluminescence	2	no	no	14
colorimetry	2500–25000	no	no	15
electrochemical	1250	no	no	16
HPLC	20–30	no	no	18
LC/MS	0.005	no	no	17
fluorescence	<5[c]	yes	yes	this work

[a] Defined as the minimum detectable amount of the enzymatic reaction product putrescine. [b] n.d. = no limit of detection has not been reported. [c] 384-well format.

Figures and Figure Legends

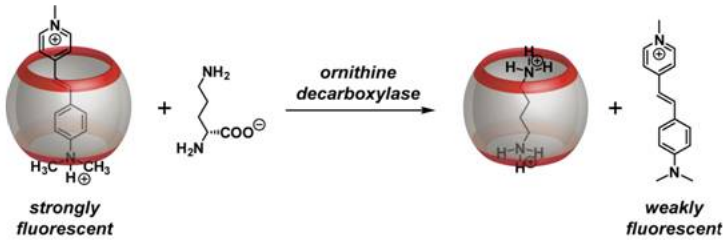

Scheme 1. Working principle of the fluorescence-based supramolecular tandem enzyme assay for ornithine decarboxylase (ODC).

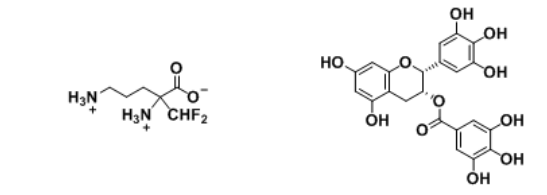

D,L-α-difluoromethylornithine (DFMO)

(–)-epigallocatechin gallate (EGCG)

Chart 1. Chemical structures of inhibitors

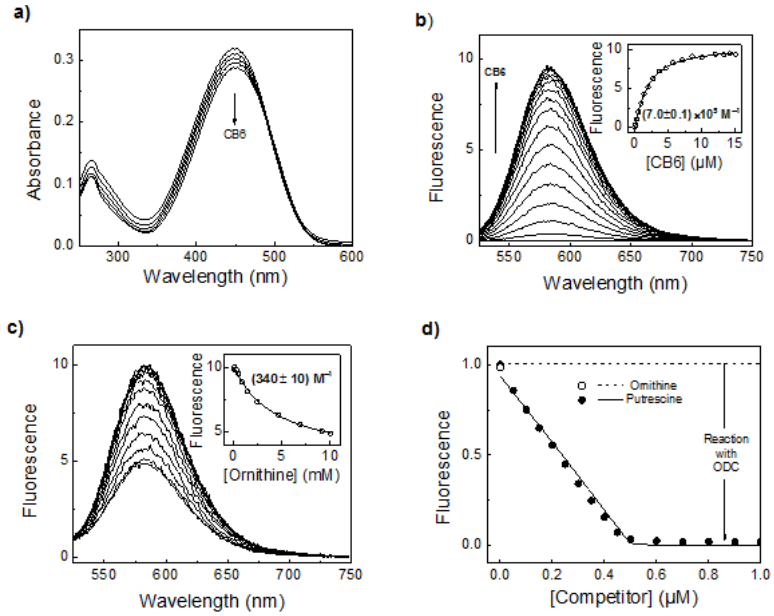

Figure 1. Determination of the binding constant of DSMI to CB6 and response of the reporter pair to the substrate L-ornithine and the product putrescine. a) Absorption spectral changes upon addition of CB6 (0 to 6 μM) to 10 μM DSMI. b) Fluorescence changes upon addition of CB6 (0 to 15 μM) to 3 μM DSMI with corresponding titration plot (inset). c) Competitive fluorescence titration of L-ornithine with corresponding titration plot (inset). d) Competitive fluorescence titration plot for L-ornithine (open circles and dashed line) and putrescine (closed circles and solid line). The arrow indicates the expected fluorescence change upon conversion of ornithine into putrescine by ODC. Excitation and emission wavelengths for all measurements were λ_{exc} = 450 nm and λ_{em} = 582 nm. Panels a) and b) show data in 10 mM Tris-HCl, pH 7.5, panels c) and d) in 10 mM Tris-HCl, 0.1 mM EDTA, 2.5 mM DTT, 0.1 mM PLP, 0.1% Tween 80, pH 7.5.

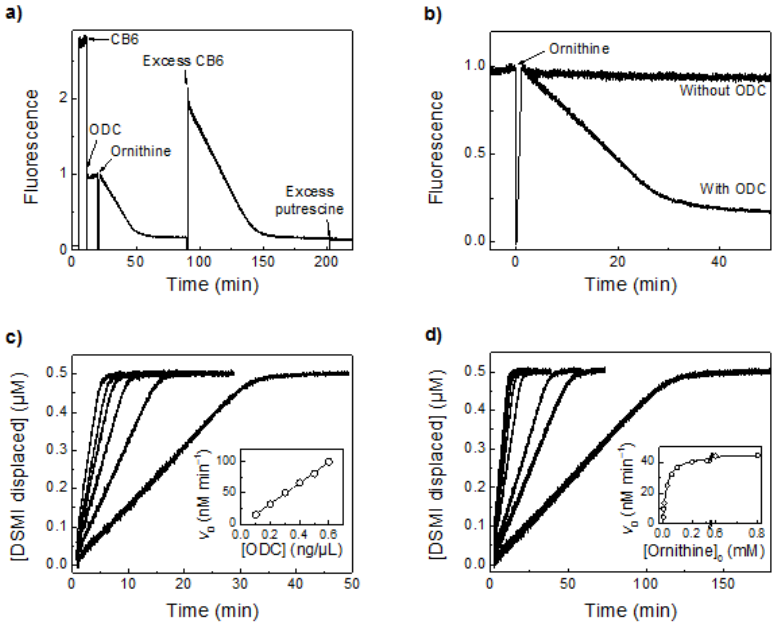

Figure 2. Continuous fluorescence enzyme assays with ODC. a) Fluorescence intensity (λ_{exc} = 450 nm, λ_{em} = 582 nm) of a solution of 3 μM DSMI in 10 mM Tris-HCl, pH 7.5, at 37 °C continuously monitored upon addition of 0.5 μM CB6, 200 μM L-ornithine, and 0.3 ng/μL ODC (added from a stock solution containing EDTA, DTT, PLP, and Tween 80 to afford final concentrations of 0.1 mM EDTA, 2.5 mM DTT, 0.1 mM PLP, and 0.1% Tween 80). For control purposes, excess CB6 (2 μM) and putrescine (1 mM) were also added at later stages. b) Comparison of the fluorescence changes in the presence and absence of ODC. c) Dependence of the initial reaction rate on enzyme concentration (with 200 μM L-ornithine). d) Dependence of the initial reaction rate on substrate concentration (with 0.3 ng/μL ODC).

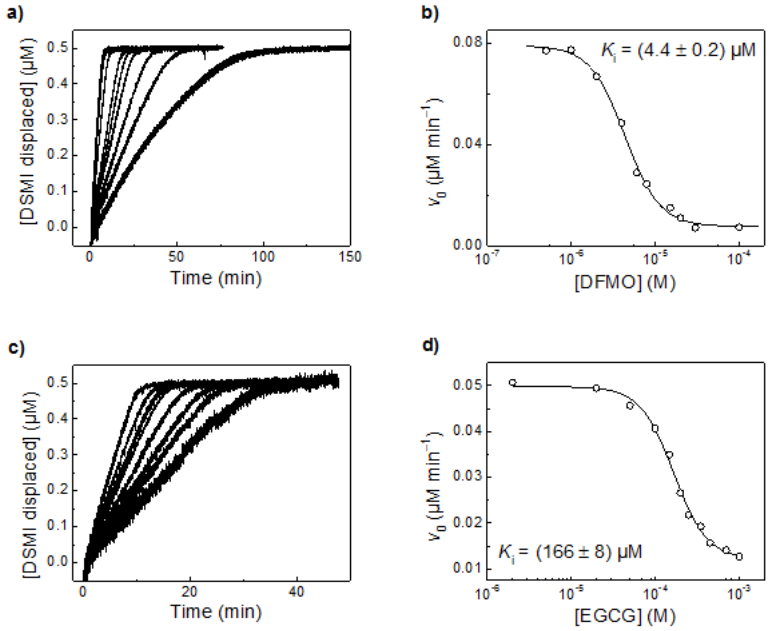

Figure 3. Determination of inhibition constants of DFMO (a,b) and EGCG (c,d). a,c) Continuous changes in fluorescence intensity (λ_{exc} = 450 nm, λ_{em} = 582 nm) recorded with 200 μM L-ornithine, 1 ng/μL ODC, 0.5 μM CB6, and 3 μM DSMI in 10 mM Tris-HCl, 0.1 mM EDTA, 2.5 mM DTT, 0.1 mM PLP, 0.1% Tween 80, pH 7.5, at 37 °C and varying amounts of a) DFMO (0.5 to 100 μM) or c) EGCG (2 to 1000 μM). Panels b) and d) show the corresponding dose-response curves, fitted according to the Hill equation.

10.3.2 Characterization of Mixed Ligand Shells on Gold Nanoparticles

Characterization of Mixed-Ligand Shells on Gold Nanoparticles by Transition Metal and Supramolecular Surface Probes

Mohamed Nilam,[a] Mostafa Ahmed,[a,b] Mohammad A. Alnajjar,[a] Andreas Hennig*[a]

We report herein two methods to characterize the surface of mixed-ligand shell gold nanoparticles, which was explored with gold nanoparticles containing varying molar ratios of 3-mercaptopropionic acid (MPA) and 3-mercapto-1-propanesulfonate (MPS) or 11-mercaptoundecanoic acid (MUA) and triethylene glycol mono-11-mercaptoundecyl ether (TEG) in their ligand shell. Incubation of gold nanoparticles with a solution containing the transition metal cation Ni^{2+} allows to extract Ni^{2+} depending on the number of negatively charged surface groups and reaction of surface carboxylic acid groups with an aminomethyladamantane derivative allows to extract the supramolecular host molecule cucurbit[7]uril (CB7) depending on the number of reactive surface groups. In both methods, remaining surface probes in the supernatant could be conveniently quantified in homogeneous solution after a simple centrifugation step. An excellent linear correlation between the amount of Ni^{2+} extracted and the ligand density of MPA and MPS in MPA/MPS gold nanoparticles or MUA in MUA/TEG gold nanoparticles afforded a simple and reliable assay method to determine the number of negatively charged surface groups. The supramolecular CB7 assay enabled the determination of the accessible ligand density of reactive surface carboxylic acid groups and revealed a striking difference in the number of surface groups that can be reacted to MPA/MPS gold nanoparticles or and MUA/TEG gold nanoparticles, which suggests a simple method to probe the surface structure of mixed monolayer gold nanoparticles.

Introduction

Gold nanoparticles (AuNPs) have attracted increasing interest from various scientific disciplines owing to their ease of synthesis together with the possibility to form self-assembled monolayers with small-molecule ligands on their surface.[1] These surface ligands impart colloidal stability to the AuNPs and they enable further post-functionalization with application-relevant molecules, for example by conversion of surface carboxylic acid groups into amides, which is key for numerous applications of AuNPs, e.g. in (bio)sensing and imaging, drug delivery, catalysis and materials science.[1-8] Despite this enormous application potential, the resulting nanoparticles and, in particular, their surface functional groups remain, however, often poorly characterized[9-12] although a rigorous quality control of parameters such as surface ligand densities, coupling efficiencies, and surface functional group accessibilities is of utmost importance to ensure reproducibility and elucidate meaningful structure-function relationships of nanomaterials.

Numerous surface functional characterization methods have been established for nanoparticles, e.g. inductively coupled plasma mass spectrometry (ICP-MS) and optical emission spectroscopy (ICP-OES),[13] thermogravimetric analysis (TGA),[14] NMR spectroscopy,[15, 16] Fourier transform infrared spectroscopy (FTIR),[17, 18] absorption and fluorescence spectroscopy,[19, 20] X-ray photoelectron spectroscopy (XPS)[11, 21] various titration methods,[22-24] and electrospray-differential mobility analysis.[25, 26] Furthermore, specialized methods have been developed, e.g. methods involving enzyme-cleavable ligands to probe domain formation in mixed ligand shells on AuNPs.[27] However, a large fraction of these techniques require expensive or specialized instrumentation and well-trained users, such that more simple yet reliable methods are highly desirable.

Within our previous efforts to mutually validate various surface functional group quantification methods,[28-33] we have communicated two methods to investigate grafted poly(acrylic acid) shells of varying chain lengths on the surface of polymer microparticles. Both methods rely on the capability of a particle surface to specifically bind a surface probe and thereby extract it from solution (Scheme 1). In the NiPV assay, binding between negatively charged surface carboxylate groups and the divalent Ni^{2+} ion is used and remaining Ni^{2+} in the supernatant is quantified by the transition metal ion indicator pyrocatechol violet (PV).[32] In the CB7 assay, surface carboxylate groups are first reacted with *N*-(adamantylmethyl)-butane-1,4-diamine (AMADA-Put), which then allows to extract the supramolecular host cucurbit[7]uril

(CB7) and to subsequently quantify remaining CB7 in the supernatant by the fluorescent dye acridine orange (AO).[33] This established the NiPV assay as a reliable and simple method to determine the *total* number of negatively charged surface carboxylate groups, whereas the CB7 assay can be used to determine the number of *accessible* surface carboxylate groups, i.e. the number of surface groups that can be functionalized with a chemical derivatization method.[31, 33]

Herein, we now evaluate both of our methods with two series of mixed-ligand shell protected AuNPs (Scheme 1). In the first series, the number of reactive surface carboxylate groups was varied and the number of negatively charged groups was kept constant by using varying molar ratios of 3-mercaptopropionic acid (MPA) and 3-mercapto-1-propanesulfonate (MPS), whereas in the second series, varying molar ratios of 11-mercaptoundecanoic acid (MUA) and triethylene glycol mono-11-mercaptoundecyl ether (TEG) were used to vary both, negatively charged and reactive surface groups.[34-36] The composition of the mixed-ligand shells was quantified with the aid of ^{1}H NMR as an established method,[37, 38] which allowed us to correlate the results from the NiPV and CB7 assay to the ligand composition. This confirmed, first, that our NiPV assay reliably reports the total number of negatively charged surface groups in mixed-ligand shell protected AuNPs, and second, established the CB7 assay as a method to determine structure-reactivity relationships for chemical derivatization methods on surfaces.

Experimental

Materials

Hydrogen tetrachloroaurate (III) trihydrate, 3-mercaptopropionic acid (MPA), sodium 3-mercapto-1-propanesulfonate (MPS), 11-mercaptoundecanoic acid (MUA), triethylene glycol mono-11-mercaptoundecyl ether (TEG), sodium citrate tribasic dihydrate, pyrocatechol violet (PV), nickel(II) chloride, 5,5'-dithiobis(2-nitrobenzoic acid) (DTNB), acridine orange (AO), and maleic acid were obtained from Sigma-Aldrich (Steinheim, Germany). Cucurbit[7]uril (CB7) and *N*-adamantylmethylbutane-1,4-diamine (AMADA-Put) were synthesized according to the literature.[33, 39] The pH of the buffers was adjusted by addition of NaOH and HCl. NANOpure (Thermo Scientific, >18.2 MΩ·cm) water was used in the preparation of all solutions, and all glassware and Teflon coated stir bars were washed with aqua regia (4:1 ratio of concentrated HCl and HNO_3 by volume) and rinsed thoroughly with water. *Caution: Aqua regia is toxic and corrosive. It should be handled in a fume hood only with proper personal protective equipment.*

AuNP Synthesis

Fairly uniform size gold nanoparticles were prepared by the citrate reduction method.[40] Therefore, 250 mL of 1 mM $HAuCl_4$ in water was heated to boiling, and then, 25 mL of 38.8 mM trisodium citrate in water was added under stirring. After colour change of the solution from light yellow to wine red, heating was continued for 15 min. Finally, the solution was cooled to room temperature. Ligand exchange was then performed by addition of varying concentrations of ligands (see Table 1 for details) to the as prepared AuNPs and stirring overnight at room temperature.[37] The mixed-ligand shell AuNPs were subsequently concentrated to 1.5 mL by repeated centrifugations at 16400 rcf, and finally washed five times with millipore water to remove any remaining ligand in solution to afford AuNP stock solutions of ca. 1.5 µM.

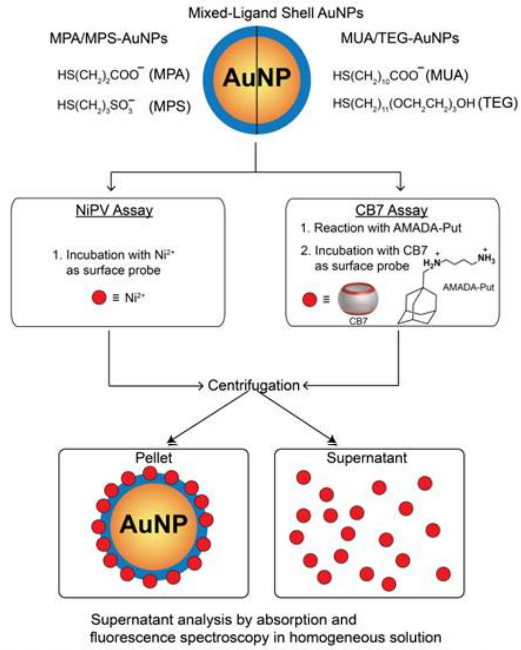

Scheme 1 Principle of the NiPV assay and CB7 assay applied to mixed-ligand shell gold nanoparticles (AuNPs). The surface probe (Ni^{2+} or CB7) is incubated with the particles and the unbound probe is quantified with a suitable dye (pyrocatechol violet (PV) for Ni^{2+} and acridine orange (AO) for CB7) in the supernatant after centrifugation.

Instrumentation

Absorption measurements were performed with a Varian Cary 4000 spectrophotometer in 1.0 mL quartz glass cuvettes (d = 0.33 cm) from Hellma Analytics (Germany). Fluorescence was measured with a Varian Eclipse spectrofluorometer in 3.0 mL polystyrene cuvettes from Sigma-Aldrich (Steinheim, Germany). ^{1}H NMR spectra were recorded on a Jeol ECS400 MHz and chemical shifts (δ) are reported in ppm relative to TMS (δ = 0 ppm). Particle size was analyzed by TEM with a Zeiss EM900 and by dynamic light scattering (DLS) with a Malvern Zetasizer Nano ZS with a 173° backscatter measurement angle.

^{1}H NMR Analysis

In all NMR measurements, a relaxation delay of 3 s was used. NMR samples were prepared by concentrating the AuNPs by centrifugation for 25 min at 16400 rcf, followed by digestion

with 20 µL aqua regia overnight, and dilution with D_2O to a total volume of 700 µL. To quantify the ligand concentration, 5 mM maleic acid (traceable certified reference material, product no. 92816 from Sigma-Aldrich) was used as an internal reference. The ligand concentration was converted into ligand densities using the AuNP concentrations determined by absorption spectroscopy[52] and the size of the AuNPs determined by TEM.

NiPV Assay

Varying amounts of the as prepared AuNP stock solutions were incubated with 200 µM Ni^{2+} for 10 min in 10 mM Hepes, pH 7.5 (total volume 600 µL). After centrifugation for 25 min at 16400 rcf, 500 µL of the supernatant were taken and diluted to 1000 µL with 10 mM Hepes, pH 7.5. PV was added from a freshly prepared stock solution to afford a final PV concentration of 80 µM. Absorption spectra were recorded immediately after PV addition and the absorbance at 650 nm was plotted against the volume of the particle stock solution.

Supramolecular CB7 Assay

Ligand-capped AuNPs (10 mg) were washed into 660 µL of 0.1 M MES, pH 5.0. AMADA-Put (80 µL of a 40 mM stock solution) was added and the reaction was initiated by addition of 100 µL of 100 mg/mL 1-ethyl-3-(3-dimethylaminopropyl)carbodiimide (EDC) hydrochloride freshly dissolved in 4 °C cold water. After 3 hours reaction time, the functionalized AuNPs were washed 5 times with 1 mL of 10 mM $(NH_4)_2HPO_4$, pH 7.2. For the supramolecular assay, aliquots of the AuNPs were diluted with 10 mM $(NH_4)_2HPO_4$, pH 7.2 and 16 µM CB7 was added to afford a final volume of 300 µL. The solution was mixed for 10 min and then centrifuged for 30 min at 16400 rcf. 200 µL of the supernatant were transferred into a 3 mL polystyrene cuvette and diluted to 2 mL with 10 mM $(NH_4)_2HPO_4$, pH 7.2. 4 µL of 1 mM of acridine orange in 10 mM $(NH_4)_2HPO_4$ was added into the cuvette and fluorescence spectra were recorded (λ_{exc} = 450 nm and λ_{em} = 510 nm for analysis).

Results and Discussion

Synthesis of AuNPs

Mixed-ligand shell protected AuNPs were synthesized by a modified Turkevich method[40, 41] and subsequent ligand exchange in water with mixtures of sodium 3-mercaptopropanoate and 3-mercapto-1-propanesulfonate to afford MPA/MPS-AuNPs or sodium 11-mercaptoundecanoate and triethylene glycol mono-11-mercaptoundecyl ether to afford MUA/TEG-AuNPs (Table 1, Chart S1 for structures in the ESI†). Remaining ligands in solution were removed by repeated centrifugation and washing cycles until no thiols could be detected in solution by Ellman's reagent (limit of detection = 0.3 µM, Fig. S1 in the ESI† for details).[42, 43]

The AuNPs were subsequently characterized by UV/VIS absorption spectroscopy, transmission electron microscopy (TEM), and dynamic light scattering (DLS). This consistently indicated an average diameter of the AuNP core of (21 ± 3) nm by TEM (Fig. S2 in the ESI†), which is in excellent agreement with a maximum of the surface plasmon resonance band at 522 to 523 nm for all AuNP preparations (Fig. S3 in the ESI†).[44, 45] Furthermore, DLS gave an average hydrodynamic diameter of the nanoparticles dispersed in solution of 27 to 30 nm.[46, 47] No aggregation of the purified and concentrated AuNPs was observed and no ligand dissociation could be detected by Ellman's reagent within a period of five months storage at 4 °C (Fig. S1(c) in the ESI†).[48]

Surface Group Analysis by ^{1}H NMR

Solution-based as well as solid-state quantitative NMR spectroscopy (qNMR) has been established as a reliable method for surface group quantification of nano- and microparticles with the potential for metrological traceability.[28, 31, 49] In the case of small AuNPs (<3 nm), surface-bound ligands can be directly quantified in solution-based NMR,[50, 51] whereas increasing size of the particle core leads to line broadening.[15, 37]

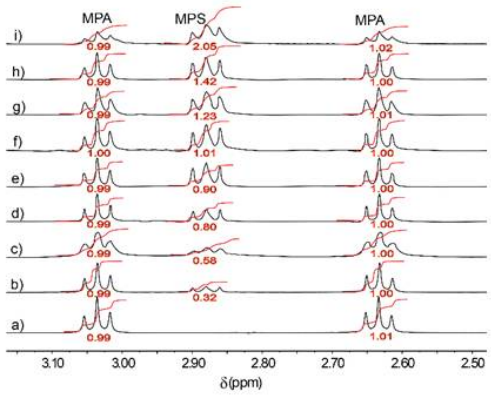

Fig. 1 ^{1}H NMR spectra of MPA/MPS-AuNPs after digestion with aqua regia and subsequent dilution with D_2O (pD 1.6). The MPA/MPS-AuNPs were prepared with varying molar ratios of MPA and MPS during ligand exchange: a) MPA only, b) 1:1, c) 1:2, d) 1:5, e) 1:10, f) 1:15, g) 1:30, h) 1:50, i) 1:83.

As an alternative, we dissolved the AuNP core with aqua regia and subsequently quantified the ligands in homogeneous solution.[37] In order to obtain the molar ratio of surface-bound ligands, the integrated peak areas of the triplet peaks at 3.04 ppm and 2.63 ppm assigned to MPA and the peak at 2.88 ppm for MPS were compared for MPA/MPS-AuNPs (Fig. 1), and the integrated peak areas of the triplet peaks at 2.17 ppm and 3.34 ppm assigned to MUA and TEG were compared for MUA/TEG-AuNPs (Fig. S4 in the ESI†). This indicated that the molar ratio of surface-bound ligands significantly deviated from that in the solution (Table 1). This presumably originates from different adsorption/desorption rates of the two ligands during ligand exchange and was also reported for mixed monolayers composed of MPA and poly(ethylene glycol).[3, 18, 36]

Table 1 Quantification of surface functional group by ^{1}H NMR, NiPV assay, CB7 supramolecular assay and coupling yield.

AuNPs	Ligand molar ratio		Ligand density by ^{1}H NMR (ligands/nm^2)[c]			NiPV assay (ligands/nm^2)[d]	CB7 assay (ligands/nm^2)[e]	Coupling Yield (%)
	added[a]	found[b]	total	ligand 1	ligand 2			
MPA/MPS	only MPA		6.35	6.35	n.a.	6.21	0.184	2.9
	1 : 1	1 : 0.3	6.10	4.69	1.41	6.07	0.177	3.8
	1 : 2	1 : 0.6	5.85	3.66	2.19	5.80	0.139	3.8
	1 : 5	1 : 0.8	5.57	3.09	2.48	5.68	0.114	3.7
	1 : 10	1 : 0.9	5.29	2.78	2.51	5.03	0.105	3.8
	1 : 15	1 : 1.0	4.44	2.22	2.22	4.08	0.0617	2.8
	1 : 30	1 : 1.2	4.40	2.00	2.40	4.22	0.0421	2.1
	1 : 50	1 : 1.4	4.32	1.80	2.52	4.18	0.0326	1.8
	1 : 83	1 : 2.0	4.26	1.42	2.84	4.19	0.0231	1.6
MUA/TEG	only MUA		4.88	4.88	n.a.	4.78	0.135	2.8
	100 : 1	36 : 1	3.89	3.78	0.11	3.75	0.0783	2.1
	20 : 1	3.0 : 1	2.52	1.89	0.63	1.85	0.0402	2.1
	10 : 1	2.5 : 1	1.53	1.09	0.44	1.03	0.0218	2.0
	5 : 1	2.5 : 1	1.42	1.01	0.41	0.92	0.0201	2.0
	2 : 1	1.15 : 1	1.59	0.85	0.74	0.49	0.0108	1.3
	1 : 1	0.80 : 1	1.50	0.67	0.83	0.45	0.00676	1.0
	only TEG		2.12	n.a.	2.12	n.a.	n.a.	n.a.

[a] For MPA/MPS-AuNPs, 0.1 mM MPA (1.0, 0.5, 0.05, 0.03 mM for 1:1, 1:2, 1:50, 1:83, respectively) and varying concentrations of MPS were used during ligand exchange; for MUA/TEG-AuNPs, 1 mM MUA and varying TEG concentrations were used. AuNPs containing only MPS as surface ligands could not be prepared, because addition of MPS to the AuNP solution led to an immediate aggregation of the AuNPs. [b] By ^{1}H NMR spectroscopy, see main text. [c] Standard deviation 4.5%. [d] Standard deviation 3.0%. [e] Standard deviation 9.0%.

The total ligand densities (Table 1) were determined by using 5 mM maleic acid as an internal standard and comparing the integrated peak areas of maleic acid (singlet at 6.20 ppm) with the integrated peak areas of the respective ligand peaks. This gave the concentration of ligands,[11, 37, 38] which were converted into ligand densities using the AuNP concentrations (determined by absorption spectroscopy)[52] and the size of the AuNPs (determined by TEM). The values for AuNPs covered with MPA or MUA (ca. 6.3 and 4.9 ligands/nm^2) agreed well with recently reported values obtained by ICP-MS.[13, 53] For mixed-ligand shell protected AuNPs, the total ligand density systematically decreased with increasing amounts of MPS or TEG (Table 1), which is in accordance with the larger size of MPS and TEG compared to MPA and MUA, respectively.[11] The comparably low values for AuNPs coated with TEG were additionally confirmed by TGA (Fig. S5 in the ESI†). The overall reproducibility of AuNP synthesis, ligand exchange, and our ^{1}H NMR-based quantification method was determined by measuring replicates of individually prepared batches of AuNPs and indicated an excellent coefficient of variation (*CV* = 2.6%, Fig. S6 in the ESI†).

NiPV Assay

We have previously explored binding of divalent transition metal cations to grafted chains of poly(acrylic acid) on the surface of polymer micro-and nanoparticles.[32] This established a linear relationship between the number of surface-bound Ni^{2+} dications and the number of surface carboxylate groups and suggested a simple method to quantify the number of surface carboxylate groups. In the resulting NiPV assay, remaining Ni^{2+} in solution is quantified after a centrifugation step by addition of pyrocatechol violet (PV) as a colorimetric transition metal cation indicator.[54]

Since binding of divalent transition metal cations to surface carboxylate groups on AuNPs was indicated in the design of sensor systems,[55-58] we were now interested to explore the NiPV assay with mixed-ligand shell protected AuNPs. Therefore, the mixed-ligand shell AuNPs were incubated with a Ni^{2+}-containing solution and PV was added to the supernatant

after centrifugation. A linear decrease in the absorption spectra at 650 nm (Fig. 2a, Fig. S7, and Fig. S8 in the ESI†) immediately indicated a particle-dependent extraction of Ni^{2+} from solution, and control experiments confirmed that the absorption spectra from the plateau region (>30 µL in Fig. 2a) correspond to the absorption spectrum of PV in the absence of Ni^{2+}. Furthermore, unfunctionalized AuNPs or AuNPs containing TEG only (no negatively charged surface groups) gave no change in absorbance at 650 nm.

Within our previous work,[32] we established that the resulting change in PV absorbance is related to the ligand density of surface carboxylate groups according to the following equation:

$$\text{Ligand Density} = n\frac{[\text{Ni}^{2+}]\,V\,a}{(A_{\text{PV}} - b)\,c\,A}$$

Therein, $[Ni^{2+}]$ is the Ni^{2+} concentration and V the total volume during incubation of Ni^{2+} with the particles (here: 200 µM and 600 µL), a is the slope and b the y- intercept of the initial linear decrease in the titration plots, A_{PV} the absorbance of PV in absence of Ni^{2+}, c the stock concentration of the particles (mol/L), and A the total surface area of all particles (nm^2). The value of n represents a stoichiometry factor, which relates the amount of extracted Ni^{2+} ions to a ligand density of surface groups.

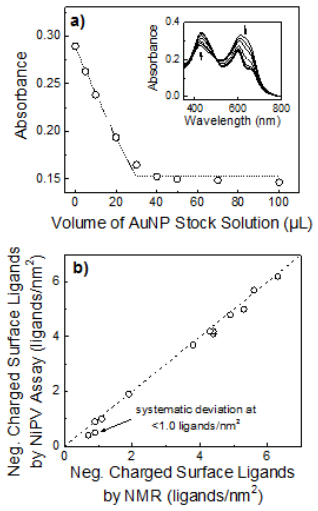

Fig. 2 Result of NiPV assay for quantification of negatively charged surface functional groups on AuNPs a) Dependence of the absorbance at 650 nm versus the volume of MPA/MPS (1:15)-AuNPs and respective absorption spectra (inset) b) Correlation between the ligand densities of negatively charged surface functional groups on MPA/MPS and MUA/TEG-AuNPs determined by ^{1}H NMR and by the NiPV assay. The dashed line indicates the ideal correlation and was not obtained by a linear fit.

By using this equation, we now found an excellent correlation ($R2 > 0.99$) between the ligand density of negatively charged surface groups on mixed-ligand shell AuNPs and the results of the NiPV assay, in which the stoichiometry factor n was identical for both series of AuNPs (Fig. 2b). To our surprise, it also agreed with the previously established value of $n = 2.65$ for grafted poly(acrylic acid) chains on polymer particles, which suggests that under the experimental conditions, the number of extracted Ni^{2+} ions is mainly determined by the overall surface charge density of the particle and largely independent of the chemical nature of the surface. Our results were overall highly reproducible (CV = 1.3%, Table S1 in the ESI†), but also suggested that at least ca. 1.0 negatively charged ligands/nm^2 are required. Below this threshold value, a systematic underestimate by the NiPV assay of ca. 30–40% was noted (see penultimate two rows of Table 1 and arrow in Fig. 2b).

Supramolecular CB7 Assay

In addition to the total number of surface groups, it is also often of interest how many molecules can be conjugated to the surface ligand shell of particles. This parameter has been termed the number of accessible (or available) surface functional groups and several methods have been developed to determine this parameter. For example, fluorescein isothiocyanate or a complex of Cu^{2+} with the chelator DOTA-NHS was reacted to amine-functionalized AuNP surfaces and quantified after AuNP digestion with aqua regia by fluorescence spectroscopy or ICP-MS.[19] Similarly, labelling with a chelator and subsequent binding of a radiotracer has been used to probe the surface of polymer microspheres.[59] Additionally, attempts have been made to relate the number of accessible (or available) surface functional groups to surface structure.[19, 29, 31, 33, 59-61]

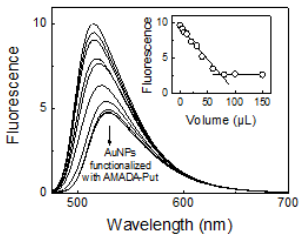

Fig. 3 Results of CB assay for quantification of accessible surface functional groups on MPA/MPS(1:50)-AuNPs. Shown is the variation of fluorescence spectra with increasing volume of AuNP stock solution (see main text for details). The inset shows the particle-dependent change at λ_{em} = 510 nm.

We have previously established a simple method to determine the number of accessible surface groups, which does not require any dissolution of the particle core and avoids the use of radioactive material.[33] Therein, *N*-(adamantylmethyl)-butane-1,4-diamine (AMADA-Put) was used to explore the efficiency of EDC-mediated amide coupling to surface carboxylates on polymer particles, and the resulting

ligand density of AMADA-Put was determined with the macrocyclic host cucurbit[7]uril (CB7) as a surface probe according to Scheme 1. In the CB7 assay, the extremely strong (K_a ca. 10^{15} M^{-1}) supramolecular host-guest interaction between CB7 and AMADA-Put ensures quantitative binding down to the picomolar range.[62] As a consequence, CB7 can be extracted from solution with surface-bound AMADA-Put and remaining CB7 is then quantified by addition of a suitable fluorescent dye, e.g. acridine orange (AO), which shows an increased and hypsochromically shifted fluorescence when bound to CB7.[33]

This method was now also explored with the mixed-ligand shell protected AuNPs. The resulting fluorescence spectra showed a clear decrease in fluorescence intensity with increasing amounts of AMADA-Put-functionalized AuNPs (Fig. 3 and Fig. S9-S10 in the ESI†), which is in accordance with a AuNP concentration-dependent extraction of CB7 from solution. Moreover, the fluorescence intensity after incubation with an excess of AuNPs coincided with the intensity of AO in absence of CB7, which is consistent with complete extraction of CB7 from solution with excess AuNPs. Additionally, TEG-AuNPs without accessible surface carboxylate groups and AuNPs, which were incubated with AMADA-Put in the absence of the amide coupling reagent EDC, were also tested. These control experiments indicated no extraction of CB7 and thus exclude any unspecific binding of CB7 to the mixed-ligand shell protected AuNPs.

The linear dependence of the fluorescence intensity on the volume of added AuNP stock solution allows determining the number of accessible surface groups according to the following equation:

$$\text{Accessible Ligand Density} = \frac{[\text{CB7}]\ V\ a}{(I_{\text{AO}} - b)\ c\ A}$$

Therein, [CB7] is the CB7 concentration and V the total volume during incubation of CB7 with the AMADA-Put-modified AuNPs (here: 200 µM and 24 µL), a is the slope and b the y- intercept of the initial linear decrease in the titration plots, I_{AO} the fluorescence intensity of AO in absence of CB7, c the stock concentration of the particles (mol/L) determined by UV-vis absorption spectroscopy, and A the total surface area of all particles (nm²).

Overall, the results from the supramolecular CB7 assay (Table 1) were in line with a decreasing amount of reactive surface functional carboxylate groups with increasing amounts of unreactive MPS or TEG on the nanoparticle surface. The maximum ligand density of AMADA-Put as determined with the CB7 assay was ca. 0.18 ligands/nm², which falls below the value of 0.48 ligands/nm² determined for self-assembled monolayers of CB7 or the comparably sized β-cyclodextrin on planar gold surfaces.[63, 64] This can be rationalized by considering that the surface is first functionalized with the much smaller AMADA-Put ligand and then by adding CB7. This affords the possibility that two AMADA-Put ligands are so close that binding of CB7 to both AMADA-Put is prevented by sterical reasons.

Interestingly, a striking difference was revealed when the dependence of the accessible ligand density on the molar fraction and on the ligand density of the carboxylic acid surface groups were compared for the mixed MPA/MPS and MUA/TEG monolayers by the CB7 assay (Fig. 4). This indicated that the amount of surface-coupled AMADA-Put/CB7 complex was significantly decreased with only ca. 3% of TEG, whereas up to 20% of unreactive MPS had no measureable influence on the accessible surface ligand density in MPA/MPS-AuNPs.

A potential reason for this difference is the length of the TEG ligand in combination with its folded mushroom conformation, which could prevent access of the EDC coupling reagent to MUA surface carboxylic acid groups.[65-67] In addition, a different capability of the two series to form (nano)domains on the surface of mixed-ligand shell protected AuNPs may play a role.[68-70] Since the sterically demanding AMADA-Put/CB7 complex occupies a much larger surface area than the ligands, randomly distributed unreactive ligands would not reduce the resulting surface coverage significantly, whereas unreactive ligands organized in small domains would create unreactive patches on the AuNP surface thus leading to a reduced accessible ligand density.

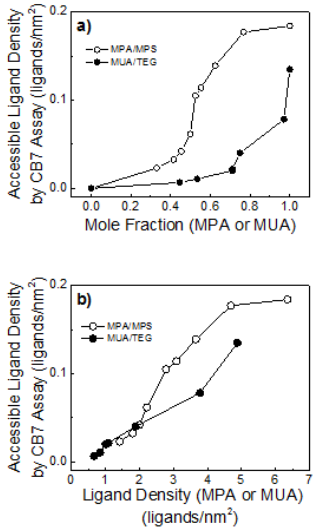

Fig. 4 Dependence of the accessible ligand density on a) the mole fraction and b) the ligand density of reactive surface carboxylate groups in mixed ligand-protected MPA/MPS-AuNPs (open circles) and MUA/TEG-AuNPs (filled circles).

Conclusions

In conclusion, we have evaluated herein a transition metal-based and a supramolecular method to probe the surface of mixed monolayers on MPA/MPS and MUA/TEG-AuNPs. The colorimetric NiPV assay revealed that the amount of surface-bound Ni^{2+} was in excellent correlation with the surface ligand density of negatively charged MPA, MPS, or MUA surface

groups as determined by quantitative ^{1}H NMR. Furthermore, the supramolecular CB7 assay easily revealed the accessible ligand density of reactive surface carboxylic acid groups and presents a simple fluorescence-based method to probe the surface structure of mixed monolayer particles. Overall, it has been recently pointed out that particle surface are often not well characterized,[13] and in particular, attempts to relate the number of total functional groups to the number of accessible functional groups are still very rare.[31, 71] The latter have, however, a demonstrated potential to reveal so far missing structure-function relationships of nanomaterials.[19, 72]

Conflicts of interest

There are no conflicts of interest to declare.

Acknowledgements

Financial support from the DAAD (57190254) and the Deutsche Forschungsgemeinschaft (HE 5967/4-1) is gratefully acknowledged. We also thank Prof. Dr. Werner M. Nau for his generous support.

References

1 X. Yang, M. Yang, B. Pang, M. Vara and Y. Xia, *Chem. Rev.*, 2015, **115**, 10410.

2 V. Biju, *Chem. Soc. Rev.*, 2014, **43**, 744.

3 J. C. Love, L. A. Estroff, J. K. Kriebel, R. G. Nuzzo and G. M. Whitesides, *Chem. Rev.*, 2005, **105**, 1103.

4 K. Saha, S. S. Agasti, C. Kim, X. Li and V. M. Rotello, *Chem. Rev.*, 2012, **112**, 2739.

5 H. Hakkinen, *Nat. Chem.*, 2012, **4**, 443.

6 D. A. Giljohann, D. S. Seferos, W. L. Daniel, M. D. Massich, P. C. Patel and C. A. Mirkin, *Angew. Chem. Int. Ed.*, 2010, **49**, 3280.

7 C. Vericat, M. E. Vela, G. Benitez, P. Carro and R. C. Salvarezza, *Chem. Soc. Rev.*, 2010, **39**, 1805.

8 C. Kim, S. S. Agasti, Z. Zhu, L. Isaacs and V. M. Rotello, *Nat. Chem.*, 2010, **2**, 962.

9 J. Hühn, C. Carrillo-Carrion, M. G. Soliman, C. Pfeiffer, D. Valdeperez, A. Masood, I. Chakraborty, L. Zhu, M. Gallego, Z. Yue, M. Carril, N. Feliu, A. Escudero, A. M. Alkilany, B. Pelaz, P. del Pino and W. J. Parak, *Chem. Mater.*, 2017, **29**, 399.

10 E. Colangelo, J. Comenge, D. Paramelle, M. Volk, Q. Chen and R. Lévy, *Bioconjugate Chem.*, 2017, **28**, 11.

11 A. M. Smith, K. A. Johnston, S. E. Crawford, L. E. Marbella and J. E. Millstone, *Analyst*, 2017, **142**, 11.

12 K. E. Sapsford, K. M. Tyner, B. J. Dair, J. R. Deschamps and I. L. Medintz, *Anal. Chem.*, 2011, **83**, 4453.

13 H. Hinterwirth, S. Kappel, T. Waitz, T. Prohaska, W. Lindner and M. Lämmerhofer, *ACS Nano*, 2013, **7**, 1129.

14 K. B. Sebby and E. Mansfield, *Anal. Bioanal. Chem.*, 2015, **407**, 2913.

15 M. J. Hostetler, J. E. Wingate, C. J. Zhong, J. E. Harris, R. W. Vachet, M. R. Clark, J. D. Londono, S. J. Green, J. J. Stokes, G. D. Wignall, G. L. Glish, M. D. Porter, N. D. Evans and R. W. Murray, *Langmuir*, 1998, **14**, 17.

16 B. Zhou, M. Shen, I. Banyai and X. Shi, *Analyst*, 2016, **141**, 5390.

17 H. Zhou, X. Li, A. Lemoff, B. Zhang and B. Yan, *Analyst*, 2010, **135**, 1210.

18 D.-H. Tsai, M. Davila-Morris, F. W. DelRio, S. Guha, M. R. Zachariah and V. A. Hackley, *Langmuir*, 2011, **27**, 9302.

19 X. Xia, M. Yang, Y. Wang, Y. Zheng, Q. Li, J. Chen and Y. Xia, *ACS Nano*, 2012, **6**, 512.

20 R. Bonomi, A. Cazzolaro and L. J. Prins, *Chem. Commun.*, 2011, **47**, 445.

21 M. D. Torelli, R. A. Putans, Y. Tan, S. E. Lohse, C. J. Murphy and R. J. Hamers, *ACS Appl. Mater. Interfaces*, 2015, **7**, 1720.

22 P. P. Pillai, B. Kowalczyk, W. J. Pudlo and B. A. Grzybowski, *J. Phys. Chem. C*, 2016, **120**, 4139.

23 A. Clavier, M. Seijo, F. Carnal and S. Stoll, *Phys. Chem. Chem. Phys.*, 2015, **17**, 4346.

24 G. Charron, D. Hühn, A. Perrier, L. Cordier, C. J. Pickett, T. Nann and W. J. Parak, *Langmuir*, 2012, **28**, 15141.

25 N. Clouet-Foraison, F. Gaie-Levrel, L. Coquelin, G. Ebrard, P. Gillery and V. Delatour, *Anal. Chem.*, 2017, **89**, 2242.

26 S. Guha, M. Li, M. J. Tarlov and M. R. Zachariah, *Trends Biotechnol.*, 2012, **30**, 291.

27 L. Duchesne, G. Wells, D. G. Fernig, S. A. Harris and R. Lévy, *ChemBioChem*, 2008, **9**, 2127.

28 A. Hennig, P. M. Dietrich, F. Hemmann, T. Thiele, H. Borcherding, A. Hoffmann, U. Schedler, C. Jager, U. Resch-Genger and W. E. S. Unger, *Analyst*, 2015, **140**, 1804.

29 P. M. Dietrich, A. Hennig, M. Holzweber, T. Thiele, H. Borcherding, A. Lippitz, U. Schedler, U. Resch-Genger and W. E. S. Unger, *J. Phys. Chem. C*, 2014, **118**, 20393.

30 A. Hennig, S. Hatami, M. Spieles and U. Resch-Genger, *Photochem. Photobiol. Sci.*, 2013, **12**, 729.

31 A. Hennig, H. Borcherding, C. Jaeger, S. Hatami, C. Würth, A. Hoffmann, K. Hoffmann, T. Thiele, U. Schedler and U. Resch-Genger, *J. Am. Chem. Soc.*, 2012, **134**, 8268.

32 A. Hennig, A. Hoffmann, H. Borcherding, T. Thiele, U. Schedler and U. Resch-Genger, *Anal. Chem.*, 2011, **83**, 4970.

33 A. Hennig, A. Hoffmann, H. Borcherding, T. Thiele, U. Schedler and U. Resch-Genger, *Chem. Commun.*, 2011, **47**, 7842.

34 A. Raman, C. Jaime and V. F. Puntes, *Langmuir*, 2017, **33**, 14502.

35 S. K. Meena, C. Goldmann, D. Nassoko, M. Seydou, T. Marchandier, S. Moldovan, O. Ersen, F. Ribot, C. Chanéac, C. Sanchez, D. Portehault, F. Tielens and M. Sulpizi, *ACS Nano*, 2017, **11**, 7371.

36 J. Comenge and V. F. Puntes, *ScienceOpen Research*, 2015, DOI: 10.14293/S2199.

37 A. M. Smith, L. E. Marbella, K. A. Johnston, M. J. Hartmann, S. E. Crawford, L. M. Kozycz, D. S. Seferos and J. E. Millstone, *Anal. Chem.*, 2015, **87**, 2771.

38 L. E. Marbella and J. E. Millstone, *Chem. Mater.*, 2015, **27**, 2721.

39 C. Marquez, F. Huang and W. M. Nau, *IEEE Trans. Nanobiosci.*, 2004, **3**, 39.

40 C. C. Huang and H. T. Chang, *Chem. Commun.*, 2007, **28**, 1215.

41 J. Kimling, M. Maier, B. Okenve, V. Kotaidis, H. Ballot and A. Plech, *J. Phys. Chem. B*, 2006, **110**, 15700.

42 J. R. Winther and C. Thorpe, *Biochim. Biophys. Acta*, 2014, **1840**, 838.

43 M. Moser, R. Schneider, T. Behnke, T. Schneider, J. Falkenhagen and U. Resch-Genger, *Anal. Chem.*, 2016, **88**, 8624.

44 M. E. Ali, U. Hashim, S. Mustafa, Y. B. Che Man and K. N. Islam, *J Nanomater.*, 2012, 10.1155/2012/103607.

45 J. Jana, M. Ganguly and T. Pal, *RSC Adv.*, 2016, **6**, 86174.

46 T. Zheng, S. Bott and Q. Huo, *ACS Appl. Mater. Interfaces*, 2016, **8**, 21585.

47 S. Bhattacharjee, *J. Control. Release*, 2016, **235**, 337.

48 A. M. Jackson, J. W. Myerson and F. Stellacci, *Nat. Mater.*, 2004, **3**, 330.

49 I. Moreels, B. Fritzinger, J. C. Martins and Z. Hens, *J. Am. Chem. Soc.*, 2008, **130**, 15081.

50 B. Schuetze, C. Mayer, K. Loza, M. Gocyla, M. Heggen and M. Epple, *J. Mater. Chem. B*, 2016, **4**, 2179.

51 X. Liu, M. Yu, H. Kim, M. Mameli and F. Stellacci, *Nat. Commun.*, 2012, **3**, 1182.

52 X. Liu, M. Atwater, J. Wang and Q. Huo, *Colloids Surf. B*, 2007, **58**, 3.

53 M. R. Ivanov and A. J. Haes, *Anal. Chem.*, 2012, **84**, 1320.

54 S. M. Butterfield, A. Hennig and S. Matile, *Org. Biomol. Chem.*, 2009, **7**, 1784.

55 Y. Kim, R. C. Johnson and J. T. Hupp, *Nano Lett.*, 2001, **1**, 165.

56 Z. Liu, M. Cao, Y. Chen, Y. Fan, D. Wang, H. Xu and Y. Wang, *J. Phys. Chem. B*, 2016, **120**, 4102.

57 S. M. C. Ritchie, L. G. Bachas, T. Olin, S. K. Sikdar and D. Bhattacharyya, *Langmuir*, 1999, **15**, 6346.

58 R. C. Major and X. Y. Zhu, *J. Am. Chem. Soc.*, 2003, **125**, 8454.

59 S. Huang, R. Joso, A. Fuchs, L. Barner and S. V. Smith, *Chem. Mater.*, 2008, **20**, 5375.

60 M. Zheng and X. Huang, *J. Am. Chem. Soc.*, 2004, **126**, 12047.

61 B. Panella, A. Vargas, D. Ferri and A. Baiker, *Chem. Mater.*, 2009, **21**, 4316.

62 D. Shetty, J. K. Khedkar, K. M. Park and K. Kim, *Chem. Soc. Rev.*, 2015, **44**, 8747.

63 J. F. Young , H. D. Nguyen , L. Yang, J. Huskens, P. Jonkheijm and L. Brunsveld *ChemBioChem.*, 2010, **11**, 180.

64 L. Yang, A. Gomez-Casado, J. F. Young, H. D. Nguyen, J. Cabanas-Danés, J. Huskens, L. Brunsveld and P. Jonkheijm, *J. Am. Chem. Soc.*, 2012, **134**, 19199.

65 C. A. Simpson, A. C. Agrawal, A. Balinski, K. M. Harkness and D. E. Cliffel, *ACS Nano*, 2011, **5**, 3577.

66 J. P. Folkers, P. E. Laibinis and G. M. Whitesides, *Langmuir*, 1992, **8**, 1330.

67 M. L. Carot, V. A. Macagno, P. Paredes-Olivera and E. M. Patrito, *J. Phys. Chem. C*, 2007, **111**, 4294.

68 Q. Ong, Z. Luo and F. Stellacci, *Acc. Chem. Res.*, 2017, **50**, 1911.

69 K. M. Harkness, A. Balinski, J. A. McLean and D. E. Cliffel, *Angew. Chem. Int. Ed.*, 2011, **50**, 10554.

70 E. S. Cho, J. Kim, B. Tejerina, T. M. Hermans, H. Jiang, H. Nakanishi, M. Yu, A. Z. Patashinski, S. C. Glotzer, F. Stellacci and B. A. Grzybowski, *Nat. Mater.*, 2012, **11**, 978.

71 N. Graf, A. Lippitz, T. Gross, F. Pippig, A. Holländer and W. E. S. Unger, *Anal. Bioanal. Chem.*, 2010, **396**, 725.

72 L. Tong, E. Lu, J. Pichaandi, P. Cao, M. Nitz and M. A. Winnik, *Chem. Mater.*, 2015, **27**, 4899.

10.3.3 Gold Nanoparticles-Based Colorimetric Sensing

Gold Nanoparticle Aggregation Enables Colorimetric Sensing Assays for Enzymatic Decarboxylation

Mohamed Nilam, Andreas Hennig, Werner M. Nau and Khaleel I. Assaf*

Monitoring enzymatic processes is of fundamental importance for the understanding of the associated biological phenomena. In this work, we show that amino acid decarboxylase activity can be readily monitored by a colorimetric assay with gold nanoparticles (AuNPs), which undergo selective product-induced AuNPs aggregation. Once the carboxylate group is eliminated, the resulting diamine products trigger AuNPs aggregation, leading to a significant color change. Furthermore, the new method provides a rapid way for potential inhibitor screening.

Development of highly sensitive assays for the determination of enzymatic activities is of fundamental importance. Gold nanoparticles (AuNPs) have recently emerged as novel sensors.[1] They have been used for the detection of small molecules,[2] proteins,[3] DNA,[4] and metal ions.[5] AuNP-based colorimetric assays are built on the unique phenomenon that leads to a color change from red to blue when AuNPs aggregate.[6] The color change can be easily detected by naked eye. The extremely high extinction coefficients of AuNPs make them highly sensitive, such that they can be used in nanomolar concentrations.[7] AuNPs have shown potential applications for monitoring enzymatic activity and screening of inhibitors.[8] Guarise and coworkers have developed an assay to study protease activity based on cysteine containing short peptides at the ends, which lead to AuNPs aggregation, while the cleaved peptides are unable to induce aggregation.[8c] Similarly, a new assay was developed to investigate the activity of phosphatase.[8d] The removal of the phosphate group from short peptides was triggered by the aggregation caused by the resulting dephosphorylated peptides. The activity of L-3,4-dihydroxyphenylalanine (L-Dopa) decarboxylase has recently been studied.[8e] Contrary to native L-Dopa, the resulting dopamine was able to induce AuNPs aggregation; therefore, the reaction was monitored by the color change. Herein, we have investigated the enzymatic activity of lysine and histidine decarboxylases (LDC and HDC) using citrate-AuNPs. Despite the known examples, which provided proof-of-principle, potential assay applications would require improved responses which we now tried to achieve through an optimized molecular design. In particular, we reasoned that the best aggregation response should be achieved with diamines, with two interaction sites, which could act as ideal internanoparticle bridges.[9] Accordingly, the amino acid decarboxylation reactions can be monitored with diamine products-induced AuNP aggregation (Scheme 1).

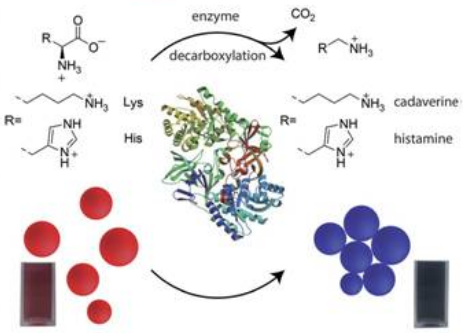

Scheme 1. Assay principle illustrating the colorimetric response of AuNPs in the course of enzymatic decarboxylase reaction.

The AuNPs aggregation is indicated by an instant red to blue color change. As the color change depends on the product concentration, this method enables both quantitative and qualitative analyses. Decarboxylation reactions play an important role in many diverse biochemical pathways in both plants and animals.[10] In particular, they represent a biosynthetic pathway for the production of polyamines, which are essential in many biological processes *e.g.*, in cell growth and differentiation, as well as in cancer development.[11] Their enzymatic reactions have been previously followed by

laborious manometric,[12] radiometric[13] or multistep colorimetric methods,[14] which are unsuitable for high-throughput screening. In our laboratory, we have developed sensitive fluorescence-based assays for a real-time monitoring of the enzymatic activity of decarboxylases.[15] The assays are based on the reversible supramolecular host-guest complexation between a fluorescent dye and a macrocyclic host, which is accompanied by a change of the dye fluorescent properties.[16] In the course of an enzymatic reaction, the production of a strong competitor (product) leads to a displacement of the dye from the host with an instant fluorescence response. The use of AuNPs provides, compared to alternative, a convenient and simple colorimertic response for monitoring enzymatic activity.

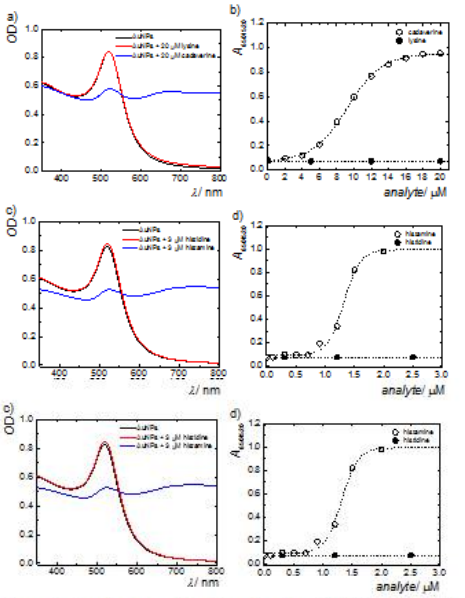

Figure 1. Experiments with lysine (top) and histidine (bottom). Left: Absorption spectral changes of AuNPs (1 nM) with the substrate and the product in 10 mM sodium phosphate buffer (pH 6.5). Right: Dependence of the ratio of the absorbance values at 520 and 650 nm on substrate and the product concentration.

AuNPs were synthesized by citrate-mediated reduction of $HAuCl_4$ citrate[5a, 16] in aqueous solution (see ESI) [5a, 17 5a, 17 5a, 17 5a, 17 5a, 17] and were characterized by using UV-Vis and DLS (see ESI, Fig. S1). The prepared AuNPs showed a maximum absorption at 520 nm and a size of 15 nm. Diamines (cadaverine and histamine) were found to completely form AuNPs aggregates at low micromolar concentrations (Figure 1), while the parent amino acids (lysine and histidine) did not cause any significant aggregation at such low micromolar concentrations, due to the shielding of the amino group by the adjacent carboxylate group. Considerable aggregation occurs only at millimolar concentrations of the amino acid substrate (see ESI, Fig. S2 and Fig. S5). For example, AuNPs start to aggregate at 2 µM cadaverine, while at this concentration of lysine no aggregation was observed (Figure 1a,1b). With histamine, the AuNPs start to aggregate at submicromolar concentrations and fully aggregate with dark blue color at 20 µM; again no aggregation was observed for histidine at such low micromolar concentrations (Figure 1c,1d).

The aggregation was further supported by DLS data. The size of the dispersed AuNPs changes from 15 nm to > 100 nm with the diamines (ESI, Fig. S4 and Fig. S7). The absorbance ratio of 650 and 520 nm, A650/520, as a function of the substrate and product concentration is shown in Figure 1. This clearly demonstrates that the substrate and the product affect the AuNPs differently, such that the enzymatic decarboxylation reaction can be monitored colorimetrically using the AuNPs. In contrast to the previously reported assay for L-Dopa decarboxylase, our assay showed a much higher sensitivity, in which the decaboxylation products induced a complete aggregation at very low micromolar concentrations, while for the monoamine dopamine, a much higher concentration was required (ca. 200 µM).[8a] This demonstrates that the design principle, involving diamines as products, is essential to obtain functional assays. The limits of detection (LOD) for cadaverine and histamine were determined as 2.5 and 0.9 µM, respectively. These values are comparable to alternative functional assays.[15a, 18]

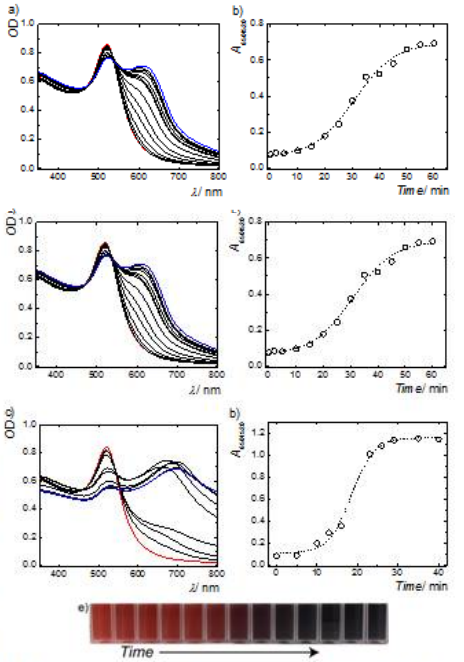

Figure 2. Experiments with lysine (top) and histidine (bottom). Left: Colorimetric enzyme assay using AuNPs (1 nM) in 10 mM sodium phosphate buffer (pH 6.5), 1 mM amino acid, 200 µg ml^{-1} enzyme, and 0.1 mM PLP. Right: Dependence of the ratio of the absorbance values at 520 and 650 nm on reaction time. Changes in the AuNPs color with reaction time (e).

Lysine and histidine decarboxylases, LDC and HDC, have been tested as representative amino acid decarboxylases. Experimentally, a typical reaction mixture containing 10 mM phosphate buffer (pH 6.5), 1 mM amino acid, 0.1 mM pyridoxal 5'-phosphate (PLP) as a cofactor,[19] and 200 µg ml^{-1} enzyme, was prepared and kept at 37 °C. To monitor the enzymatic reaction, aliquots from the mixture were taken (40 µL for LDC

or 4 µL of HDC) at given reaction time, added into a 2-ml solution of the AuNPs (concentration 1 nM), and incubated for 3-5 minutes before UV-Vis absorption measurements were recorded. In the course of the enzymatic reaction, the original peak at 520 nm of the AuNPs broadened, a new peak at ~700 nm appeared (Figure 2a,2c), and the color changed progressively from red to blue (Figure 2e). Under these experimental conditions, neither the enzyme nor the PLP coenzyme stabilize or destabilize the AuNPs, only at very high concentrations the enzyme makes the AuNPs less sensitive to aggregation. The ratio A650/520 as a function of reaction time is shown in Figure 2. The LDC reaction was almost complete after 60 minutes (Figure 2b), and that of HDC after 30 minutes (Figure 2d). The values of A650/520 can be converted to product concentrations according to the calibration curves shown in Figures 1b and 1d.

We further tested the reaction at different substrate concentrations (Figure 3). For example, the LDC reaction was studied at different lysine concentrations (0.5 - 1.5 mM). As expected, the reaction was slower at low substrate concentration (0.5 mM) and fast at higher concentrations (*e.g.*, 1.5 mM). The HDC activity was also tested with various enzyme concentrations (ESI, Figs. S11-S13).

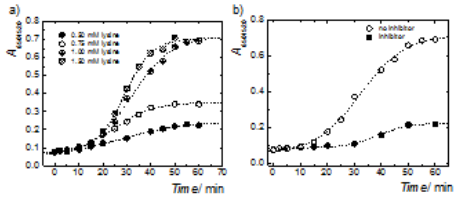

Figure 3. a) Colorimetric enzyme assay for LDC using AuNPs (1 nM) in 10 mM sodium phosphate buffer (pH 6.5), at different lysine concentrations, 200 µg mL^{-1} LDC, and 0.1 mM PLP. b) Colorimetric enzyme assay for LDC using AuNPs (1 nM) in 10 mM sodium phosphate buffer (pH 6.5), 1 mM lysine, 200 µg mL^{-1} HDC, and 0.1 mM PLP, with and without inhibitor (DL-alpha-difluoromethylornithine).

The developed assay can also be used to investigate enzyme inhibitors. DL-alpha-difluoromethylornithine, a well-known inhibitor for LDC,[19] was tested as an example (Figure 3b). The enzyme was incubated with 50 µM DL-alpha-difluoromethylornithine for 10 minutes at 37 °C, lysine was added, and the reaction was followed by UV-Vis in the same manner as for the uninhibited reaction. As expected, for an efficient inhibition, no significant color change was observed after 60 minutes (Figure 3b), with 65% inhibition in agreement with the reported IC50 value.[19]

Conclusions

In summary through an optimized molecular design, we introduce a simple, quick, and economic assay to monitor enzymatic decarboxylation reactions. The assay was applied for histidine and lysine decarboxylases, and can also be adapted for arginine, ornithine, and other decarboxylases. The parent amino acids had no effect on the AuNPs, while the resulting diamine products induced AuNPs aggregation with a visible color change from red to blue. A remarkable decrease in the enzyme activity was observed in the presence of an inhibitor, allowing for potential inhibitor screening.

Acknowledgements

This work was supported by DFG within grant NA-686/8 as part of the priority program SPP 1807 "Control of London Dispersion Interactions in Molecular Chemistry" (W.M.N.).

Notes and references

1 (a) R. Elghanian, J. J. Storhoff, R. C. Mucic, R. L. Letsinger and C. A. Mirkin, *Science*, 1997, **277**, 1078; (b) C. C. Huang, Z. Yang, K. H. Lee and H. T. Chang, *Angew. Chem. Int. Ed.*, 2007, **46**, 6824; (c) K. Saha, S. S. Agasti, C. Kim, X. N. Li and V. M. Rotello, *Chem. Rev.*, 2012, **112**, 2739; (d) R. Sardar, A. M. Funston, P. Mulvaney and R. W. Murray, *Langmuir*, 2009, **25**, 13840; (e) D. A. Giljohann, D. S. Seferos, W. L. Daniel, M. D. Massich, P. C. Patel and C. A. Mirkin, *Angew. Chem. Int. Ed.*, 2010, **49**, 3280.

2 (a) Z. S. Wu, S. B. Zhang, M. M. Guo, C. R. Chen, G. L. Shen and R. Q. Yu, *Anal. Chim. Acta*, 2007, **584**, 122; (b) K. L. Ai, Y. L. Liu and L. H. Lu, *J. Am. Chem. Soc.*, 2009, **131**, 9496.

3 V. Pavlov, Y. Xiao, B. Shlyahovsky and I. Willner, *J. Am. Chem. Soc.*, 2004, **126**, 11768.

4 R. Baron, B. Willner and I. Willner, *Chem. Commun.*, 2007, 323.

5 (a) C. C. Huang and H. T. Chang, *Chem. Commun.*, 2007, 1215; (b) Y. J. Kim, R. C. Johnson and J. T. Hupp, *Nano Lett.*, 2001, **1**, 165; (c) C. Y. Lin, C. J. Yu, Y. H. Lin and W. L. Tseng, *Anal. Chem.*, 2010, **82**, 6830.

6 (a) K. Sato, K. Hosokawa and M. Maeda, *J. Am. Chem. Soc.*, 2003, **125**, 8102; (b) S. K. Ghosh and T. Pal, *Chem. Rev.*, 2007, **107**, 4797; (c) J. S. Lee, M. S. Han and C. A. Mirkin, *Angew. Chem. Int. Ed.*, 2007, **46**, 4093.

7 (a) H. J. Chen, X. S. Kou, Z. Yang, W. H. Ni and J. F. Wang, *Langmuir*, 2008, **24**, 5233; (b) X. O. Liu, M. Atwater, J. H. Wang and Q. Huo, *Colloids Surf., B*, 2007, **58**, 3.

8 (a) Z. X. Wang, R. Levy, D. G. Fernig and M. Brust, *J. Am. Chem. Soc.*, 2006, **128**, 2214; (b) X. Y. Xu, M. S. Han and C. A. Mirkin, *Angew. Chem. Int. Ed.*, 2007, **46**, 3468; (c) C. Guarise, L. Pasquato, V. De Filippis and P. Scrimin, *Proc. Natl. Acad. Sci. USA*, 2006, **103**, 3978; (d) Y. Choi, N. H. Ho and C. H. Tung, *Angew. Chem. Int. Ed.*, 2007, **46**, 707; (e) S. Y. Park, D. Kwon, H. Mok and B. H. Chung, *Analyst*, 2013, **138**, 3146; (f) M. Wang, X. G. Gu, G. X. Zhang, D. Q. Zhang and D. B. Zhu, *Langmuir*, 2009, **25**, 2504; (g) J. Oishi, Y. Asami, T. Mori, J. H. Kang, T. Niidome and Y. Katayama, *Biomacromolecules*, 2008, **9**, 2301; (h) R. R. Liu, R. S. Liew, H. Zhou and B. G. Xing, *Angew. Chem. Int. Ed.*, 2007, **46**, 8799.

9 H. M. Zakaria, A. Shah, M. Konieczny, J. A. Hoffmann, A. J. Nijdam and M. E. Reeves, *Langmuir*, 2013, **29**, 7661.

10 (a) A. S. Tippens, S. V. Davis, J. R. Hayes, E. C. Bryda, T. L. Green and C. A. Gruetter, *Inflammation Res.*, 2004, **53**, 390; (b) M. A. Perez-Amador, J. Leon, P. J. Green and J. Carbonell, *Plant Physiol.*, 2002, **130**, 1454.

11 (a) E. W. Gerner and F. L. Meyskens, Jr., *Nat. Rev. Cancer*, 2004, **4**, 781; (b) S. L. Nowotarski, P. M. Woster and R. A. Casero, Jr., *Expert Rev Mol Med*, 2013, **15**, e3; (c) R. A. Casero, Jr. and L. J. Marton, *Nat. Rev. Drug. Discov.*, 2007, **6**, 373.
12 K. Soda and M. Moriguchi, *Biochem. Biophys. Res. Commun.*, 1969, **34**, 34.
13 S. Tanase, B. M. Guirard and E. E. Snell, *J. Biol. Chem.*, 1985, **260**, 6738.
14 A. P. H. Phan, T. T. Ngo and H. M. Lenhoff, *Anal. Biochem.*, 1982, **120**, 193.
15 (a) A. Hennig, H. Bakirci and W. M. Nau, *Nat. Methods*, 2007, **4**, 629; (b) A. Praetorius, D. M. Bailey, T. Schwarzlose and W. M. Nau, *Org. Lett.*, 2008, **10**, 4089; (c) W. M. Nau, G. Ghale, A. Hennig, H. Bakirci and D. M. Bailey, *J. Am. Chem. Soc.*, 2009, **131**, 11558; (d) M. Nilam, P. Gribbon, J. Reinshagen, K. Cordts, E. Schwedhelm, W. M. Nau and A. Hennig, *SLAS Discovery*, 2017, doi:10.1177/2472555216689288.
16 (a) R. N. Dsouza, U. Pischel and W. M. Nau, *Chem. Rev.*, 2011, **111**, 7941; (b) G. Ghale and W. M. Nau, *Acc. Chem. Res.*, 2014, **47**, 2150.
17 (a) G. Frens, *Nature Phys. Sci.*, 1973, **241**, 20; (b) K. C. Grabar, R. G. Freeman, M. B. Hommer and M. J. Natan, *Anal. Chem.*, 1995, **67**, 735.
18 (a) F. Botrè, C. Botrè, G. Lorenti, F. Mazzei, F. Porcelli and G. Scibona, *Sens. Actuator B-Chem.*, 1993, **15**, 135; (b) S. Kochhar, P. K. Mehta and P. Christen, *Anal. Biochem.*, 1989, **179**, 182.
19 Y. Takatsuka, M. Onoda, T. Sugiyama, K. Muramoto, T. Tomita and Y. Kamio, *Biosci. Biotechnol. Biochem.*, 1999, **63**, 1063.

10.3.4 Host-Guest Complexation Affects Perylene-Based Dye Aggregation

Host-Guest Complexation Affects Perylene-Based Dye Aggregation

Mohamed Nilam, Chusen Huang, Shreya Karmacharya, Gyan H. Aryal, Liming Huang, Werner M. Nau and Khaleel I. Assaf

A fluorescent perylene-based dye (**PDI**) was designed with two aromatic moieties at the imide position of the perylene core. The dye displayed contrasting behaviour with water-solube macrocycles. Cucurbit[*n*]urils (CB7 and CB8) reduced the self-aggregation of the dye molecules, while sulfonatocalixarenes (SCX4 and SCX5) and sulfonato-γ-cyclodextrin (S-β-CD) resulted in a complexation-enhanced aggrgation. In regard to potential applications, the CB8•**PDI** complex served as an excellent reporter pair inside cells to detect the uptake of neurotransmitters by fluorescence.

Introduction

Perylene diimides (**PDIs**) serve as building blocks for the development of functional materials.[1] **PDI** dyes have excellent absorption and fluorescent properties as well as outstanding thermal and photochemical stability.[2] **PDIs** are well-known for the formation of H- or J-type aggregates in aqueous solution.[2] Water-soluble **PDIs** have been studied in several lines of research, such as for biomedical as well as optoelectronic applications[3-6] and the construction of supramolecular architectures.[7] In water, however, even when hydrophilic groups are attached to the **PDI** core,[8] the dyes tend to form aggregates through π-π stacking in water, invariably resulting in an undesirable fluorescence quenching[9] and limiting their practical value, e.g., in confocal microscopy.

Among the hydrophilic groups tested have been ionic groups, such as cationic ammonium as well as anionic carboxylate, sulfonate and phosphonate groups,[10] or non-ionic residues such as polyglycerol,[11] polyethylene glycol,[12] and entire dendrons.[13] Recently, supramolecular host-guest complexation has been successfully used as an alternative, noncovalent method to inhibit aggregation of **PDIs** in water by using water-soluble macrocycles, such as cucurbit[*n*]urils (CB*n*)[14-20] or cyclodextrins (CDs).[21] Specifically, complexation of **PDI** derivatives by CB8 suppresses their aggregation and enhances their fluorescence through the formation of stable host-guest complexes in aqueous solution.[14,15] In contrast to CB8-based inclusion complex formation, other macrocycles, such as calixarenes (CXs) are known to enhance aggregation of **PDI** dyes in water.[22]

Herein, we have investigated the aggregation behaviour of a **PDI** dye with different macrocycles, such as CB*n* (CB7 and CB8), sulfonatocalixarenes (SCX4 and SCX5), β- and γ-CD, and sulfonato-β-CD (S-β-CD), see Scheme 1. The binding of the analytes with different host molecules and the photophysical properties of the host-guest complexes were investigated by UV-visible and fluorescence spectroscopy, ^{1}H NMR spectroscopy, isothermal titration calorimetry (ITC), and dynamic light scattering (DLS). Further, we have performed associative binding assays inside cells with the CB8•**PDI** reporter pair and studied the uptake of selected neurotransmitters (tryptamine, tryptophanamide, and serotonin).

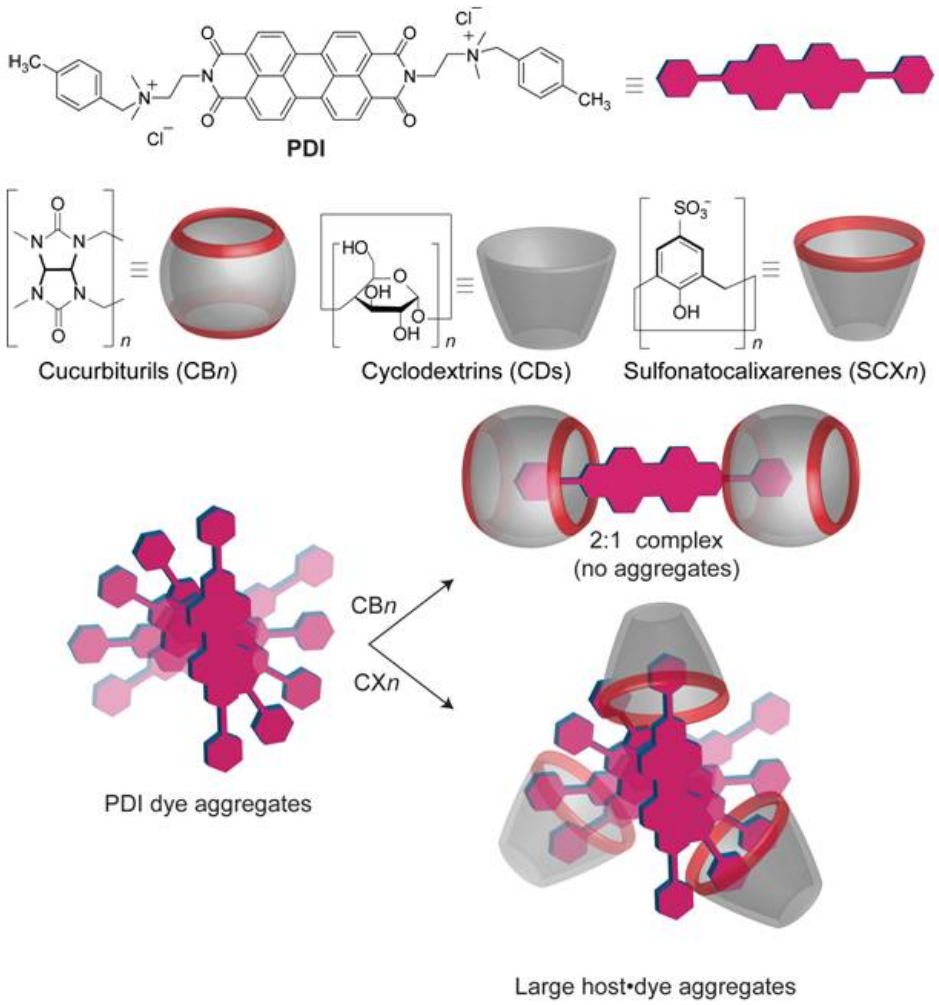

Scheme 1. Chemical and cartoon representations of the PDI dye, the investigated macrocyclic hosts, and potential binding modes with different hosts.

Results and discussion

^{1}H NMR experiments were performed to establish the formation of host-guest complexes with the different macrocycles in aqueous solution. SCX4 and SCX5, β- and γ-CD, as well as S-β-CD, produced no obvious complexation-induced ^{1}H NMR shifts (Fig. S3 in ESI†), and the aggregation of **PDI** remained unchanged or increased slightly (as demonstrated by optical spectroscopy, see below).[23] The smallest homologue, CB6, did not interact significantly with **PDI** either, as reflected by insignificant changes in the ^{1}H NMR of **PDI** in the presence of CB6. In contrast, the addition of CB7 to **PDI** in D_2O led to complexation-induced chemical shifts, namely, the methyl protons (H9) and toluene protons (H7,8) shifted up-field and the perylene protons (H1,2) down-field (Fig. 1). The former indicated the encapsulation of the toluene residue inside the cavity of CB7,[24] while the latter effect indicated the deaggregation of **PDI**.[25, 26] It is also expected that the ammonium groups are positioned near the carbonyl portals, on account of strong ion-dipole interactions, which leads us to the structural assignment shown in Fig. 1. Previous studies had shown that the intermediary CB7 cavity is too small to accommodate the perylene core itself.[15] However, the next larger CB homologue, CB8, allowed a deep stoichiometric immersion of **PDI**, signaled by a large downfield shift of the protons of the perylene-core (Fig. S2 in the ESI†). The downfield shift is therefore a direct indicator of an effective deaggregation of **PDI**.

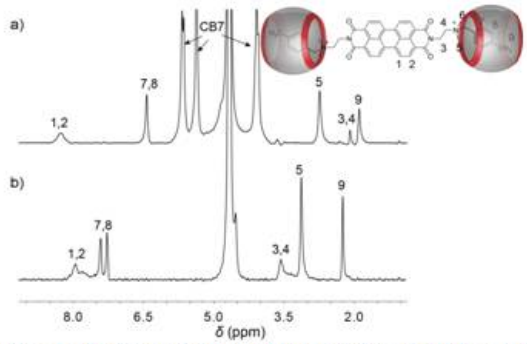

Fig. 1 ^{1}H NMR spectra of a) 0.5 mM **PDI** and b) dye 0.5 mM **PDI** with 1.0 mM CB7 in D_2O.

The encapsulation of the **PDI** inside a macrocycle cavity affects its photophysical properties,[14,15] which was studied by using UV-visible and fluorescence spectroscopy. The addition of CB7 to an aqueous solution of **PDI** (up to 5 μM) did not change the absorption, while higher concentrations (> 5 μM) resulted in a hyperchromic and hypsochromic shift from 538 nm to 533 nm, with multiple isosbestic points. These changes are characteristic for the monomeric form (Fig. 2a). The addition of CB7 (5 μM) to **PDI** also increased its fluorescence emission (Fig. 2b). The quantum yield of **PDI** in water (ϕ_f =0.01; rhodamine 6G was used as reference with ϕ_f = 0.95 in water[27]) was markedly enhanced upon complexation with CB7 (0.51 ± 0.01). In contrast, complexation of **PDI** by CB8 resulted in a gradual increase in its maximum absorption around 530 nm (Fig. 2c). This is consistent with dye deaggregation, which was confirmed by the similarity with the UV-visible absorption spectra of **PDI** in methanol, where the dye exists in its deaggregated form (see ESI†). The fluorescence intensity of **PDI** increased upon the addition of CB8 as well, accompanied by a sizable bathochromic shift (from 547 to 557 nm). The quantum yield of the CB8•**PDI** complex in water was found to be virtually quantitative (0.91 ± 0.01), in agreement with the observed trend for another **PDI** dye derivative.[14] This result indicated that CB8 monomerizes **PDI** very efficiently in water by host-guest complexation. The complexation of **PDI** with the CB*n* macrocycles was further investigated by

electrospray ionization mass spectrometry (see ESI†), which revealed 1:1 and 2:1 complexes as viable stoichiometries in the gas phase with both, CB7 and CB8.

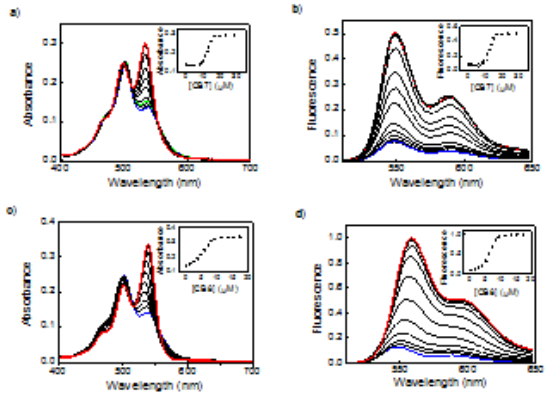

Fig. 2 Absorption (a,c) and fluorescence (b,d, λ_{exc} = 500 nm) spectra of **PDI** in water (5.0 μM) upon addition of CB7 (a,b) and CB8 (c,d). The corresponding titration curves are shown in the insets.

For comparison, we investigated the complexation of **PDI** with other families of water-soluble macrocyclic hosts. The addition of the negatively charged sulfonate-calixarenes (SCX4 and SCX5) resulted in a considerable reduction and broadening of the absorption bands and a complete quenching of the fluorescence emission, which suggested complexation-induced aggregation (Fig. S7 in ESI†).[22] The absorption band at 538 nm was bathochromically shifted to 560 nm in the presence of SCX4 or SCX5 as well as of S-β-CD, which demonstrated an increased electronic coupling of the **PDI** chromophore.[22, 23] Job's plot analysis revealed higher-order host-guest binding stoichiometries of the **PDI** complexes with the negatively charged host molecules (Fig. S9 in ESI†), reminiscent of the interactions of a perylene dye and thiazole orange.[23, 28] For comparison, the addition of native CDs resulted in insignificant binding with **PDI** (β-CD) or with a very low association constant (K_a = 48 ± 6 M^{-1}), see Fig. S8 in ESI†.

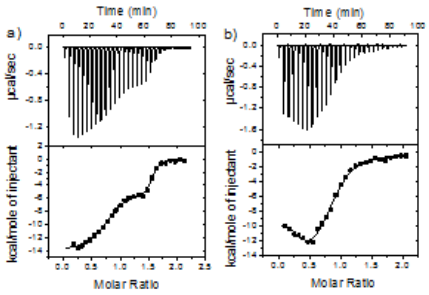

Fig. 3 ITC isotherms for the titration of a) CB7 (300 μM) into 30 μM **PDI** and b) **PDI** (400 μM) into 40 μM CB8 in water at 25 °C. Note that the titration in b) is a reverse one due to the limited solubility of uncomplexed CB8.

Isothermal titration calorimetry (ITC) experiments were performed with **PDI** as guest and CB7 and CB8 as host molecules in aqueous solution. The data (Fig. 3) verified the postulated 2:1 binding stoichiometry, and ITC experiments afforded binding constants of K_{a1} = (1.3 ± 0.9) × 10^8 M^{-1} and K_{a2} = (4.7 ± 1.7) × 10^5 M^{-1} with CB7 and K_{a1} = (5.5 ± 2.5) × 10^6 M^{-1} and K_{a2} = (5.2 ± 1.6) × 10^5 M^{-1} with CB8. Compared to a previously published dye with only one aromatic ring attached to the perylene core[15, 29] or only a perylene core,[14] the effective binding affinity ($K_{a1}K_{a2}$ > $10^{12}M^{-1}$) is higher with two aromatic ring attached to the perylene core.

Table 1. Hydrodynamic diameter[a] of PDI and its assemblies with different host molecules.

Macrocycle	Hydrodynamic diameter (nm)
none	444
CB8	0
CB7	70
β-CD	394
γ-CD	319
SCX4	1128
SCX5	1578
S-β-CD	2902

[a] Error as standard deviation is 10%, excess host was added to ensure the complexation.

We further evaluated the aggregation/deaggregation of **PDI** in the presence and absence of the investigated host molecules via dynamic light scattering (DLS). Addition of CB*n* decreased the hydrodynamic diameter (Table 1) indicating the partial (CB7) or complete (CB8) disassembly of the **PDI** aggregates. The parent CDs showed a slight reduction in hydrodynamic diameter. In contrast, the anionic macrocycles S-β-CD, SCX4, and SCX5 resulted in higher hydrodynamic diameters compared to free **PDI**. This clearly indicated that these hosts increased the aggregation process, presumably by electrostatic interactions, which reduces Coulombic repulsion in the stacked dye aggregates (see Scheme 1).[30-32]

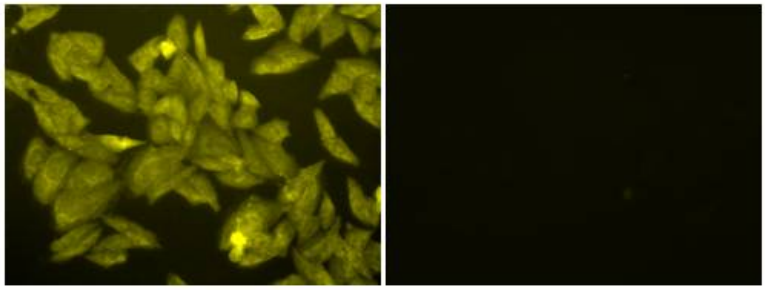

Fig. 4. Fluorescence microscopy image of CHO-K1 cells incubated with 5 μM of **PDI** and 25 μM CB8 at ambient temperature for 30 minutes (left) before and (right) after addition of 25 μM tryptamine.

diameter. In contrast, the anionic macrocycles S-β-CD, SCX4, and SCX5 resulted in higher hydrodynamic diameters compared to free **PDI**. This clearly indicated that these hosts increased the aggregation process, presumably by electrostatic interactions, which reduces Coulombic repulsion in the stacked dye aggregates (see Scheme 1).[30-32]

The stoichiometric nature of the CB8•**PDI** (2:1) complexes allows their use as reporter pairs in chemo- and bio-sensing applications, such as supramolecular tandem membrane assays.[33-39] Accordingly, we developed a robust and convenient fluorescent assay to monitor the uptake of neurotransmitters (tryptamine, tryptophanamide, and serotonin) into cells. This application presents an example of tandem membrane assay in an associative variant (formation of a ternary complex).[39-41] Note that the larger cavity of CB8 is known to be capable of complexing two aromatic molecules,[42] such that the CB8•**PDI** complex should allow subsequent binding of an aromatic analyte into the residual cavity space, leading to a net fluorescence quenching.[40] The complexation of neurotransmitters such as tryptamine, tryptophanamide, and serotonin, which had previously been shown to have micromolar affinity to CB8•perylene

complexes,[40] was first shown to be transferable to the CB8•**PDI** complexes in aqueous solution, see ESI†, with the expected switch-off response upon analyte addition. CHO-K1 cells were subsequently incubated by CB8•**PDI** and the uptake of neurotransmitters was monitored by fluorescence microscopy (Fig. 4). In detail, the uptake of the neurotransmitter into the cells that had been pre-incubated with CB8•**PDI** reporter pair resulted in an effective fluorescence quenching. Incubation of cells with **PDI** only showed weak fluorescence, demonstrating that CB8 is required for effective **PDI** uptake (Fig. 4 and Fig. S10 in the ESI†). In the fluorescence microscopy experiment, the CB8•**PDI** complex showed excellent photostability, as expected from related CB*n*•dye complexes.[14, 43-45]

Conclusions

In summary, we have investigated the host-guest complexation and aggregation/deaggregation behaviour of a PBI dye as chromophore in aqueous solution with several molecular receptors. Only CB7 and CB8 reduced the self-aggregation of **PDI** in water markedly, with concomitant significant changes in its photophysical properties. Negatively charged host molecules led to complexation-induced aggregation. We demonstrated the practical use of the resulting CB8•**PDI** complex to a sensing and assaying application, namely the uptake of neurotransmitters into CHO cells.

Experimental section

Material and methods. All chemicals except **PDI** were obtained from Sigma-Aldrich (Steinheim, Germany) and used as received. CB8 and CB7 were purchased from Strem Chemicals (Kehl, Germany) or synthesized according to the literature.[46, 47] β-, γ-CD and sulfonated-β-cyclodextrin were obtained from Cyclolab (Budapest, Hungary).
Synthesis of compound 2. 3,4,9,10-perylenetetracarboxylic dianhydride (**1**) (2.00 g, 5.1 mmol) and *N,N*-dimethyl ethylenediimide (1.36 g, 15.3 mmol) were added in 40 mL of DMF in a round-bottom flask. The mixture was stirred at 80 °C for about 12 hours under nitrogen. The reaction mixture was cooled down to ambient temperature and precipitated out with excess acetone. The precipitate was filtered using a medium porosity fritted glass filter and washed with excess acetone. The resulting red solid was dried at 100 °C in a vacuum oven overnight to yield 2.63 g of product **2** (97% yield). ^{1}H-NMR (400 MHz, CF_3COOD): δ 8.99 (d, J = 8.0 Hz, 4H), 8.91 (d, J = 8 Hz, 4H), 4.90 (br, 4H), 3.84 (br, 4H), 3.29 (s, 12H); ^{13}C-NMR (100 MHz, CF_3COOD): δ 165.8, 136.0, 132.8, 129.0, 126.1, 124.2, 121.3, 58.0, 43.8, 36.1; MALDI-TOF: m/z = 533.94 [M^++H] (calc'd. 533.59 for $C_{32}H_{29}N_4O_4^+$).

Synthesis of PDI. Compound **2** (0.10 g, 0.19 mmol), *N,N*-diisopropylethylamine (DIEA, 200 µL), and 4-methylbenzyl bromide (1.00 g, 5.4 mmol) were added to toluene (15 mL) in a round-bottom flask. The resulting mixture was stirred at 110 °C under nitrogen for 48 hours. The reaction mixture was cooled down to ambient temperature and ethyl acetate was added to form precipitate. A solid was collected using a centrifuge and washed with excess ethyl acetate. The solid was dried at 110 °C in a vacuum oven overnight. The resulting solid was re-dissolved in 5 mL of ultra-pure water and added into an anion (Cl^-) exchange column (Dowex 1-X8, 100-200 mesh, J.T. Baker Chemical Company). The column was eluted with excess ultra-pure water and a red solution was collected. The collected red solution was dried using a Labconco freeze dryer (Freezone 2.5 Liter -84 °C Benchtop) for 24 hours. A total of 0.098 g (0.12 mmol, 63% yield) of product **PDI** was collected. ^{1}H-NMR (400 MHz, DMSO-d_6): δ 9.03 (d, 4H), 8.66 (d, 4H), 7.53 (d, 4H), 7.35 (d, 4H), 4.67 (s, 4H), 4.60 (br, 4H), 3.60 (br, 4H), 3.37 (s, 12H), 2.48 (s, 6H) ppm; ^{13}C-NMR (100 MHz, DMSO-d_6): δ 163.2, 140.6, 134.6, 133.4, 129.9, 125.3, 124.7, 123.1, 67.5, 60.4, 49.7, 34.2, 21.3 ppm; MALDI-TOF: m/z = 744.99 $[M]^{2+}$ + 2H (calc'd. 744.90 for $C_{48}H_{48}N_4O_{42}^+$).

Spectroscopic measurements. Absorbance measurements were performed with a Varian Carry 4000 spectrophotometer. Fluorescent measurements were carried out with Varian Carry Eclipse spectrofluorometer. All spectroscopic measurements were performed in 3.5 mL quartz glass cuvette (Hellma Analytics, Müllheim, Germany). Hydrodynamic diameter was analysed by dynamic light scattering (DLS) with a Malvern Zetasizer nano ZS. Fluorescence microscopy images were captured by a Zeiss Axiovert 200 with a BP 546/LP 590 filter set through an Evolution QEi Media Cybernatics camera by using a 40x objective, and processed with ImageJ 1.47d (National Institute of Health USA). ITC experiments were performed with VP-ITC form Microcal Inc. (Northampton, MA, USA) at 25 °C.

Cell experiments. CHO-K1 cells (hamster Chinese ovary) were grown on a 6-well plate in F-12 Ham medium and incubated in a humidified 37 °C, 5% CO_2 incubator (herein, the cell concentration was not calculated but the concentration was the same for all 6 plates). Cells were attached overnight (for about 12 hours, when there were about 80% confluent cells in each well) and washed with DPBS three times. Then, 1 mL of paraformaldehyde (PFA, 4%) was loaded into each well and kept for 30 minutes. The cells were washed with PBS buffer for three times, subsequently incubated with 5 μM **PDI** and 25 μM CB8 for 30 minutes at ambient temperature, and then washed with PBS buffer. Neurotransmitter was then added to the cells and fluorescence microscopy images were recorded. As a control experiment, 5 μM dye (without host) was loaded inside cell by incubation for 30 minutes at ambient temperature and then washed with PBS buffer.

Conflicts of interest

There are no conflicts to declare.

Acknowledgements

Financial support from the DFG (NA 686/11-1) is gratefully acknowledged. We also thank Klaudia Brix and Maren Rehders for support with the cell culture facility and Mathias Winterhalter for instrument access.

Notes and references

1. S. S. Babu, V. K. Praveen and A. Ajayaghosh, *Chem. Rev.*, 2014, **114**, 1973-2129.
2. F. Würthner, C. R. Saha-Möller, B. Fimmel, S. Ogi, P. Leowanawat and D. Schmidt, *Chem. Rev.*, 2016, **116**, 962-1052.
3. F. Yukruk, A. L. Dogan, H. Canpinar, D. Guc and E. U. Akkaya, *Org. Lett.*, 2005, **7**, 2885-2887.
4. M. Sun, K. Müllen and M. Yin, *Chem. Soc. Rev.*, 2016, **45**, 1513-1528.
5. S. Chen, P. Slattum, C. Wang and L. Zang, *Chem. Rev.*, 2015, **115**, 11967-11998.
6. T. Weil, T. Vosch, J. Hofkens, K. Peneva and K. Müllen, *Angew. Chem. Int. Ed.*, 2010, **49**, 9068-9093.
7. F. Würthner, *Chem. Commun.*, 2004, **14**, 1564-1579.
8. C. Huang, S. Barlow and S. R. Marder, *J. Org. Chem.*, 2011, **76**, 2386-2407.
9. B. Zhang, H. Soleimaninejad, D. J. Jones, J. M. White, K. P. Ghiggino, T. A. Smith and W. W. H. Wong, *Chem. Mater.*, 2017, **29**, 8395-8403.
10. A. Nowak-Król and F. Würthner, *Org. Chem. Front.*, 2019, **6**, 1272-1318.
11. A. T. Zill, K. Licha, R. Haag and S. C. Zimmerman, *New J. Chem.*, 2012, **36**, 419-427.
12. T. Heek, C. Fasting, C. Rest, X. Zhang, F. Würthner and R. Haag, *Chem. Commun.*, 2010, **46**, 1884-1886.
13. M. Bagui, T. Dutta, H. Zhong, S. Li, S. Chakraborty, A. Keightley and Z. Peng, *Tetrahedron*, 2012, **68**, 2806-2818.
14. F. Biedermann, E. Elmalem, I. Ghosh, W. M. Nau and O. A. Scherman, *Angew. Chem. Int. Ed.*, 2012, **51**, 7739-7743.
15. G. H. Aryal, K. I. Assaf, K. W. Hunter, W. M. Nau and L. Huang, *Chem. Commun.*, 2017, **53**, 9242-9245.

16. S. T. J. Ryan, J. Del Barrio, I. Ghosh, F. Biedermann, A. I. Lazar, Y. Lan, R. J. Coulston, W. M. Nau and O. A. Scherman, *J. Am. Chem. Soc.*, 2014, **136**, 9053-9060.
17. T. Du, W. Yuan, Z. Zhao and S. Liu, *Chem. Commun.*, 2019, **55**, 3658-3661.
18. G. H. Aryal, K. W. Hunter and L. Huang, *Org. Biomol. Chem.*, 2018, **16**, 7425-7429.
19. Q. Xu, J.-L. Wang, Y.-L. Luo, J.-J. Li, K.-R. Wang and X.-L. Li, *Chem. Commun.*, 2017, **53**, 2241-2244.
20. S. T. J. Ryan, R. M. Young, J. J. Henkelis, N. Hafezi, N. A. Vermeulen, A. Hennig, E. J. Dale, Y. Wu, M. D. Krzyaniak, A. Fox, W. M. Nau, M. R. Wasielewski, J. F. Stoddart and O. A. Scherman, *J. Am. Chem. Soc.*, 2015, **137**, 15299-15307.
21. M. Zhu, G. H. Aryal, N. Zhang, H. Zhang, X. Su, R. Schmehl, X. Liu, J. Hu, J. Wei and J. Jayawickramarajah, *Langmuir*, 2015, **31**, 578-586.
22. D.-S. Guo, B.-P. Jiang, X. Wang and Y. Liu, *Org. Biomol. Chem.*, 2012, **10**, 720-723.
23. D.-S. Guo and Y. Liu, *Acc. Chem. Res.*, 2014, **47**, 1925-1934.
24. R. Wang, D. Bardelang, M. Waite, K. A. Udachin, D. M. Leek, K. Yu, C. I. Ratcliffe and J. A. Ripmeester, *Org. Biomol. Chem.*, 2009, **7**, 2435-2439.
25. Z. Chen, A. Lohr, C. R. Saha-Möller and F. Würthner, *Chem. Soc. Rev.*, 2009, **38**, 564-584.
26. Z. Chen, V. Stepanenko, V. Dehm, P. Prins, L. D. A. Siebbeles, J. Seibt, P. Marquetand, V. Engel and F. Würthner, *Chem.: Eur. J.*, 2007, **13**, 436-449.
27. D. Magde, G. E. Rojas and P. G. Seybold, *Photochem. Photobiol.*, 1999, **70**, 737-744.
28. V. Lau and B. Heyne, *Chem. Commun.*, 2010, **46**, 3595-3597.
29. G. H. Aryal, R. ViK, K. I. Assaf, K. W. Hunter, L. Huang, J. Jayawickramarajah and W. M. Nau, *ChemistrySelect*, 2018, **3**, 4699-4704.
30. D. Görl, X. Zhang and F. Würthner, *Angew. Chem. Int. Ed.*, 2012, **51**, 6328-6348.
31. T. H. Rehm, M. R. Stojković, S. Rehm, M. Škugor, I. Piantanida and F. Würthner, *Chem. Sci.*, 2012, **3**, 3393-3397.
32. Y. Shao, G.-Z. Yin, X. Ren, X. Zhang, J. Wang, K. Guo, X. Li, C. Wesdemiotis, W.-B. Zhang, S. Yang, M. Zhu and B. Sun, *RSC Adv.*, 2017, **7**, 6530-6537.
33. A. Hennig, H. Bakirci and W. M. Nau, *Nat. Methods*, 2007, **4**, 629-632.
34. R. N. Dsouza, A. Hennig and W. M. Nau, *Chem.: Eur. J.*, 2012, **18**, 3444-3459.
35. M. Nilam, P. Gribbon, J. Reinshagen, K. Cordts, E. Schwedhelm, W. M. Nau and A. Hennig, *SLAS Discov.*, 2017, **22**, 906-914.
36. A. Norouzy, Z. Azizi and W. M. Nau, *Angew. Chem. Int. Ed.*, 2015, **54**, 792-795.
37. G. Ghale and W. M. Nau, *Acc. Chem. Res.*, 2014, **47**, 2150-2159.
38. B. T. Nguyen and E. V. Anslyn, *Coord. Chem. Rev.*, 2006, **250**, 3118-3127.
39. G. Ghale, A. G. Lanctôt, H. T. Kreissl, M. H. Jacob, H. Weingart, M. Winterhalter and W. M. Nau, *Angew. Chem. Int. Ed.*, 2014, **53**, 2762-2765.
40. F. Biedermann, D. Hathazi and W. M. Nau, *Chem. Commun.*, 2015, **51**, 4977-4980.
41. F. Biedermann, G. Ghale, A. Hennig and W. M. Nau, *ChemRxiv*, 2019, DOI: 10.26434/chemrxiv.9735152.v1.
42. F. Biedermann and W. M. Nau, *Angew. Chem. Int. Ed.*, 2014, **53**, 5694-5699.
43. M. D. Rahn, T. A. King, A. A. Gorman and I. Hamblett, *Appl. Opt.*, 1997, **36**, 5862-5871.
44. J. Mohanty, K. Jagtap, A. K. Ray, W. M. Nau and H. Pal, *ChemPhysChem*, 2010, **11**, 3333-3338.
45. M. A. Alnajjar, J. Bartelmeß, R. Hein, P. Ashokkumar, M. Nilam, W. M. Nau, K. Rurack and A. Hennig, *Beilstein J. Org. Chem.*, 2018, **14**, 1961-1971.
46. J. Kim, I.-S. Jung, S.-Y. Kim, E. Lee, J.-K. Kang, S. Sakamoto, K. Yamaguchi and K. Kim, *J. Am. Chem. Soc.*, 2000, **122**, 540-541.
47. C. Marquez, H. Fang and W. M. Nau, *IEEE Trans. Nanobiosci*, 2004, **3**, 39-45.

Electronic Supplementary Information (ESI)

Host-Guest Complexation Affects Perylene-Based Dye Aggregation

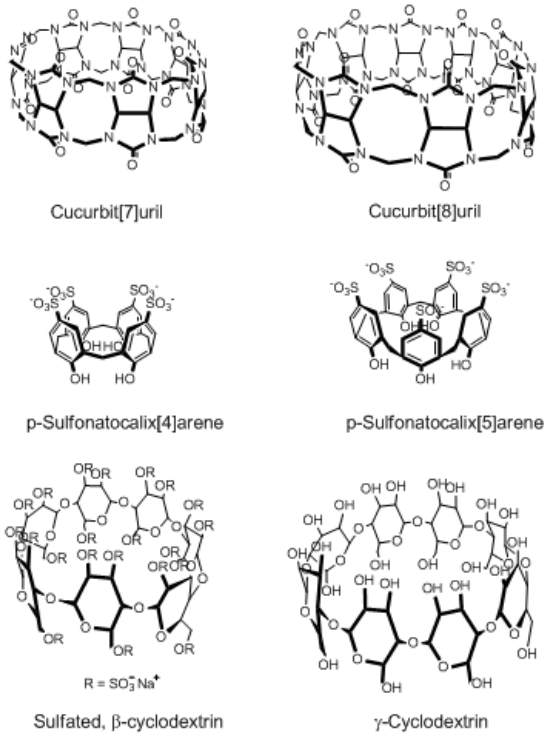

Fig. S1. Chemical structures of the investigated host molecules.

Determination of Fluorescence Quantum Yield

The fluorescence quantum yields of the complex ($\phi_{CB8\cdot PDI}$) was determined according to literature.[1] In brief, the integrated peak area of the fluorescence emission of the CB8•**PDI** complex ($I_{CB8\cdot PDI}$) and the standard (I_{st}) as well as their respective absorbance values at the excitation wavelength ($A_{CB8\cdot PDI}$ and A_{st}) were entered in the below equation, which contained the quantum yield of the standard (ϕ_{st}) as reference.

$$\Phi_{CB8.PDI} = \Phi_{St} \times \frac{I_{CB8.PDI} * A_{St}}{I_{St} * A_{CB8.PDI}}$$

Rhodamine 6G was used as standard with ϕ_{st} = 0.95 in water. Correction curves for the fluorescence measurements were obtained with a dye kit certified by the Federal Institute for Material Research and Testing (BAM, Germany).[2]

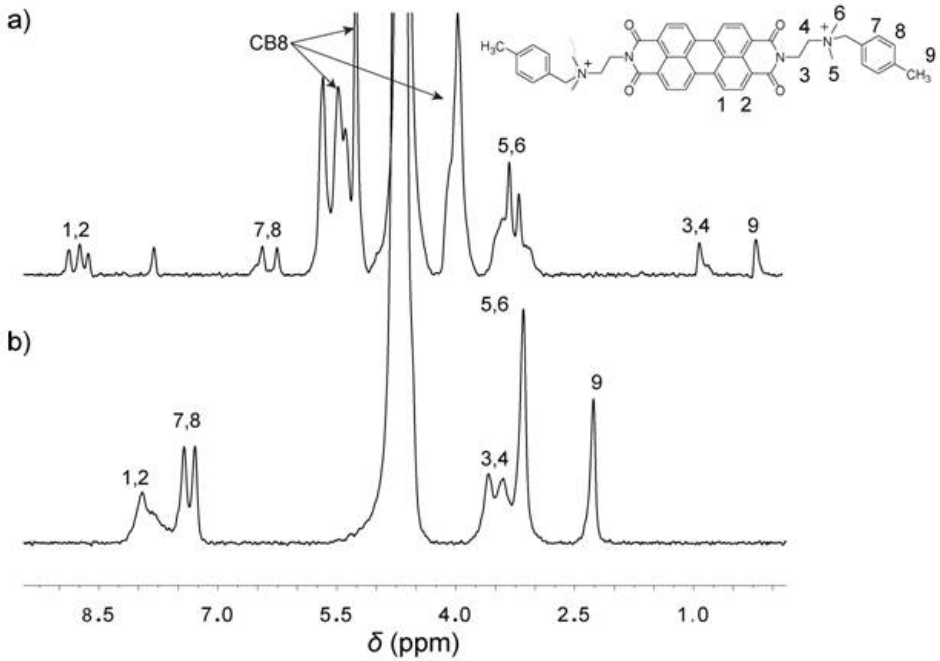

Fig. S2. ^{1}H NMR spectra in D_2O for a) 0.5 mM PDI and 1.0 mM CB8 (the solubility of CB8 increased upon addition of PDI) and b) 0.5 mM PDI only.

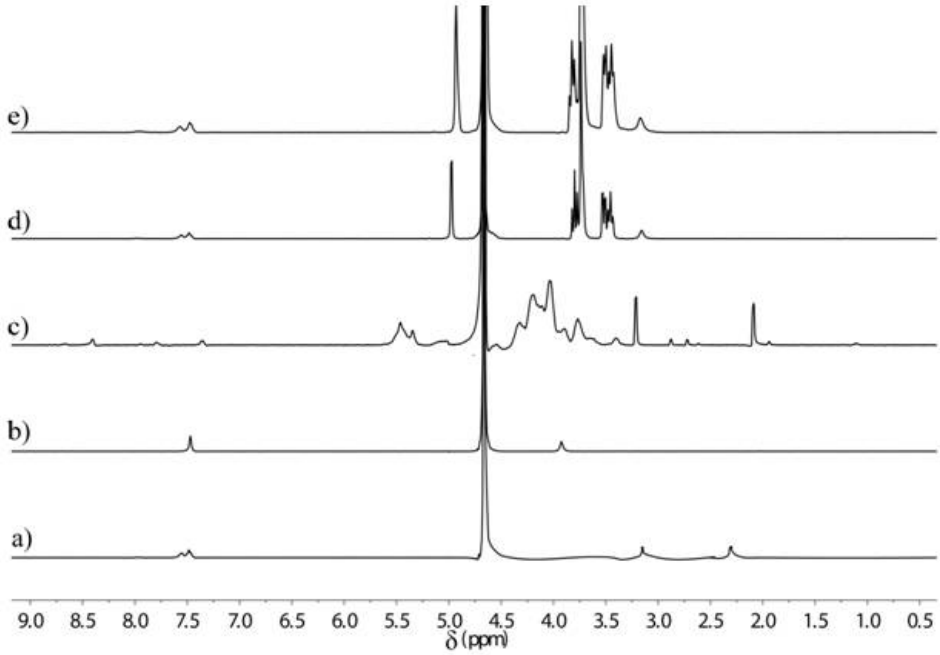

Fig. S3. ^{1}H NMR spectra in D_2O for a) 0.5 mM PDI only, b) 0.5 mM PDI and 0.5 mM SCX4, c) 0.5 mM PDI and 0.5 mM S-β-CD, d) 0.5 mM PDI and 0.5 mM γ-CD, and e) 0.5 mM PDI and 0.5 mM β-CD.

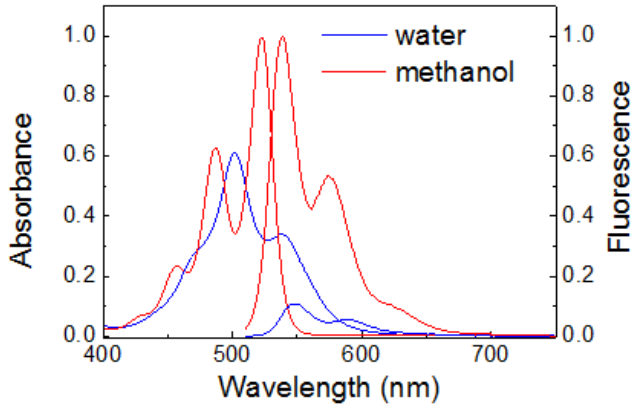

Fig. S4. Absorption and fluorescence spectra of PDI (12 μM) in water and methanol (λ_{exe} = 500 nm).

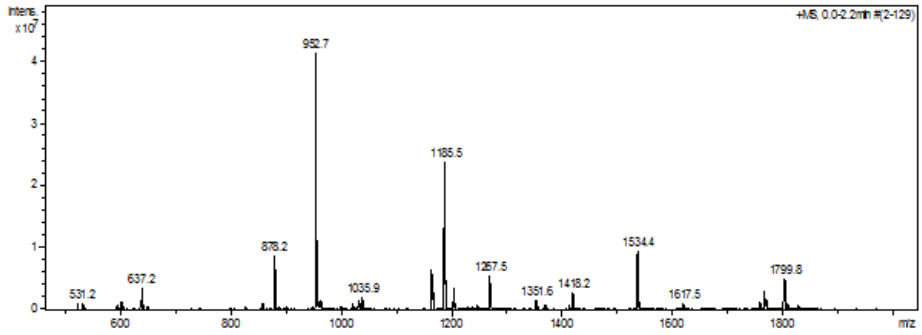

Fig. S5. ESI-MS (positive) spectrum of CB7•**PDI**. Signals at m/z of 952.7, 1185.5, and 1534.4 correspond to $[CB7•\mathbf{PDI}]^{2+}$, $[CB7\text{-}Na]^{+}$, and $[2CB7•\mathbf{PDI}]^{2+}$, respectively.

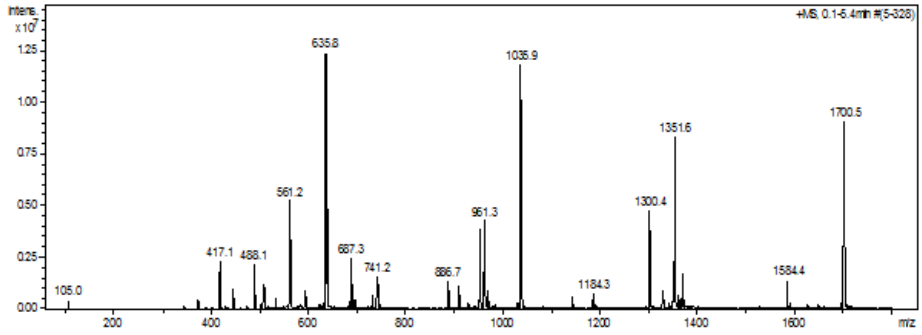

Fig. S6. ESI-MS (positive) spectrum of CB8•**PDI**. Signals at m/z of 417.1, 687.3, 1035.9, 1351.6, and 1700.5 correspond to $[\mathbf{PDI}]^{2+}$, $[CB8\text{-}2Na]^{2+}$, $[CB8•\mathbf{PDI}]^{2+}$, $[CB8\text{-}Na]^{+}$, and $[2CB8•\mathbf{PDI}]^{2+}$, respectively.

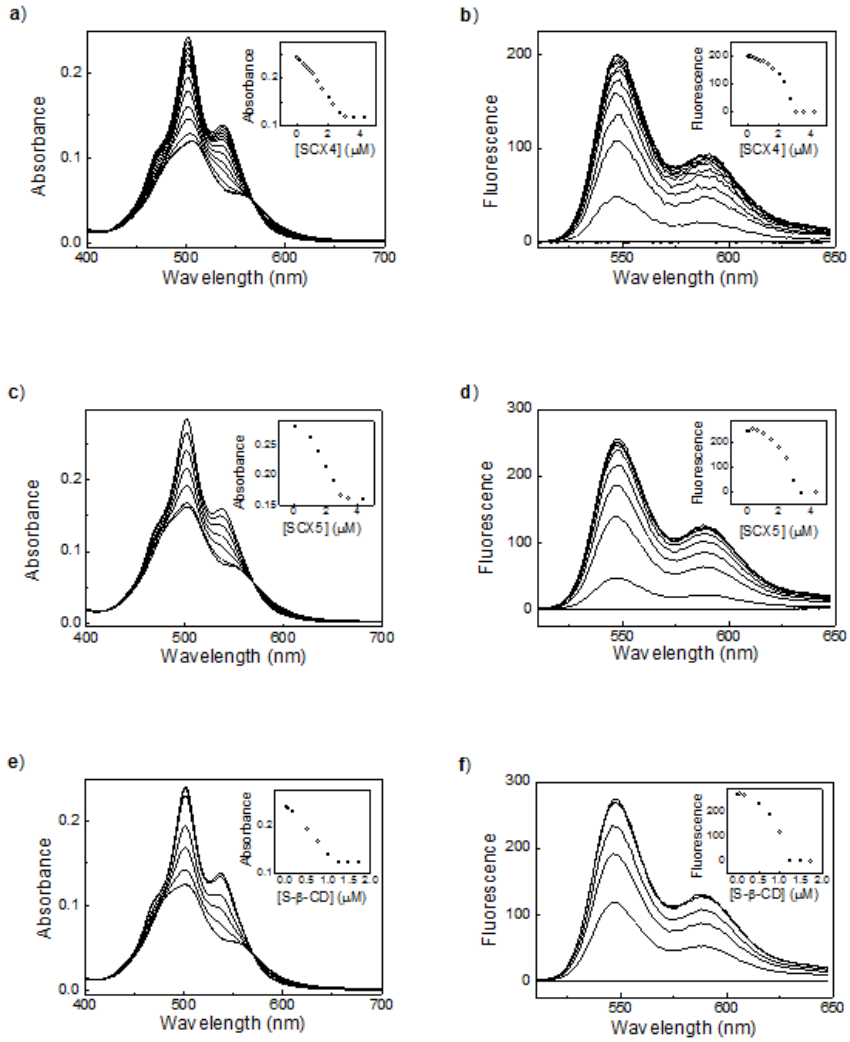

Fig. S7. Absorption (a, c, e) and fluorescence (b, d, f, λ_{exc} = 500 nm) spectra of PDI in water (5.0 μM) upon addition of SCX4 (a, b), SCX5 (c, d) and S-β-CD (e, f). The corresponding titration curves are shown in the insets.

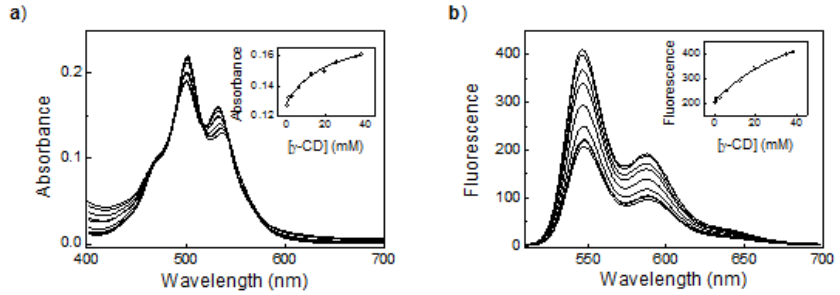

Fig. S8. Absorption and fluorescence spectra of PDI (5.0 μM) upon addition of γ-CD a) absorption spectra b) fluorescence spectra (λ_{exc} = 500 nm). The corresponding titration curves are shown in the insets.

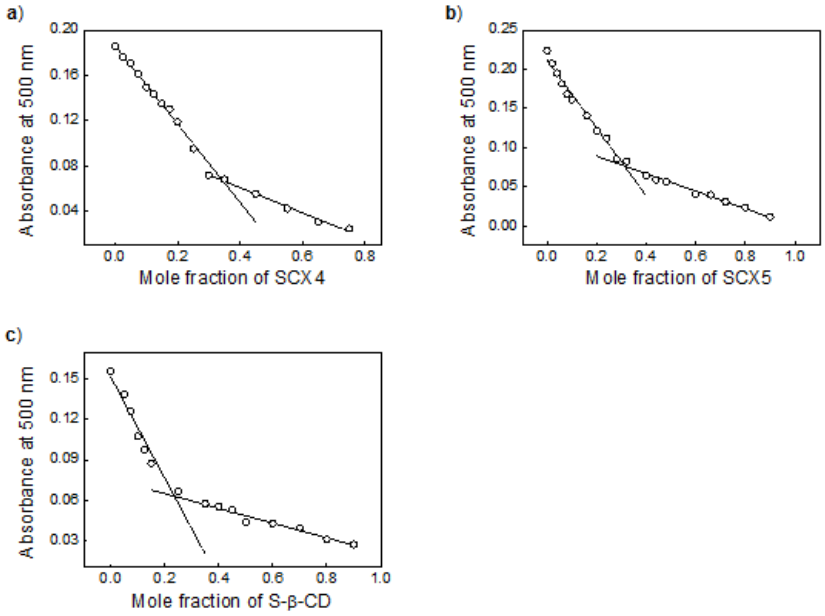

Fig. S9. Job's plots for a) SCX4, b) SCX5, and c) S-β-CD upon complexation with PDI in water. The total host and guest concentration is constant. Job's plots indicated that higher-order of host-guest binding stoichiometries of the PDI complexes with the negatively charged host molecules.

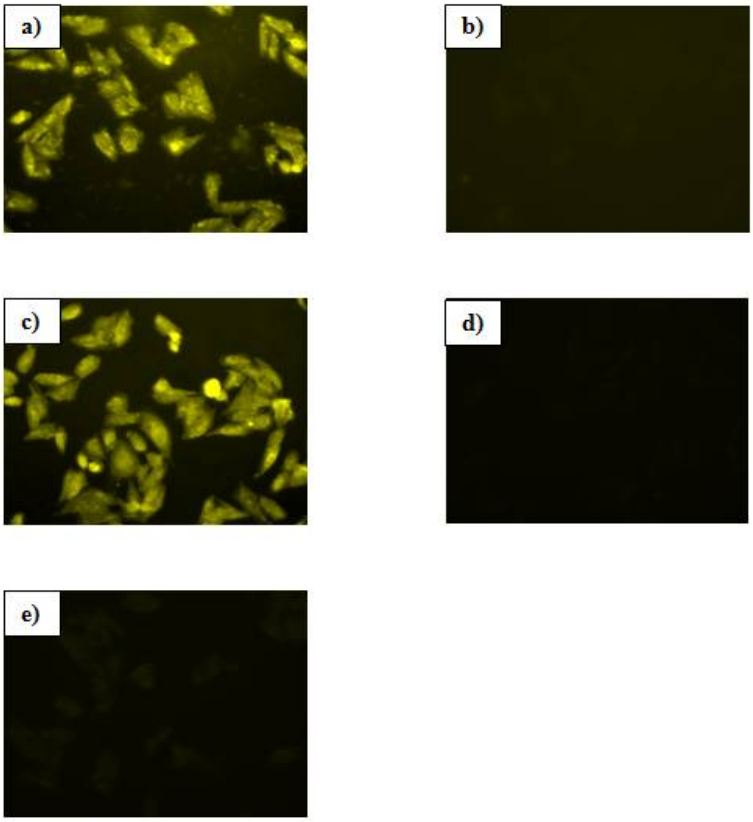

Fig. S10. Fluorescence microscopy images of CHO-K1cells incubated with 5 μM PDI and 25 μM CB8 at ambient temperature for 30 min a) before and b) after addition of 50 μM tryptophanamide, c) before and d) after the addition of 200 μM serotonin, and e) dye only without CB8 and without analyte (weak fluorescence).

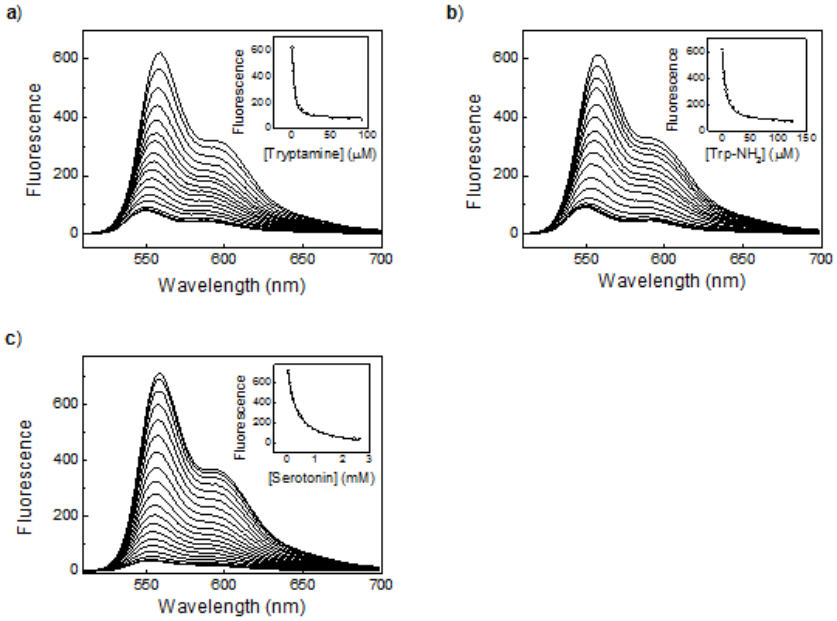

Fig. S11. Fluorescence titration of 5 μM PDI and 25 μM CB8 in water upon addition of a) tryptamine, b) tryptophanamide, and c) serotonin. The insets show the corresponding fluorescence titration plots.

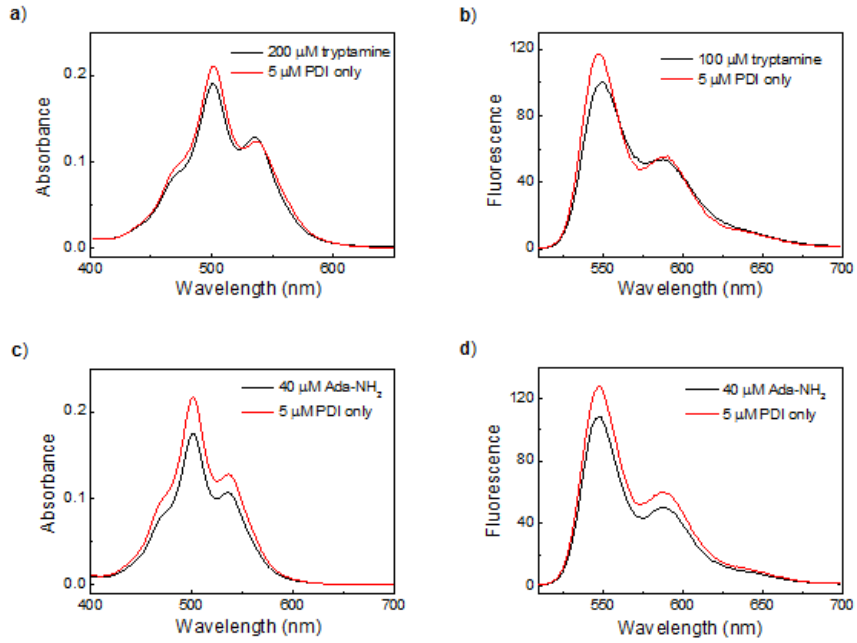

Fig. S12. Optical response of CB8•**PDI** (25 μM CB8, 5 μM **PDI**) upon the addition of two different analytes. a) absorption and b) fluorescence spectra upon addition of 100 μM tryptamine (an associative binding is proposed) and c) absorption, d) fluorescence spectra upon addition of 40 μM adamantylamine (a displacement of **PDI** is proposed).

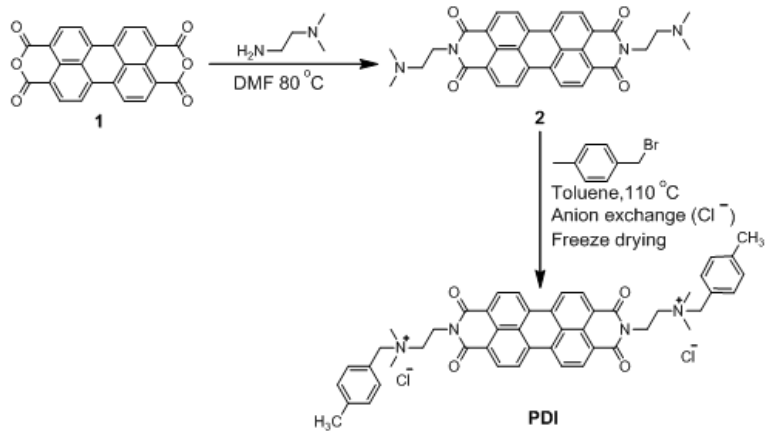

Scheme S1. Synthesis of PDI.

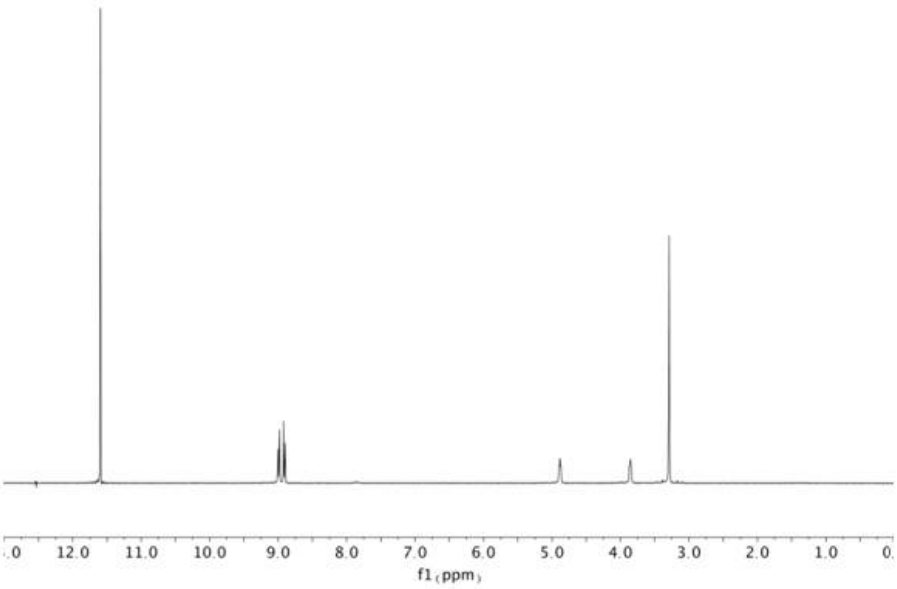

Fig. S13. ^{1}H-NMR spectra of 2 in CF_3COOD.

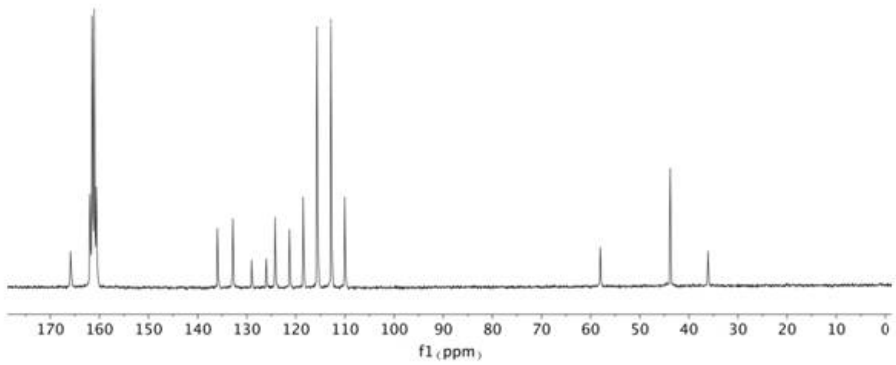

Fig. S14. ^{13}C-NMR spectra of **2** in CF_3COOD.

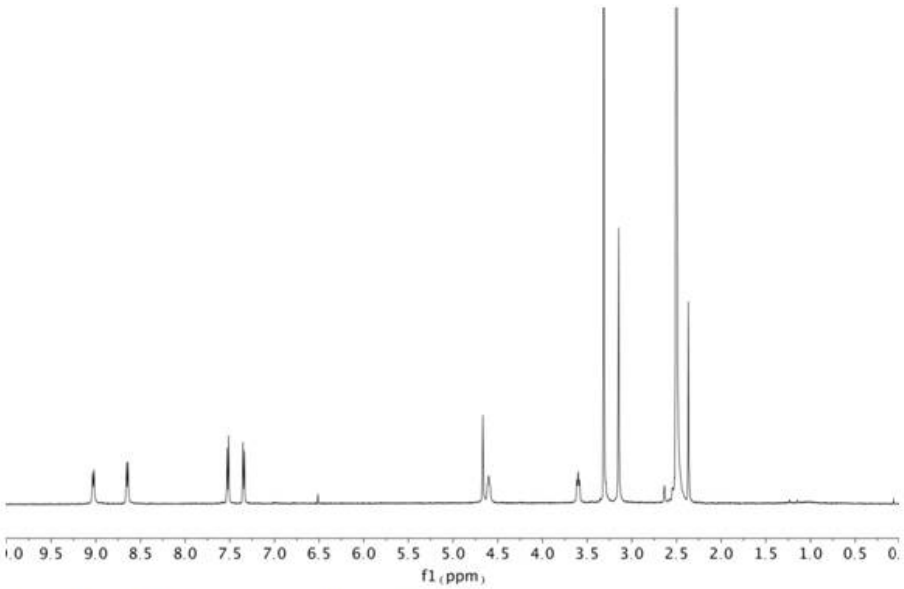

Fig. S15. ^{1}H-NMR spectra of PDI in DMSO-d_6.

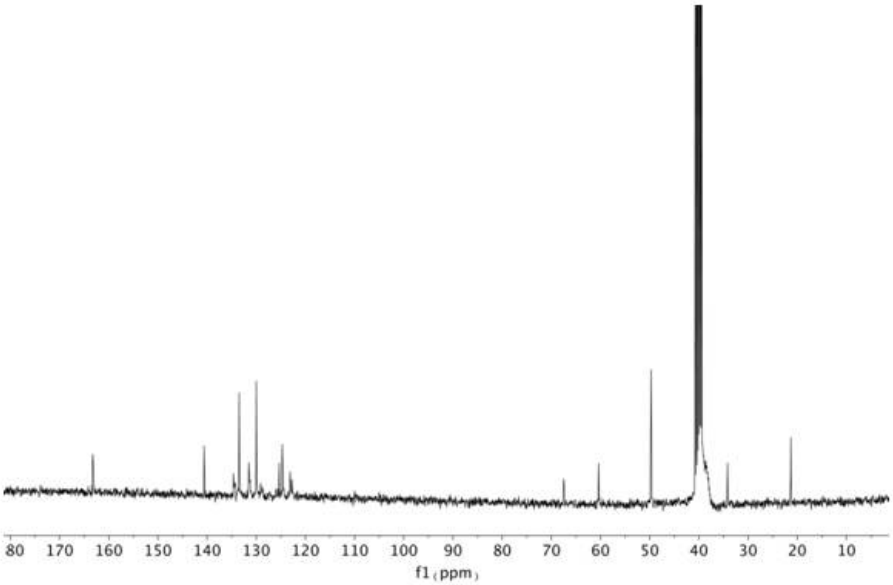

Fig. S16. ^{13}C-NMR spectra of **PDI** in DMSO-d_6.

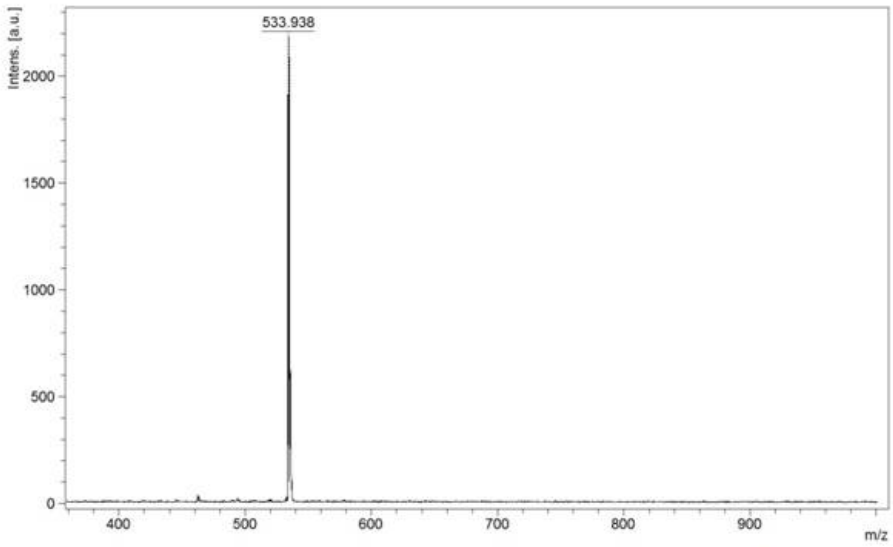

Fig. S17. MALDI mass of **2** in methanol using 2,5-dihydroxybenzoic acid (DHB) as a matrix. (M^{2+} + H): observed 533.94 Da, calculated mass 733.59 Da.

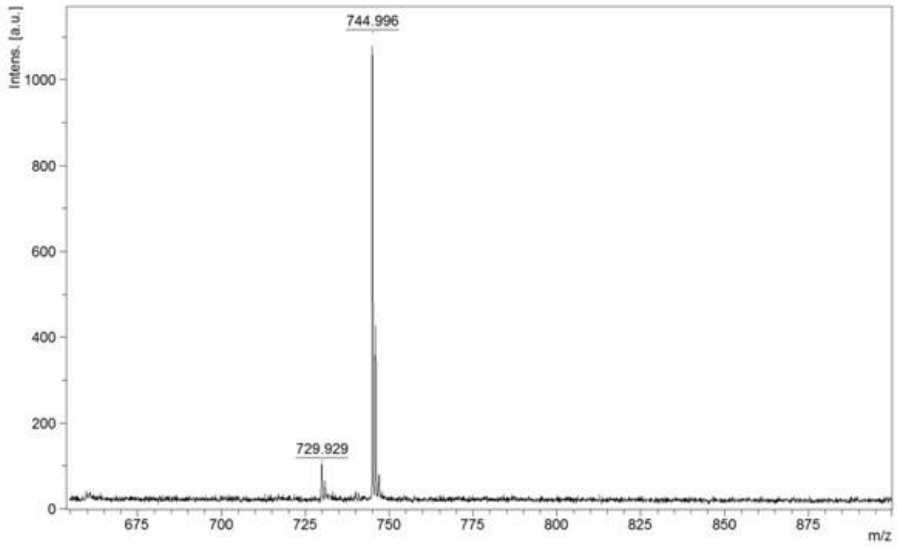

Fig. S18. MALDI mass of **PDI** in methanol using 2,5-dihydroxybenzoic acid (DHB) as a matrix. (M^{2+} + 2H): observed 744.99 Da, calculated mass 744.90 Da.

References

1. C. Würth, M. Grabolle, J. Pauli, M. Spieles and U. Resch-Genger, *Nat. Protoc.*, 2013, 8, 1535-1550.
2. U. Resch-Genger, K. Hoffmann and A. Hoffmann, *Ann. N. Y. Acad. Sci.*, 2008, 1130, 35-43.